1994

Charge Redistribution And Electronic Behaviour Of Gold-coper Alloys: Bulk And Surface Studies

Markus Kuhn

Charge Redistribution and Electronic Behaviour of Au-Cu Alloys: Bulk and Surface Studies

by

Markus Kuhn

Department of Chemistry

Submitted in partial fulfilment
of the requirements for the degree of
Doctor of Philosophy

Faculty of Graduate Studies
The University of Western Ontario
London, Ontario
October, 1993

ISBN 0-315-90534-4

Canada

ABSTRACT

The electronic and physical properties of noble metals and their alloys have been the focus of research for many years. They are considered prototypes for the investigation of full *d*-band interactions and Friedel charge screening.

We have studied a series of bulk Au-Cu alloys, with varying compositions and ordering, in order to determine the nature and amount of charge transfer between the two components. We also examine the validity of two models; charge compensation and *d-d* repulsion. To probe the electronic behaviour upon alloying, we employ two techniques, namely photoemission and X-ray absorption. From photoemission, we find unique behaviour in the alloy valence band, indicating separate contribution from each component and distinctive movement showing the validity of the *d-d* repulsion model. Semi-quantitative results for the amount of *d* charge transfer (independently determined by X-ray absorption experiments) and conduction charge transfer from Mössbauer isomer shifts, clearly show that Au loses *d* charge but is overcompensated by a gain of *s-p* charge giving the Au site a small overall gain of charge in line with electroneutrality and electronegativity arguments. It was found that the amount of charge transfer is directly related to the local configuration of the alloy (number of Cu neighbours around the Au site) and that the valence band behaviour is dependent on the dilution of Au-Au interactions (and also Cu-Cu interactions).

Also of more recent importance, is the study of model bimetallic catalysts, such as Au on Ru(001) and Cu on Ru(001). We have focussed not only on these bimetallic

systems but also on a trimetallic system, Au-Cu on Ru(001). Using the results of the bulk study, indicating unique behaviour upon alloying especially in the valence band, we have found that co-deposition of these components, at room temperature and in the monolayer regime, leads to alloy formation which is not observable in the bulk. We propose a mechanism based on the heats of adsorption of the components, the heat of formation of Au-Cu alloys, and the role of the substrate in reducing the activation barrier.

ACKNOWLEDGEMENTS

I would like to thank a number of people with whom I have associated with over the past few years.

First and foremost, I would like to thank Dr. T.K. Sham, my supervisor, for his encouragement and support, especially through the more difficult times. Without his enthusiastic tutelage I would not be where I am today.

I would like to thank certain people for their technical assistance without whose help the experiments would not have been possible; Kim Tan at CSRF, Johnny Kirkland of Naval Research Laboratories located at NSLS, Gerry Lamble at NSLS, and Dan Wallace at SRC.

I would also like to thank my lab compatriots, past and present; Arthur Bzowski, Ramaswami Sammynaiken, Steve Naftel, Xiong Jiang, and Drs. Detong Jiang and Z.H. Lu. Also a heartfelt thanks to my fellow basement dwellers; Dr. Nils Petersen, Dr. Dave Bjarneson, Ali Paprica, Paul Wiseman, and Glenn Munro.

Lastly, I would like to thank my wife, Mary (and the little one), for all her support and understanding and my parents for putting up with the "professional student".

I dedicate this work to my wife and my parents.

TABLE OF CONTENTS

SECTION I: Au-Cu BULK ALLOYS

CHAPTER THREE

CHAPTER FOUR

CHAPTER FIVE

LIST OF TABLES

LIST OF FIGURES

CHAPTER ONE

General Introduction

1.1 Introduction

Noble metals, and their alloys, have played an important role throughout the history of mankind. In ancient times their role was determined by their unique physical properties and relative availability (or lack thereof). Some of the first tools and weapons were crafted from deposits of copper. Later, gold and silver (also copper) became the primary metals for currency, on which ancient civilizations based their economy. This was due, not only because of their relative scarcity (especially of gold and silver) and attractiveness, but because these metals were easy to meld and shape to the desired product. Coins could be produced with the symbol or likeness of the current narcissistic despot, for all of the subjects to be reminded of during their daily activities, a practice that has continued to this day. Artisans also took advantage of these properties to create works of art that have survived through the ages.

Some properties of these metals have long been known. Gold, it was found, was inert to contamination while copper and silver were found to be fairly reactive in the environment. Melting of these metals was easily accomplished and these metals were found to be completely miscible forming solid solutions (alloys) throughout the

compositional range. The quest for possession of these metals, Au in particular, has spawned a mass pursuit leading to countless wars, pirates, and gold rushes and has even literally led to the extermination of peoples (by the Spanish in Central and South America).

Given the importance of these metals, they and their alloys have been the focus of studies for many centuries. We could begin by mentioning that the first "scientific" study could have been the attempt by alchemists in the middle ages to produce gold from more abundant, and less desirable, elements such as lead. More recently, with the advent of the industrial revolution, the bulk macroscopic properties of Au and Au-Cu alloys (the focus of this study), such as conductivity, resistivity, and the associated composition-temperature dependence have been determined rigorously. Until this century, however, no determination of the microscopic properties, electronic and physical, could be made to shed light on the macroscopic behaviour. The formulation of quantum mechanics and the experimental developments that it has spawned has allowed examination of the electronic interaction and physical structure of the pure metals and their alloy counterparts.

Since they have been well studied, noble metal alloys are considered prototypes for investigating a variety of questions regarding metal-metal interactions. As was stated previously, Au-Cu alloys are completely miscible in the bulk and form solid solutions throughout the compositional range. Another feature of these alloys is that they form superlattice phases in certain composition regimes (as will be described in Section 3.5). This allows the study of the disorder-order transition. It is for these reasons that the

samples prepared for this study not only vary in their composition but also in their order. For both metals their electronic configuration has changed upon going from their atomic state to their metallic state. Overlapping of the valence levels, upon solid formation, leads to a band structure characterized by a nominally full *d* band lying a few eV below the Fermi level and a conduction band (with mainly *s-p* character due to hybridization) that spans the Fermi level. This allows the study of "filled" *d*-band interactions. At low compositions of either constituent, these alloys have long been used as prototypes for the study of Friedel charge screening.[1] This involves considering the low composition constituent as an impurity in the high composition lattice and thereby allows determination of what effect this perturbation has on the local electronic environment mainly in terms of the screening ability of itinerant electrons.

Despite the volume of recent work on this system debate still occurs on the amount of *d-d* interaction, the nature of the Au-Cu bond itself (i.e. the direction and amount of charge transfer), and what influence the local environment has on the electronic properties of the system.

Au is the most electronegative of the metallic elements and therefore upon alloying with Cu, for example, an overall transfer of charge from the Cu site to the Au site is expected. This overall charge transfer, however, must be small to preserve electroneutrality required by metallic systems. Positive ^{197}Au Mössbauer isomer shifts[2,3] do indeed show an increase of contact density at the nucleus (mainly *s* charge) at the Au

site, in Au-Cu alloys relative to pure Au.[a] However, relative to pure Au, positive Au 4*f* core level shifts indicate an apparent depletion of charge at the Au site not only for the Au-Cu system but for a variety of other Au intermetallics.[3,4,5,6,7,8,9] At first glance, the apparent collapse of the Au core levels towards the nucleus would indicate that charge has been lost from the Au site allowing a larger effective Coulombic potential for the remaining electrons. These same trends, Mössbauer and Au core level shifts, have also recently been observed for Au-Ag alloys[10] and other Au intermetallics (such as Au-Ti[11] and Au-Ta[12] alloys). A charge compensation model[4] has often been used to explain these apparent inconsistencies, that is that, upon alloying, Au loses valence *d* charge but is overcompensated by a gain of mainly *s-p* charge from Cu. Because of the larger screening ability of the *d* electrons, even with a comparable gain of *s-p* electrons, their loss leads to a higher effective Coulombic potential for the remaining electrons thereby causing a positive Au 4*f* core level shift. In addition, the overcompensation of *s-p* charge gives the Au site an overall gain of charge in line with electronegativity arguments.

Much debate has occurred as to the nature and extent of the Au and Cu *d*-band interactions in both experiment and theory (calculations), especially in the case of the Cu_3Au alloy.[8,13,14,15,16,17,18,19,20,21,22,23,24] As early as 1962, Catterall *et al.*[13] had published work supporting the idea that the alloy *d* band is merely a superposition of the respective constituent *d*-band components. Since then, both the localized[8,16,21,22] and mixed band[13,14,15,17,28] views have had experimental support with theoretical models (calculations)

---

[a] The Mössbauer results along with the upcoming discussion on core level shifts and the charge compensation model will be elaborated on in Chapter 3.

indicating some overlap but with reasonably well-defined "Au" and "Cu" regions.[18,19,23,24] The localized approach is sometimes referred to as the *d-d* repulsion model and can be viewed as the repulsive overlap of filled constituent bands resulting in separation of those bands. The mixed band view, on the other hand, points to extensive *d* band mixing resulting in the loss of well-defined "Au" and "Cu" regions in the valence band. It has also been shown by calculations (not as much so by experiment) that the order-disorder transition has an effect on the valence band features exhibited by these *d* states.[18,19,20,24] In this study we will attempt to answer the questions regarding the nature of the Au-Cu bond in terms of charge transfer and valence band behaviour focussing on the validity of the charge compensation and *d-d* repulsion models.

Given that we have concerned ourselves with attempting to answer some fundamental questions regarding the nature of the Au-Cu interactions in their bulk state upon alloying, we have ignored the more recent and important use of noble metals, that is their role in bimetallic catalysis. Cu, especially, appears as a component in many bimetallic catalysts used in important industrial processes.[25,26] The electronic structure of bimetallic surfaces is of great relevance in the design of new materials. Of particular interest are bimetallic materials of which the components do not form alloys or metallic compounds in the bulk, yet they interact significantly at the interface when one component is adsorbed on the surface of the other. Many fundamental studies have been performed to determine the electronic and physical structure of these systems which are responsible for this catalytic behaviour.[25,26,27,28,29] Cu-Ru is the most representative bimetallic system and therefore has generated a great deal of research.[25,26,30,31,32,33,34,35,36]

Cu is found to be greatly perturbed upon adsorption and that this leads to radically changed electronic and chemical properties compared to those exhibited in the bulk. The most typical system studied is the Cu adsorption on the (001) face of a Ru crystal (for the hexagonal-close-packed structure that crystalline Ru exhibits, the crystal plane studied is the (0001) face but through convention the terminology has been shortened to (001)).

Not only are we interested in the separate behaviour of Au and Cu thin films on Ru(001), but in light of our bulk Au-Cu studies, we are also interested in the behaviour of co-deposited Au-Cu thin films (trimetallic system). It would be interesting to compare the interactions of these components on the Ru surface with that of the bulk alloys. A fundamental question to be answered is what conditions are required for alloying of Au-Cu to occur on Ru(001) and if an alloy is formed how does its electronic and physical behaviour compare to that of its bulk counterpart. Each co-deposition will form a unique system, in that, there has been no previous work performed on co-deposited Au-Cu thin films in the monolayer regime. It is hoped that a systematic study of Au-Cu interactions in the bulk system, as a function of composition and ordering, will show us distinctive alloying behaviour, both in the valence band and core levels at both constituent sites, which we can use as a basis to understand the electronic interactions that occur in our surface species.

To reach that goal we will use a variety of experimental techniques to probe the electronic interactions between Cu and Au both in the bulk and on the Ru(001) substrate. Chapter 2 will focus on the most general technique used for both the bulk and surface studies, namely photoemission. Also in Chapter 2 will be a section dealing with the use

of synchrotron radiation as a source for not only the photoemission experiments but also X-ray absorption experiments carried out on the bulk alloys. The remainder of the thesis will be divided into two sections. Chapters 3, 4, and 5 will deal with the bulk Au-Cu system while Chapters 6 and 7 will concentrate on the surface Au-Cu system.

1.2 References

1. J. Friedel, Philos. Mag. **43**, 153 (1952).

2. P.G. Huray, L.D. Roberts, and J.D. Thomson, Phys. Rev. B **4**,2147 (1971).

3. T.K. Sham, R.E. Watson, and M.L. Perlman, Ad. Chem. Series **194** ACS.39 (1981).

4. R.E. Watson, J. Hudis, and M.L. Perlman, Phys. Rev. B **4**, 4139 (1971).

5. T.K. Sham, M.L.Perlman, and R.E. Watson, Phys. Rev. B **9**, 539 (1979).

6. G.K. Wertheim, R.L. Cohen, G. Crecelius, K.W. West, and J.H. Wernick, Phys. Rev. B **20**, 860 (1979).

7. P.M. Th. M. van Attekum, G.K. Wertheim, G. Crecelius, and J.H. Wernick, Phys. Rev. B **22**, 3998 (1980).

8. W. Eberhardt, S.C. Wu, R. Garrett, D. Sondericker, and F. Jona, Phys. Rev. B **31**, 8285 (1985).

9. V.L. Morruzzi, A.R. Williams, and J.F. Janak, Phys. Rev. B **10**, 4856 (1974).

10. C.C. Tyson, A. Bzowski, P. Kristof, M. Kuhn, R. Sammynaiken, and T.K. Sham, Phys. Rev. B **45**, 8924 (1992).

11. A. Bzowski and T.K. Sham, J. Vac. Sci. Tech. July/August, (1993) in press.

12. R. Sammynaiken, M. Kuhn, and T.K. Sham (to be published).

13. J.A. Catterall and J. Trotter, Proc. Phys. Soc. **79**, 691 (1962).

14. S.B. DiCenzo, P.H. Citrin, E.H. Hartford Jr., and G.K. Wertheim, Phys. Rev. B **34**, 1343 (1986).

15. G.K. Wertheim, Phys. Rev. B. **36**, 4432 (1987).

16. T.K. Sham, A. Bzowski, M. Kuhn, and C.C. Tyson, Sol. St. Com. **80**, 29 (1991).

17. G.K. Wertheim, L.M. Mattheiss, and D.N.E. Buchanan, Phys. Rev. B **38**, 5988 (1988).

18. B. Ginatempo, G.Y. Guo, W.M. Temmerman, J.B. Staunton, and P.J. Durham, Phys. Rev. B **42**, 2761 (1990).

19. I.A. Abrikosov, Y.H. Vekilov, and A.V. Ruban, Phys. Lett. A **154**, 407 (1991).

20. Z.W. Lu, S.-H. Wei, and A. Zunger, Phys. Rev. B **45**, 10314 (1992).

21. A. Stuck, J. Osterwalder, T. Greber, S. Hüfner, and L. Schlapbach, Phys. rev. Lett. **65**, 3029 (1990).

22. G.S. Sohal, C. Carbone, E. Kisker, S. Krummacher, A. Fattah, W. Uelhoff, R.C. Albers, and P. Weinberger, Z. Phys. B **78**, 295 (1990).

23. J.W. Davenport, R.E. Watson, and M. Weinert, Phys. Rev. B **37**, 9985 (1988).

24. P. Weinberger, A.M. Boring, R.C. Albers, W.M. Temmerman, Phys. Rev. B **38**, 5357 (1988).

25. J.H. Sinfelt, Bimetallic Catalysts (Wiley, New York, 1983).

26. J.H. Sinfelt, Rev. Mod. Phys. **51**, 569 (1979).

27. (a) M.W. Smale and T.S. King, J. Catal. **119**, 441 (1989).
(b) K.S. Kim, J.E. Sinfelt, S. Eder, K. Markert, and K. Wandelt, J. Phys. Chem. **91**, 2337 (1987).

28. J.A. Rodriguez and D.W. Goodman, in: New Trends in CO Activation, Ed. L. Guczi (Elsevier, Amsterdam, 1991). Chap. III.

29. (a) C.H.F. Peden and D.W. Goodman, J. Catal. **104**, 347 (1987).
(b) C.H.F. Peden and D.W. Goodman, Ind. Eng. Chem. Fundam. **25**, 58 (1986).
(c) D.W. Goodman and C.H.F. Peden, J. Chem. Soc. Faraday Trans. 1, **83**, 1967 (1987).

30. J.C. Vickerman, K. Christmann, G. Ertl, P. Heimann, F.J. Himpsel, and D. Eastman, Surf. Sci. **134**, 367 (1983).

31. J.E. Houston, C.H.F. Peden, D.S. Blair, and D.W. Goodman, Surf. Sci. **167**, 427 (1986).

32. (a) J.E. Houston, C.H.F. Peden, P.J. Feibelman, and D.R. Hamann, Phys. Rev. Lett. **56**, 375 (1986).
(b) J.E. Houston, C.H.F. Peden, P.J. Feibelman, and D.R. Hamann, Surf. Sci. **195**, 457 (1987).

33. C. Harendt, K. Christmann, W. Hirschwald, and J.C. Vickerman, Surf. Sci. **165**, 413 (1986).

34. C. Park, E. Bauer, and H. Poppa, Surf. Sci. **187**, 86 (1987).

35. T.K. Sham, T. Ohta, T. Yokoyama, Y. Kitajima, M. Funabashi, N. Kosugi, and H. Kuroda, J. Chem. Phys. **88**, 475 (1988).

36. T.K. Sham, J. Hrbek, and K.H. Tan, Surf. Sci. **236**, 259 (1990).

CHAPTER TWO

Photoemission and Synchrotron Radiation: General Theory

2.1 Introduction

One of the most important tools for probing the electronic states within an atom, molecule, or solid is the use of elementary particles such as electrons, positrons, protons and also photons. Of particular importance is the use of electrons and photons since they are easily available and their interaction with matter is reasonably well understood. A typical spectroscopic experiment would have a source of which any number of conditions may be known: intensity, direction, or energy. The source would impinge upon the sample and the result of the interaction would be measured by determining the energy, direction, or intensity of the escaping particles (electrons or photons) or even by measuring the mass and/or energy of fragments created by the interaction.

The photoemission process, as revealed by its name, involves the use of photons as the source impinging upon the system under study and ejecting electrons which are then analyzed. Figure 2.1 gives an indication of the variables which are involved in a the photoemission process.

There are many photon sources available but to study the electronic structure of

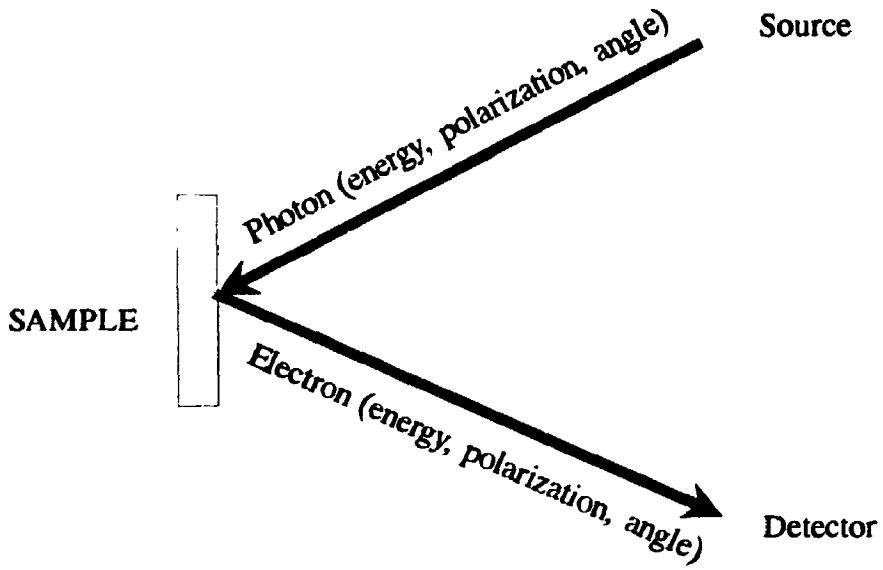

Figure 2.1: Representative drawing of the photoemission process. The variables include: energy, polarization and both azimuthal and polar angles.

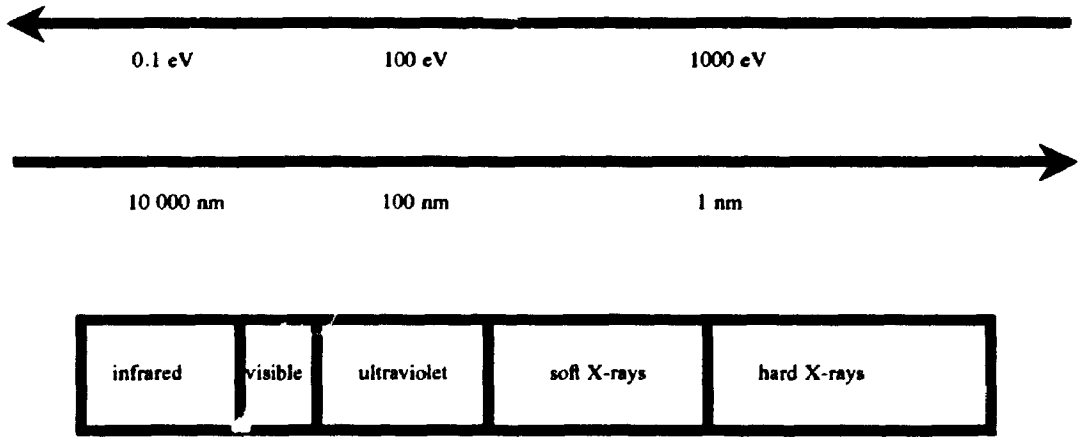

Figure 2.2: Representation of the energy spectrum. A source with an minimum energy of a few eV is required to probe valence shells while excitation of core levels requires a source with a higher energy.

a system the energy of the source must be sufficient to interact with the electronic level (band) in question. Figure 2.2 gives an overview of the energy spectrum and what can be probed at specific regions. Obviously, for probing electronic states, starting with the valence band or highest occupied electronic state the energy must be on the order of a few eV. This would mean a source emitting light in the infrared to visible region. Of equal importance, however, is the study of deeper levels within the system. This requires light which varies from ultraviolet to hard X-rays. Conventional sources such as X-ray anodes and UV (ultraviolet) lamps are excellent sources in their respective regions but are limited because they are basically single energy sources. The use of a tunable source over these regions gives the extra ability to perform X-ray absorption experiments and to take advantage of the cross-sectional differences associated with varying energies of the source. A synchrotron source emits light over a wide spectral range and is the perfect source for performing photoemission (and other) experiments not only for the spectral range but also because of other properties that will be discussed later.

One other factor that comes into play in photoemission experiments is the actual experimental setup. Generally the source will have an energy in the range of 10 to 1500 eV which would readily be quenched in the atmosphere as the light interacts with the medium. Therefore, high vacuum (HV) and ultrahigh vacuum (UHV) experimental systems are required to allow the light to interact with the sample and maintain the purity of the sample. For this reason the spectral range is sometimes referred to as vacuum ultraviolet. Hard X-rays can propagate through atmosphere and this requirement is not as stringent except that to maintain sample purity the interaction region should be in an

HV or UHV environment.

The next two sections will deal specifically with the theory and use of photoemission and synchrotron light. Photoemission is the primary technique used in this study and other techniques such as X-ray absorption, thermal desorption, etc. will be discussed in the sections in which they appear. Synchrotron light was also the source for some of the photoemission studies and all of the X-ray absorption studies. Other sources such as an X-ray anode will be discussed in the sections in which they first appear.

2.2 Photoemission[1,2]

The first observation of the photoelectric effect was made by Hertz[3] in 1887 when he found that sparking between electrodes occurs more easily if the negative electrode is first illuminated by uv radiation. After the discovery of the electron, Thompson[4] showed that this effect occurred because of the emission of electrons as a result of interactions with photons. An explanation was given by Einstein[5] in 1905 in which a quantum treatment was used and the photon was postulated with an energy of $h\nu$. Using the law of conservation of energy:

$$h\nu + E_i = E_f + E_k \tag{2.1}$$

where $h\nu$ is the energy of the incoming photon, E_i is the initial energy of the system, E_f is the total energy of the system after ejection of the electron, and E_k is the kinetic energy of the ejected electron. Both the incoming photon energy and outgoing electron energy are experimentally measured parameters and we can define the ionization energy of a particular level $I(j)$, as the difference between the final state energy $E_f(j)$ (ion) and the initial state energy E_i (neutral).

$$I(j) = E_f(j) - E_i \tag{2.2}$$

Using Koopmans' theorem[6] we can relate the ionization energy to the one electron orbital energy ϵ_j, and define it as the binding energy, $E_b(j)$. This assumes that the photoemission process is a one electron process and that the remaining electrons are frozen in relation to the time frame of the photoelectron process. Photoemission, however, is inherently

a many-body process but can be treated by a single-particle approximation. It is also noted that relaxation does occur as the core hole is created. A large body of work has been done to calculate theoretical ionization energies and has included the effects of electron-electron correlation and orbital relaxation. Using equations 2.1 and 2.2 we are left with the following expression:

$$h\nu - E_k(j) = E_b(j) \tag{2.3}$$

where the binding energy, $E_b(j)$, is defined as the energy required to promote an electron from the j^{th} level to the vacuum level.

After ejection of the photoelectron the system is left with a core or valence hole and the decay of the core hole occurs through two mechanisms, fluorescence and Auger decay. For lighter elements ($Z < 30$) the Auger decay mechanism dominates. Simply stated, Auger decay involves the filling of the hole by a higher level electron with a subsequent ejection of another electron from the donor shell or higher. The main characteristic of these electrons is that they will have a constant kinetic energy independent of the incident photon energy since their energy will be approximately equivalent to the difference in energy between the hole and the donor shell. For heavier elements fluorescence becomes the dominant decay mechanism. In this scheme the hole is again filled by a higher level electron but instead of emission of another electron the energy is dissipated via emission of a photon which has again a characteristic energy which is related to the difference in energy between the hole and donor shell. The availability and radial distribution of donor electrons reflects itself in the lifetime of the hole. According to the Heisenberg uncertainty principle the photoelectron linewidth is

inversely proportional to the lifetime of the hole:

$$\Delta E \approx \frac{h}{2\pi\tau} \tag{2.4}$$

where ΔE is the linewidth (eV), $h/2\pi$ is the Dirac constant, and τ is the lifetime of the hole. For deep core holes there is a larger availability of electrons to fill the hole therefore the lifetime is short and the linewidth is broad. Therefore emission lines from shallow core levels have much narrower linewidths.

As complicated as the photoemission process is for an isolated atom, further complications become evident when dealing with solids and in this case, metallic systems. To examine photoemission from solids we use the three-step model used extensively by Berglund and Spicer.[7] The first step is the interaction of the photon with an electron and the ejection of that electron from a core or valence shell. The second step is the migration of the electron to the surface of the sample. The last step is the escape of the electron to the vacuum.

The main difference between the photoemission process for an isolated atom as compared to an atom in a solid is the potential barrier posed by the crystal surface to electron escape. The difference in the energy between the Fermi level and vacuum level is defined as the work function, Φ. Therefore the binding energy is now defined as:

$$E_B = h\nu - E_K - \Phi \tag{2.5}$$

Figure 2.3 indicates the electronic levels that are dealt with when a typical photoemission experiment on a metallic system is carried out.

In examining Figure 2.3 we note that the Fermi levels of both the sample and the

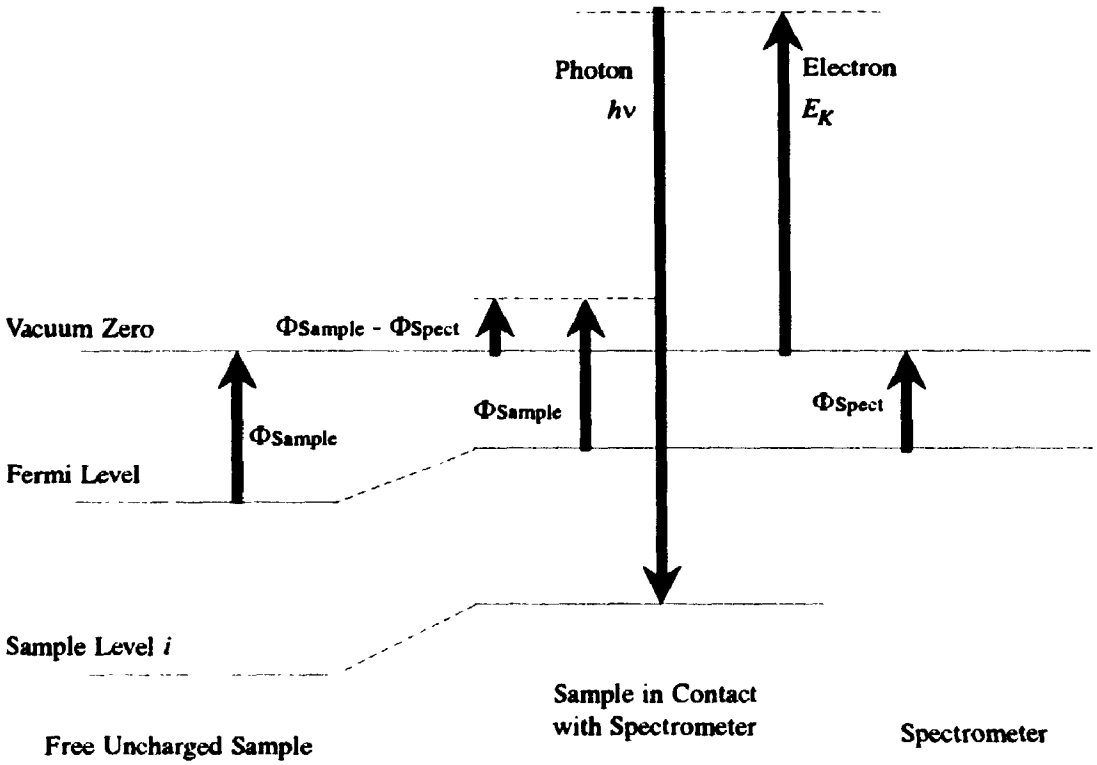

Figure 2.3: Energy level diagram for a metallic sample. At the left is the sample free and uncharged. At the right is the sample in electronic contact with the spectrometer.

spectrometer are equalized. For this reason binding energies are quoted relative to the Fermi level and a standard emission level (i.e. Au 4*f*) is used to calibrate the spectrometer. In some cases a well-defined Fermi level onset is used to measure binding energies.

We can see that absolute theoretical determination of binding energy values would be difficult with the effects of relaxation and correlation being hard to determine. Yet, if we want to examine relative changes between systems, such as an alloy and its pure constituent counterparts, some of these difficulties are alleviated as these effects will effectively cancel each other out assuming, of course, that relaxation and correlation effects are similar in the two systems. In practice, for metallic systems, the core level shifts (chemical shifts) are small (1 eV or less). In insulators they can range to a few eV. If an atom is in a different chemical environment charge redistribution will occur. The electronic levels, therefore, interact with a different spatial distribution of electrons leading to changed effective potentials and thereby an electronic shift is experienced during photoemission. Simply stated, and assuming negligible differences in relaxation effects, an increase in electron density at a site will lead to a shift to lower binding energies (the electrons experience less of a Coulombic interaction), while a decrease of electron density will lead to the opposite shift. Metallic systems have small chemical shifts because of conduction electrons which can effectively screen the core hole and also because they must maintain electroneutrality thereby limiting the amount of charge transfer. Insulators, on the other hand, are more ionic and can have large amounts of charge transfer, and with the lack of conduction electron screening of the core hole

(although this is somewhat alleviated by screening through polarization), the shifts are very large. With this in mind, it becomes very important that when examining a system, such as a Au-Cu alloy, with inherently small chemical shifts, that the narrowest and most intense core level be examined. For this reason this study probes the Au 4*f* and the Cu 2*p* emission levels for examination of chemical shifts.

In a typical experimental setup the number of electrons per unit time with a specific kinetic energy is measured with an electron analyzer. An energy region is scanned and the intensity of the electron signal is plotted against the kinetic energy. From this the core and valence densities of states which have an energy less than $h\nu$-Φ are probed.

The photoemission process has other inherent features which can be used to the experimentalist's advantage.

As mentioned before, the escaping electron has other variables which can be measured, namely spin and angle. The former variable is hard to determine because of the difficulty of getting an analyzer with the sensitivity to distinguish between electron spins. The latter variable can be probed by using an analyzer with a small angle of collection and varying the angle that the spectrometer makes with the sample surface. This technique is known as angle-resolved photoemission and with a crystal sample, band mapping can be accomplished. In our experiments we did not perform true angle-resolved photoemission because we are dealing with core levels and alloy specimens and the analyzer used operates in an angle-integrated mode. However, the collection angle is small enough for us to observe angle-dependent effects due to different sampling

depths.

Returning to the three step model, we now examine step two in which the photoelectron must now travel through the solid to the surface. During this process the electron can suffer energy losses because of inelastic scattering. Even though the photon penetrates hundreds of Angstroms into the sample, only those electrons produced near the surface will be able to escape into vacuum without suffering any energy loss. The average distance that an electron can travel in a solid, without losing energy, is referred to as the mean free path (Figure 2.4). The mean free path follows a universal curve dependent only on the kinetic energy of the electron. We can clearly see a minimum at a kinetic energy of about 50 eV.[8]

The escape depth of the photoelectron is given by the following phenomenological relationship:

$$\frac{I}{I_0} = e^{-t/\lambda} \tag{2.6}$$

where I_0 is the photoelectron intensity or cross-section, I is the intensity of the photoelectrons which have not suffered any energy loss, t is the distance from the interaction to the surface, and λ is the mean free path of the electron. If we integrate Equation 2.5 with respect to the sampling depth, t, we can determine the amount of signal that originates within a certain depth. If we vary the electron free mean path, as determined by the kinetic energy, we can change the ratio of the bulk versus surface intensity. The smaller the mean free path the more surface contribution to the photoelectron signal. Another method of increasing the surface contribution to the

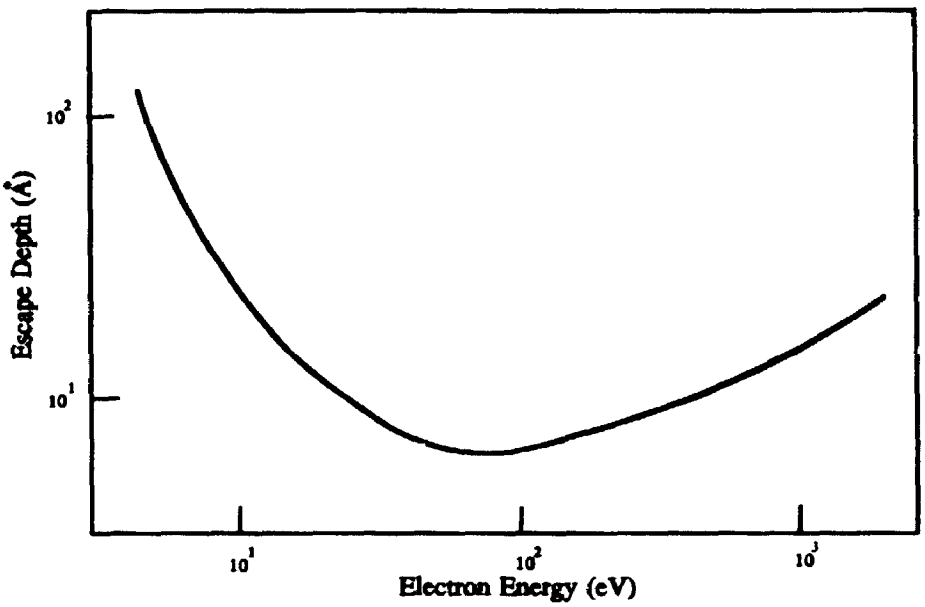

Figure 2.4: Universal curve for the mean free path of electrons as a function of their kinetic energy. Most of the experimental data closely follows the curve thereby showing little dependence upon the material.

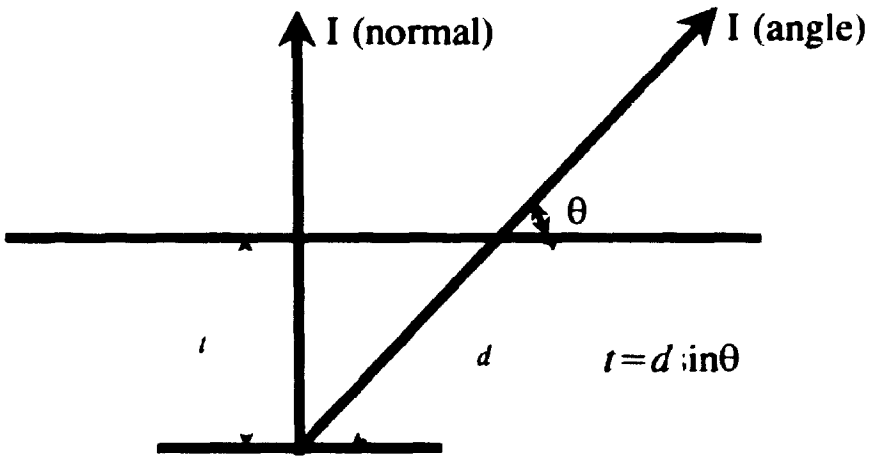

Figure 2.5: Schematic of the effective sampling depth as a function of the take-off angle.

photoelectron signal is to change the angle of detection from that of normal to the surface to some angle θ, as the effective sample depth varies as $\sin\theta$ (Figure 2.5).

The last important feature of the photoemission process is the cross-sectional dependence of the intensity of emission upon the incoming photon energy. The differential cross-section is defined as:

$$\frac{d\sigma_v}{d\Omega} = 4\pi^2 \alpha h\nu \, |\langle f|\hat{r}|i\rangle|^2 \tag{2.7}$$

where $d\sigma_v/d\Omega$ is the differential cross-section per unit energy per unit solid angle, α is the fine structure constant ($\sim 1/137$), $h\nu$ is the incident photon energy and $<f|\hat{r}|i>^2$ is the dipole matrix element for the transition from an initial state, i, to a final state, f.

The initial state wavefunction for core levels in atoms, molecules, and solids can be adequately described by a normalized hydrogenic form:

$$\phi_i = \frac{P_{nl}(r)}{r} Y_m^l(\theta,\phi) \tag{2.8}$$

containing a spatial, (P_{nl}/r), and angular, (Y_m^l), component. The final state wavefunction is more complicated because at low kinetic energies the final state is modified by the system itself. In this study we will assume that the kinetic energy of the photoelectron is high enough that the final state can be approximated by a plane wave. For calculation of the cross-section we must incorporate the dipole selection rule $\Delta l = \pm 1$ and thereby express the final state plane wave in terms of partial waves that have the proper angular component.

Several aspects of cross-sectional dependence are thereby revealed. The overall

intensity for a $\Delta l = +1$ transition dominates over a -1 transition. The spatial overlap can sometimes change radically as a function of photon energy leading to maxima and minima in the cross-sectional curves. Assuming the angular overlap to be a constant as the photoelectron energy changes, the final state wavelength is a function of the kinetic energy of the outgoing electron. The higher the kinetic energy the more frequent the oscillations in the final state wavefunction. This leads to changing constructive and destructive overlap with the initial state wavefunction. At certain energies there is a strong overlap with the initial state wavefunction and a maximum is experienced. If the initial state wavefunction has a node (i.e. when $n=l+2$ or greater) there occurs at a specific energy range a minimum which is named the Cooper minimum (Figure 2.6).[9,10] This becomes a valuable tool in experiments in that, by varying the initial photon energy (thereby varying the photoelectron kinetic energy), the signal from a fixed emission level can be enhanced or attenuated. Calculations have been performed to evaluate cross-sectional dependencies for most atomic cases. Complications occur for solids and molecules. The core levels are sufficiently atomic-like for the atomic case to hold but deviations occur when dealing with valence bands since the initial state wavefunction is hard to determine (hydrogenic orbitals no longer hold). Yet, experimentally, the cross-sectional dependency of the solid still follows the approximate pattern of the atomic counterpart although usually they are shifted somewhat in energy. A last feature that is revealed is that as the kinetic energy of the photoelectron increases far above the initial state threshold the overlap keeps decreasing and the cross-section falls off slowly and almost linearly.

Photoemission has many diverse applications, as shown here, but it is obvious that to take advantage of the sensitivity of the technique for probing specific depths and for enhancing or attenuating specific chemical species, a tunable photon source would be most advantageous.

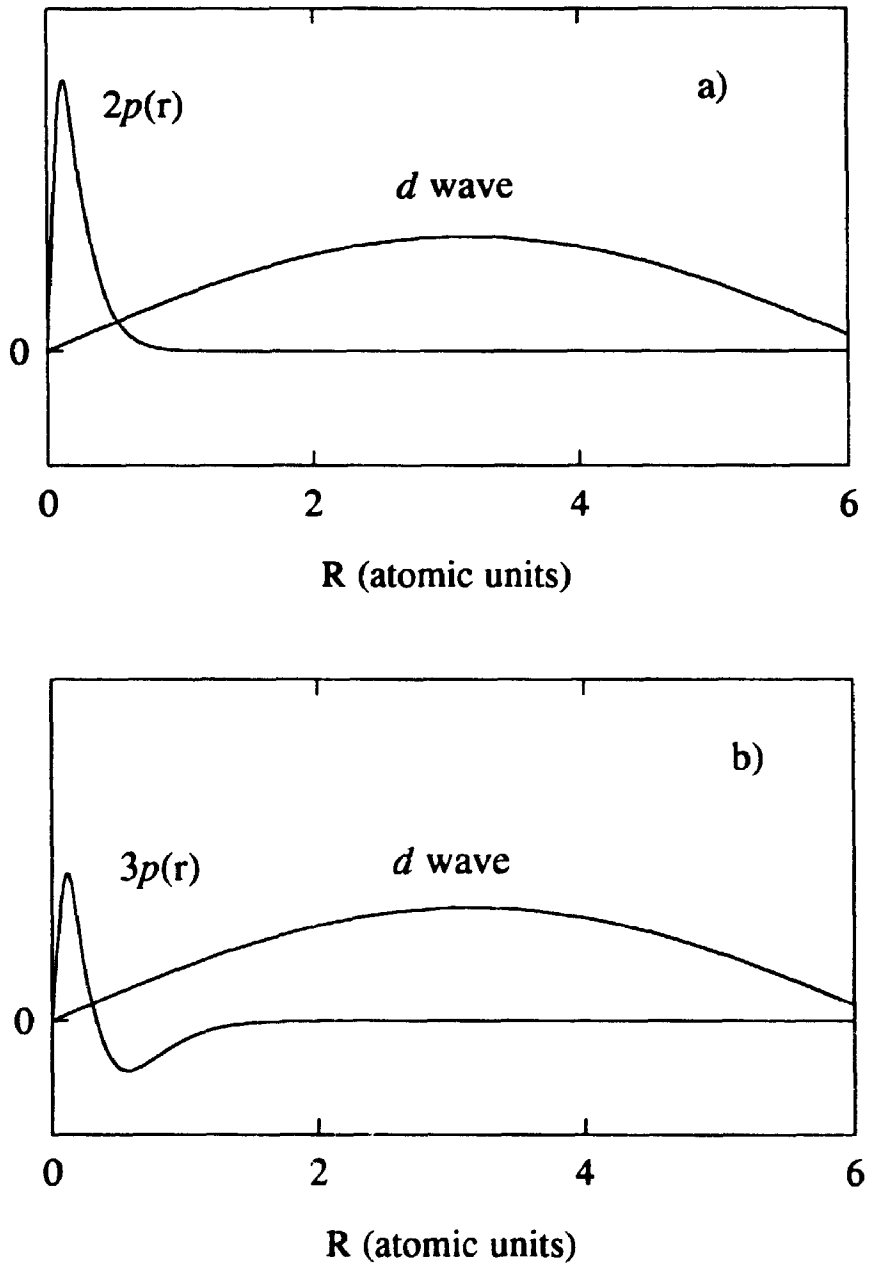

Figure 2.6: Representative core level wavefunctions and a representative *d* wave to show the cross-sectional overlap. In a) a $2p$ function overlap is positive b) a $3p$ function has a negative overlap portion because of a node leading to a cross-sectional minimum.

2.3 Synchrotron Radiation[11]

Synchrotron radiation is the electromagnetic radiation emitted by electrons or positrons as they travel in large circular orbits at relativistic velocities. Characteristics of synchrotron radiation can be described by the classical treatment by Larmor of accelerated charged particles.[12] The following formula describes the power radiated by an accelerated charge.

$$P = \frac{2}{3}\frac{e^2}{c^3}\left|\frac{dV}{dt}\right|^2 \tag{2.9}$$

Even with the theoretical description of synchrotron radiation, experimental observation was not achieved until the 1940's with the development of electron accelerators. It was found that emission of synchrotron radiation limited the energy achievable by accelerators such as the betatron.[13] This nuisance was first experimentally observed in 1946 at General Electric Laboratories in Schenectady.[14] Finally, in the 1950's, it was recognized that synchrotron radiation could have powerful applications in ultraviolet and soft X-ray research[15] and potentially in the hard X-ray region.[16]

Because of the cost and novelty of building a synchrotron radiation facility, the first dedicated experiments were carried out parasitically on elementary particle accelerators, a relationship that did not fare well for synchrotron radiation researchers since parameters for operating the rings were to enhance elementary-particle research and were not suited for efficient synchrotron radiation use. These were so-called first generation sources.

In 1966, the electron storage ring, *Tantalus*, became the first dedicated synchrotron source. A storage ring has the great advantage of being able to provide a continuous source of photons which decays over a period of a few hours. This led to the development of second generation sources of which about 20 had been built by the mid-1980's including a 1-GeV ring, *Aladdin*, at the Synchrotron Radiation Centre (SRC), in Madison, Wisconsin, and two storage rings, ultraviolet and hard X-ray, at the National Synchrotron Light Source (NSLS), at Brookhaven National Laboratories. These sources will be the focus of a general description of characteristics exhibited by second generation sources since these facilities were used in this study.

Figure 2.7 shows a schematic which represents the general features of a synchrotron facility. The major components are:

1) injection system

2) storage ring

3) bending magnets

4) radiofrequency cavity

5) quadrupole magnets (hexapoles also as focussing optics)

6) beam ports

In general, electrons are generated in the injection system where they are accelerated to some value below that of the final operating energy. They are then injected into the ring in bunches and ramped to relativistic speeds where they are stored for several hours. The ring consists of straight section with magnets to bend the electrons in their orbit upon which tangential emission of synchrotron radiation occurs.

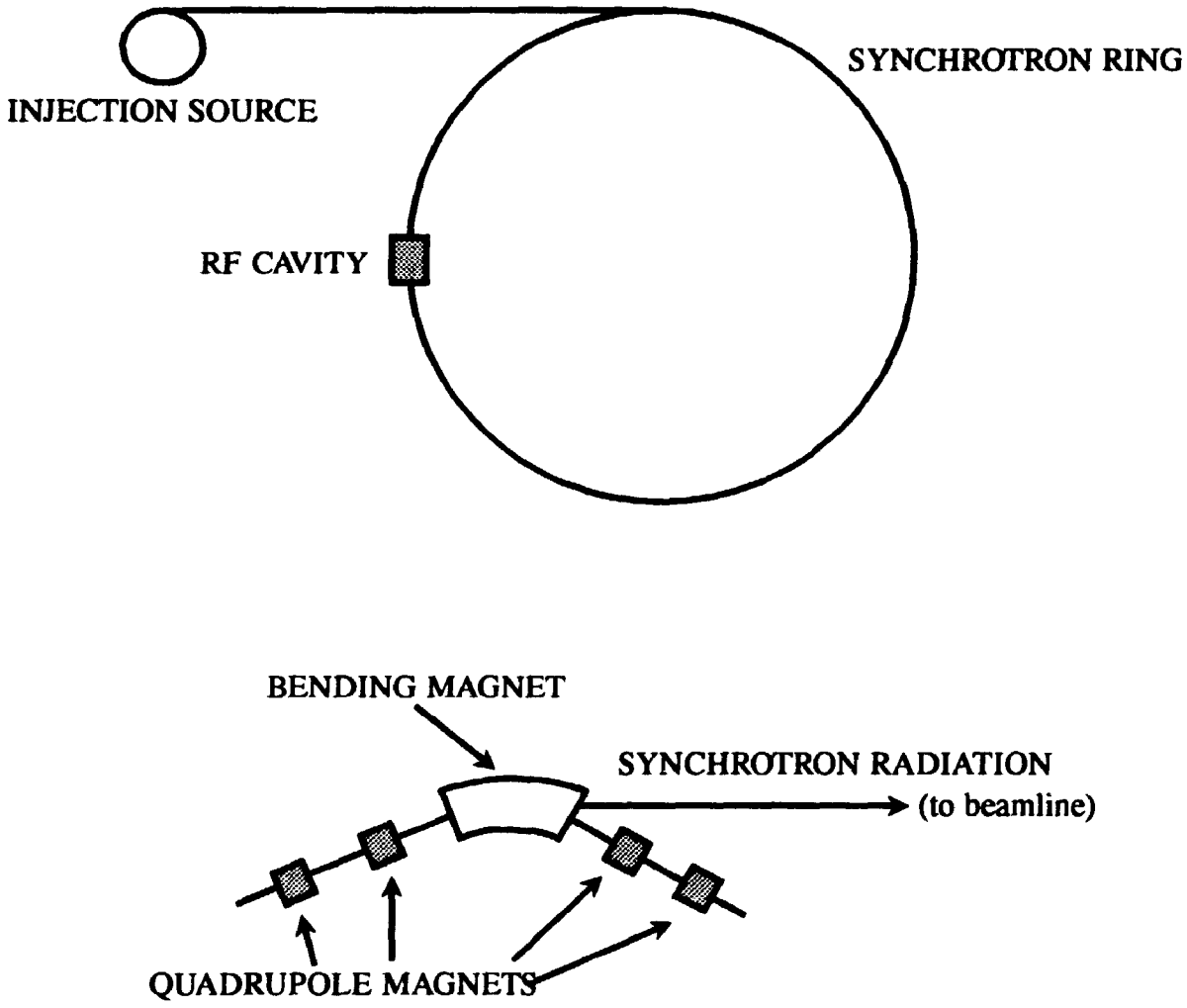

Figure 2.7: Representation of a typical second generation storage ring. The major components are; injection system, vacuum ring that stores the electrons, radiofrequency cavity, quadrupole magnets, and bending magnets with associated beam ports.

Beam ports are thus located off-of the bending magnets. A radiofrequency cavity is used to restore the energy lost by the electrons due to synchrotron radiation emission. Quadrupole and hexapole magnets are used to focus and defocus the electron beam. This requirement is inherent in electron storage rings as without such focussing and defocussing the beam becomes unstable and decays rapidly. This is known as the alternate gradient principle.

A synchrotron source as outlined here exhibits many ideal experimentally favourable characteristics. The photon flux is high (several orders of magnitude more intense than that from conventional sources) and exhibits a large tunable spectral range (from infrared to hard X-ray and beyond). The beam is highly collimated and due to the relativistic nature of the emission it is also highly polarized. It also exhibits time structure on the order of nanoseconds as the electrons orbit the ring in bunches which travel at relativistic speeds (microsecond repetition rate is typical). These characteristics can be deduced from general formulae based on accelerator physics.

Using equation 2.9 and defining a new parameter, $\gamma = E/m_0c^2$, we arrive at:

$$P = \frac{2e^2c\gamma^4}{3\rho^2} = \frac{2e^2cE^4}{3\rho^2(m_0c^2)^4} \qquad (2.10)$$

where ρ is the radius of curvature in the bending magnet and is independent of the radius of the ring. It is noted that the power radiated increases as the fourth power of the ring energy and decreases as the fourth power of the rest mass. This explains why lighter elementary particles such as electrons and positrons are used to generate synchrotron radiation.

The energy generated has a large spectral distribution. Two main criteria affect the range and maximum energy achieved. These are the energy of the ring and the radius of curvature in the bending magnets. We define a parameter which is called the critical wavelength, λ_c, of the ring, i.e. the energy at which the maximum flux of photons occurs:

$$\lambda_c = \frac{4\pi\rho}{3\gamma^3} \tag{2.11}$$

Thus, for example, the *Aladdin* storage ring with an operating energy of 0.8 GeV and with a radius of curvature of 2.0833 m has a critical wavelength of 22.7 Å (546 eV). Figure 2.8 shows the spectral distribution and flux of the *Aladdin* storage ring operating at 0.8 GeV and 200 mA and at 1.0 GeV and 100 mA.

In the plane of the orbit the synchrotron radiation is 100% polarized parallel to the plane and is elliptically polarized above and below the plane. But because of the tangential emission most of the flux is in the plane and there is little vertical distribution. This is shown in Figure 2.9.

The electrons are injected in bunches and travel the ring in periods in the nanosecond scale. The *Aladdin* storage ring, for example has a revolutionary period of 297 nanoseconds and a 19.8 ns interbunch period. The ring operates normally with a number of bunches but for special time resolved experiments it can operate with a single bunch. Because of the microsecond period, to restore the energy of the electrons at each revolution, the cavity must operate at the MHz frequency, therefore radiofrequencies are required.

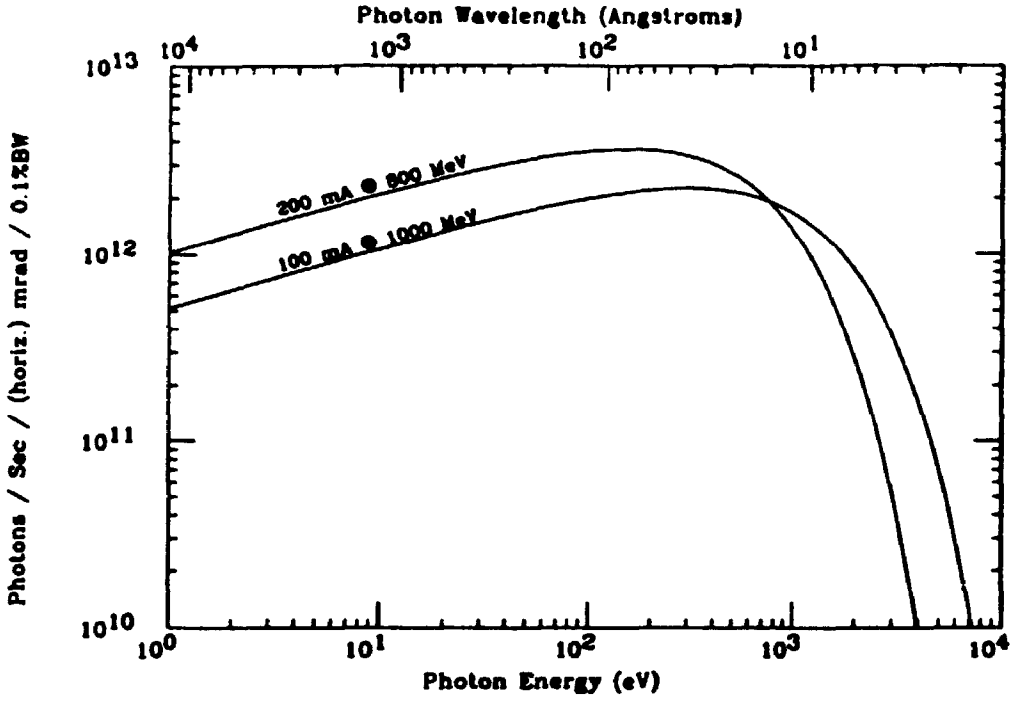

Figure 2.8: Bending magnet flux of the *Aladdin* ring under two typical operating conditions (from SRC publication, "An Invitation to See the Light", 1993).

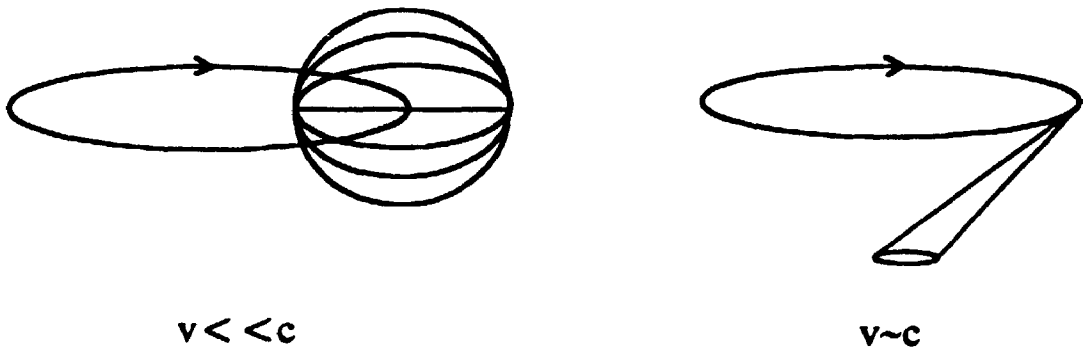

Figure 2.9: Electromagnetic emission from an electron in a circular orbit for the case where $v << c$ and $v \sim c$ (relativistic).

These are the general features for a typical second generation synchrotron source. There are a couple of other practical operating parameters which come up. The lifetime of the ring usually ranges from a couple of hours to half a day. The higher energy rings have a longer lifetime. The main source of the electron beam decay is interaction with residual gas particles in the vacuum system (neutral and ionic). Therefore an ultrahigh vacuum system, typically in the 10^{-11} Torr regime, is required to store the beam. Even so the nature of synchrotron radiation itself helps to decay the beam. The emission of synchrotron radiation bombards the surface of the vacuum tank and causes desorption of particles which then interact with the electron beam. The ionic particles can be trapped in the beam. This ion trapping problem can be resolved by application of a slight negative voltage on electrodes within the ring or by the use of positrons. Lastly, mention must be made of the actual experimental station. The radiation that comes out of the beam ports exhibits a wide spectral distribution characteristic of the particular storage ring. In a typical setup, the energy is monochromatized and sent through a variety of optics to the experimental station itself. The energy is usually tunable but the spectral region is limited by the type of monochromator. The actual experimental setup used (monochromator and experimental station) will be discussed in the experimental sections later.

Although this study was done using radiation created by bending magnets, third generation sources have now appeared such as the 7-Gev source to be built at Argonne. These new synchrotrons use straight sections with insertion devices such as wigglers and undulators to create very intense synchrotron radiation. Bending magnets are now only

used for weaker emissions, if required, and to bend the electrons to the next straight section and complete the circuit. These rings will have fluxes orders of magnitude higher and lower emittances (angular distribution parameter). With these new sources more practical applications become possible such as medical imaging and X-ray holography.

With the proper choice of monochromator it is possible to probe, selectively, different emission levels and sample depths and with a stepped monochromator absorption experiments can also be performed. The following section deals with the study of the electronic structure of a series of Au-Cu bulk alloys. Photoemission experiments were performed using a conventional X-ray lamp and a synchrotron source. X-ray absorption experiments could only be carried out at a synchrotron radiation facility.

2.4 References

1. J.H.D. Eland, Photoelectron Spectroscopy, (London, Butterworths, 1984).
2. M. Cardona, Photoemission in Solids, (New York, Springer-Verlag, 1979).
3. H. Hertz, Ann. Physik **31**, 983 (1887).
4. J.J. Thompson, Phil. Mag. **48**, 547 (1899).
5. A. Einstein, Ann. Physik **17**, 132 (1905).
6. T. Koopmans, Physica **1**, 104 (1934).
7. C.N. Berglund and W.E. Spicer, Phys. Rev. **136**, A 1030 (1964).
8. G.A. Somorjai, Chemistry in Two Dimensions, (Cornell University Press, Ithaca, 1981).
9. J.W. Cooper, Phys. Rev. Lett. **13**, 762 (1964).
10. U. Fano and J.W. Cooper, Rev. Mod. Phys. **40**, 441 (1968).
11. G. Margaritondo, Introduction to Synchrotron Radiation, (New York, Oxford University Press, 1988).
12. J. Larmor, Phil. Mag. **44**, 503 (1897).
13. D. Ivanenko and J. Pomeranchuk, Phys. Rev. **65**, 343 (1944).
14. F.R. Elder, A.M. Gurewitsch, R.V. Langmuir, and H.C. Pollock, Phys. Rev. **71**, 829 (1947).
15. D.H. Tomboulian and P.L. Harman, Phys. Rev. **102**, 1423 (1956).
16. L.G. Parratt, Rev. Sci. Instrum. **30**, 297 (1959).

SECTION I
Au-Cu BULK ALLOYS

CHAPTER THREE

Models and Experimental Considerations

3.1 Introduction

This section will focus on the investigation of the electronic behaviour of a series of bulk Au-Cu alloys to address the various issues raised in Chapter One. These issues mainly revolve around resolving the debate on the mechanism of charge redistribution and the role of the constituent *d* bands upon alloy formation.

We begin the study on a series of Au-Cu alloy thin foils especially prepared for X-ray absorption studies to be carried out in the transmission mode. These foils are also easily studied by photoemission. The rationale being employed is that, hopefully once the electronic properties of the bulk alloys are well understood, the properties of specially prepared surface Au-Cu alloys can also be deduced and explained by comparison to properties exhibited by the bulk.

To determine the electronic changes upon alloying we employ two techniques on the Au-Cu samples, photoemission and X-ray absorption. The photoemission technique is used to determine relative core level shifts and valence band behaviour e .hibited upon

alloying while the X-ray absorption technique has a two-fold purpose: 1) the study of features at and just above threshold; 2) the study of the features located 50 to 1000eV above threshold.

The binding energy shifts and corresponding Mössbauer isomer shifts will be incorporated into a conventional framework that will give semi-quantitative numbers for transfer of valence charge (mainly *s* and *d* for the noble metals) and overall charge transfer.

The X-ray absorption near edge structure (XANES) studies will give results that are incorporated in a more rigorous framework that will give quantitative and independent numbers for the transfer of *d* charge.

Valence band features will be qualitatively examined in terms of width and "apparent" splitting and the shifting of various components.

Extended X-ray absorption fine structure (EXAFS) studies are employed to find the local environment around the constituent atoms in terms of the nearest shell configuration and interatomic distances.

The following chapters will be organized as follows: Chapter 3 will expand on the models introduced in Chapter 1 and the experimental considerations for the bulk studies; Chapter 4 will focus on the experimental results and manipulation; Chapter 5 will be an analysis of the bulk Au-Cu alloy results.

3.2 Method of Determining Charge Transfer Using a Conventional Model

As was explained in Chapter One the appearance of conflicting implications of experimental data on a variety of Au intermetallics led to the development of the charge compensation model by Watson *et al.*.[1] To review quickly, "Gold is the most electronegative of metallic elements, and therefore would be expected to gain charge on formation of alloys." Mössbauer isomer shifts do show an increase in contact density (*s* and relativistic $p_{1/2}$ charge) at the Au site but a shift to higher binding energy of the Au core levels indicates a loss of charge as reviewed in the previous chapter. This apparent contradiction was resolved by invoking a compensation model in which Au loses *d* charge but is overcompensated by a gain of conduction charge upon alloy formation.

Watson *et al.* have incorporated the Mössbauer isomer and core level shifts in a conventional model which gives semi-quantitative results for charge transfer.

Before we examine shifts that occur upon alloying it is helpful to examine the effect of solid formation on shifts in core levels. There is a shift involved due to the different reference levels that the core level is measured against: vacuum level for the free atom and the Fermi level for metals. For the case of transition metals (and noble metals) there is a change in atomic configuration; i.e. $5d^9 6s^2$ for atomic Au to $5d^{9.6} 6s^{1.4}$ for metallic Au.[2,b] The implications of this reconfiguration is that a core level's Coulombic interaction with the valence electrons changes overall since the interaction of

---

[b] The expected configuration for metallic Au would be $5d^{10} 6s^1$ but due to hybridization upon solid formation the configuration becomes $5d^{9.6} 6s^{1.4}$ as calculated by Mattheiss and Dietz.[2]

a core level with *s*-type conduction charge is less than with *d* charge causing a binding energy shift. There is also a shift involved due to the compression of the atomic volume on going from the free atom to the solid. The Wigner-Seitz cell is smaller than the free atomic volume and thereby, to maintain electroneutrality, the valence charge must be compressed leading to a shift in the core levels. Valence and conduction band formation causes a small shift because of the changing structure and broadening of the bands. There are different relaxation effects for free atoms compared to bound atoms in metals since the metal has conduction electrons which can screen the core hole and cause a core level shift. The last important cause of core level shifts involves differences in correlation effects between the atom and the metal.

Following Watson *et al.* we can use these causes of core level shifts when examining what occurs upon alloying to Au core levels, using Au-Cu alloys as an example. This treatment, of course, is applicable to the other component site given that values of the various parameters that are being dealt with from the Au perspective are also known from the perspective of the other component. The following expression relates the binding energy shift, upon alloying, with most of the possible contributions mentioned previously:

$$\Delta E_B(\text{alloy-Au}) = -\Delta\Phi - \Delta n[F^o(i,v)] + [\frac{dE}{dV}\Delta V] + \Delta C + \Delta R \qquad (3.1)$$

Here ΔE_B is the measured binding energy shift, $\Delta\Phi$ is the work function change, Δn is the change in the number of valence electrons, $[F^o(i,v)]$ is an effective Slater integral for the interaction of the core level of interest, i, with the valence electron, v,

$(dE/dV)\Delta V$ is the binding energy shift due to the volume change, ΔC is the correlation change, and ΔR is the relaxation energy difference.

In developing this model several assumptions were used. In examining core level shifts between a metallic system and a related metallic alloy it is assumed that relaxation and correlation effects are similar and any differences are small compared to the uncertainty of other more influential variables.

The work function term arises from the fact that the reference of the Slater terms is the crystal zero while binding energy shifts are referenced to the Fermi level. Fermi level shifts therefore must be accounted for and can be approximated by work function differences assuming there are no large differences in the dipole barrier. The negative term arises since an increase in the work function, relative to Au, decreases the measured binding energy.

The $\Delta n[F^o(i,v)]$ term calculates the contribution to the binding energy shift due to transfer of valence charge from or to the Au site. Initial calculations used bare free atom Slater integrals of the form:

$$F^0(i,j) = \int\int P_i(r_1)^2 (1/r_>) P_j(r_2)^2 r_1^2 dr_1 r_2^2 dr_2 \qquad (3.2)$$

where the $P(r)$ terms are one-electron radial wave functions. It was found, however, that these integrals grossly overestimate the amount of binding energy shift since they are normalized to the free atomic volume and do not take into account relaxation of the valence shell upon transfer of charge.[3] The first step is to renormalize to the Wigner-Seitz cell volume. Charge transfer will leave a non-zero charge outside of the cell volume which must also be accounted for. Therefore a new parameter is defined, F^0_{latt},

which is estimated by placing a unit charge at the surface of the atomic volume sphere at the Wigner-Seitz radius on the site of interest, i.e. Au in this case. For the estimation of the effect on the binding energy shift a term defining the amount of charge transfer into or out of the sphere is used, δ. To take into account the effects of relaxation we must first determine the nature of the valence charge in question. For Au we have conduction electrons (mainly *s* character) and *d* electrons. Therefore the integrals take the form:

$$\Delta n[F^0(i,v)] = \Delta n_c[F^0(i,c)] + \Delta n_d[F^0(i,d)] \qquad (3.3)$$

where Δn_c and Δn_d are the transfer of conduction charge and *d* charge respectively. Effective integrals are calculated, to take into account the effect of relaxation, by incorporating terms which account for the addition or removal of a valence electron (conduction or *d*) from the site. Such calculations have shown a 60% reduction in the value of the $F^0(4f, 5d)$ integral as compared to the bare integral while the $F^0(4f, c)$ was reduced by about 10%.[3] This is in line with arguments that the *d* shell should the most affected by relaxation effects because of their higher screening ability.

The last term to be dealt with is the effect of volume changes on the binding energy level. An expansion or contraction in the atomic volume due to alloying of the constituent of interest will lead to binding energy shifts since the effective integrals are normalized to the Wigner-Seitz volume calculated from that of the pure metal. Both Au and Cu are f.c.c. with lattice constants of 4.08 Å and 3.61 Å, respectively. The volume of the Wigner-Seitz cell of an f.c.c. structure is given by $1/4a^3$, giving values of 17.0 Å^3 and 11.8 Å^3, respectively. If there is no change in volume on mixing two metallic

components to form an alloy, then the binding energy shifts can be attributed to chemical effects rather than due to volume expansion or contraction. For example, the lattice constants for disordered Cu_3Au and disordered Au_3Cu are approximately 3.75 Å and 3.98 Å[4,c] giving volumes of 13.2 Å^3 and 15.8 Å^3. By comparing the volumes we get:

$$\frac{V_{Cu_3Au}}{1/4V_{Au}+3/4V_{Cu}} = \frac{13.2}{(1/4)(17.0)+(3/4)(11.8)} \approx 1.008 \qquad (3.4a)$$

$$\frac{V_{Au_3Cu}}{3/4V_{Au}+1/4V_{Cu}} = \frac{15.8}{(3/4)(17.0)+(1/4)(11.8)} \approx 1.006 \qquad (3.4b)$$

showing a volume expansion of only 0.8% and 0.6%. The other Au-Cu alloys studied here follow a similar trend and it is for this reason that volume effects can be ignored here and in the upcoming discussion on Mössbauer isomer shifts.

If we define the total amount of charge transfer, δ, to equal the sum of the change in conduction and d charge, $\Delta n_c + \Delta n_d$, we are left with the following contributions to the binding energy shift upon alloying:

$$\Delta E_{B(alloy-Au)} = -(\Phi_{alloy} - \Phi_{Au}) - \Delta n_c[F^0(4f,c)] - \Delta n_d[F^0(4f,5d)] + \delta F(latt) \qquad (3.5)$$

The binding energy shifts and the work function of pure Au are experimentally derived values while the alloy work function may be known and if not a value can be estimated by assuming additivity of the values for the pure components. The effective

---

[c] These numbers are used since the samples used in Reference 4 had compositions close to those used by us. Our numbers calculated via EXAFS analysis are the same within experimental error and will be discussed in Section 4.4.

integrals can be calculated leaving two unknowns, Δn_c and Δn_d. The change of conduction charge at the Au site is available from ^{197}Au Mössbauer isomer shift data, leaving the change in *d* charge the only variable.

The Mössbauer effect involves the study of the absorption of γ radiation on nuclei and was first reported by Mössbauer in 1958.[5] The basis of the Mössbauer effect is the emission of γ radiation by radioactive nuclei, and then the absorption of those photons by other nuclei of the same type and is termed resonant absorption.[6,7,8] The environment of the nuclei affect the emission and absorption and can be measured. Figure 3.1 shows a schematic of the emission and absorption processes. The result of the absorption can be measured either by the decreased transmission of the absorber or by the decay of the absorber nuclei from the excited state. The resonances are very sharp because of the nature of the excited and ground nuclear states and energy specific since absorption can only occur with the same nuclei since the resonances and transition energies are so sharp. A typical experimental setup is shown in Figure 3.2 for both transmission measurements and backscattered measurements. The features of note are that the energy of the gamma ray is modulated by motion of the emitter (Doppler modulation) and once resonance occurs either a dip in the transmission mode spectra or a peak in the backscattered mode spectra is experienced. For the case in which the absorber and emitter are in the same chemical environment there is no observable shift.

A lot of different information can be gathered from Mössbauer spectra, electrostatic energy shifts, electric hyperfine quadrupole splitting, and magnetic hyperfine splitting. For this study we are only concerned with the first effect.

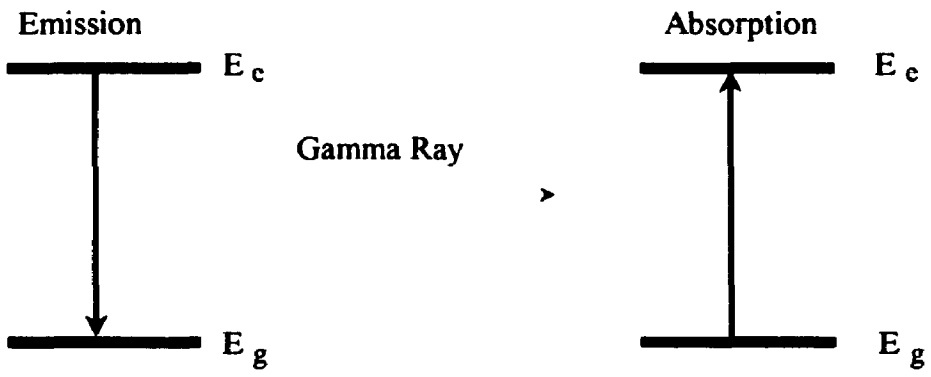

Figure 3.1: A schematic indicating the interaction between the source and the absorber. The source is created in the excited nuclear state and decays emitting a gamma ray which is absorbed and raises the absorber nucleus to its excited state.

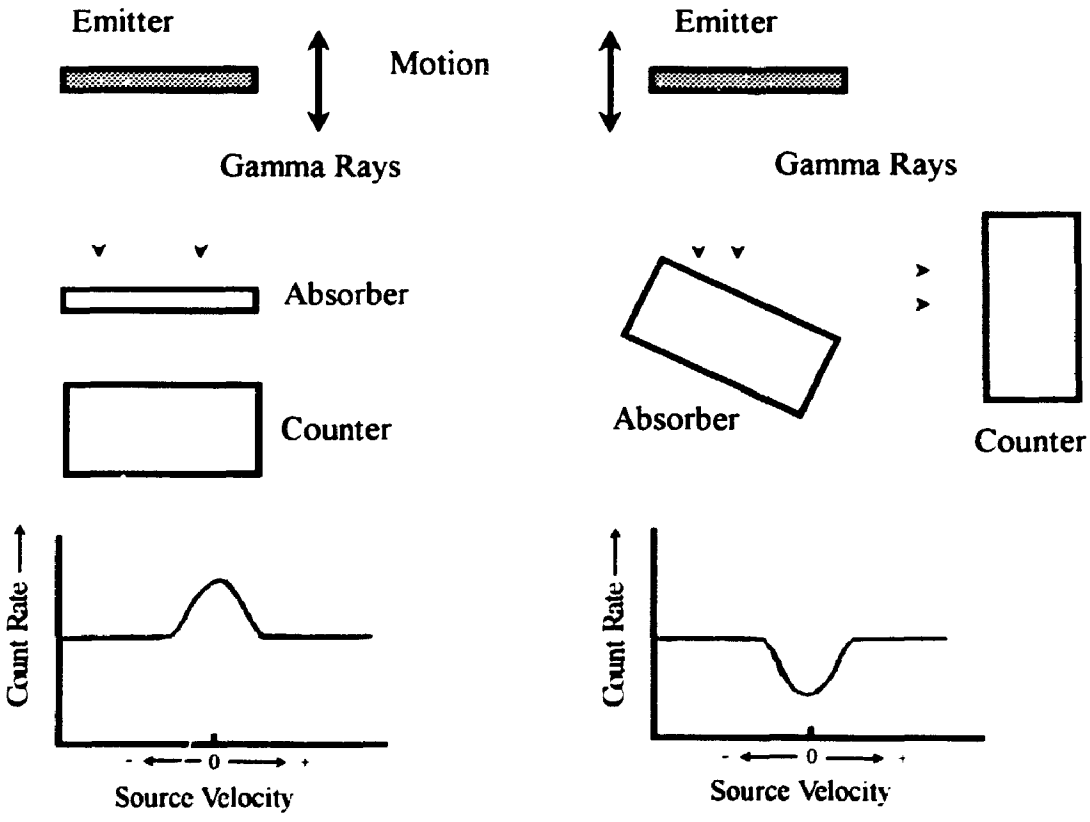

Figure 3.2: Two typical experimental setups. On the left, in the transmission mode with a thin enough sample, the source is Doppler modulated and the transmission is measured. A decrease is noted upon resonant absorption. On the right, in the backscatter mode, the counter measures the emission of the resonant gamma rays and this is plotted as an increase in the count rate.

The isomer shift (chemical shift) arises from the interaction of the electron density within the volume of the nucleus with the nuclear charge (contact density). The energy upon absorption is given by the following:

$$\frac{2\pi}{5}Ze^2\rho[R_e^2-R_g^2] \tag{3.6}$$

where Z is the atomic number, e is the electronic charge, ρ is the contact density, and the term $[R_e^2-R_g^2]$ accounts for the slight difference in radius of the nucleus as it goes from the ground state to the excited state. The actual experimental measurement is the difference in transition energies between the emitter and the absorber and so the isomer shift is given by:

$$IS=\frac{4\pi}{5}Ze^2[R\delta R](\rho_a-\rho_e) \tag{3.7}$$

The term $2[R\delta R]$ approximates the former radius term since the change in radius is so small ($\sim 0.01\%$) and the term $(\rho_a-\rho_e)$ is the contact potential difference between the absorber and the emitter. Since, other than the latter term, the former terms are characteristic of the nature of the absorber and emitter and remain constant, therefore the isomer shift is proportional to the change in the s count at the nucleus:

$$IS=a\Delta n_s \tag{3.8}$$

Attempts had been made to relate the isomer shift to an absolute number in the change of s count. Focussing on the Au system, it had been originally suggested that an a value of 8 mm s^{-1} represents the complete transfer of a 6s electron.[9,10,11] This relationship could not explain some experimental results, such as that for the metallic

$AuAl_2$ system, which showed an isomer shift of approximately 7 mm s^{-1}. It is unreasonable to assume that Au would gain approximately 0.9 electrons in a metallic system that must maintain electroneutrality. Calibration of the *s* charge in Au-Sn alloys[3] was performed using Knight-shift hyperfine constants to find the change in conduction charge which was then related to the Mössbauer isomer shifts.[3,12,13] It was found that the quantitative relationship between the isomer shift and the conduction charge transfer should be:

$$\Delta n_c = 0.086 \times IS \tag{3.9}$$

giving a value of approximately 12 mm s^{-1} for the constant *a*. This discrepancy is associated with the fact that for metallic systems (especially those involving valence *d* charge) the transfer of *d* charge to or from the site cannot be ignored. The screening of the *s* charge is substantially affected by the gain or loss of *d* charge and thereby affects the contact potential experienced by the absorbing nucleus. Another effect that must be accounted for is that of volume changes. Since the contact density of the emitter is determined within a Wigner-Seitz volume of the pure metal any changes to that volume upon alloy formation will change the relative contact density that is measured and must be adequately accounted for before assigning the shifts to chemical effects.[14,15] Fortunately, in our study on Au-Cu alloys, there is negligible expansion of the volume, as discussed previously, and therefore these affects can be ignored.

We have, therefore, a method of calculating the conduction charge transfer, Δn_c, which can be incorporated in Equation 3.3, to determine the overall charge and *d* charge transfer at the Au site. The same operation could be performed on Au-Cu alloys from

the Cu perspective. This involves determining the Slater integrals at the Cu site but unfortunately also involves determining the conduction charge transfer. There is no Mössbauer isomer shift data from the Cu perspective since there is no available excited state source and therefore Mössbauer experiments cannot be performed.

3.3 Method of Determining *d* Hole Counts using XANES Data

As was mentioned in the introduction of this chapter we have performed X-ray absorption experiments on the series of Au-Cu alloys with a two-fold purpose. Figure 3.3 shows a typical absorption spectrum taken in the transmission mode for the Au L_3 edge. This is a transition from the Au $2p_{3/2}$ state and is divided into two regions. The transmission intensity of an X-ray absorption process is given by:

$$I_t = I_0 e^{-\mu(h\nu)t} \tag{3.10}$$

where I_t is the transmitted X-ray flux, I_0 is the initial X-ray flux, μ is the absorption coefficient, and t is the sample thickness. The axes in Figure 3.3 are $\ln(I_0/I_t)$ (equivalent to $\mu(h\nu)t$) versus the photon energy $h\nu$. The excitations are from the core state of interest into bound, quasibound and continuum levels as the photon energy is increased. For this particular section we are interested in excitations just at and above threshold. The excitations into the continuum will be examined later.

The near edge region, as we have defined here, occurs from the threshold to approximately 50 eV above and has a strong absorption feature with some structure above the edge. The inset of the figure shows a scaled comparison of the near edges of pure Au and $Cu_{19}Au$. Of note here is the sharp intense peak at the edge observable for the $Cu_{19}Au$ system as compared to the pure Au sample. This peak has been denoted as the whiteline.

Mott[16] first interpreted such whitelines (and lack of) in the L edges of platinum metal. He noted that there was a strong whiteline in the L_3 (denotes the $2p_{3/2}$ core level)

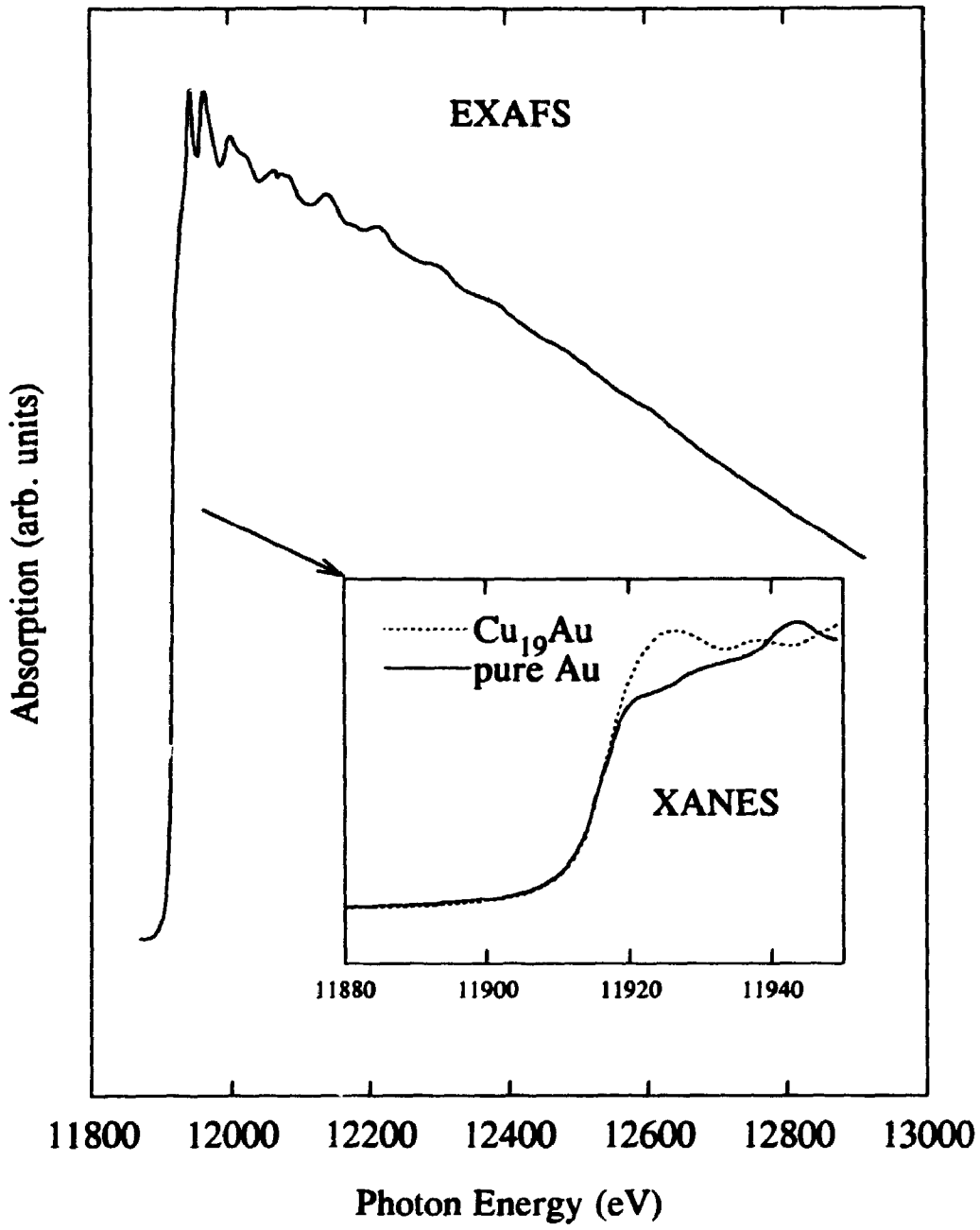

Figure 3.3: X-ray absorption spectra of the L_3 edge of pure Au showing the sharp rise and subsequent, almost linear, fall of the absorption coefficient. The two regions of interest are labelled as XANES and EXAFS. The inset shows the XANES region of $Cu_{19}Au$ and pure Au, clearly indicating the larger feature above the edge for the $Cu_{19}Au$ sample.

edge but no apparent whiteline in the L_1 (denotes the $2s$ core level) or L_2 (denotes the $p_{1/2}$ core level) edges. He explained these observations using an atomic argument. For atomic excitation from states defined by the quantum numbers nlj into unoccupied states $n'l'j'$ the following dipole selection rules apply, $\Delta l=\pm 1$ and $\Delta j=0,\pm 1$. For the platinum atom with localized empty d states the transition from the $2s$ level is forbidden ($\Delta l=\pm 1$) and no whiteline is seen even though an absorption edge is seen for transitions to disperse states of p symmetry and p-like continuum states. The origin of the whiteline in the L_3 edge and lack of, in the L_2 edge, is explained by spin-orbit coupling. For atomic Pt the empty d states have $j=5/2$ symmetry due to spin-orbit coupling. Using the selection rule of $\Delta j=0,\pm 1$ it can be easily seen that the only allowable transition to the empty d states of $j=5/2$ character is from the $2p_{3/2}$ core level or the L_3 edge. Transitions into empty s states are also allowed but the matrix element of this transition is usually an order of magnitude lower ($\Delta l=-1$ versus $\Delta l=+1$) and the s states are usually dispersed in energy as compared to d states. In extending this to the observations for Pt metal an assumption must be made that atomic spin-orbit coupling has not broken down by band formation (i.e. that the unoccupied d states still retain the j values as good quantum numbers). Should spin-orbit coupling break down we would expect the spectra for metallic Pt to contain states of both $j=5/2$ and $j=3/2$ character. Experimental spectra of Cauchois and Manescu[17] and Coster and De Lang[18] indeed show that spin-orbit coupling is still valid in agreement with the observations of Mott.

Extending this picture to the system of our interest, Au-Cu alloys, a qualitative assessment of d charge transfer could be achieved by comparing our Au L edge spectra

for the alloy with that of pure Au. A decrease in the whiteline area would indicate a gain of *d* charge at the Au site while an increase in the whiteline area would indicate a loss of *d* charge at the Au site. Of more interest, however, would be to determine actual numbers for the amount of *d* charge transfer which could then be directly compared and correlated with the Δn_d values calculated by the previously mentioned conventional model based on binding energy and Mössbauer isomer shifts.

Following the model developed by Brown *et al.*,[19] and expanded by Mattheiss and Dietz,[2] and Mansour *et al.*[20] the area under the whiteline can lead to the determination of the number of *d* holes of $j=5/2$ and $j=3/2$ character. This model was developed specifically for the Pt *L* edges but using various approximations this has been extended for the study of the Au *L* edges.

The probability per unit time for a transition from an initial state, *i*, to a final state, *f*, by a perturbation H' (in this case the perturbation is a photon, i.e. $H'=Ae^{ikr}$) is given by Fermi's Golden Rule:

$$W=\frac{2\pi}{\hbar}|\langle f|H'|i\rangle|^2\rho(E_f) \qquad (3.11)$$

where $\rho(E_f)$ is the density of final states and $\hbar$ is the Dirac constant.

Calculations performed by Brown *et al.* attempted to quantify the symmetry exhibited by the unoccupied *d* states in Pt metal to determine if indeed they were mostly of $j=5/2$ character. Using a Hamiltonian which included spin-orbit coupling and a Herman-Skillman atomic radial function for 5*d* orbitals of platinum they determined a $j=5/2$ to $j=3/2$ ratio of 14 to 1. Mattheiss and Dietz on the other hand, used relativistic

calculations which included possible hybridization with 6*s* and 6*p* bands to get a ratio of ~3. They performed similar calculations on pure Au and determined a ratio of 2.4 with the total hole count being 0.401 electrons.

Brown *et al.* have also attempted to determine theoretically the whiteline area of the Pt $2p_{3/2}$ to $5d_{5/2}$ transition. From Equation 3.11, using the dipole approximation, and relating the transition probability to the absorbance we find:

$$A = \int \mu(E)dE = \frac{2\pi^2 e^2 \hbar N_0}{mc} \bar{F}_{fi} n_h \tag{3.12}$$

where A is the area contributed by the absorbance, μ is defined by Equation 3.10, m is the free electron mass, N_0 is the number of atoms per unit volume, n_h is the number of *d*-band holes, and F_{fi} is the oscillator strength defined by:

$$F_{fi} = \left(\frac{2m\hbar\omega_i}{3\hbar^2}\right)\langle f|\hat{r}|i\rangle^2 \tag{3.13}$$

where the last term involves the matrix element of the transition to the final state and ω_i is the frequency of the initial state. To account for core hole-photoelectron interactions they used a Au 5*d* wavefunction to simulate relaxation experienced by the 5*d* wavefunction of Pt (the fully relaxed Pt atom with an *L* shell hole can be approximated by a core-equivalent $Z+1$, Au atom). They had calculated the contribution to the whiteline area by the $2p_{3/2}$ to $5d_{5/2}$ transition but they could not directly relate their calculation to experimental L_3 edge data since the whiteline area is derived by contributions not only from the $2p_{3/2}$ to $5d_{5/2}$ transition but also by the $2p_{3/2}$ to $5d_{3/2}$ transition as indicated by the selection rule of $\Delta j = 0, \pm 1$. Mattheiss and Dietz resolve

this problem by determining non-vanishing coefficients for the transition from a core state, $n'l'j'$, to a valence state, lj, by the following relationship:

$$I_{n'l'j'} \propto (2j'+1)\sum_{lj} A^{n'l'j'}_{lj}(E)N_{lj}(E) \qquad (3.14)$$

where I is the intensity of the absorption, A is a slowly varying function including the matrix element of the transition (R) and has a small energy dependence, and N is the unoccupied density of states which is also energy dependent. Values for the $(2j'+1)A/R$ non-vanishing coefficients for the transitions of our interest are given in the following Table 3.1.

$(2j'+1)$A/R		d	
		$j=5/2$	$j=3/2$
$n'p'$	$j'=3/2$	6/15	1/15
	$j'=1/2$	0	5/15

Table 3.1: Various non-vanishing coefficients for the transitions of interest, namely $2p_{1/2}\rightarrow 5d_{3/2}$, $2p_{3/2}\rightarrow 5d_{3/2}$, and $2p_{3/2}\rightarrow 5d_{5/2}$.

These values can be used in two different manners. First if we use the coefficients and substitute them in Equation 3.14, we can relate the integrated intensity (area) ratio for the L_2 and L_3 edges to the hole counts, h, by:

$$\frac{I_{L_3}}{I_{L_2}} = \frac{\frac{6}{15}(R^{5d_{5/2}}_{2p_{3/2}})h_{5/2} + \frac{1}{15}(R^{5d_{3/2}}_{2p_{3/2}})h_{3/2}}{\frac{5}{15}(R^{5d_{3/2}}_{2p_{1/2}})h_{3/2}} \tag{3.15}$$

and by further assuming that the matrix elements for the two excitation processes are the same and that their energy dependence is not strong, we are left with:

$$\frac{I_{L_3}}{I_{L_2}} = \frac{6h_{5/2} + h_{3/2}}{5h_{3/2}} \tag{3.16}$$

Also, by combining Equations 3.13 and 3.14, and incorporating the non-vanishing coefficients, an expression that directly relates the areas under the L_2 and L_3 with the d hole count can be determined:

$$A_{L_2} = \int \mu_{L_2}(E)dE = \frac{4\pi^2 e^2 N_0 E_{L_2}}{3\hbar c}(R^{2p_{1/2}}_{5d})\frac{h_{3/2}}{3} \tag{3.17a}$$

$$A_{L_3} = \int \mu_{L_3}(E)dE = \frac{4\pi^2 e^2 N_0 E_{L_3}}{3\hbar c}(R^{2p_{3/2}}_{5d})\frac{(6h_{5/2} + h_{3/2})}{15} \tag{3.17b}$$

where again the slight energy dependence of the matrix element as it is summed over the unoccupied d band is ignored.

There now exists an independent method of determining the d hole count at the Au site which can be compared to that which is derived from the conventional model. To solve Equations 3.17a and 3.17b an estimation of the value of the matrix element

must be made and the areas somehow rigorously determined from the experimental spectra. These factors will be discussed in Section 4.4 as well as the sensitivity of this technique when qualitatively examining the Cu K edge ($s \rightarrow p$ transition) and comparing the results to resonant photoemission.

3.4 Method of Determining Local Structure and Configuration using EXAFS Data

In this section we are concerned with the absorption spectrum 50 eV above the edge and beyond as shown in Figure 3.3. This region exhibits oscillations in the absorption coefficient which are labelled Extended X-ray Absorption Fine Structure (EXAFS).

These structures are closely related to the molecular and solid potentials and are absent in atomic absorption spectra. They involve excitations of the photoelectrons not into bound or quasibound states but into the continuum. The origin of the oscillating behaviour is the backscattering of the more energetic photoelectron wave by nearest-neighbour sites and constructive and destructive interference as the outgoing photoelectron wave interacts with the backscattered wave (Figure 3.4). This behaviour modulates the observed absorption coefficient and the lack of nearest neighbours explains the absence of this behaviour in atomic spectra.

The first attempt to explain theoretically this behaviour was made more than 60 years ago.[21] Since then, using single scattering theory, the analysis of the EXAFS spectrum has developed to the extent that local information can be deduced. Figure 3.4 shows the dominant single scattering pathway but multiple scattering pathways exist which manifest themselves in the lower energy region just above the edge. This complicated region is now the focus for many theoretical studies.

Rewriting Equations 3.12 and 3.13 we have:

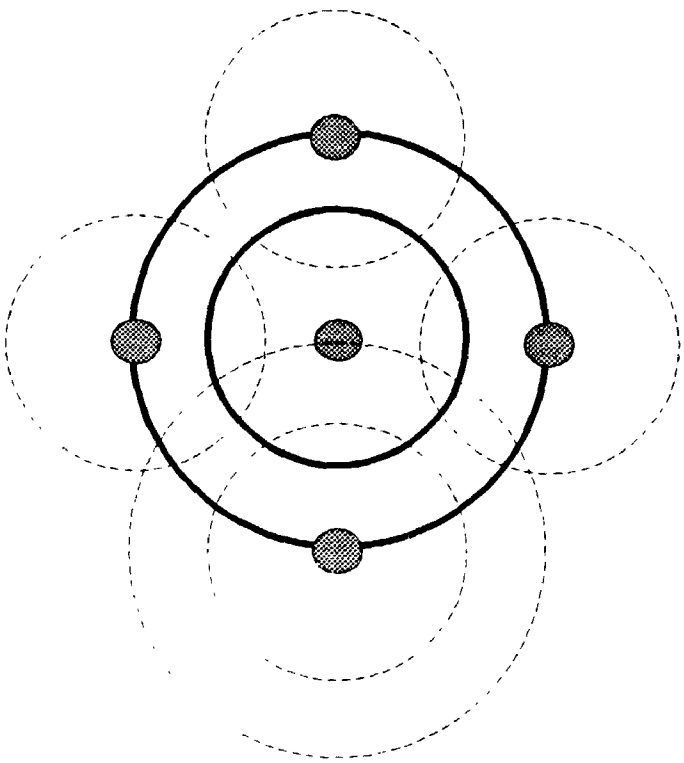

Figure 3.4: Schematic picture of the photoelectron wave function originating from the centre atom. The solid circles are the outgoing wavefunction while the hatched circles are the backscattered wave function.

$$\mu = \frac{4\pi^2 \omega e^2 N_0}{3c} |\langle f|\hat{r}|i\rangle|^2 \rho(E_f) \tag{3.18}$$

where all the terms have been previously defined except for ω, which is the frequency of the X-ray. The density of final states is assumed to be that of the free electron as the energy is high enough that band effects are negligible. The matrix element involves a core state, i, which does not vary with the X-ray energy. The modulation occurs in the final state wavefunction, f, and it is from here that a quantitative formulation of the EXAFS is made. We will only note the main factors that contribute to the final expression, since there are many good reviews on the derivation of the EXAFS formula, including that by Stern.[22]

As was stated previously, the origin of EXAFS is the modulation of the outgoing photoelectron wave by constructive and destructive interference with the wave that is backscattered by the nearest-neighbour shell.

The outgoing spherical photoelectron wave can be described by:

$$\frac{1}{r} e^{ikr} \tag{3.19}$$

The scattered wave originates at a distance r_i and its amplitude depends on the amplitude of the original wave and the nature of the scatterer. The amplitude of a backscattered wave at the origin of the absorber site is given by:

$$T_i(2k) \frac{e^{i2kr_i}}{r_i^2} \tag{3.20}$$

where $T_i(2k)$ is the contribution to the amplitude by the nature of the scatterer, and the

term $2kr_i$ is the phase shift of a wave that travels to the scatterer and back in a constant potential. Unfortunately, the potential is not a constant and a term must be included to account for the varying potential from both the absorber and scatterer. If we expand the e^{ix} term ($e^{ix}=\cos x+i\sin x$) and retain the imaginary part and include the appropriate proportionality constant, we are left with:

$$\chi_i(k)=\frac{m}{2\pi\hbar^2k^2}T_i(2k)\sin(2kr_i+\delta_i(k)) \tag{3.21}$$

Two other factors must be included in the EXAFS equation: the lifetime of the core hole and of the ejected electron, and the vibration between the absorber and scatterer.

In terms of the effect on the EXAFS equation the electron lifetime is more important than the lifetime of the core hole and the familiar mean free path relationship (Equation 2.6) is used for a distance of $2r_i$ travelled by the electron.

The vibrational component is assumed to be gaussian and is given by:

$$e^{-2k^2\sigma_i^2} \tag{3.22}$$

where σ_i is the root-mean-square deviation due to absorber-scatterer vibration.

We must now sum over the number of nearest neighbours N_i, at a distance r_i and include the possibility of different types of atoms at different distances and include a term to account for amplitude reduction due to many-body effects, leaving us with the final EXAFS formula:

$$\chi(k)=\sum_i \frac{N_i}{kr_i^2} S_0^2 F_i(k) e^{-2r/\lambda} e^{-2k^2\sigma_i^2} \sin[2kr_i+\delta_i(k)] \qquad (3.23)$$

where all the terms, except for the sine term, account for the amplitude, and the sine term accounts for the phase. To elucidate structural factors such as nearest-neighbour distance and configuration, from this formula, a detailed analysis of the experimental spectra, which will be performed in Section 4.4, is required in determining the local structure of these alloys.

3.5 Sample Preparation and Characterization

Both Au and Cu are face centre cubic (fcc) metals and are completely miscible in the bulk forming solid solutions throughout the compositional range. This is shown in the Au-Cu phase diagram in Figure 3.5.[23] In examining Figure 3.5 it is clear that the Au-Cu system is also a classical example of order-disorder transitions with superlattice phases around stoichiometric compositions $Cu_{0.75}Au_{0.25}$, $Cu_{0.5}Au_{0.5}$, and $Au_{0.75}Cu_{0.25}$ (henceforth denoted Cu_3Au, AuCu, and Au_3Cu).

Au-Cu alloy ingots (atomic compositions 5.0-95.0; 12.5-87.5; 25.0-75.0; 50.0-50.0; 75.0-25.0) were prepared from 99.99% pure metals.[d] Accurately weighed amounts were melted under H_2 at about 1500 K in boats made of pure silica. Each melt, while kept in rapid motion, was quenched under H_2. The ingots were rolled into polycrystalline foils with thicknesses of about one absorption length at the Au L_3 edge.[24,e] Under these conditions Cu_3Au, AuCu and Au_3Cu exist in their disordered states. Further preparations were done on the Cu_3Au, AuCu and Au_3Cu samples by annealing in an evacuated quartz tube for two weeks at just below the transition temperature for their respective stoichiometric composition (i.e. 493 K for AuCu and 435 K for Au_3Cu), as indicated by the Au-Cu phase diagram, to achieve their respective ordered states. The

---

[d] All the bulk alloy ingots were prepared by Walter Kunnmann of Brookhaven National Laboratory, Upton, N.Y.

[e] The absorption length at the Au L_3 edge is given by Equation 3.10 setting $\mu t = 1$ and solving for t. Using tables from Reference 24, the absorption coefficient at the Au L_3 edge is 105.3 cm^2g^{-1} x density of Au, giving a thickness of approximately 5×10^{-6} m or 0.2 mil.

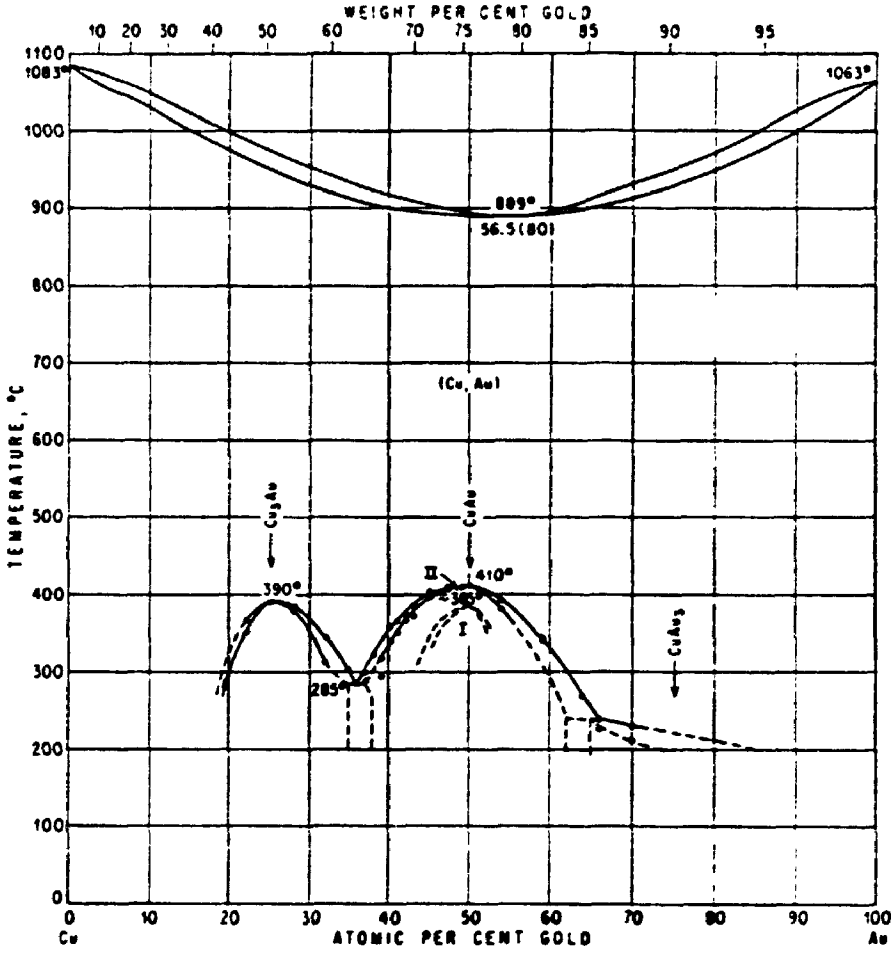

Figure 3.5: The Au-Cu phase diagram as taken from Reference 23. The three superlattice phases are centred around Au percentage, 25, 50 and 75.

degree of order and disorder was checked with both Cu *K* and Au L_3 edge EXAFS. Figure 3.6 shows a simplified analysis in which a baseline subtraction was performed to simulate the falling absorption coefficient. The data were then truncated from about 50 eV to 1000 eV above the edge and converted to k space with a weighting of k^3 to enhance oscillations far above the edge. The last step is a spline background subtraction. In general, the disordered samples exhibited weaker oscillations as seen in Figure 3.6.

Both the annealed Cu_3Au and Au_3Cu alloys form an ordered cubic $L1_2$ structure (Figure 3.7) while under the aforementioned conditions the AuCu alloy forms an ordered tetragonal $L1_0$ type of structure (denoted by AuCu I). There also exists a higher temperature ordered phase denoted by AuCu II (the structure of these two alloys is very complicated). $Cu_{0.875}Au_{0.125}$ and $Cu_{0.95}Au_{0.5}$ do not form superlattice structures according to the phase diagram.

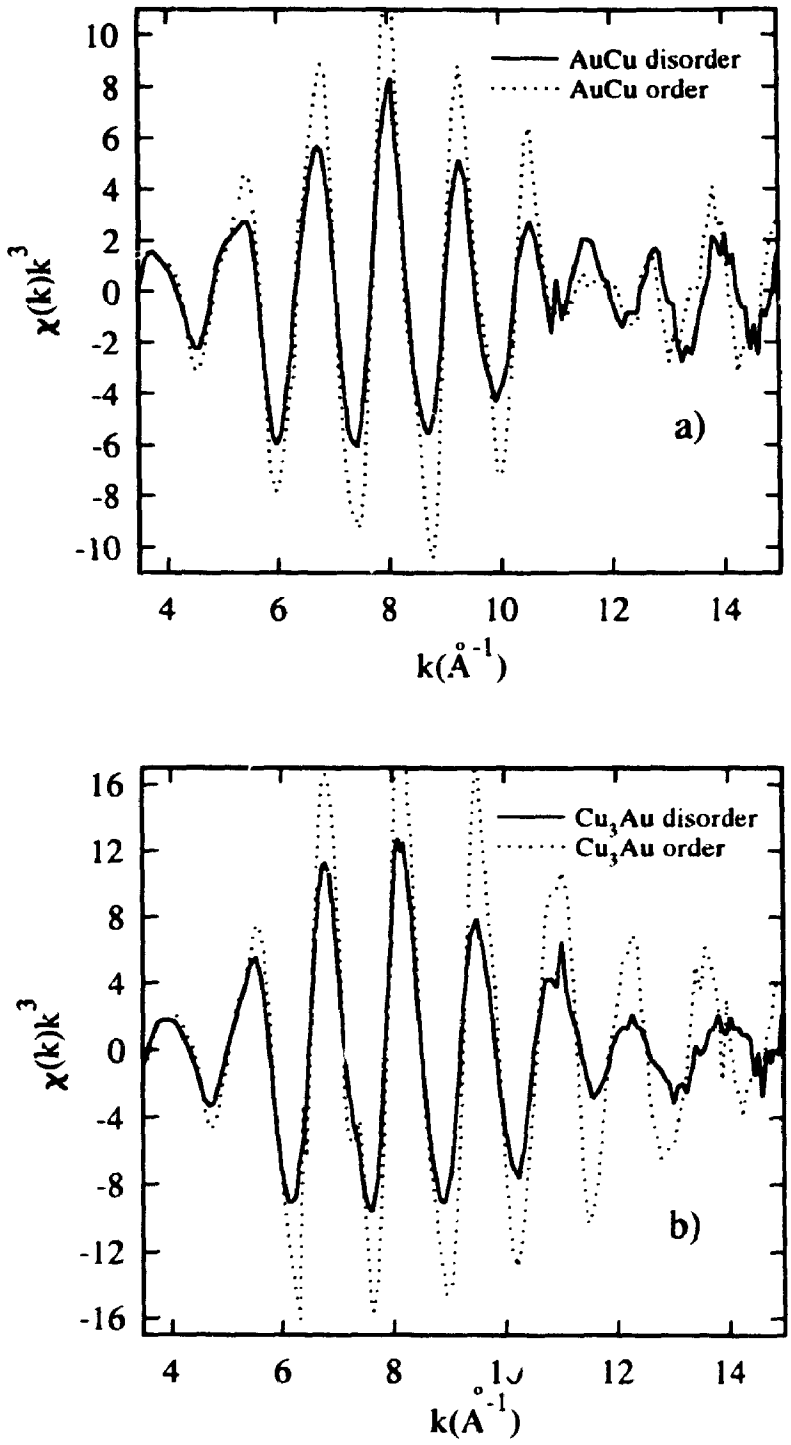

Figure 3.6: EXAFS of a) AuCu order-disorder alloys (upper panel) and b) Cu_3Au order-disorder alloys (lower panel). The EXAFS spectra were normalized to the edge jump of one atom and then truncated 50 eV to approximately 1000 eV above the Au L_3 threshold at 11917 eV. A linear background subtraction was done, then a conversion to k space with a weighting of k^3, followed by spline subtraction. The amplitudes are directly comparable.

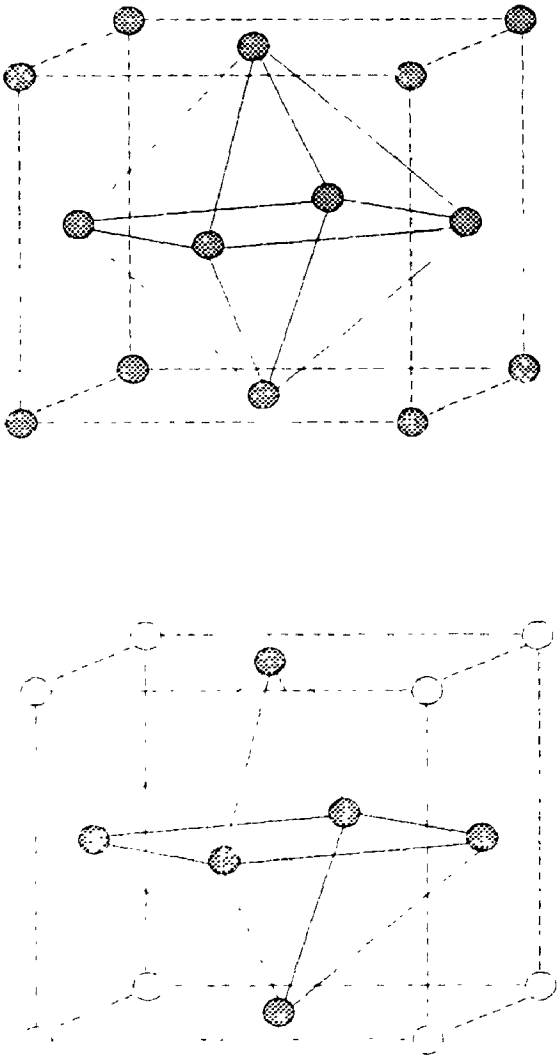

Figure 3.7: Representation of the fcc structure (top diagram) for both pure Au and Cu. The bottom diagram represents the $L1_2$ structure adopted by both ordered Cu_3Au and Au_3Cu. For the case of Cu_3Au the open circles represent Au while the filled circles represent Cu. The opposite applies for the Au_3Cu alloy.

3.6a X-ray Photoelectron Spectroscopy (XPS) Setup

The measurement of the core level binding energies was performed using a standard laboratory XPS system. The system used was the Surface Science XPS spectrometer (SSX-100) located at Surface Science Western.

This spectrometer uses a monochromatic Al $K\alpha$ X-ray source, a 180° hemispherical electron analyzer using channel plates as the electron detection method and with a sampling size as small as 100 μm. The overall resolution (photon and instrumental) is $\sim$0.6 eV. All measurements were made at normal emission. The pumping system consists of a series of turbomolecular pumps and ion pumps which maintain the base pressure in the main analysis chamber at 1×10^{-9} Torr. Figure 3.8 gives an overview of the setup of the Surface Science system.

Several features in this system are noteworthy. There is an isolated sample introduction system which allows for sample transfer without degradation of the analysis chamber vacuum. The sample mounting system consists of a stage which allows for multiple samples. The stage was in electrical contact with the rest of the system (equalization of the Fermi levels) but could not be used for heating or cooling of the samples, therefore all measurements were done at room temperature. A microscope system was employed to position the sample in the focal point of the analyzer such that the X-ray source and electron window were oriented properly for maximum incident photon flux and electron detection. This system allows visual selection of the sample area of interest and is also linked with the ion sputter gun such that site-specific

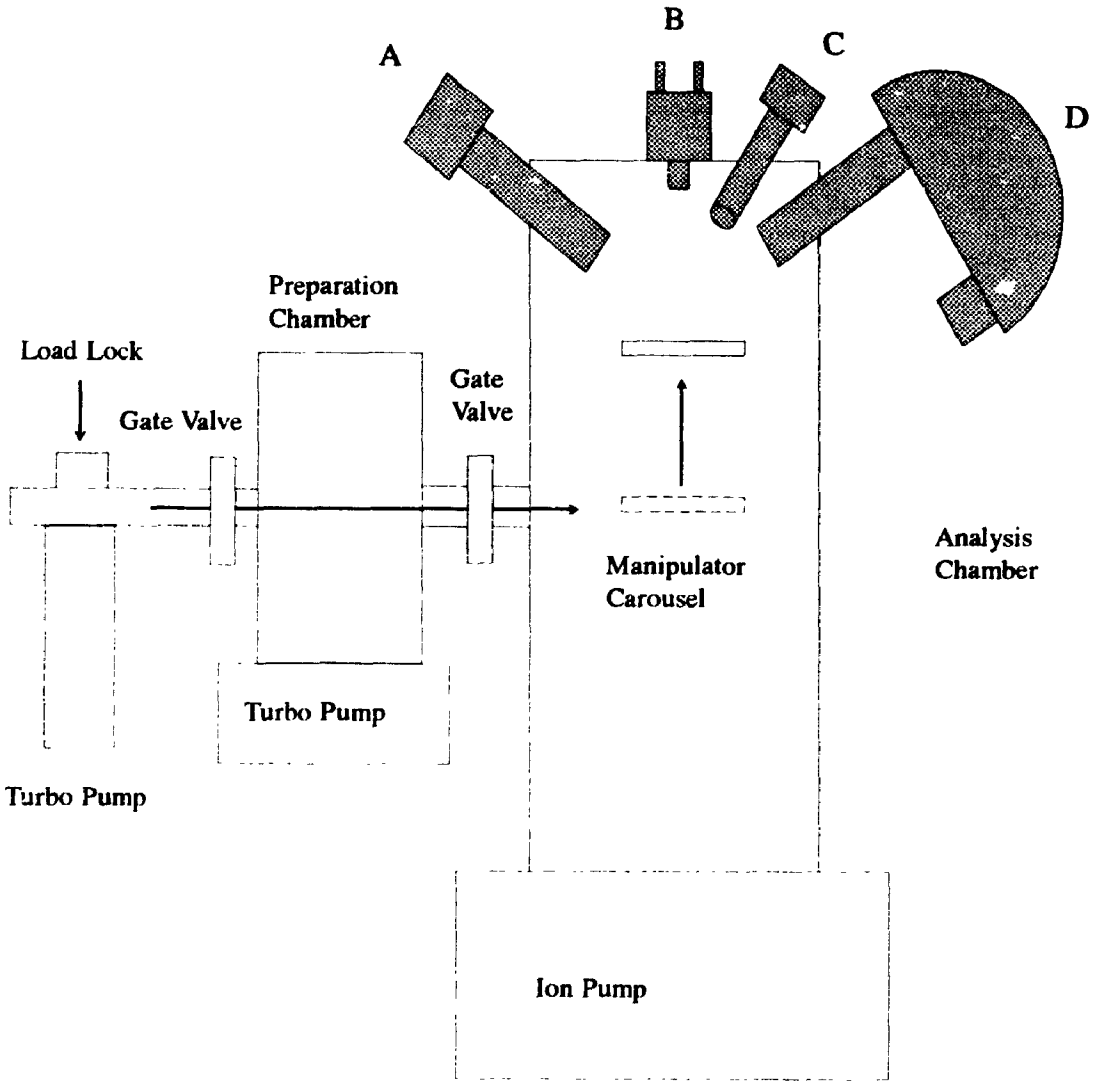

Figure 3.8: Schematic of the setup of the Surface Science Western XPS system. A) Al $K\alpha$ X-ray lamp as the source; B) microscope for sample alignment; C) ion sputter gun for sample cleaning; D) electrostatic hemispherical electron analyzer with multichannel detection.

bombardment for sample cleaning can be performed.

Al $K\alpha$ X-rays are produced by electron bombardment of an Al anode ejecting a $1s$ (K) electron. Filling of the core hole by higher level electrons induces the emission of a photon (and also Auger electrons) whose energy depends upon the level of the donor electron. The main decay mechanism is the $2p \rightarrow 1s$ (termed α) transition releasing a photon with an energy of 1486.6 eV. Other competing decay mechanisms manifest themselves as satellites structures to the Al $K\alpha$ main line and therefore monochromatization (using a quartz crystal) is necessary to reduce the photon resolution to less than 1 eV. As was explained in Chapter 2 the resolution is also limited by the lifetime of the core hole which in this case is short and thereby the linewidth is broad. The high energy of the photon source leads to a lower cross-section of the levels of interest, namely core and valence, since the photon energy is much higher than the emission thresholds, as was also previously explained. Therefore a high flux is required to increase the sensitivity of detection. Even with these limitations, the bulk electronic properties of Au-Cu alloys, with reference to binding energy shifts, are more conveniently deduced from use of an XPS system than from synchrotron radiation techniques. There are two major reasons for this. Even though a source, with an energy in the range of the emission level of interest, would have a high cross-section for that emission level, the study of *bulk* properties would be limited as the photoelectron would have a low kinetic energy and therefore originate mostly from the surface region (shorter mean free path). For the XPS system, excitation of the Cu $2p$ and Au $4f$ core levels leads to photoelectrons with kinetic energies ranging from 500 eV to 1400 eV and

subsequently with much longer escape depths. Also, to again minimize surface contributions, the experiments were performed at normal emission. The other reason that the XPS system is more advantageous to study the binding energy shifts of the Au-Cu system, is that there was not a monochromator available, for synchrotron studies, that had as high resolution as the XPS in the energy regime of 1000 eV to 1500 eV.

The photoelectrons are collected via a hemispherical analyzer using multichannel plate detection. The plates have the advantage of higher count rates and thereby quicker scan rates than the usual channeltron electron detection system. The resolution of the system is dictated by the pass energy or the energy window for allowing electrons into the analyzer if the system is run under a constant pass energy mode. The lower the pass energy the higher the resolution but there is a sacrifice in the sensitivity.

The samples were cut into pieces ~5mm x 5mm. They and the mounts were precleaned in a methanol and/or acetone ultrasound bath to remove organic contaminants. They were then quickly mounted onto the transfer rod through a load lock system and the pressure was taken down to high vacuum ($\sim 10^{-6}$ Torr). The main analysis chamber was opened to the transfer rod and the samples were mounted onto the manipulator carousel. After a short pump-down period the samples were ready for analysis. Using the microscope the samples were moved to the optimum position and a quick wide scan from 0 eV to 1000 eV was usually performed to check for contamination, specifically carbon at a binding energy of 284 eV and oxygen at 543 eV. The scans were recorded as a function of kinetic energy but were converted to binding energy by including the work function of the spectrometer. Since the work function of the spectrometer changes

over a period of time a standard, such as pure Au 4*f*, was used to recalibrate the spectrometer. This could also be checked by direct measurement of the onset of the Fermi level exhibited by these samples. All the samples, as-introduced, displayed large carbon and oxygen signals and were cleaned by sputtering with argon ions with an energy of 1 keV for a period of 15 to 30 minutes to remove the contaminants. The pressure in the analysis chamber remained in the 10^{-7} Torr regime during sputtering. This process was repeated until no carbon or oxygen signal was detected. For the samples in this study, pure Au required the least amount of sputtering while Cu required the most. The spectra were taken at the highest resolution and with a sampling spot size of 300μm. With computer control, multiple regions could be scanned during one experimental sitting. Multiple scans were also performed to enhance the signal-to-noise ratio and to compensate for the low cross-sections of the emissions levels of interest. The step size in the kinetic energy ramping is $\sim$0.05 eV. The resulting spectra were then converted to ASCII code format for analysis, at first by manual digitization and later by direct conversion.

Also of importance is the contribution to the photoemission signal by the resolution of the photon and the instrument. The Lorentzian photoelectron lineshape (with a Gaussian component due to phonon broadening) will be convoluted by the Gaussian contributions of both the photon and instrument, a value of 0.6 eV, limiting the achievable width of the observed photoemission signal.

3.6b Synchrotron Photoemission Experimental Setup

Photoemission experiments were performed at *Aladdin*, the 1 GeV synchrotron ring located at the University of Wisconsin, Madison, Wisconsin. The beamline used was the Canadian Grasshopper which has an energy range from approximately 50 eV to 1000 eV. The higher energy region (300 eV and higher) is not that usable due to the low photon energy resolution.

The beamline itself consists of a series of optical elements including apertures, mirrors, and a monochromator. Apertures allow synchrotron light to enter the beamline and serve the purpose of defining the photon beamsize and increasing the resolution by reducing the opening angle (at the cost of losing flux). Mirrors are positioned for vertical and horizontal focussing and collimation. The monochromator selects the desired photon energy.

The optical elements for the Canadian Grasshopper beamline are shown in Figure 3.9 and are outlined below.[25] The synchrotron radiation is incident upon a gold-coated curved mirror (M_0) collecting 14 mrad of horizontal radiation and focussing it horizontally into the monochromator. The first optical element in the monochromator is a mirror (M_1) which vertically focuses the beam at a grazing angle into the entrance slit and slit mirror (M_2). The radiation is directed from there onto a plane grating at a grazing angle which disperses the radiation. The desired photon energy is selected by the relative positions of M_1, M_2, and the grating. The entrance slit, grating, and exit slit follow a rotation on a Rowland circle which fixes the exit slit and outgoing photon beam

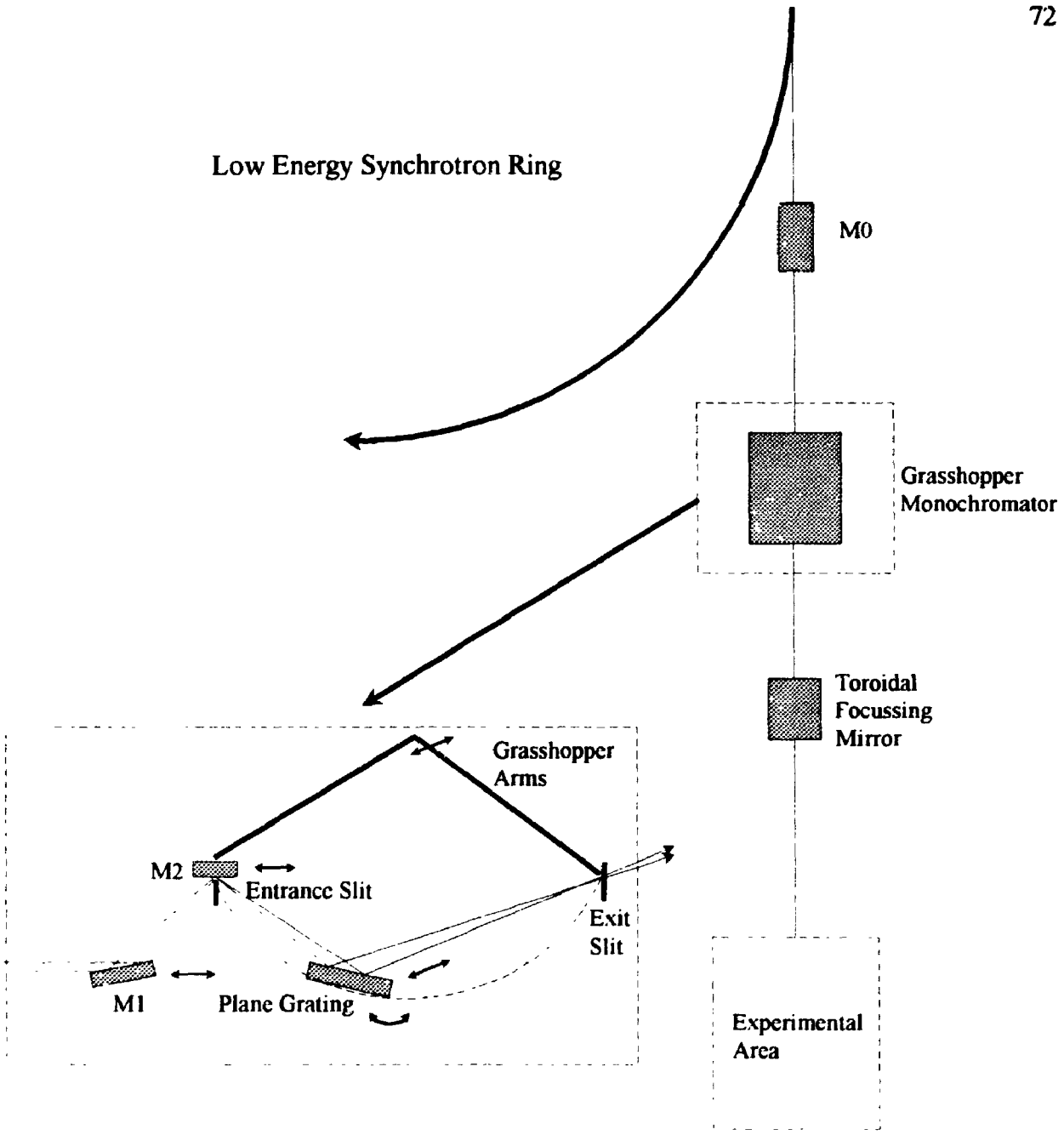

Figure 3.9: Schematic representation of the CSRF Grasshopper beamline located at SCR. The typical energy of the ring is 800 MeV. The optical elements, M_0, M_1, M_2-entrance slit, plane grating, exit slit, and toroidal mirror are described in the text. Of note is the insert of the Grasshopper monochromator which shows the fixed exit slit by the relative movements of M_1, M_2-entrance slit, and plane grating. The large "arms" of the monochromator give rise to the nickname, Grasshopper.

angle, thereby the focal point of the monochromatized radiation in the experimental station remains fixed. The last optical element is a toroidal mirror which focusses the beam both horizontally and vertically into the experimental station as a beam approximately 5 mm wide by 2 mm high. Due to the relatively low energy of the photons and the subsequent interaction with residual gas molecules, the whole system is under ultrahigh vacuum (UHV) in the 10^{-11} Torr regime. This is achieved by a combination of ion and sublimation pumps in the monochromator and ion and cryopumps for the other elements.

The grating equation for a plane grating is given by:

$$n\lambda = d(\sin\alpha + \sin\beta) \tag{3.24}$$

where n is the order of the diffraction, λ is the wavelength, d is the distance between grating lines and is given by the ruled width divided by the number of lines, α is the angle of incidence, and β is the angle of diffraction The angular dispersion of the grating is defined by differentiating Equation 3.24:

$$\frac{d\beta}{d\lambda} = \frac{n}{d\cos\beta} \tag{3.25}$$

The resolution is proportional to the order of the diffraction and inversely proportional to the line spacing, therefore the resolution increases as the number of lines per cm on the grating are increased and increases as we go to higher order light. We also note that the Grasshopper monochromator operates at a grazing angle of incidence whereas the Stainless Steel Seya monochromator operates at normal incidence.

The overall photon resolution for the Grasshopper beamline is given by:

$$\frac{\Delta E}{E}=\frac{\Delta \lambda}{\lambda} \tag{3.26}$$

where $\Delta\lambda$ is given by:

$$\Delta \lambda(\text{Å})=x\times\text{slitwidth}(\mu m) \tag{3.27}$$

where x=0.008 (Å μm^{-1}) for the 600 line/mm grating and x=0.008/3 (Å μm^{-1}) for the 1800 line/mm grating which were used in this study. Using the relation $\lambda(\text{Å})E(\text{eV})$=12 398, the resolution in eV is defined as:

$$\Delta E=\frac{\Delta \lambda E^2}{12398} \tag{3.28}$$

The slitwidth for these studies was usually set at 50 μm, a compromise between high resolution and sufficient flux. Therefore, with a 600 line/mm grating a photon resolution of 0.32 eV is achievable at 100 eV and with a 1800 line/mm grating a photon resolution of 0.11 eV is achieved at the same photon energy. It is clear that the photon resolution of the incident radiation from the Grasshopper beamline is much higher than for the XPS system at lower photon energies but that because of the E^2 dependence the resolution quickly becomes comparable to that of the XPS system once photon energies of 200 eV and higher are reached.

Also of importance is the flux of photons that leave the monochromator as a function of photon energy.[26] The flux increases with the photon energy and peaks at about 530 eV with a 1200 line/mm grating. Two dips in the emission occur at the C and

O 1*s* binding energies due to absorption from these contaminants on the optical components.

The radiation enters an experimental chamber similar to that used in the XPS experiments but with a larger variety and number of analytical and spectroscopic tools which were not used in this particular study. Of importance is the presence of a Leybold 180° hemispherical analyzer using a channeltron in this case, for electron detection and amplification. The analog current signal is converted into pulses which are then read by a counter. Under computer control, the analyzer is allowed to step to the next kinetic energy and stabilize before a signal count is taken. Figure 3.10 is a schematic of the chamber used in this study with an indication of the location and orientation of the incoming photon beam, analyzer, and sputter gun. The chamber is pumped by a Perkin-Elmer TNBX system which consists of an ion pump and titanium sublimation pump.

The sample manipulator consists of a stage for x-y-z motion and a shaft containing two isolated Cu rods with a rotary piece to allow change of the angle, θ. The insulated Cu rods protrude approximately two inches from the bottom of the shaft into the chamber. The shaft acts as a Dewar for sample cooling while the isolated Cu rods allow for heating. The samples were cut into pieces approximately 10 mm x 5 mm and cleaned successively in methanol and acetone ultrasound baths. The samples were then spot welded across two tungsten wires, and the two tungsten wires attached to the Cu rods by in-line connectors. The manipulator was then mounted unto the chamber.

The chamber must now be oriented with the fixed beamline. This requires height and angular adjustments and since a visible photon beam could not be used while the

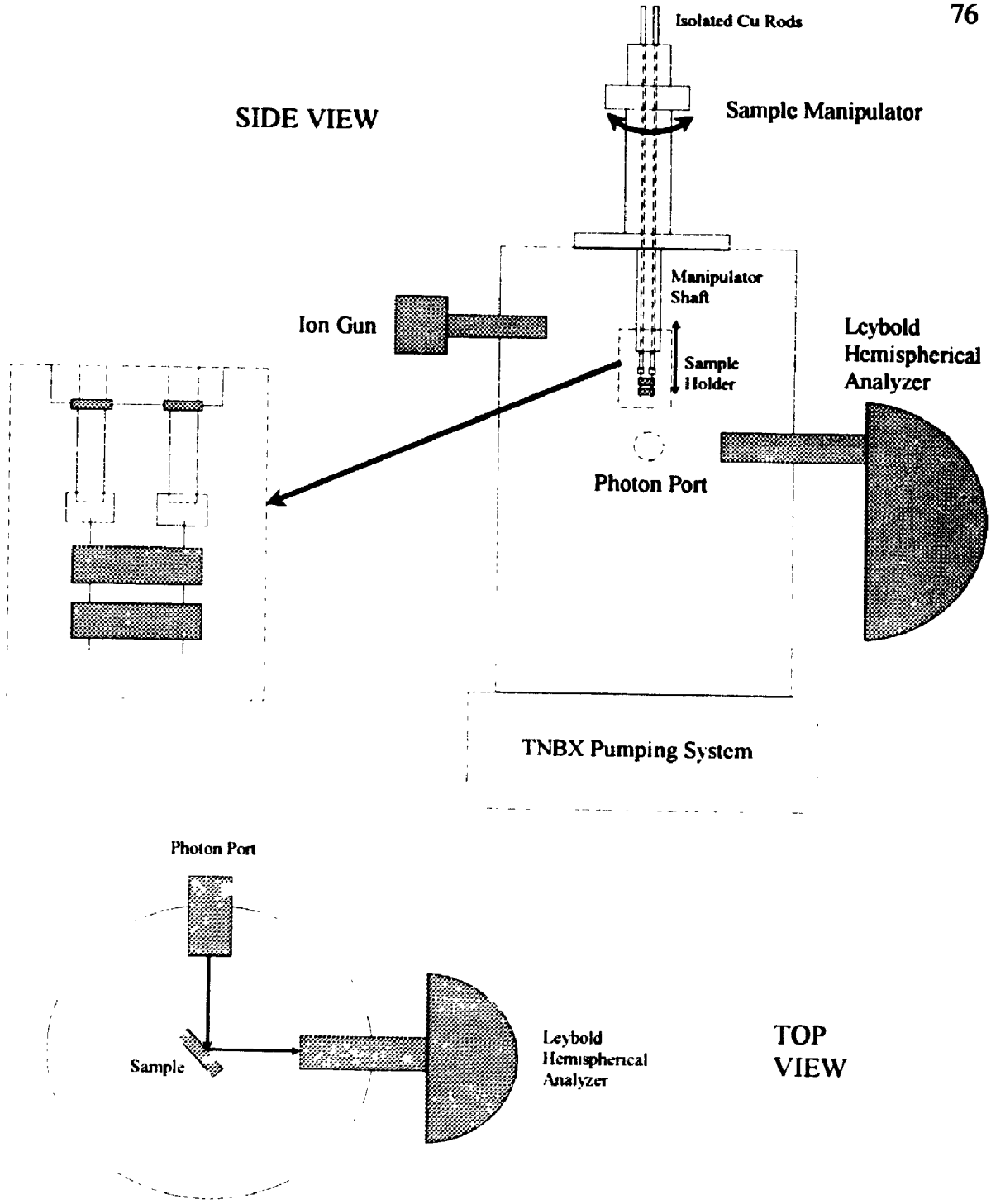

Figure 3.10: Diagram of the experimental chamber and the impo tant analytical devices used in this study. The insert shows the sample mount and the top view gives shows the relative angles of the photon beam, sample, and analyzer.

chamber was still at atmosphere the initial orientation is rough. The valved photon port on the beamline is attached to the chamber port by flexible bellows.

The chamber is then roughed down to 10^{-6} Torr using a portable turbo pump and then pumped to 10^{-8} using the ion pump. The chamber is then baked, for a period of a few days, using heating tapes and insulating aluminum foil at a temperature no higher than 150°C to maintain the integrity of Viton and Teflon seals. The contaminants in the system (mainly H_2O, H_2, and CO) are monitored by a residual gas analyzer. The presence of O_2 indicates a leak in the system. After the bakeout procedure, while the chamber is still warm (~ 50°C), the filaments in the system are degassed by operation at low currents.

The chamber is then aligned by allowing visible zero-order light (non-monochromatized) to enter the chamber. The sample is then oriented in the focal plane with respect to both the photon beam and analyzer entrance slit. The samples were again cleaned by Ar^+ sputtering at a pressure of $5x10^{-5}$ Torr for a period ranging from one-half hour to two hours depending on the sample. The samples were then annealed to a couple of hundred degrees. Cleanliness was indicated by the absence of oxygen or CO in the valence band spectra. Again the kinetic energy of the electrons was scanned, with a pass energy of 25 or 50 eV and a step size of 0.05 eV and converted directly to binding energy by direct subtraction from the photon energy. The computer control system did not allow for work function compensation. Multiple scans of each region were collected. The data was collected and converted to ASCII code for later analysis.

3.6c X-Ray Absorption Experimental Setup

The X-ray absorption experiments were performed at Beamline X11-A at the National Synchrotron Light Source located at Brookhaven National Laboratory, Upton, New York.

The energy region of interest encompasses the Cu *K* edge and Au $L_{1,2,3}$ edges. This requires a synchrotron that produces high flux at energies ranging from 9 to 14 keV. The X-ray ring at NSLS operates at 2.5 GeV and 100 mA providing sufficient flux at those energies as compared to the *Aladdin* ring (see Figure 2.8). It is beyond the limit of a plane-grating type of monochromator, such as the Grasshopper (due to the extremely small angles required), to produce photons in that energy region, therefore a double-crystal monochromator (DCM) is employed using the principle of Bragg diffraction.

Figure 3.11 is a schematic showing the components of the beamline (mirror and monochromator) and the end station. The monochromator basically consists of two parallel crystals. The Bragg equation for diffraction of radiation from a crystal is given by:

$$n\lambda = 2d\sin\theta \qquad (3.29)$$

where n is the order of the diffraction, λ is the wavelength, d is the lattice spacing of the crystal, and θ is the Bragg angle. In examining Equation 3.29, it is noted that for practical purposes the term $2d$ must be similar to the wavelength of interest to keep the Bragg angle from being to close to zero. This limits the type of crystal that can be used for a particular energy region. Another practical concern is that, although crystals with

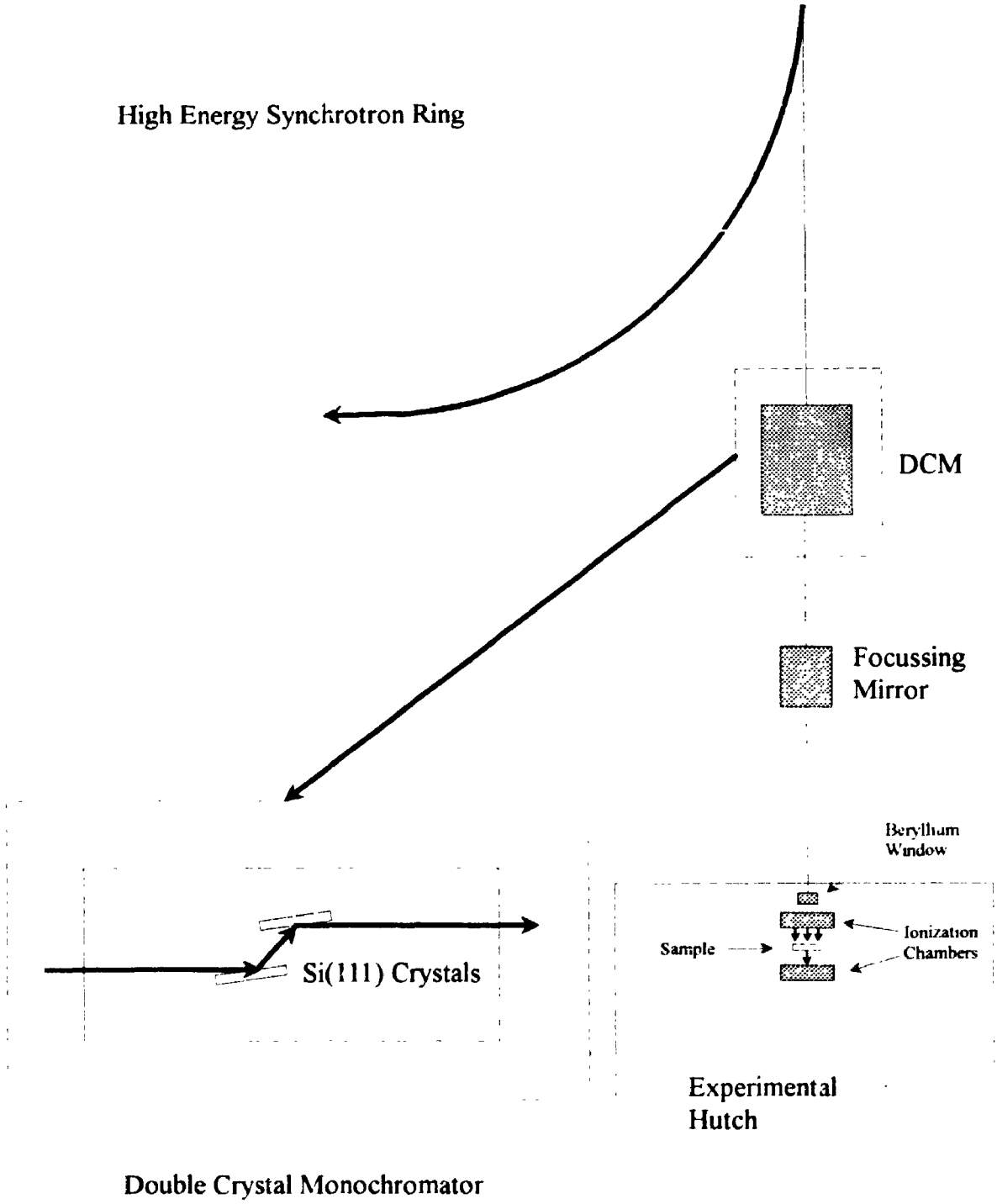

Figure 3.11: Schematic of a typical hard X-ray DCM setup. The X-ray ring at NSLS operates at an energy of 2.5 GeV. The insert shows the parallel crystal orientation of the DCM. The crystals are rotated together to maintain the beam direction and position.

the correct lattice spacing may be available, they must be easy to produce in a large enough size and exhibit properties suitable for the hard X-ray environment. They must have a small thermal expansion coefficient and large thermal conductivity to resist damage and change in properties from the heavy power load of the high energy synchrotron source. This is also alleviated somewhat by a cooling mechanism for the crystals in the monochromator. Another important property is that they cannot have absorption features in the energy range of interest. For the energy range of 9 to 14 keV Si(111) crystals, with a lattice spacing ($2d$) of 6.271 Å, are used.

The resolution of the monochromator is derived by differentiating Equation 3.29:

$$\frac{\Delta E}{E} = \frac{\Delta \lambda}{\lambda} = \Delta\theta \cot\theta \qquad (3.30)$$

The resolution, therefore, is determined by the angular spread, $\Delta\theta$, which in turn is determined by the properties of the crystal (rocking curve) and the vertical angular spread of the synchrotron radiation. For most crystals the latter effect is more important and thereby collimating mirrors are used to improve the resolution. For the X11-A beamline with two Si(111) crystals $\Delta E/E = 2\text{x}10^{-4}$ resulting in a resolution of 2 eV at 10 keV. The beamsize is 10 mm horizontal x 0.5 mm vertical with a flux of 1 x 10^{10} photons/sec at 10 keV. The monochromator was detuned to 50% of the maximum flux (on the rocking curve) to avoid harmonic content in the incident beam.

The photon beam enters an experimental hutch to isolate the experimentalist from the harmful X-rays through a beryllium window, which is transparent to photons in that energy region. The experiments were carried out in transmission mode as the sample

foils were of a thickness of the order of one absorption length. The samples were mounted between two ionization chambers to monitor I_0, the incoming flux, and I, the transmitted flux. Argon gas flowed steadily through the incoming flux chamber. The incoming X-ray beam ionizes the gas and the current produced is then amplified by Keithley current amplifiers. The I chamber was filled with a 1:5 steady flowthrough mixture of argon and nitrogen gas. The mixture was required since the transmitted flux was too low for easy detection of the argon ionization and therefore nitrogen, which has a lower ionization threshold, is added to the mixture. The use of nitrogen in the I_0 chamber leads to saturation of the signal. The experimental area was not under vacuum since the hard X-rays could easily penetrate the distance from the window through the ionization regions without significant loss of flux.

Unlike the typical photoemission experiment, X-ray absorption studies require stepped monochromator movements to provide a scan of the photon energy. This is accomplished by computer-controlled stepper motors which rotate both parallel crystals changing the Bragg angle and thereby the photon energy. Detuning of the crystal is achieved by slight rotation of one of the crystals by peizoelectric devices. Each region (or edge) was scanned at least once with step sizes that typically went as follows: 5 eV per step from 100 eV to 20 eV before the edge; 0.5 eV per step from 20 eV before the edge to 30 eV after the edge (XANES region); 3 eV per step from 30 eV to 300 eV above the edge; and 8 eV per step from 300 eV to 1000 eV above the edge. The increased step sizes were used in order to decrease the time per scan and since the EXAFS oscillations far above the edge are quite broad small step sizes were not

required. Using these parameters each scan required approximately 30 minutes to 1 hour. Another factor which affects the amount of time required for each scan is the dwell time for the monochromator. As the monochromator is stepped to each energy position, the computer allows the monochromator to stabilize before taking a reading from the counters. The original analog signal from the ionization chambers is converted into pulses which are then read by a counter interfaced with the computer control station. This dwell time is typically set at 0.5 seconds to 1 second. The collected data are then converted to ASCII code for data analysis.

3.7 References

1. R.E. Watson, J. Hudis, and M.L. Perlman, Phys. Rev. B **4**, 4139 (1971).

2. L.M. Mattheiss and R.E. Dietz, Phys. Rev. B **22**, 1663 (1980).

3. R.M. Friedman, J. Hudis, M.L. Perlman, and R.E. Watson, Phys. Rev. B **8**, 2433 (1973)

4. S.S. Lu and C.-K. Liang, Chin. Journ. Phys. **22**, 505 (1966).

5. R.L. Mössbauer, Z. Phys. **151**, 124 (1958).

6. G.M. Bancroft, Mössbauer Spectroscopy, (New York, Wiley, 1973).

7. T.C. Gibb, Principles of Mössbauer Spectroscopy, (London, Wiley, 1976).

8. R.L. Cohen, Applications of Mössbauer Spectroscopy, (New York, Academic Press, 1976).

9. L.D. Roberts, R.L. Becker, F.E. Obenshain, and J.O. Thompson, Phys. Rev. **137** A 895 (1965).

10. P.G. Huray and L.D. Roberts, Phys. Rev. B **4**, 2147 (1971).

11. R.L. Cohen, in "Mössbauer Isomer Shifts" G.K. Shenoy Ed. North-Holland, Amsterdam 1978; p. 541.

12. T.S. Chou, M.L. Perlman, and R.E. Watson, Phys. Rev. B **14**, 3248 (1976).

13. T.K. Sham, M. L. Perlman, and R.E. Watson, Phys. Rev. B **19**, 539 (1979).

14. R.E. Watson and L.H. Bennett, Phys. Rev. B **15** 502 (1977).

15. R.E. Watson and L.H. Bennett, Phys. Rev. B **17**, 3714 (1978).

16. N.F. Mott, Proc. Phys. Soc., London **62**, 416 (1949).

17. Y. Cauchois and I. Manescu, C.R. Hebd. Seances Acad. Sci. **210**, 172 (1940).

18. D. Coster and H. De Lang, Physica **15**, 351 (1949).

19. M. Brown, R.E. Peierls, and E.A. Stern, Phys. Rev. B **15**, 738 (1977).

20. A.N. Mansour, J.W. Cook, Jr., and D.E. Sayers, J. Phys. Chem. **88**, 2330 (1984).

21. R. de L. Kronig, Z. Phys. **70**, 317 (1931).

22. E.A. Stern, Phys. Rev. B **10**, 3027 (1974).

23. P.M. Hansen, "Constitution of Binary Alloys", 2nd ed. McGraw-Hill, New York, 1958.

24. W.H. McMaster, N.K. Del Grande, J. Mallett, and J.H. Hubbell, "Compilation of X-ray Cross-Sections", NTI Service, Springfield, VA, 1969.

25. K.H. Tan, G.M. Bancroft, L.L. Coatsworth, and B.W. Yates, Can. J. Phys. **60**, 131 (1982).

26. G.M. Bancroft, K.H. Tan, and J.D. Bozek, L. Phys. Can. 113 (1987).

CHAPTER FOUR

Results and Data Manipulation

4.1 Introduction

This chapter deals with the experimental spectra that were collected from the variety of sources previously mentioned. The results are divided into two distinct categories, photoemission and X-ray absorption. The data manipulation required for the extraction of the parameters required spans a whole range of complexity, from simple curve fitting for determination of binding energy shifts from the photoemission spectra to detailed manipulation of the X-ray absorption data to extract variables such as nearest-neighbour distribution.

The chapter will be divided into three sections. The first will deal with the XPS results, in terms of binding energy shifts and valence band behaviour. The second section deals with the results of the synchrotron experiments and will focus on valence band behaviour as a function of photon energy. The last section will deal with the X-ray absorption spectra. Whiteline areas will be determined from the XANES analysis and nearest shell distance and configuration will be determined from the EXAFS analysis.

4.2 XPS Core Level and Valence Band Spectra

The results of the XPS experiments are given in Figures 4.1 to 4.9. The experiments were performed on all of the previously mentioned Au-Cu polycrystalline foils, and also on representative foils of pure Cu and Au. The spectral areas of interest include the valence band, the Au $4f$ core levels, the Cu $3p$ core levels, and the Cu $2p_{3/2}$ core level.

Several features are noteworthy. There are valence band changes from that of pure Au-like to pure Cu-like as the Cu composition is increased. The combined Au $4f$ and Cu $3p$ spectra show that the ratio of the two emissions change as a function of composition, as expected. The Au $4f$ peaks are much narrower and intense than the Cu $3p$ peaks, and it is for this reason that for extraction of binding energy shifts the Au $4f_{7/2}$ and Cu $2p_{3/2}$ peaks are fitted.

Qualitative examination of binding energy shifts is easily accomplished by overlap of representative spectra. Figure 4.10 shows the binding energy shift of various alloys for the Au $4f_{7/2}$ and Cu $2p_{3/2}$ peaks as compared to the pure counterparts. As the Cu composition is increased the Au $4f_{7/2}$ peak shifts to higher binding energy (top panel Figure 4.10). As the Cu composition is decreased the Cu $2p_{3/2}$ peak shifts to lower binding energy (or as the Cu composition is increased the Cu $2p_{3/2}$ peak shifts to higher binding energy)(bottom panel Figure 4.10).

Figure 4.11 shows the shift between the ordered and disordered alloys. For both the AuCu and Cu_3Au series the ordered counterpart shifts to higher binding energy for

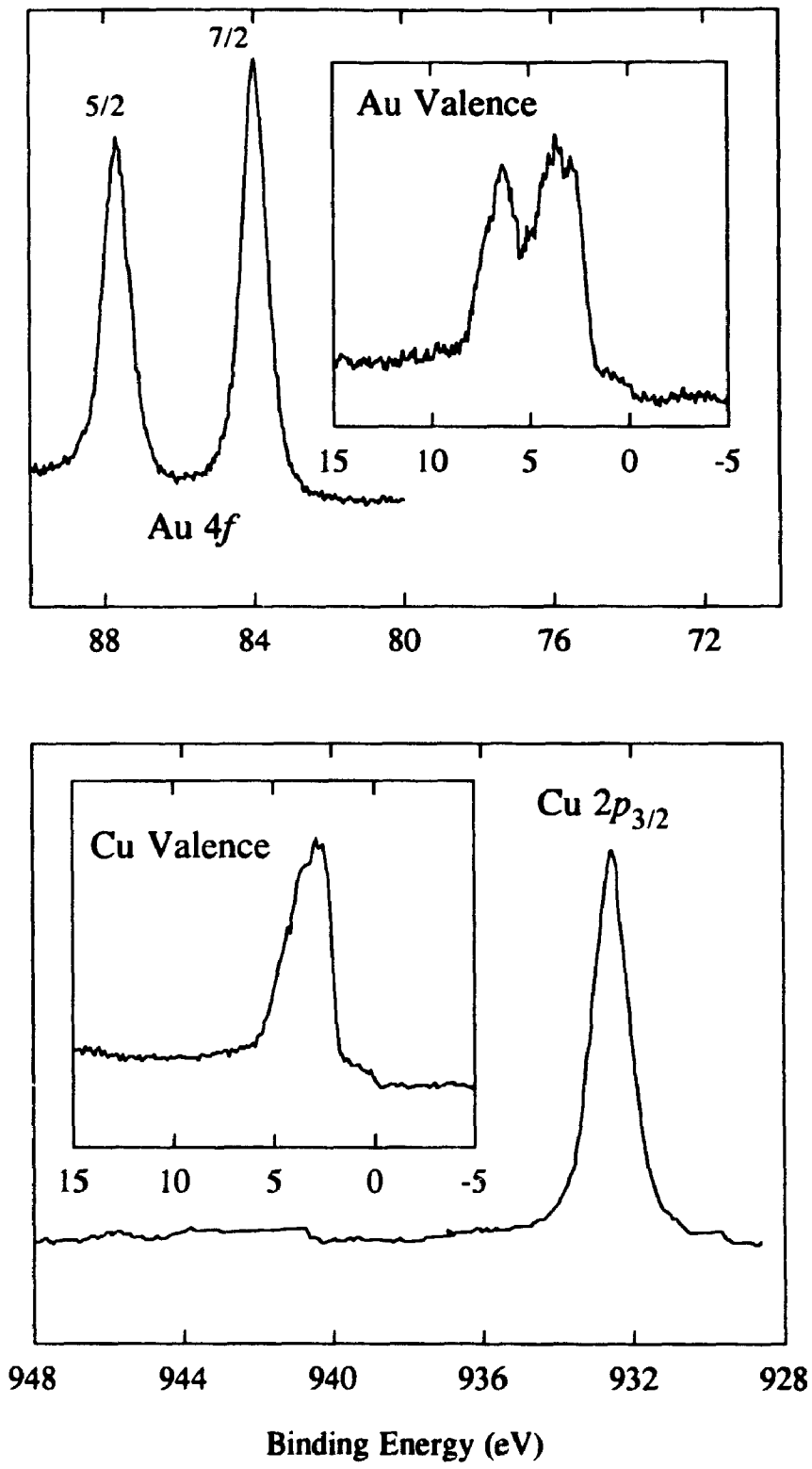

Figure 4.1: XPS results for the pure metals. The spectral areas of interest are the valence bands and the Au 4*f* and Cu $2p_{3/2}$ core levels.

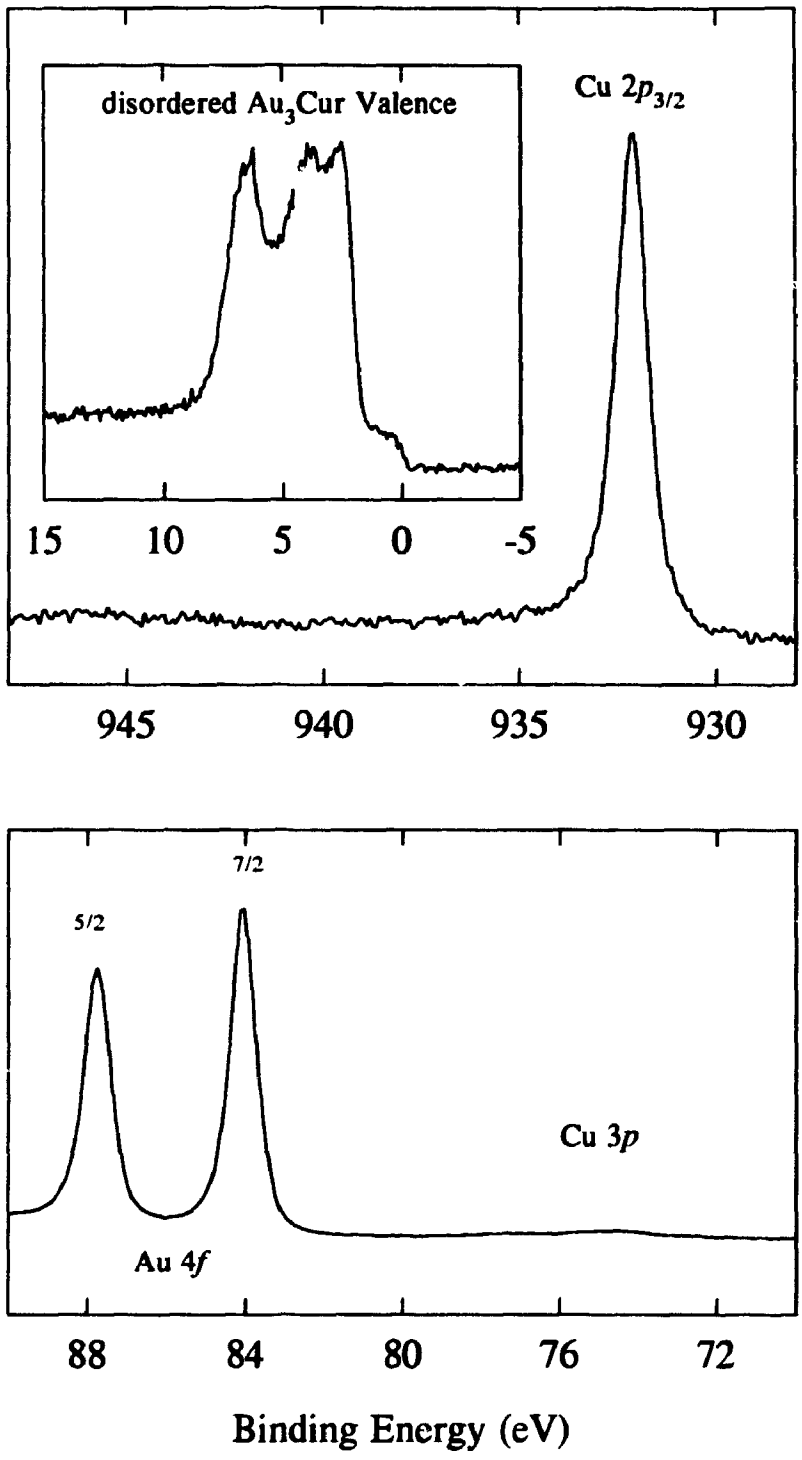

Figure 4.2: XPS results for the disordered Au_3Cu sample. The top panel shows the valence band and Cu $2p_{3/2}$ core level while the bottom panel shows a wide scan of the Au $4f$ and Cu $3p$ core levels.

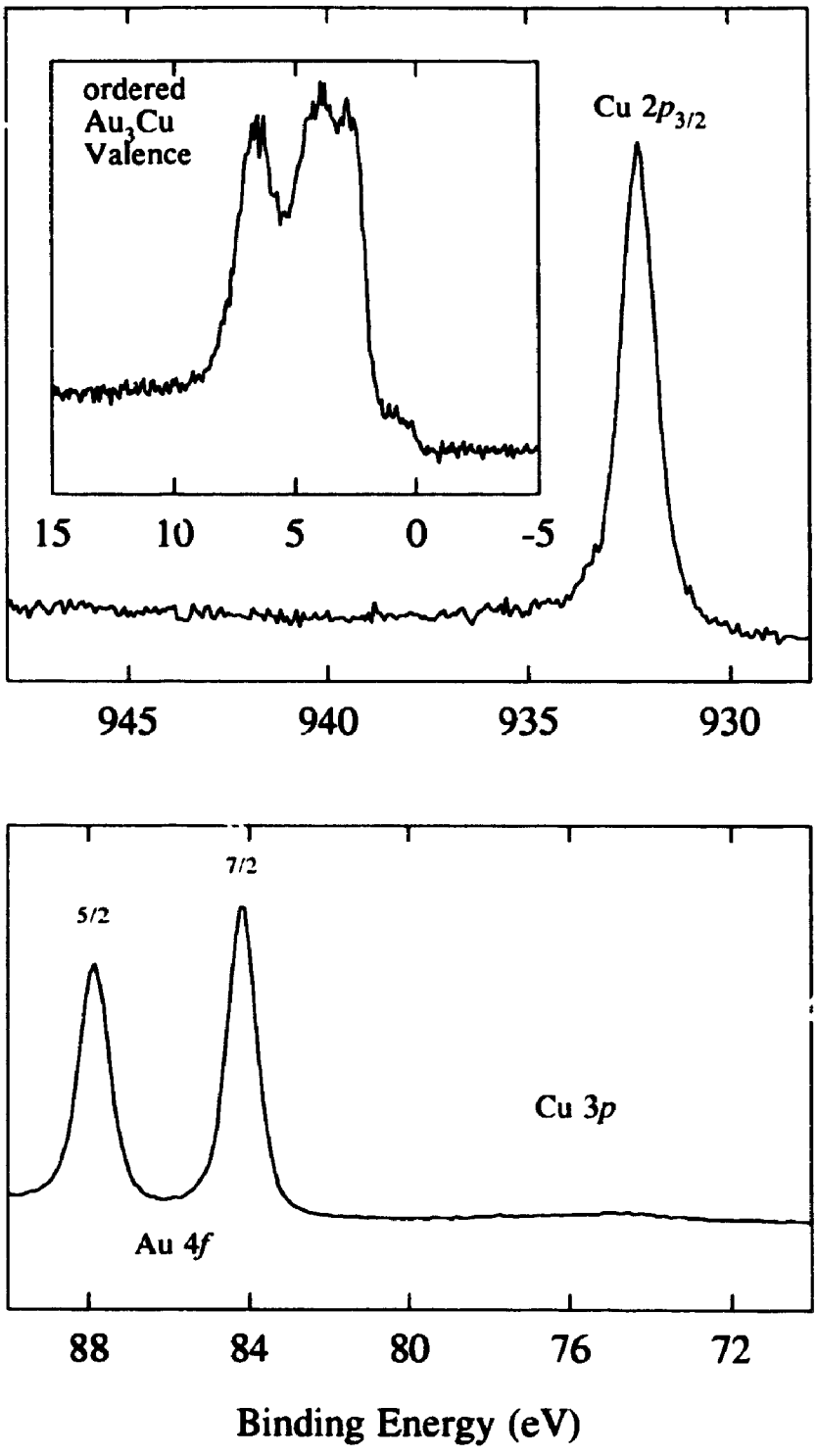

Figure 4.3: XPS results for the ordered Au_3Cu sample. The top panel shows the valence band and Cu $2p_{3/2}$ core level while the bottom panel shows a wide scan of the Au $4f$ and Cu $3p$ core levels.

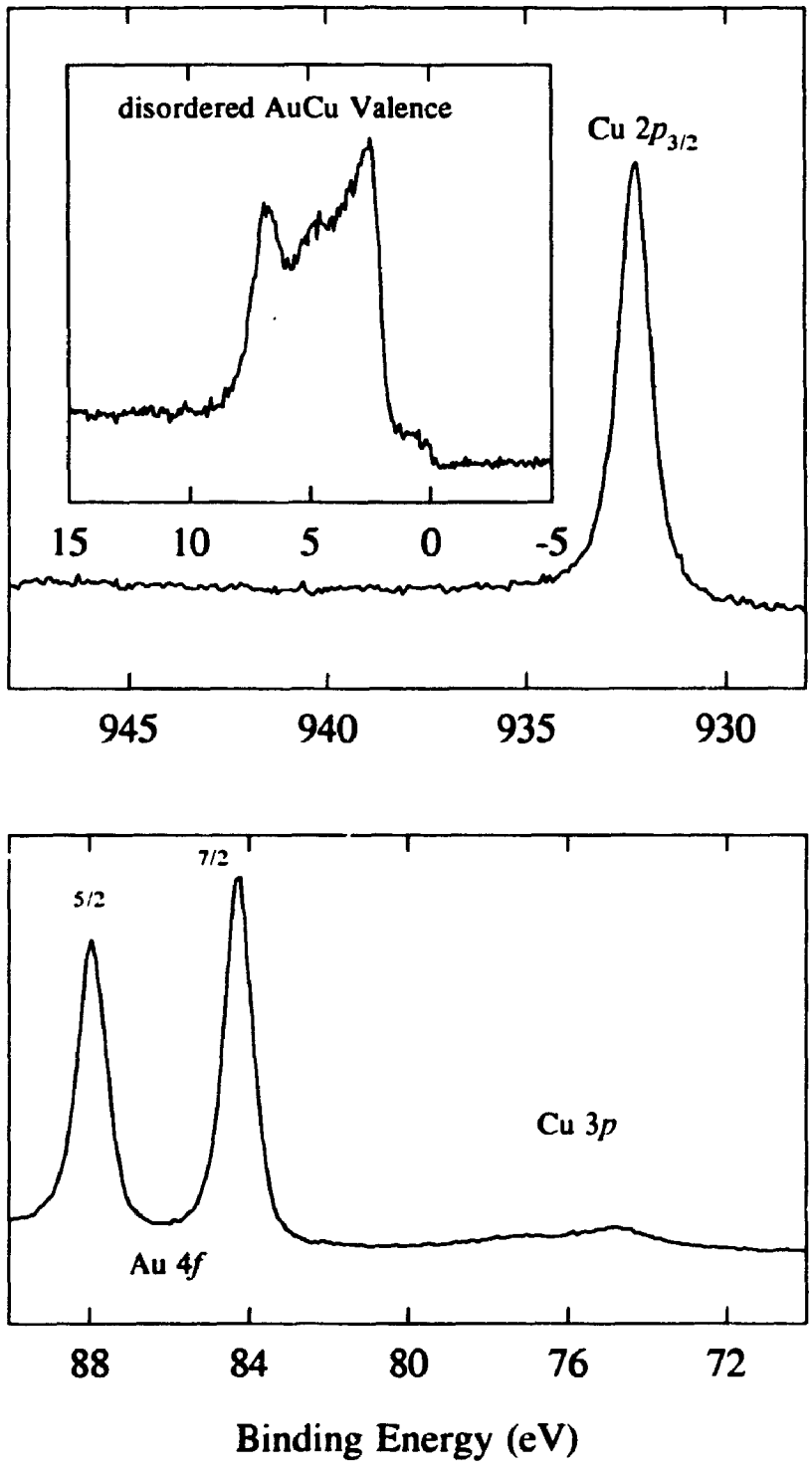

Figure 4.4: XPS results for the disordered AuCu sample. The top panel shows the valence band and Cu $2p_{3/2}$ core level while the bottom panel shows a wide scan of the Au $4f$ and Cu $3p$ core levels.

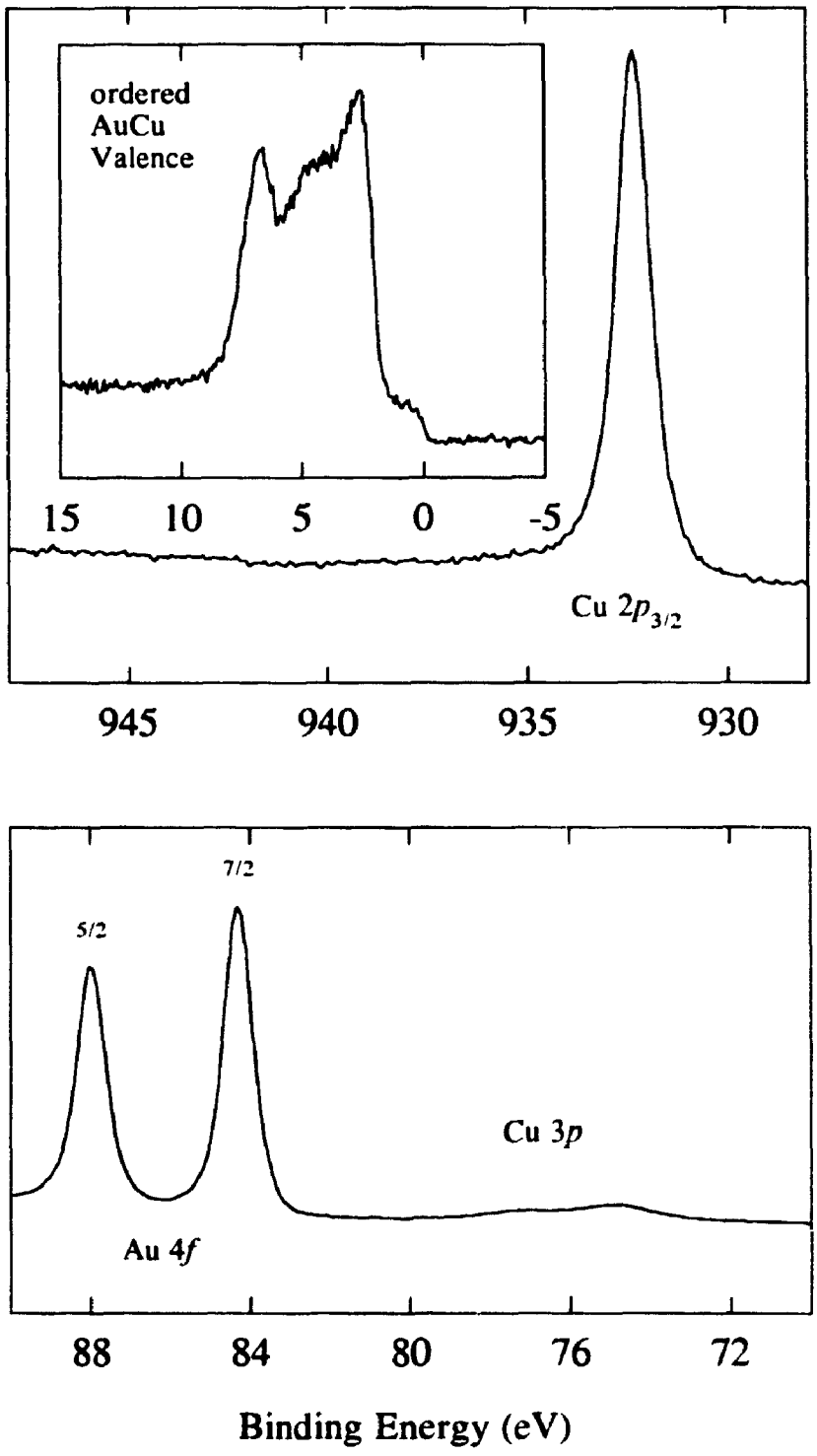

Figure 4.5: XPS results for the ordered AuCu sample. The top panel shows the valence band and Cu $2p_{3/2}$ core level while the bottom panel shows a wide scan of the Au $4f$ and Cu $3p$ core levels.

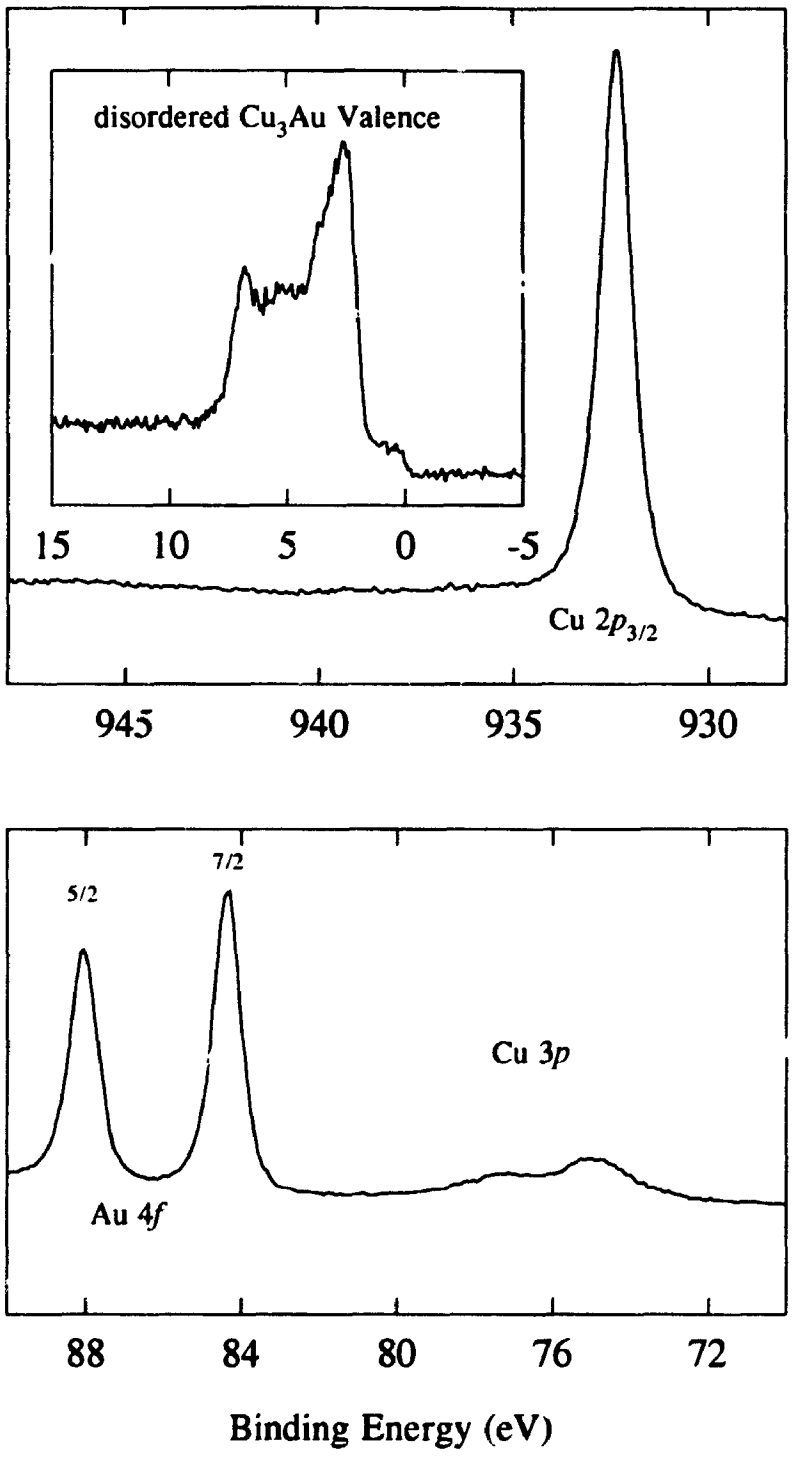

Figure 4.6: XPS results for the disordered Cu_3Au sample. The top panel shows the valence band and Cu $2p_{3/2}$ core level while the bottom panel shows a wide scan of the Au $4f$ and Cu $3p$ core levels.

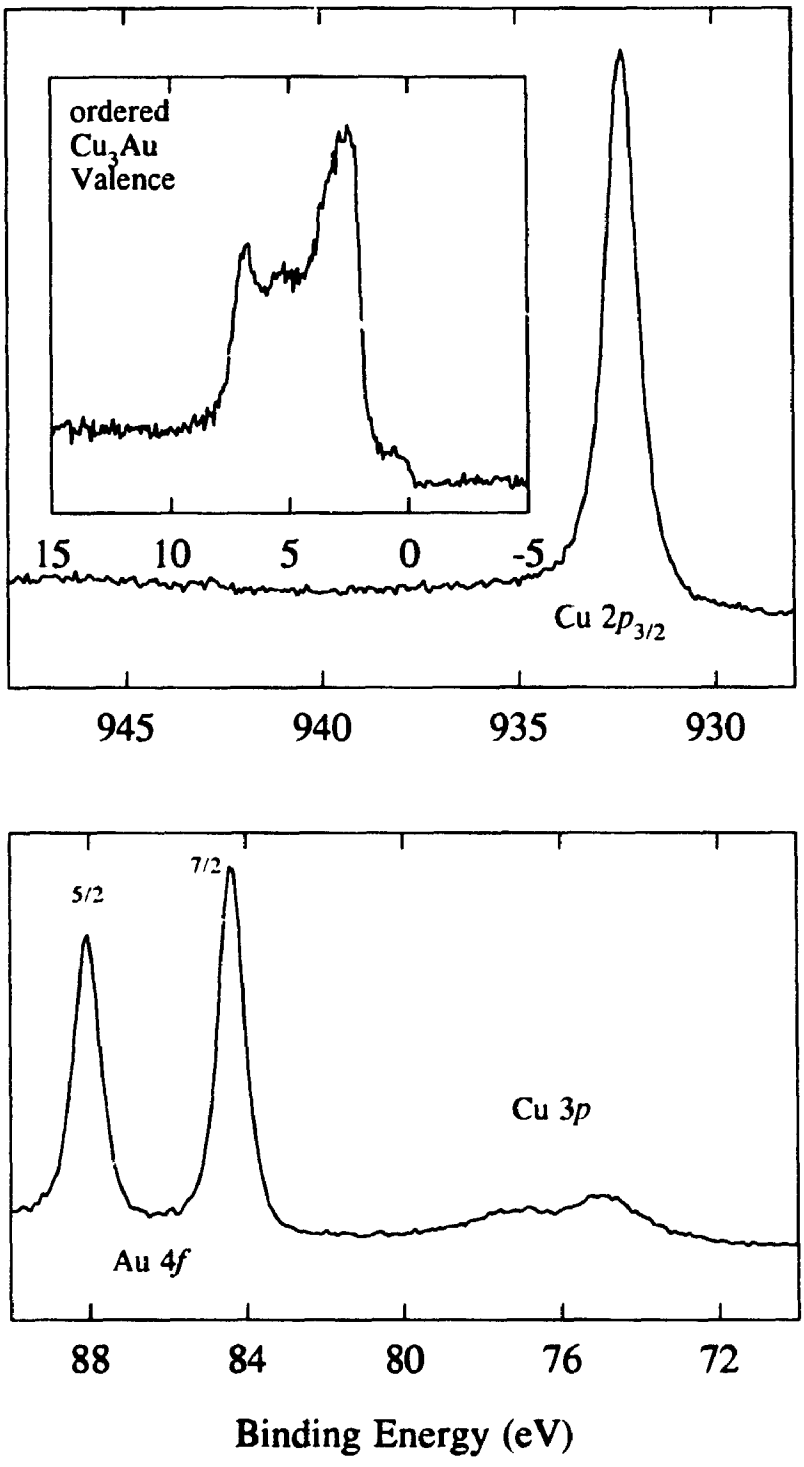

Figure 4.7: XPS results for the ordered Cu_3Au sample. The top panel shows the valence band and Cu $2p_{3/2}$ core level while the bottom panel shows a wide scan of the Au $4f$ and Cu $3p$ core levels.

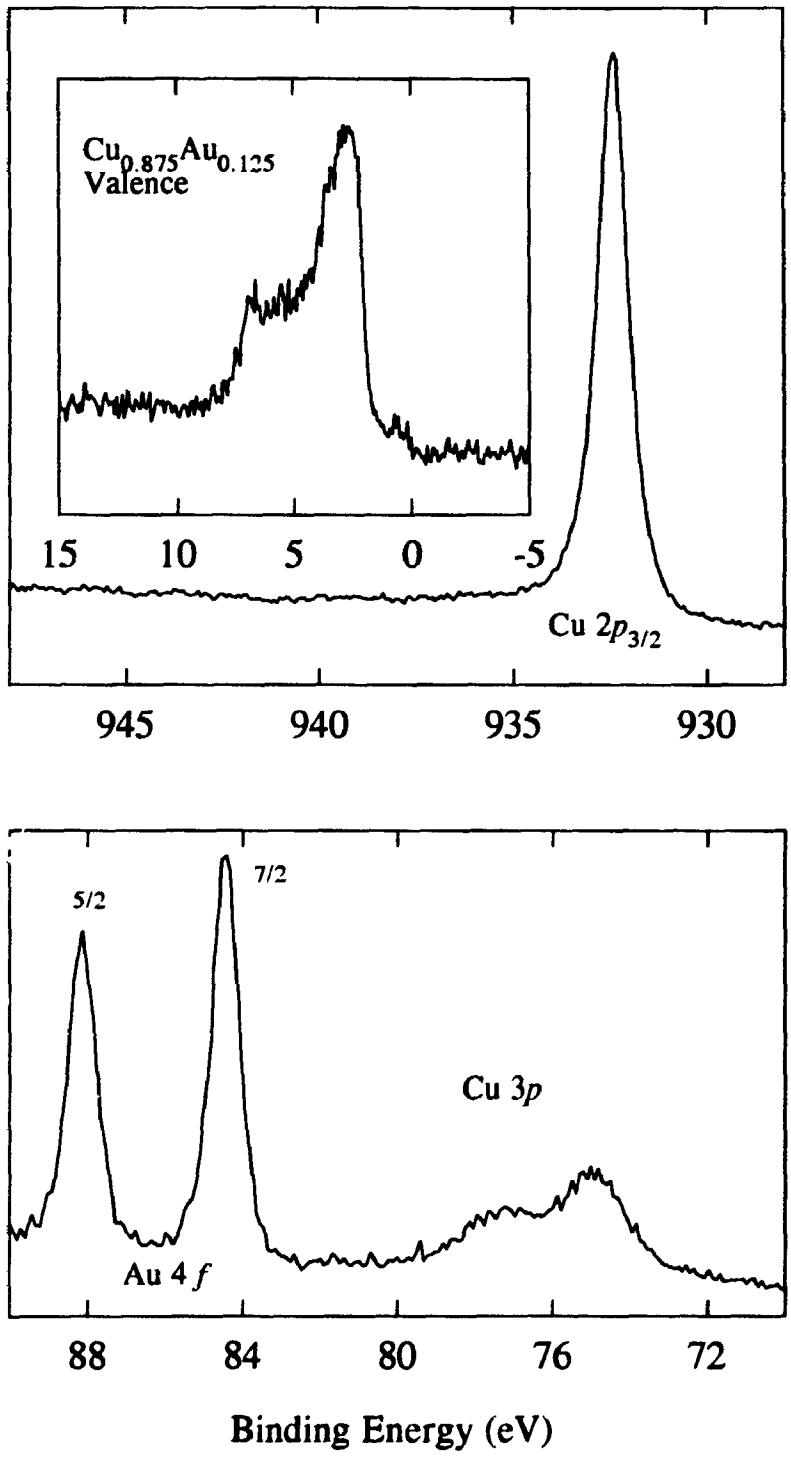

Figure 4.8: XPS results for the $Cu_{0.875}Au_{0.125}$ sample. The top panel shows the valence band and Cu $2p_{3/2}$ core level while the bottom panel shows a wide scan of the Au $4f$ and Cu $3p$ core levels.

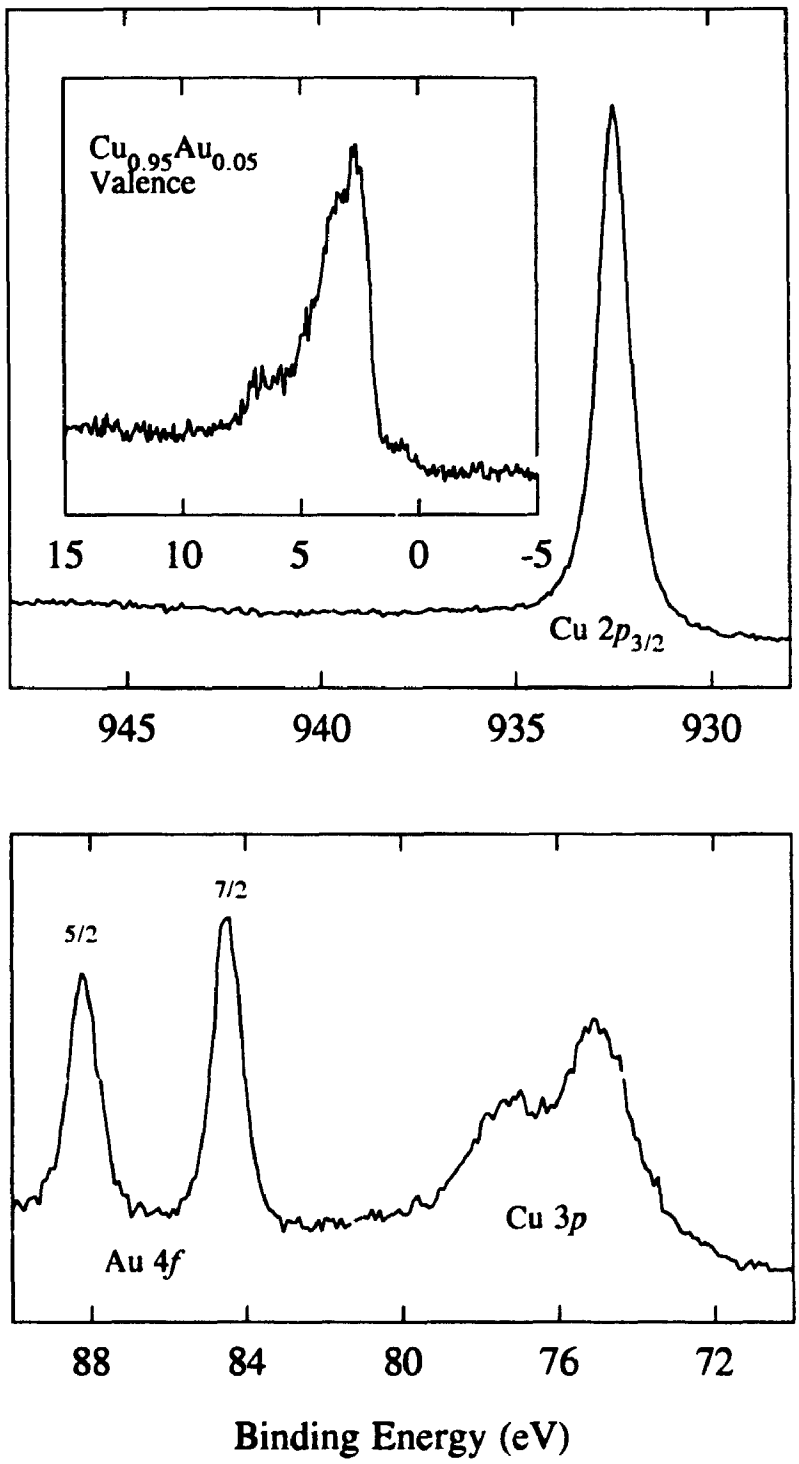

Figure 4.9: XPS results for the $Cu_{0.95}Au_{0.05}$ sample. The top panel shows the valence band and Cu $2p_{3/2}$ core level while the bottom panel shows a wide scan of the Au $4f$ and Cu $3p$ core levels.

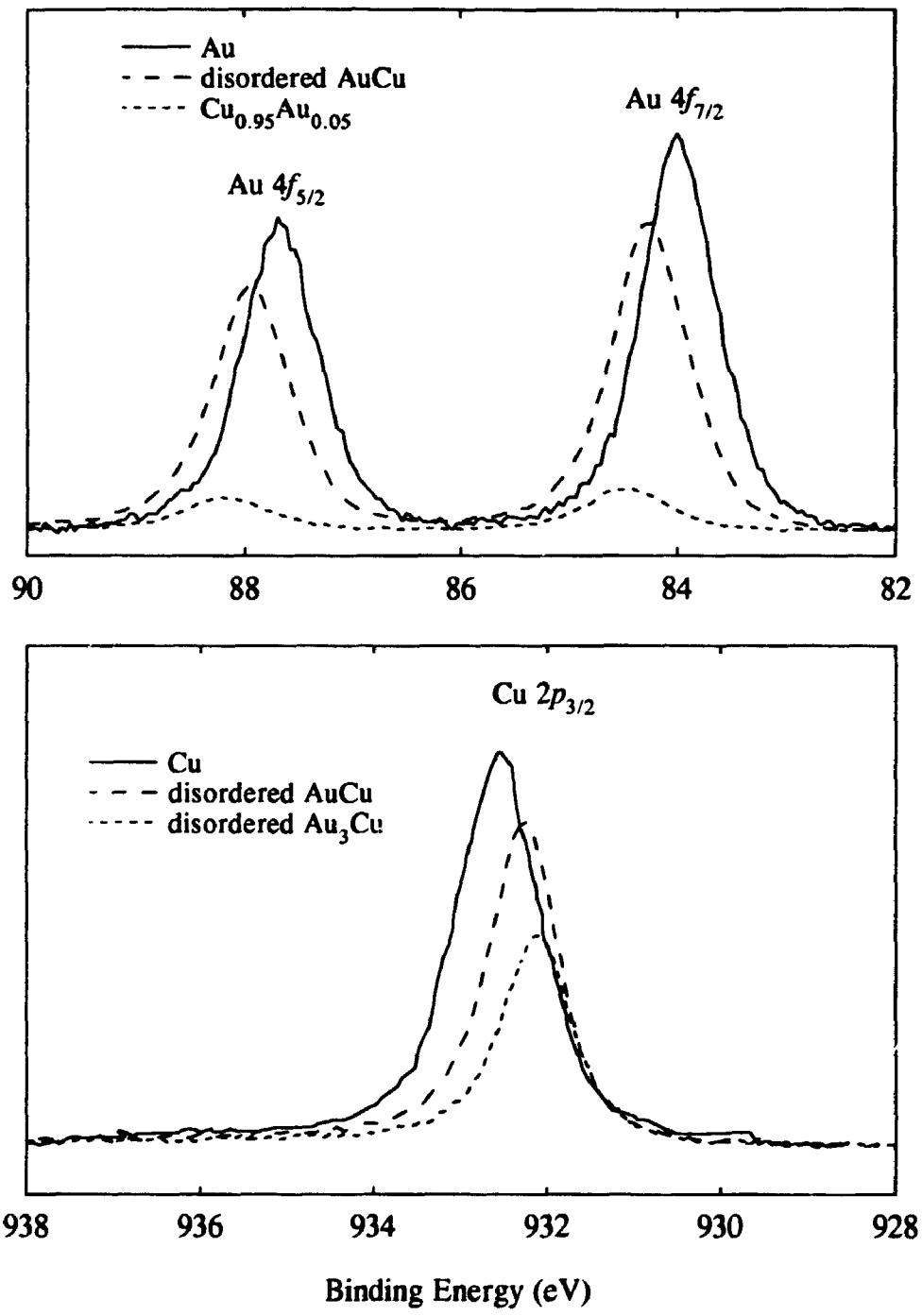

Figure 4.10: Representative spectra showing the shift to higher binding energies of the Au $4f$ core level as the Cu composition is increased (upper panel) and the corresponding shift to higher binding energies for the Cu $2p_{3/2}$ also (lower panel).

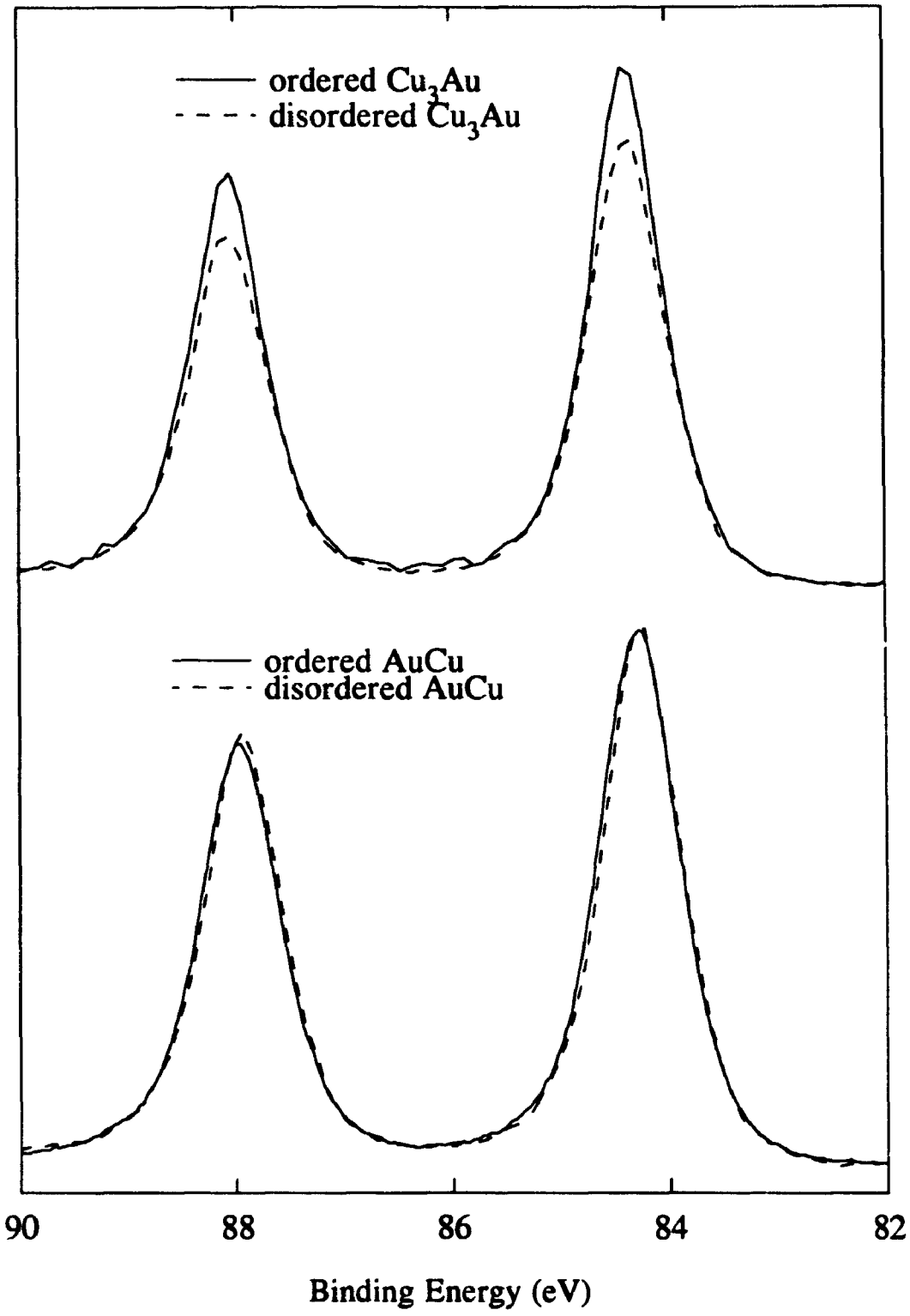

Figure 4.11: Comparison of Cu_3Au alloys (upper plot) and AuCu alloys (lower plot) in terms of their Au *4f* core level positions. There is a small noticeable shift to higher binding energies for the ordered samples.

the Au $4f_{7/2}$ core level (relative to the disordered sample), although the shift is quite small, <0.1 eV. No discernible difference can be seen for the Au_3Cu samples.

The Au $4f_{7/2}$ and Cu $2p_{3/2}$ peaks were fitted using the data analysis package at Surface Science Western. For all the spectra a polynomial background was subtracted and a 60% Gaussian-40% Lorentzian lineshape fitted to the peaks. This choice of Gaussian-Lorenztian combination was based on the inherent Lorenztian lineshape of the photoemission process to be convoluted by Gaussian contributions from the photon and instrumental resolution. The results are given in Table 4.1. Again, we note the increase in binding energy as the Cu composition is increased for both Au $4f_{7/2}$ and Cu $2p_{3/2}$ levels. The top two panels of Figure 4.13 plot the change relative to the pure components for the ordered and disordered Au-Cu series.

We have also examined the behaviour of the valence band as a function of composition and ordering. The alloy *d*-band width and the apparent (quasi) Au 5*d* spin-orbit splitting were determined as shown in Figure 4.12. The *d*-band widths were determined by measuring the immediate onset of both edges of the band as represented by bold lines in Figure 4.12. The alloy *d* band narrows, relative to pure Au, with values between those of the pure components. The experimental *d*-band width varies slowly and almost linearly in the high Au composition regime but reduces drastically once lower Au compositions (on the order of 10%) are reached. The apparent Au 5*d* spin-orbit splitting ($5d_{5/2}$-$5d_{3/2}$) was roughly determined from the spectra as shown by the arrows in Figure 4.12. We have assumed a localized model and that the Au 5*d* band retains the *j* values as good quantum numbers. The localized model is supported by photon-dependent

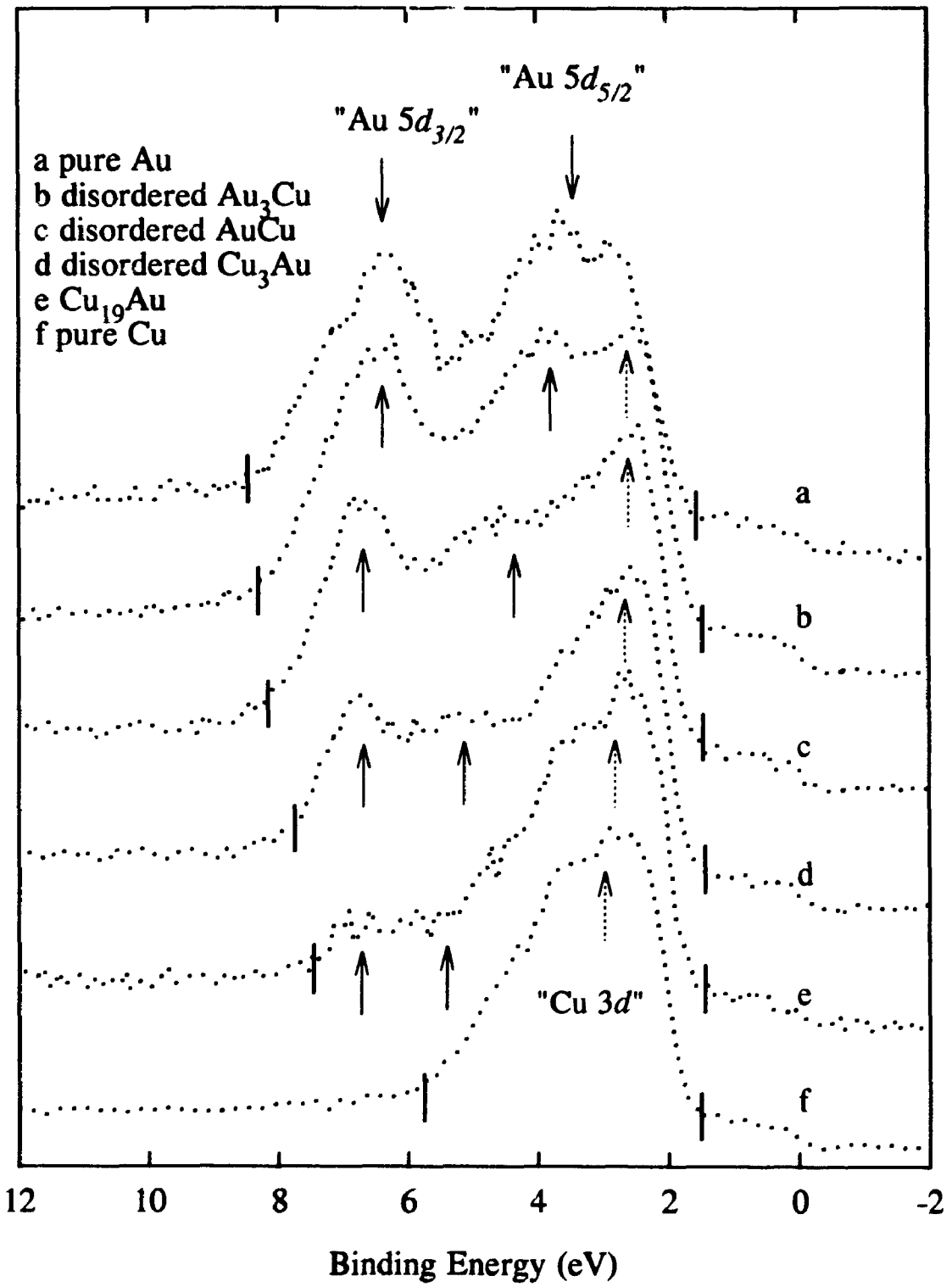

Figure 4.12: Representative valence band spectra for the Au-Cu alloy series and the pure components. The widths of the valence band are indicated by the bold lines. The solid arrows indicate the positions of the "Au" *d*-band components while the dashed arrows indicate the position of the "Cu" *d*-band centroid.

results which are to follow in discussion of the synchrotron photoemission data. The atomic terms $d_{5/2}$ and $d_{3/2}$ are used for the bands merely as a simple notation to indicate the origin of the bands. The splitting and widths of these bands arise from the interplay of an atomic spin-orbit term and a band formation term. The alloy *d*-band width and Au 5*d* spin-orbit splitting parameters are plotted in the bottom two panels of Figure 4.13 and listed in Table 4.1. Also of interest is the relative movement of the *d*-band components, Au 5*d* and Cu 3*d*. There is a shift in the "Au" contribution of the alloy *d* band in which the Au $5d_{3/2}$ band remains largely unaffected but the Au $5d_{5/2}$ band shifts away from the Fermi level and the Cu 3*d* band. The "Cu" contribution has narrowed and the centroid shifted towards the Fermi level. The position of the "Cu" contribution is given by the dashed arrows in Figure 4.12. In the valence band photoemission data, we find no significant difference between the disordered and corresponding ordered compounds in terms of alloy *d*-band widths and Au *d*-band splittings at our experimental resolution (~ 0.6 eV).

Compound	Au $4f_{7/2}$ Binding Energy (±0.05 eV)	Cu $2p_{3/2}$ Binding Energy (±0.05 eV)	Alloy *d*-band width (±0.1 eV)	Au 5*d*-band splitting (±0.1 eV)
Au	83.94	-----	6.44	2.75
disordered Au_3Cu	84.00	932.11	6.38	2.6
ordered Au_3Cu	84.00	932.27	6.32	2.6
disordered AuCu	84.19	932.26	6.19	2.2
ordered AuCu	84.25	932.38	6.19	2.2
disordered Cu_3Au	84.20	932.33	6.05	1.6
ordered Cu_3Au	84.31	932.31	6.05	1.6
$Cu_{0.875}Au_{0.125}$	84.37	932.37	5.94	1.55
$Cu_{0.95}Au_{0.05}$	84.41	932.44	5.63	1.5
Cu	-----	932.53	4.50	-----

Table 4.1: Summary of the parameters derived from the XPS spectra. The core level positions were determined first a polynomial background subtraction followed by a 60% Gaussian-40% Lorenztian peak fit. The alloy *d*-band width and Au *d*-band splittings were roughly determined as shown in Figure 4.12.

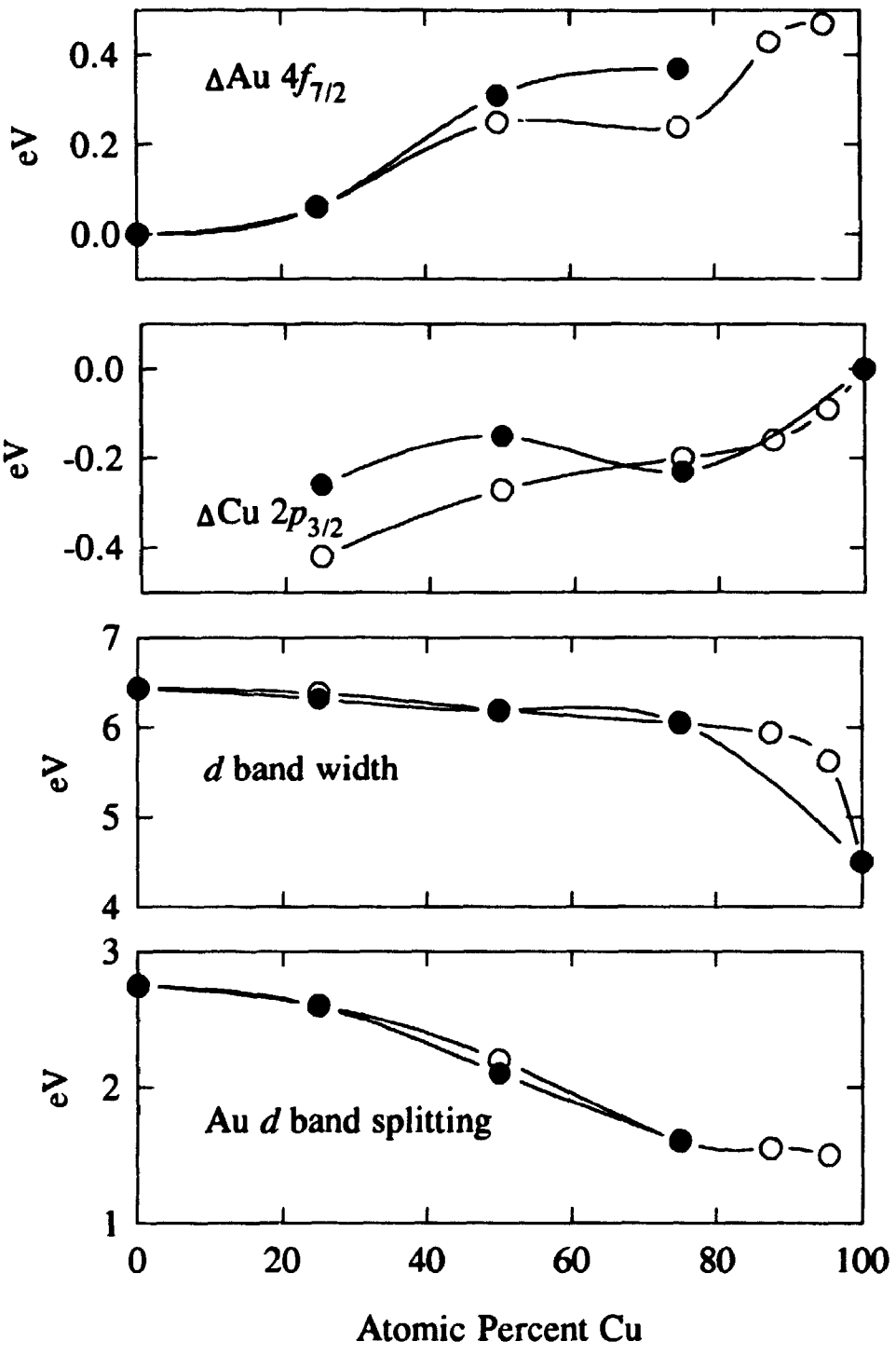

Figure 4.13: Various parameters determined from the XPS spectra are plotted as a function of Cu composition. The top panel is the Au $4f_{7/2}$ shift, the second panel is the corresponding Cu $2p_{3/2}$ shift, the third panel is the *d*-band width, while the bottom panel is the "Au" *d*-band splitting. The filled circles represent the ordered species while the open circles represent the disordered species.

4.3 Synchrotron Valence Band Spectra

The synchrotron valence band studies were performed for two specific reasons. The first is to try and observe a resonant satellite characteristic of Cu in both pure Cu and a Au-Cu alloy. This experiment requires a tunable photon source to scan across the Cu 3*p* threshold (74 eV to 77 eV). The second experiment involves using the Cooper minimum of the Au 5*d* band (roughly determined by the atomic cross-section of Au 5*d*)[1] to determine the extent of the Cu contribution to a Au-Cu alloy *d* band. This also requires a tunable photon source.

The valence band spectra of Cu recorded with photon energies across the Cu 3*p* threshold are shown in Figure 4.14. The Cu 3*d*-band centroid is located at about 3 eV below the Fermi level. At a photon energy of 74 eV a second peak emerges at 14 eV below the Fermi level. At 75.5 eV two peaks are seen, 15 and 11 eV below and are marked by arrows on Figure 4.14. At higher photon energies a broad peak is observed shifting across the spectrum from right to left. This is attributed to the Cu 3*p* Auger.

The valence band spectra of ordered Cu_3Au recorded with photon energies across the Cu 3*p* threshold are shown in Figure 4.15. The "Cu" 3*d*-band centroid is now located at about 2.5 eV with the "Au" 5*d* components occurring at 4.5 and 6 eV below the Fermi level. At a photon energy of 72 eV we observe two peaks at 15 and 11.5 eV which travel to the right as the photon energy is increased. These are indicated by the upwards arrows on Figure 4.15 and are attributed to Au 4*f* peaks due to second-order photons from the 600 line/mm grating used in this study. As we move to 75.5 eV and

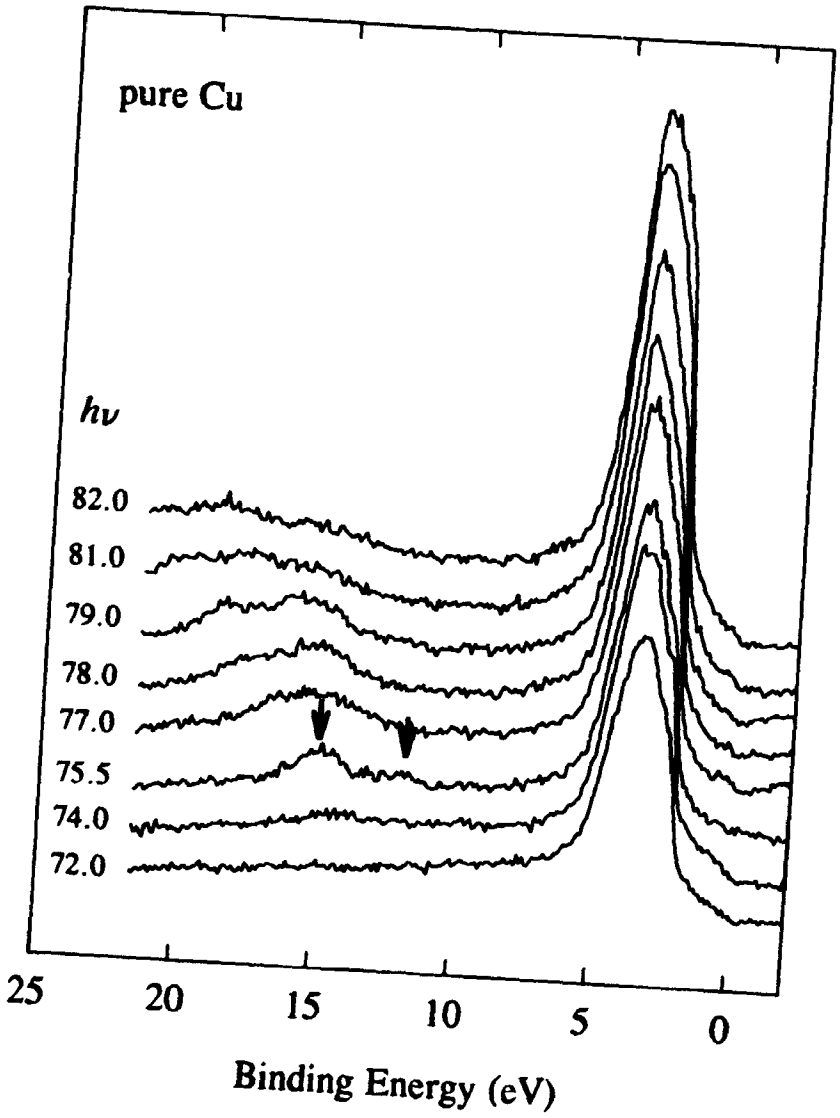

Figure 4.14: Synchrotron valence band data for pure Cu with photon energies across the Cu 3*p* threshold. The arrows indicate the position of the resonant Auger.

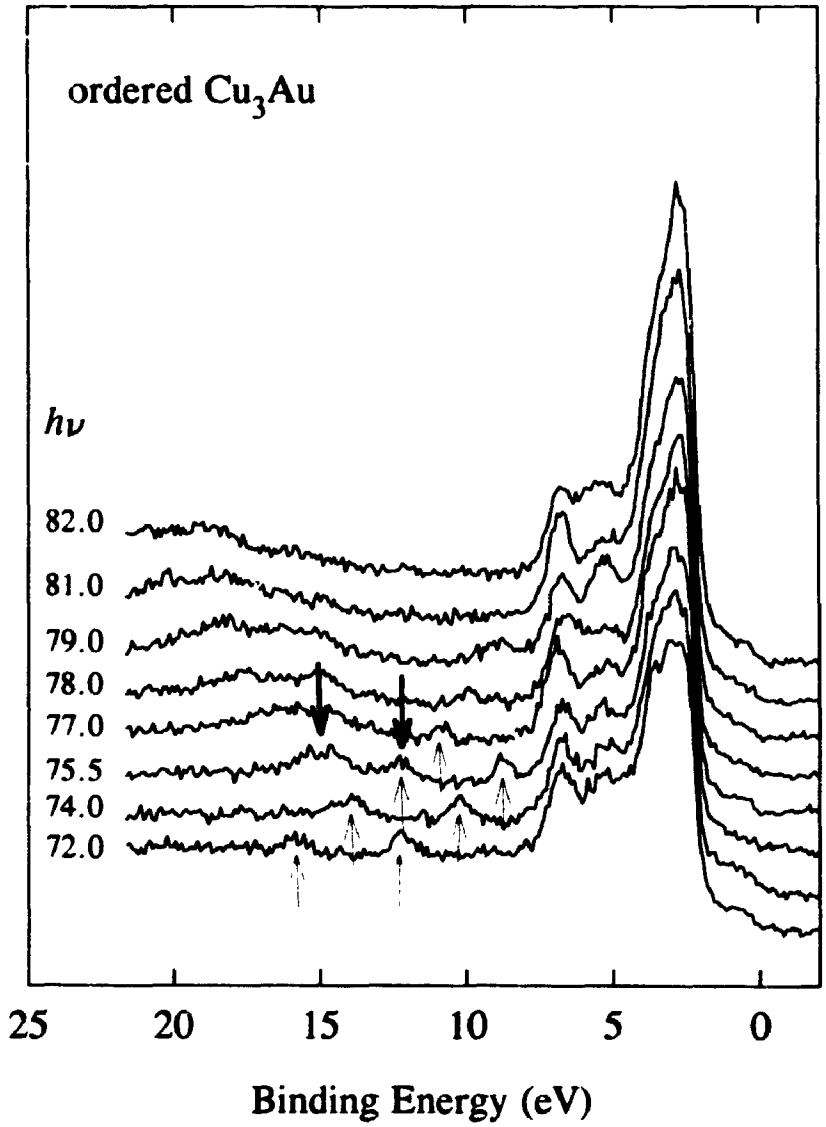

Figure 4.15: Synchrotron valence band data for ordered Cu_3Au with photon energies across the Cu $3p$ threshold. The downward arrows indicate the position of the resonant Auger while the upward arrows indicate the position of the Au $4f$ second-order peaks.

above we again see two peaks at 15 eV and 11 eV and the Cu 3*p* Auger.

The peak intensities of the satellite at 15 eV and the Cu 3*d* band at 75.5 eV for both pure Cu and ordered Cu_3Au were obtained by simple Gaussian fitting and subsequent integration under the curve. The ratio of the satellite to the main peak was found to be approximately 15% $\pm$5% for both samples. The large error is due to the weak intensity of the satellite and the difficulty in determining the areas of both the satellite and the main peak. The ordered Cu_3Au sample has the extra complication of the interference of the second-order Au 4*f* peaks.

Figure 4.16 shows the valence band for pure Au and Cu, and ordered Cu_3Au at two different photon energies which were selected in order to optimize the photoionization cross-section of interest. It is obvious that emission from the Au 5*d* band is enhanced at 60 eV and largely suppressed at 160 eV. Focussing on the 60 eV spectra, we note again the movement of the alloy *d*-band components. The upward arrows indicate the positions of the Au 5*d* components while the downward arrows indicate the centroid movement of the Cu 3*d* component. The Au $5d_{5/2}$ band moves away from the Fermi level and the Cu 3*d* band. The centroid of the Cu 3*d* band moves towards the Fermi level. There is also a significant narrowing of the Cu 3*d* band from 2.8 eV for pure Cu to 2.4 eV for the alloy. This is more apparent in the 160 eV spectrum in which Au 5*d* emission is suppressed. The centroid of the Cu *d* band again moves towards the Fermi level with a narrowing from 2.6 eV for the pure Cu sample to 2.1 eV for the alloy sample. The *d*-band widths were measured by fitting the *d* bands with a Gaussian curve and measuring the full width at half-maximum (FWHM).

The resonant and photon dependent cross-section studies were also performed on the disordered Cu_3Au sample but no difference could be discerned except for a possible slight narrowing (<0.1 eV) of the alloy *d* band at 160 eV for the ordered sample as compared to the disordered counterpart.

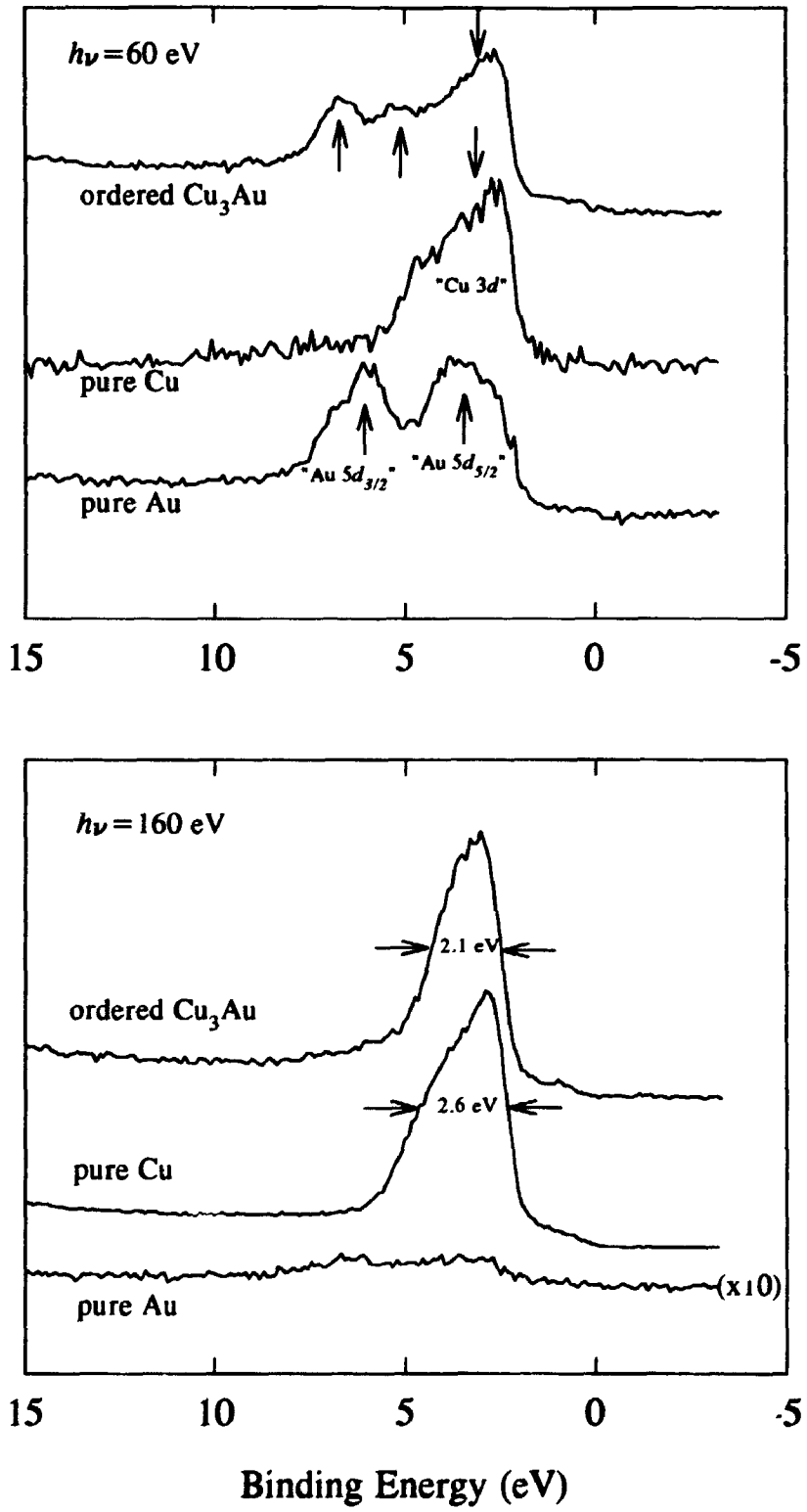

Figure 4.16: Synchrotron valence band data for pure Cu, pure Au and ordered Cu_3Au at two photons energies, 60 eV and 160 eV, selected to enhance and suppress Au *5d* emission, respectively. The widths of the Cu band are shown on the plot.

4.4 X-ray Absorption Spectra

X-ray absorption spectra were taken for the series of Au-Cu alloys and the pure components. The spectral areas of interest were the Au $L_{2,3}$ edges and the Cu K edge. To probe the unoccupied density of states from both the Au and Cu perspectives the XANES regions of the Au $L_{2,3}$ and Cu K edges are required, respectively. For EXAFS analysis the Au L_3 edge was scanned from 100 eV below to 1000 eV above the threshold. The results are in Figures 4.17 to 4.26.

We begin by focussing on the XANES spectra. For determination of whiteline areas, the near edge region must be calibrated and normalized for comparison. Figure 4.27 shows the procedure for normalization of the XANES spectra. Using the Au L_3 edge spectrum of disordered AuCu as an example we begin by a linear baseline subtraction of the pre-edge area (top panel Figure 4.27). The total X-ray absorption coefficient can be written as:

$$\mu = \mu_L + \mu_j \tag{4.1}$$

where μ_L is the absorption due to excitation of the $2p$ levels and μ_j is the absorption due to excitation of all other levels. It can be assumed that the absorption due to other emission levels would monotonically decrease over the energy region we are interested in, therefore a pre-edge subtraction would account for the contribution of these other levels. The next step is to normalize the edge jump. This is accomplished, as shown in the second panel of Figure 4.27, by extending a straight line from the region 200 to 500 eV above the edge through the near edge region and ignoring the features at the edge.

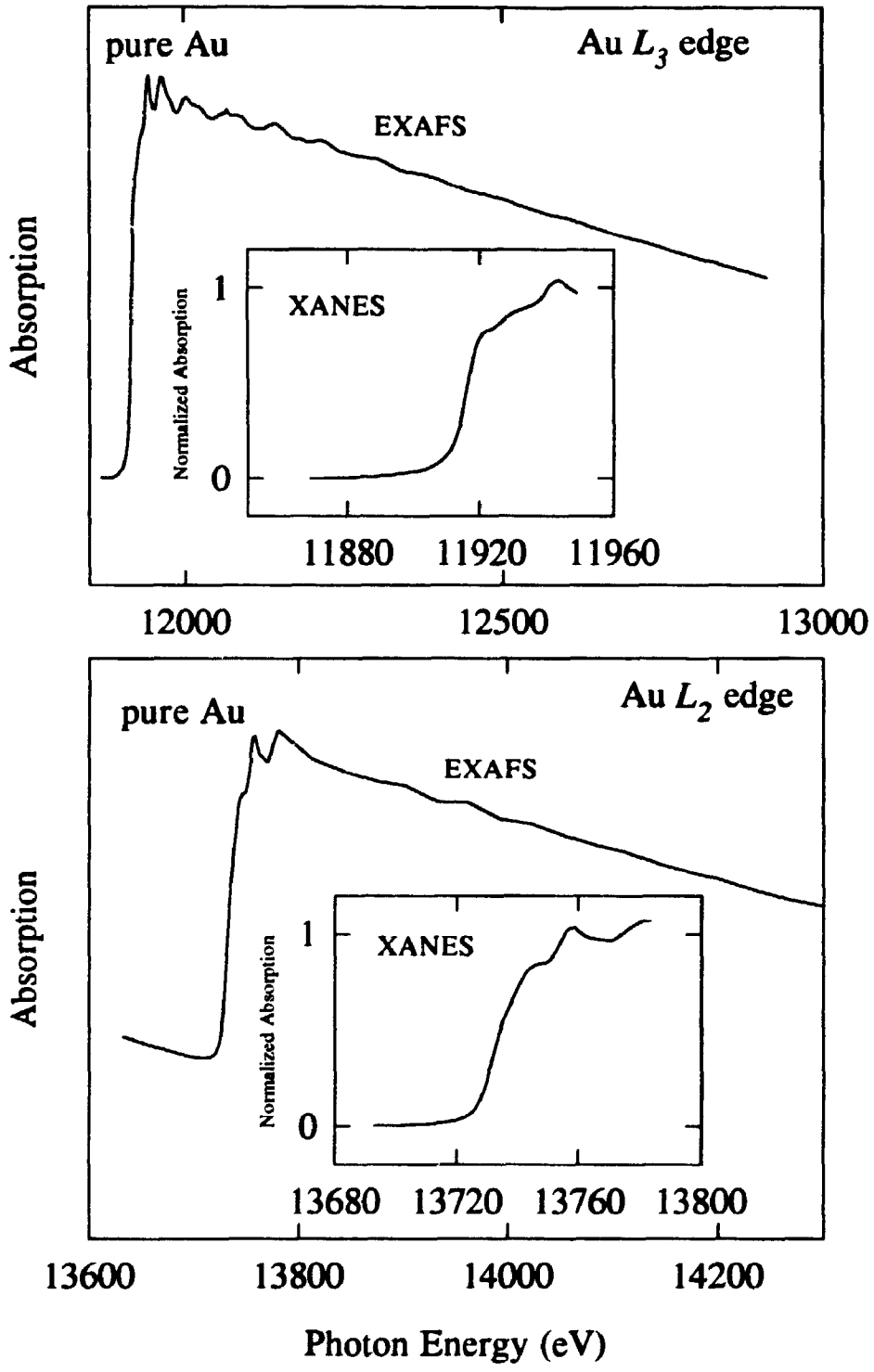

Figure 4.17: X-ray absorption spectra for pure Au and the Au L_3 edge (top panel) and the Au L_2 edge (bottom panel). The normalized XANES regions are shown in the insets.

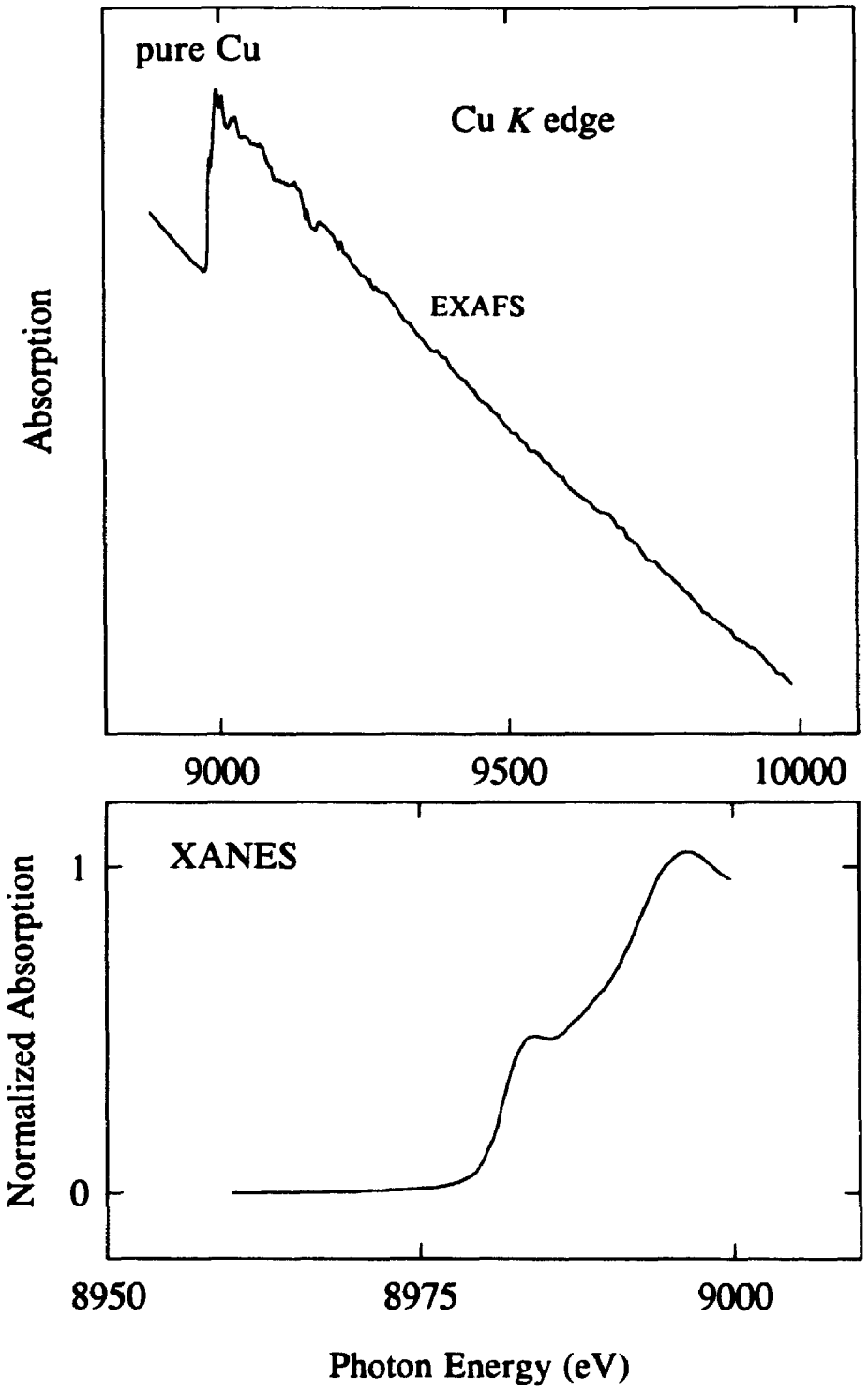

Figure 4.18: X-ray absorption spectra for pure Cu at the Cu *K* edge (top panel). The normalized XANES region is shown in the bottom panel.

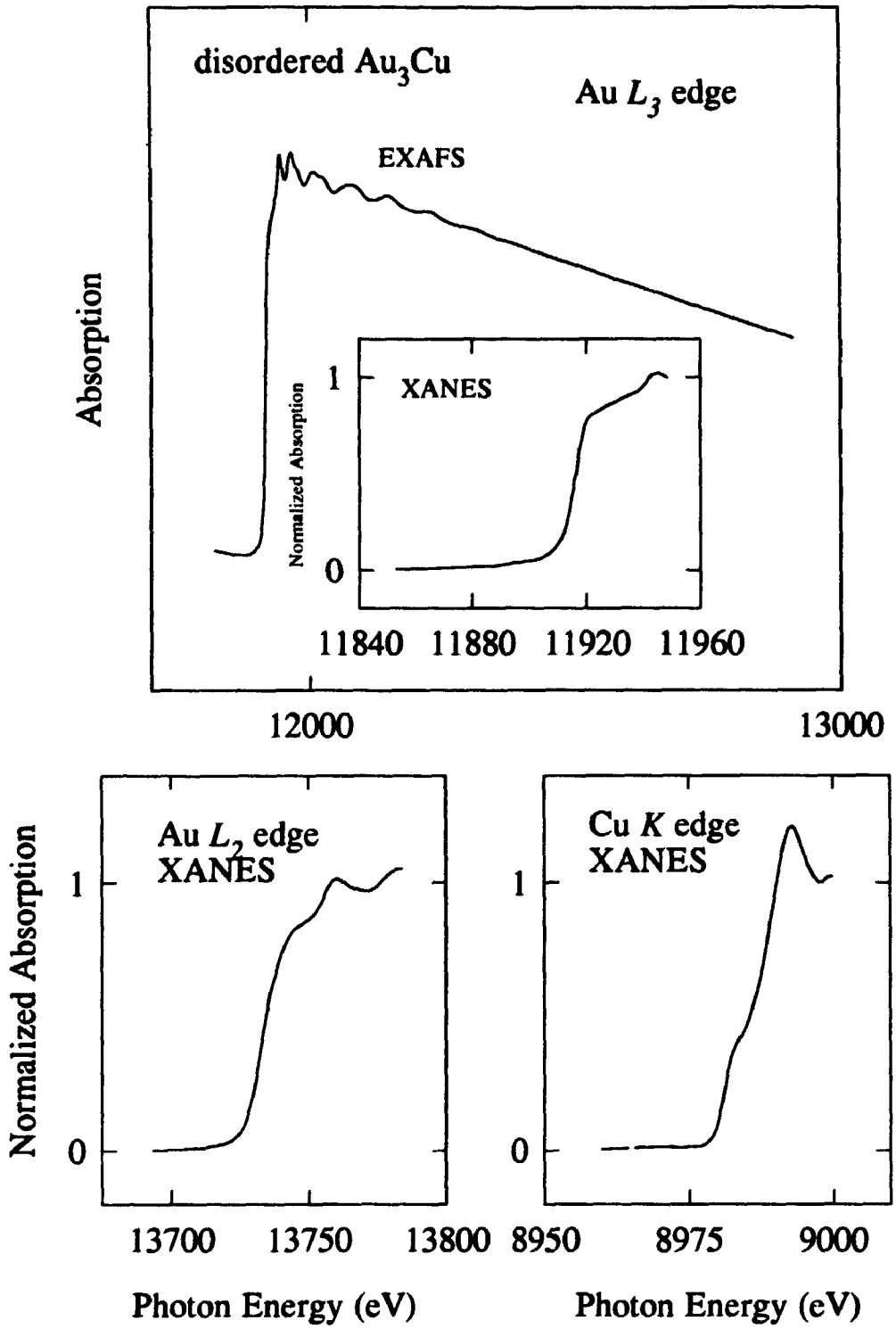

Figure 4.19: X-ray absorption spectra for disordered Au_3Cu. The top panel shows the extended Au L_3 edge with the XANES region in the inset. The bottom two panels show the XANES region for the Au L_2 and Cu K edges, respectively.

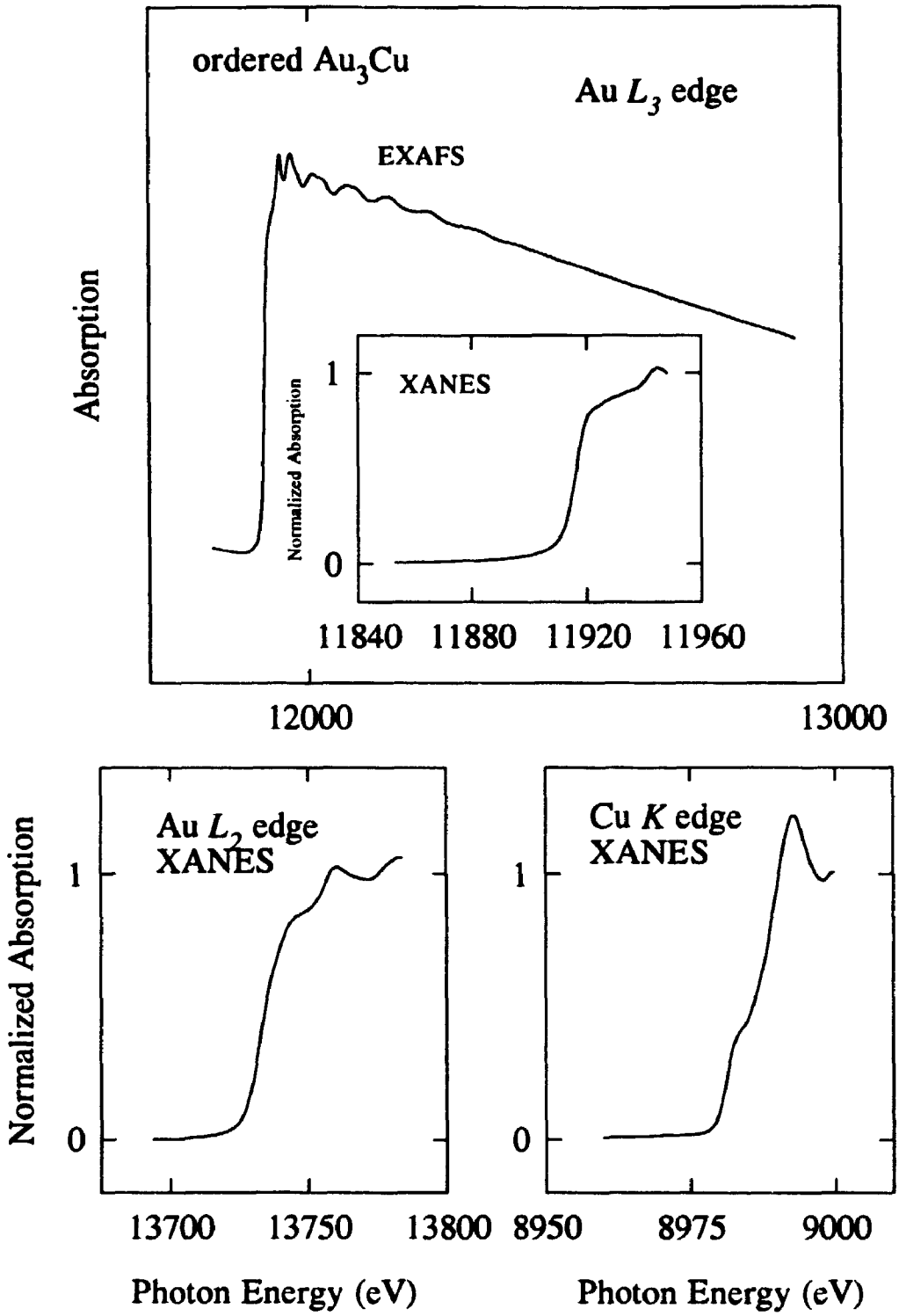

Figure 4.20: X-ray absorption spectra for ordered Au_3Cu. The top panel shows the extended Au L_3 edge with the XANES region in the inset. The bottom two panels show the XANES region for the Au L_2 and Cu K edges, respectively.

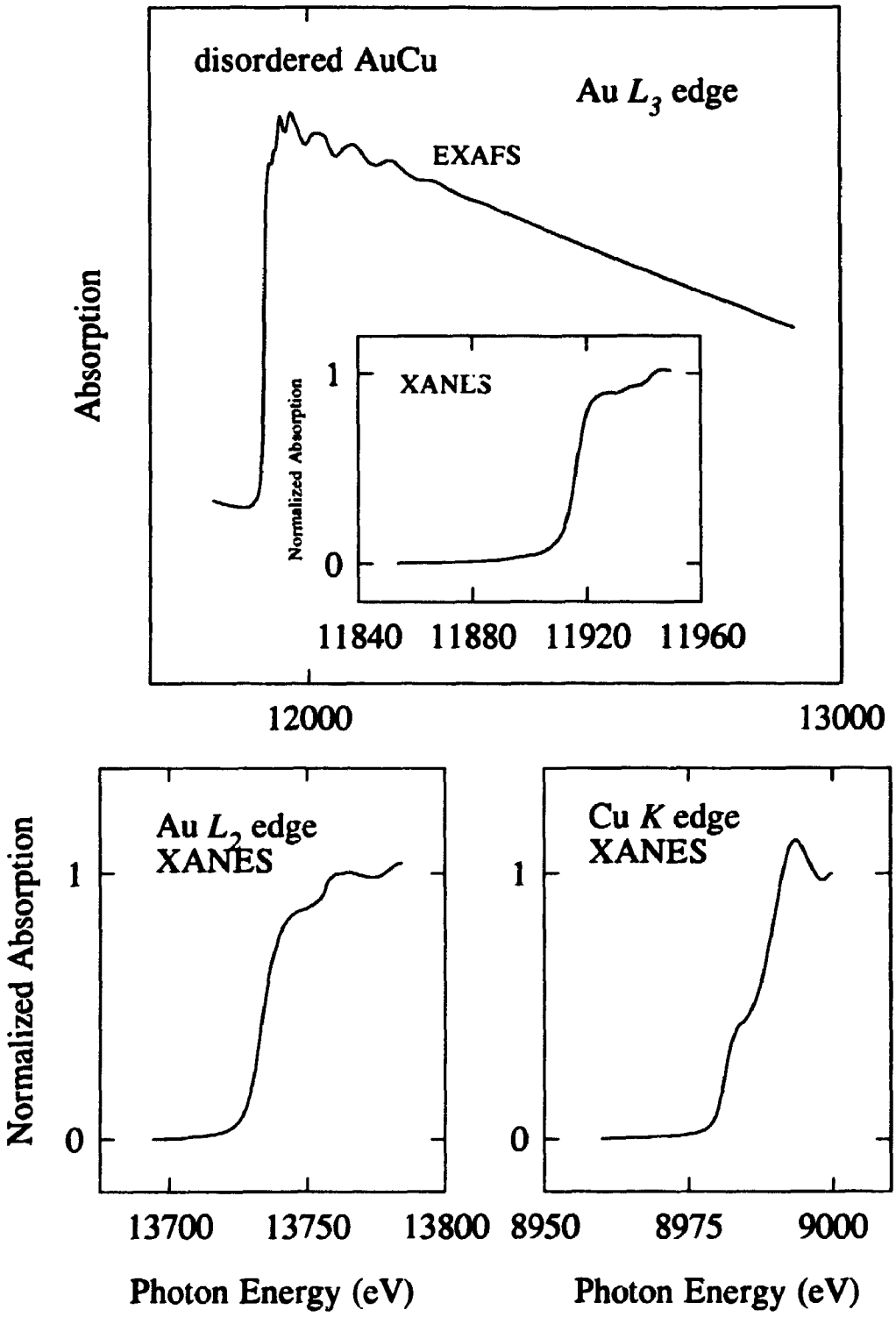

Figure 4.21: X-ray absorption spectra for disordered AuCu. The top panel shows the extended Au L_3 edge with the XANES region in the inset. The bottom two panels show the XANES region for the Au L_2 and Cu K edges, respectively.

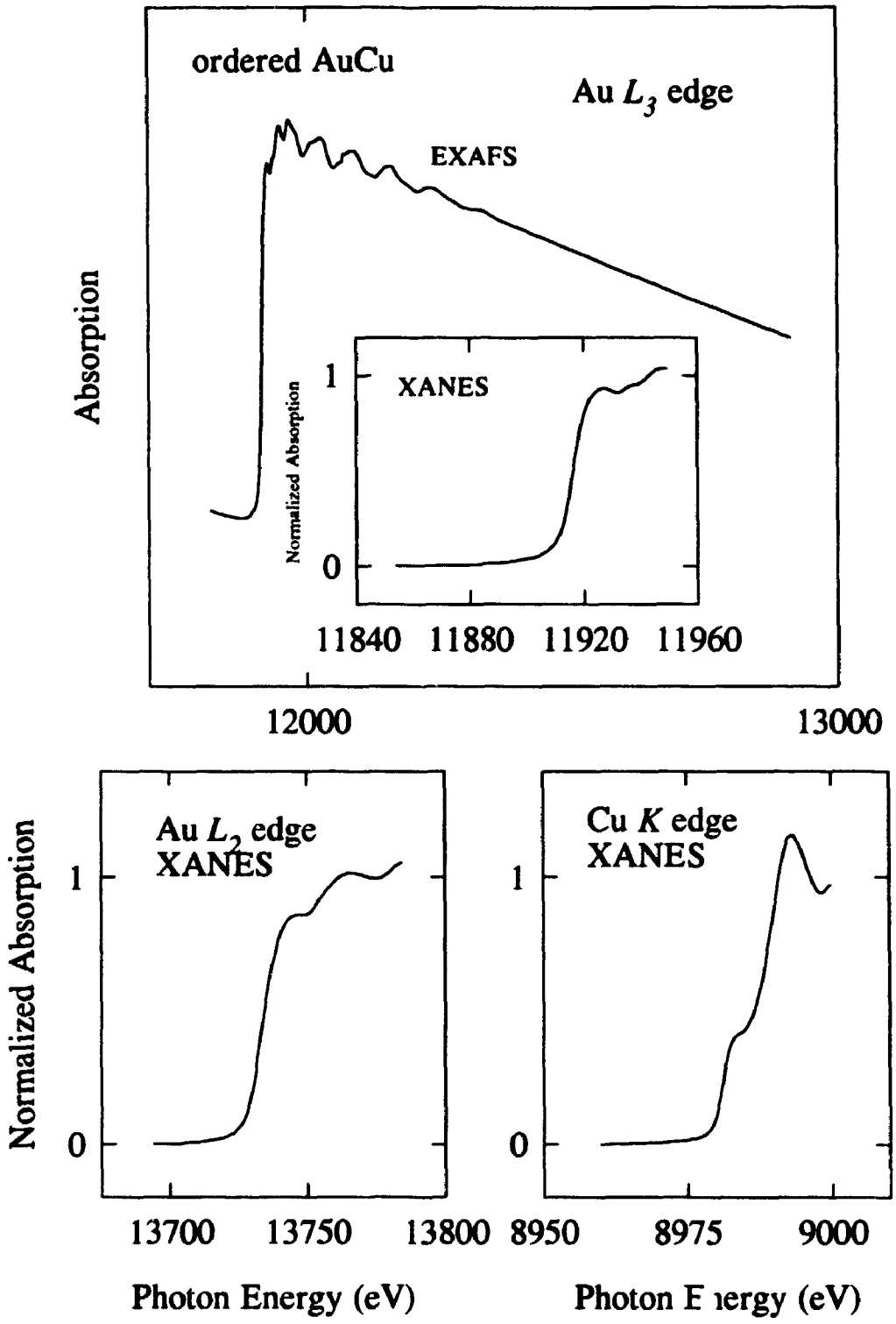

Figure 4.22: X-ray absorption spectra for ordered AuCu. The top panel shows the extended Au L_3 edge with the XANES region in the inset. The bottom two panels show the XANES region for the Au L_2 and Cu K edges, respectively.

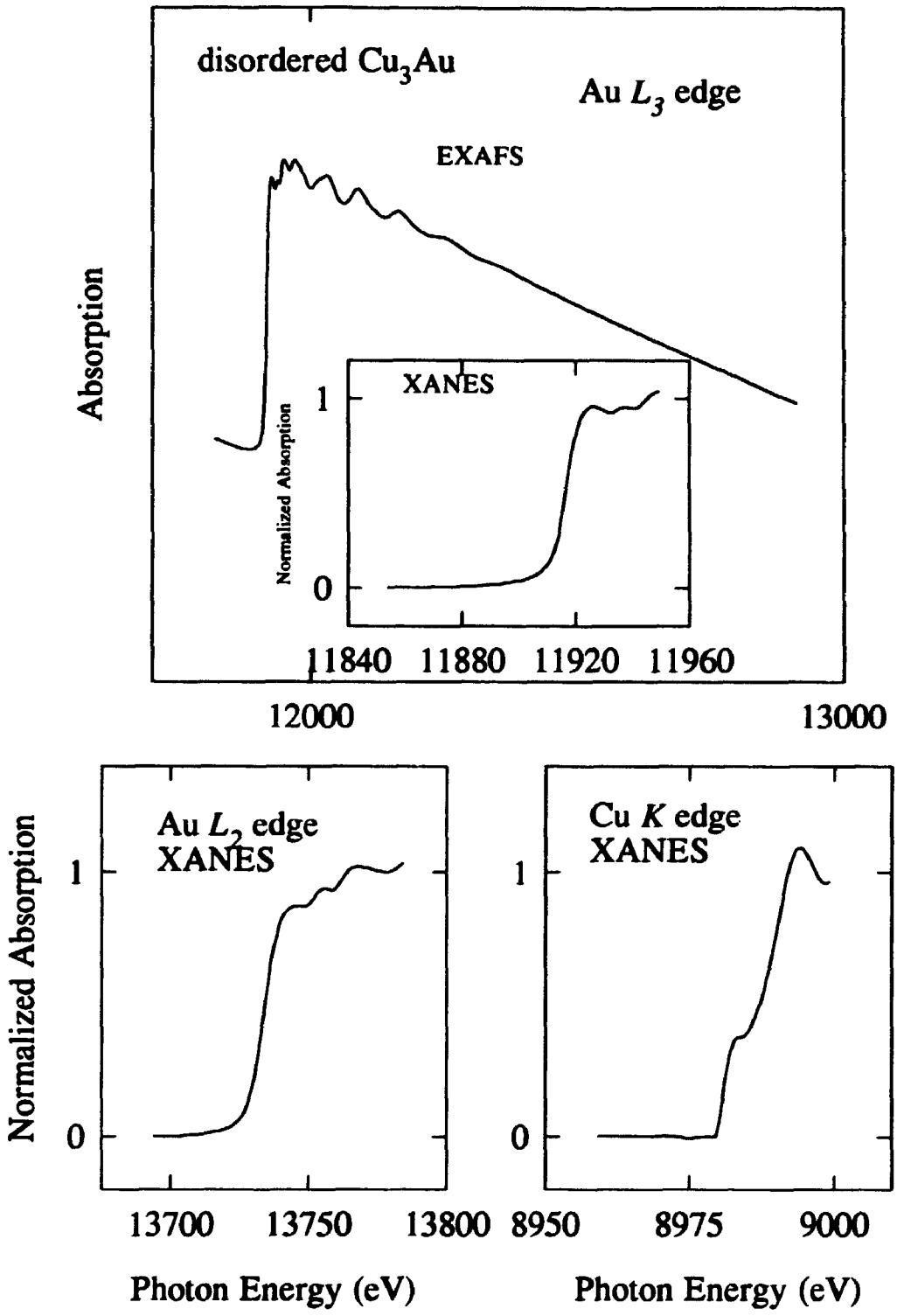

Figure 4.23: X-ray absorption spectra for disordered Cu_3Au. The top panel shows the extended Au L_3 edge with the XANES region in the inset. The bottom two panels show the XANES region for the Au L_2 and Cu K edges, respectively.

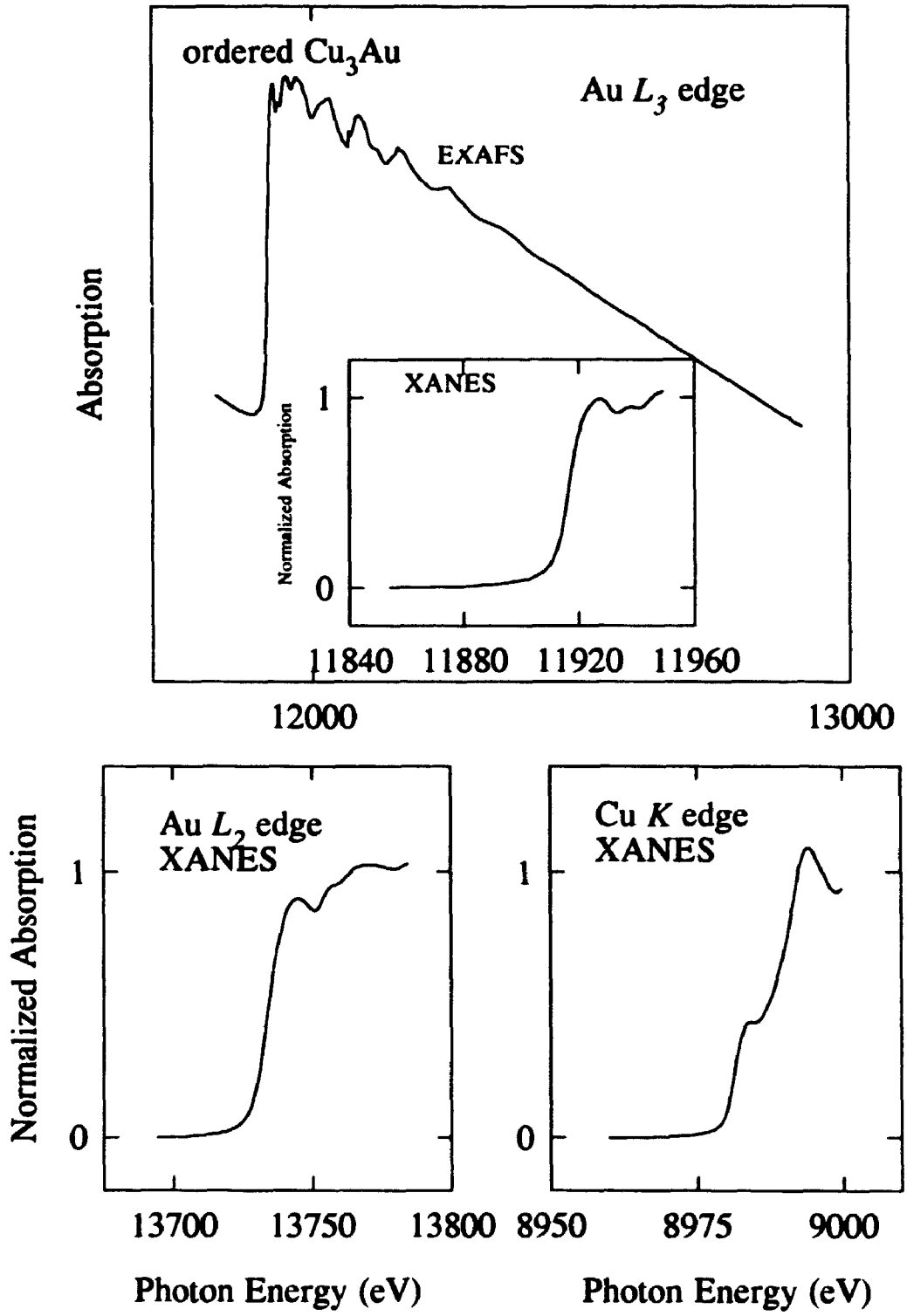

Figure 4.24: X-ray absorption spectra for ordered Cu_3Au. The top panel shows the extended Au L_3 edge with the XANES region in the inset. The bottom two panels show the XANES region for the Au L_2 and Cu K edges, respectively.

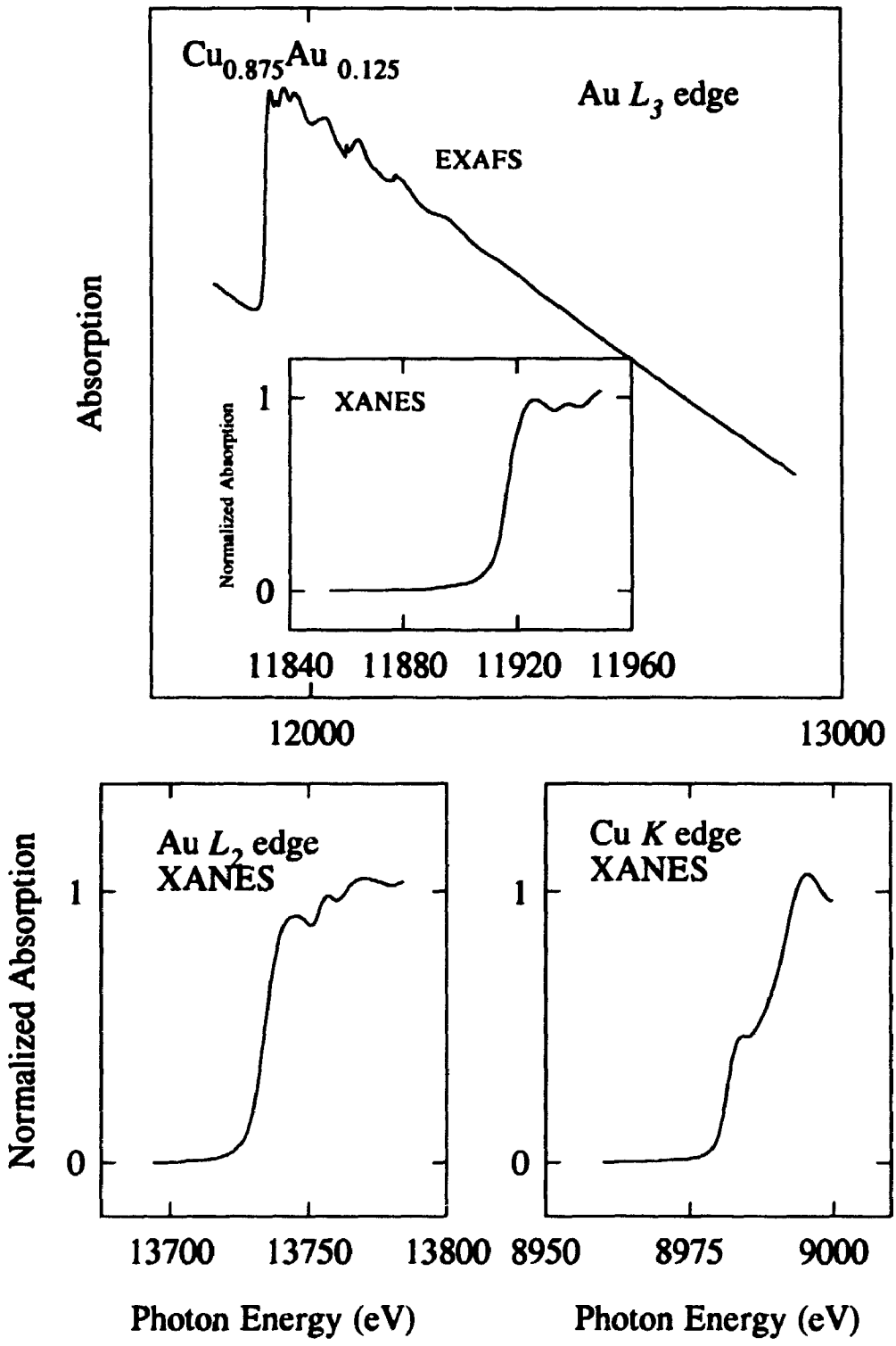

Figure 4.25: X-ray absorption spectra for $Cu_{0.875}Au_{0.125}$. The top panel shows the extended Au L_3 edge with the XANES region in the inset. The bottom two panels show the XANES region for the Au L_2 and Cu K edges, respectively.

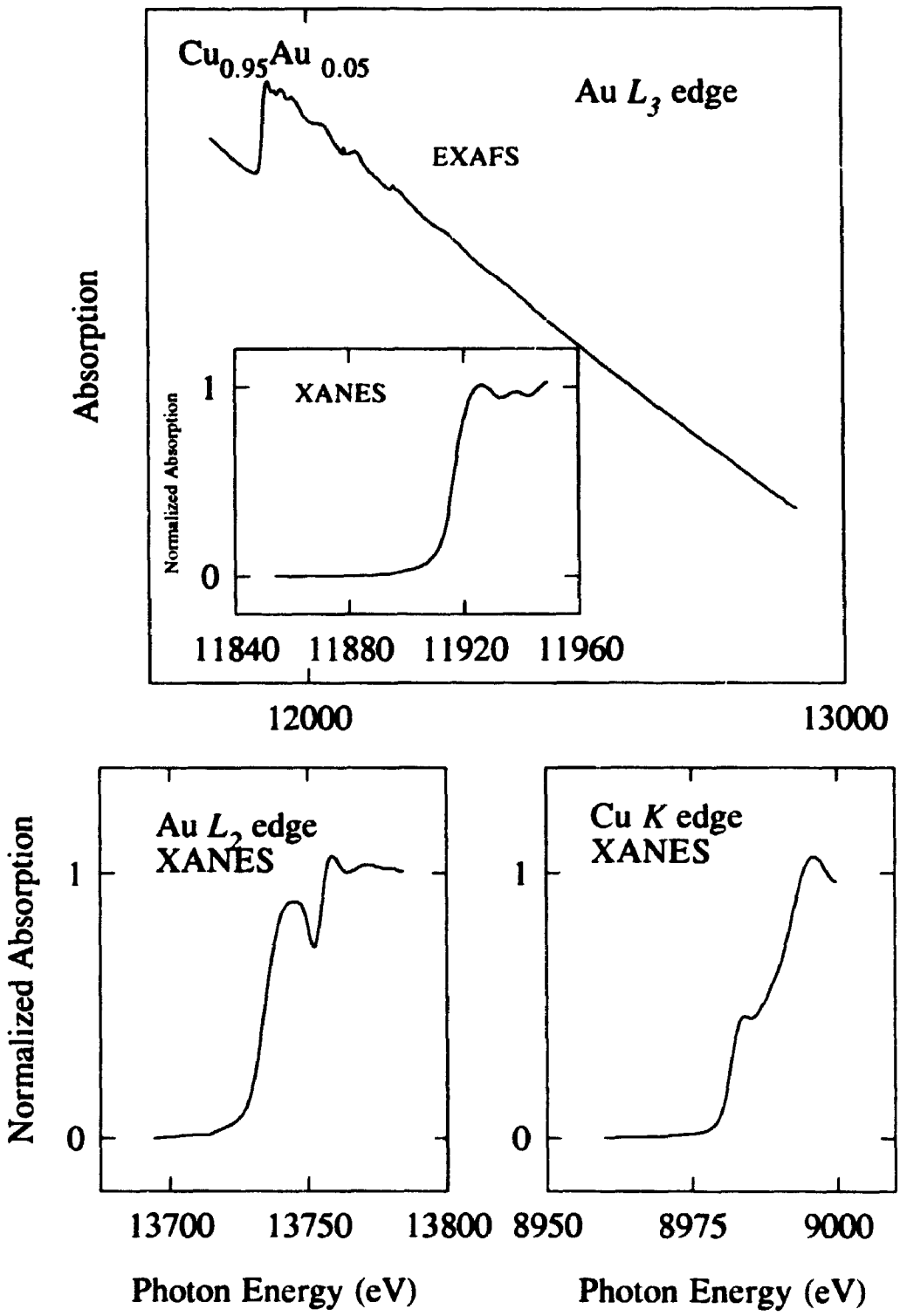

Figure 4.26: X-ray absorption spectra for $Cu_{0.95}Au_{0.05}$. The top panel shows the extended Au L_3 edge with the XANES region in the inset. The bottom two panels show the XANES region for the Au L_2 and Cu K edges, respectively.

Once the spectra are normalized there must be an energy calibration for direct comparison due to chemical shifts. There are several inherent problems with trying to line up the Fermi edges. Figure 4.28 indicates some of the possible problems associated with the calibration. After the normalization and pre-edge background subtraction the absorption coefficient is now expressed as that due to the emission solely from the $2p$ core levels, which is made up of two components, using the dipole selection rule:

$$\mu_L = \mu_d + \mu_s \tag{4.2}$$

where μ_d is the contribution of the unoccupied d states and μ_s is the contribution from unoccupied s states. The unoccupied d states will be narrow with a high density of states while the unoccupied s states will be broad and have no discernible features at the edge. In Figure 4.28 we use an arctangent function centred at 12 keV to simulate excitation into empty s states. Two Lorenztian functions with a width of 10 eV (the lifetime contribution is $\sim$8 eV for the Au L_3 edge)[2] and with amplitudes 40% and 20% of the arctangent are centred at 5 eV above the edge to simulate excitation into empty d states. If we take the inflection point of the resultant curve to be the Fermi level we note a shift of the apparent Fermi level as the density of d states is increased. The situation worsens as the density of states move closer to the edge. It is obvious that without knowing the density of unoccupied d states (the parameter which is being determined) the exact position of the Fermi level is not known. We have opted for a systematic calibration which has a small reproducible error associated with it. The inset of the top panel shows the difference between the combined Lorenztian-arctangent functions and the arctangent function. The areas were determined by truncation at the mid-way point of the

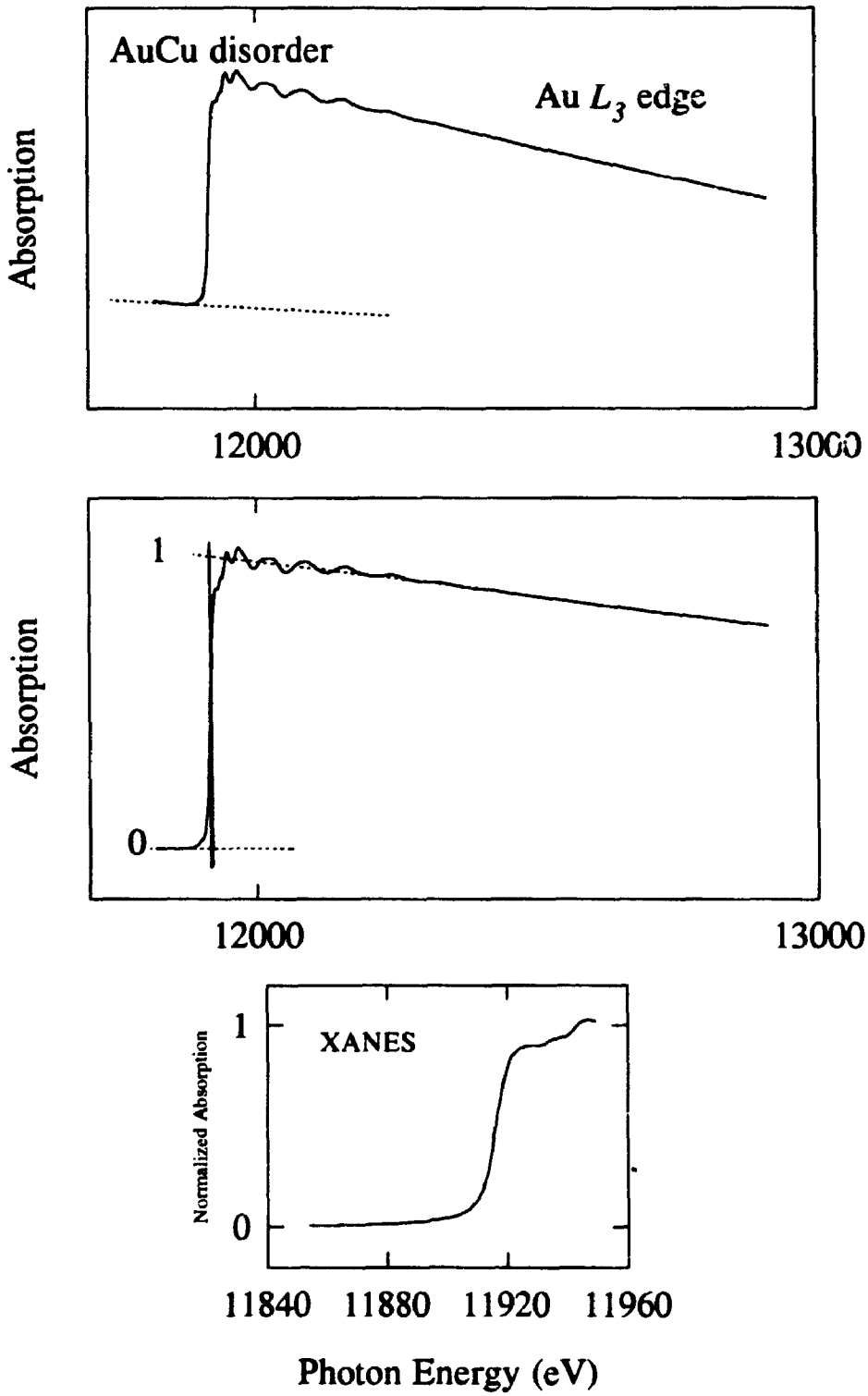

Figure 4.27: An example of the normalization of the XANES regions using the Au L_3 edge of disordered AuCu. Details of the procedure are given in the text.

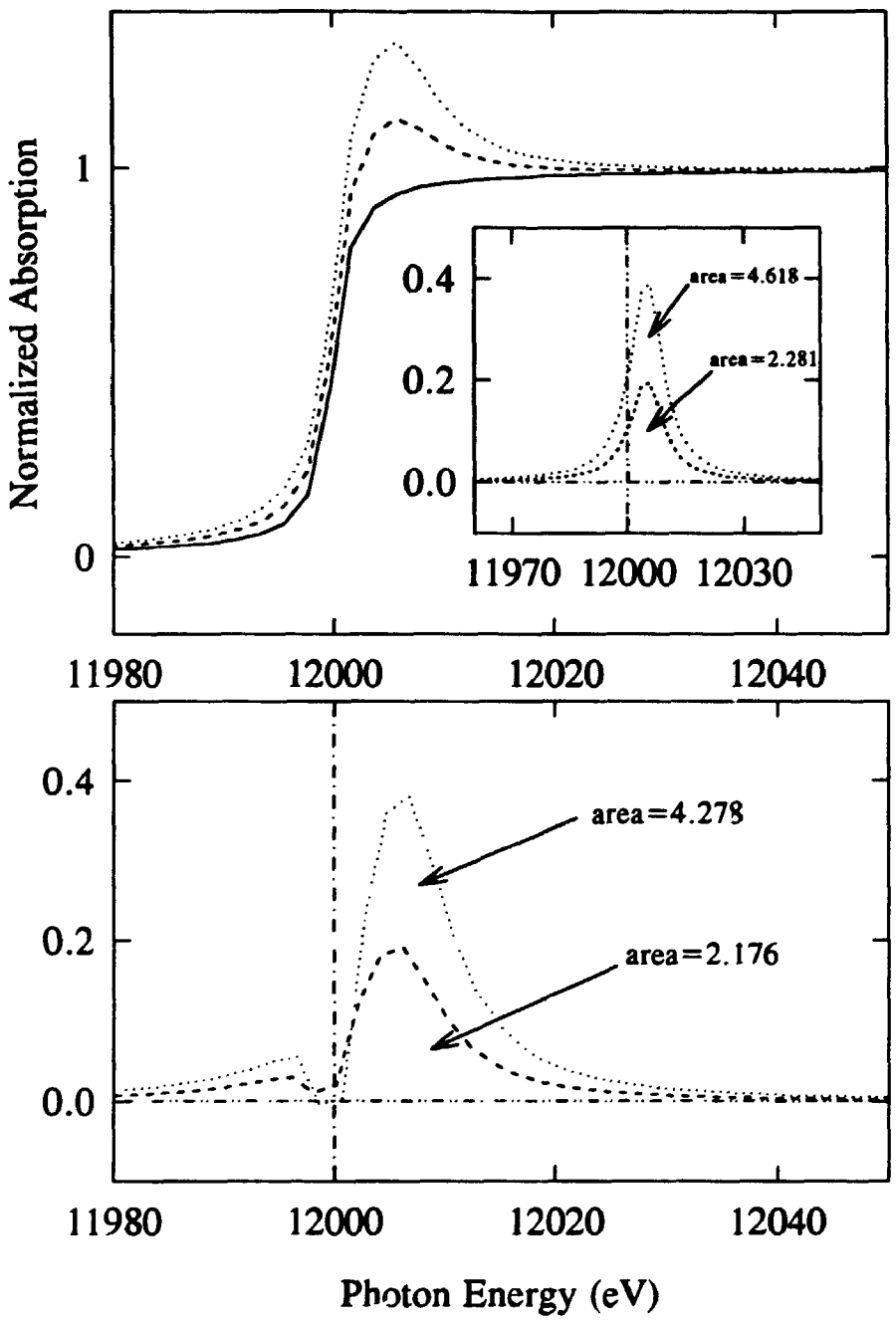

Figure 4.28: Simulated XANES for the Au *L* edge. The *s* contribution is given by an arctangent function while the *d* contribution is simulated using a Lorenztian function (top panel). The change in measured area after calibration is given in the bottom panel.

arctangent jump (12 keV). The lower panel shows the area determination after the combined Lorenztian-arctangent spectra were lined up with the midpoint of the arctangent spectra. The difference in the area is ~5% for the 20% Lorenztian function while it is ~10% for the 40% Lorenztian function. For the Au-Cu alloys the whiteline intensity is no more than 20% of the edge jump giving us a maximum error of 5% due to calibration. For the actual experimental spectra, calibration was performed by simulating an arctangent step for the edge jump (from zero to one in the normalized spectra) ignoring the whiteline area and lining up the spectra to the halfway point of the jump.

We can now make qualitative comparisons of the near edge features of the Au-Cu alloys. Representative spectra are shown for the Au $L_{2,3}$ edges in Figure 4.29. Relative to pure Au we see an increase in the whiteline area as the Cu composition is increased. Figure 4.30 shows that the ordered alloys have an increased whiteline area as compared to their disordered counterparts.

For the actual determination of whiteline areas for determination of d hole counts, as outlined in Chapter 3, we are left with two possibilities. To determine the density of unoccupied d states we must account for contribution from unoccupied s states to the absorption coefficient as shown by Equation 4.2. This can be accomplished, as outlined above, by using an arctangent function to simulate the contribution from unoccupied s states. However, it may be more advantageous to use the absorption at the pure Au edge, which does not have a sharp whiteline, to compare with the alloys. Even though, due to hybridization, pure Au does have unoccupied d states,[3] the subsequent difference in area would indicate the change in unoccupied d states upon alloying, which is essential

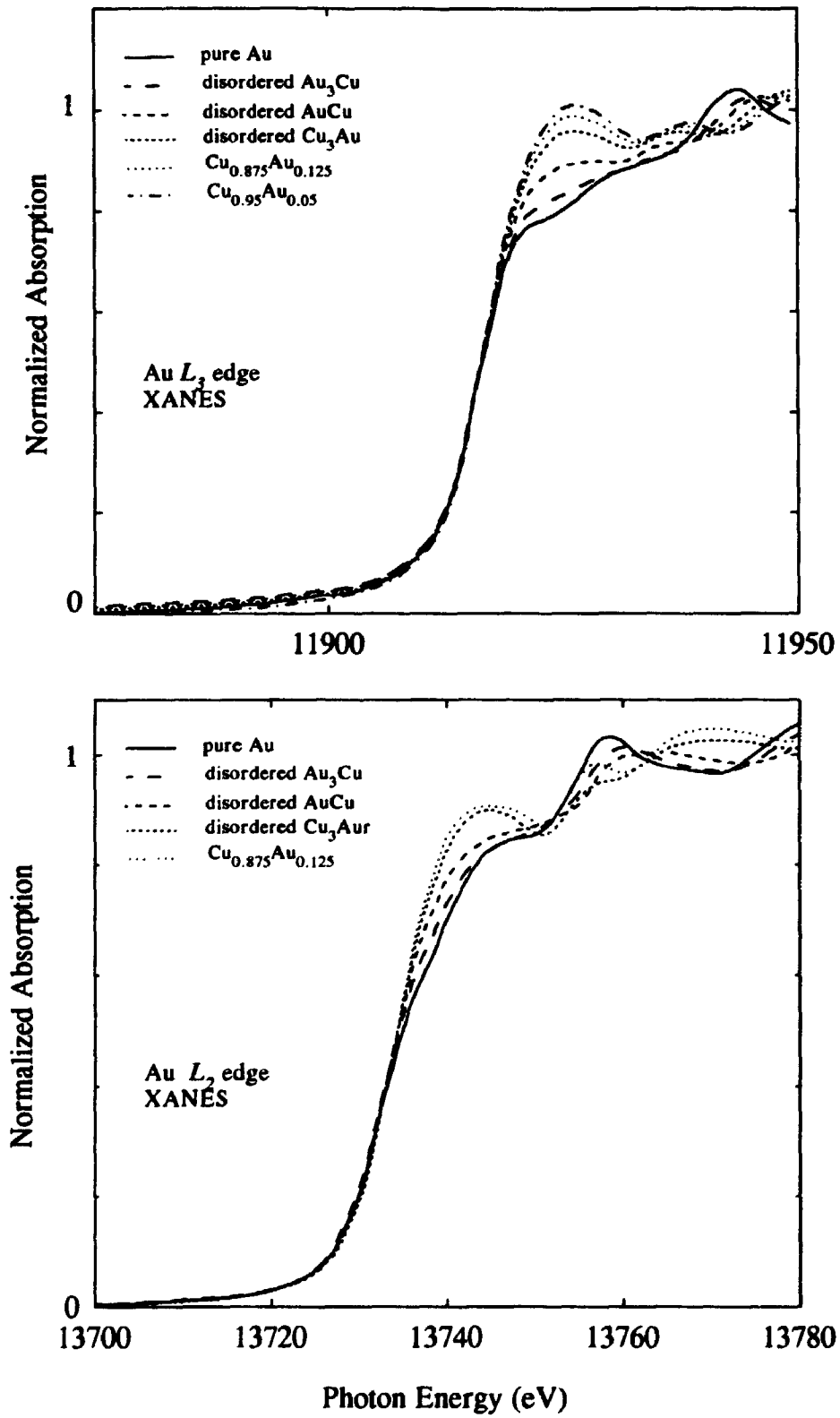

Figure 4.29: Qualitative comparison of the XANES spectra for the series of Au-Cu alloys for the Au L_3 edge (top panel) and Au L_2 edge (bottom panel).

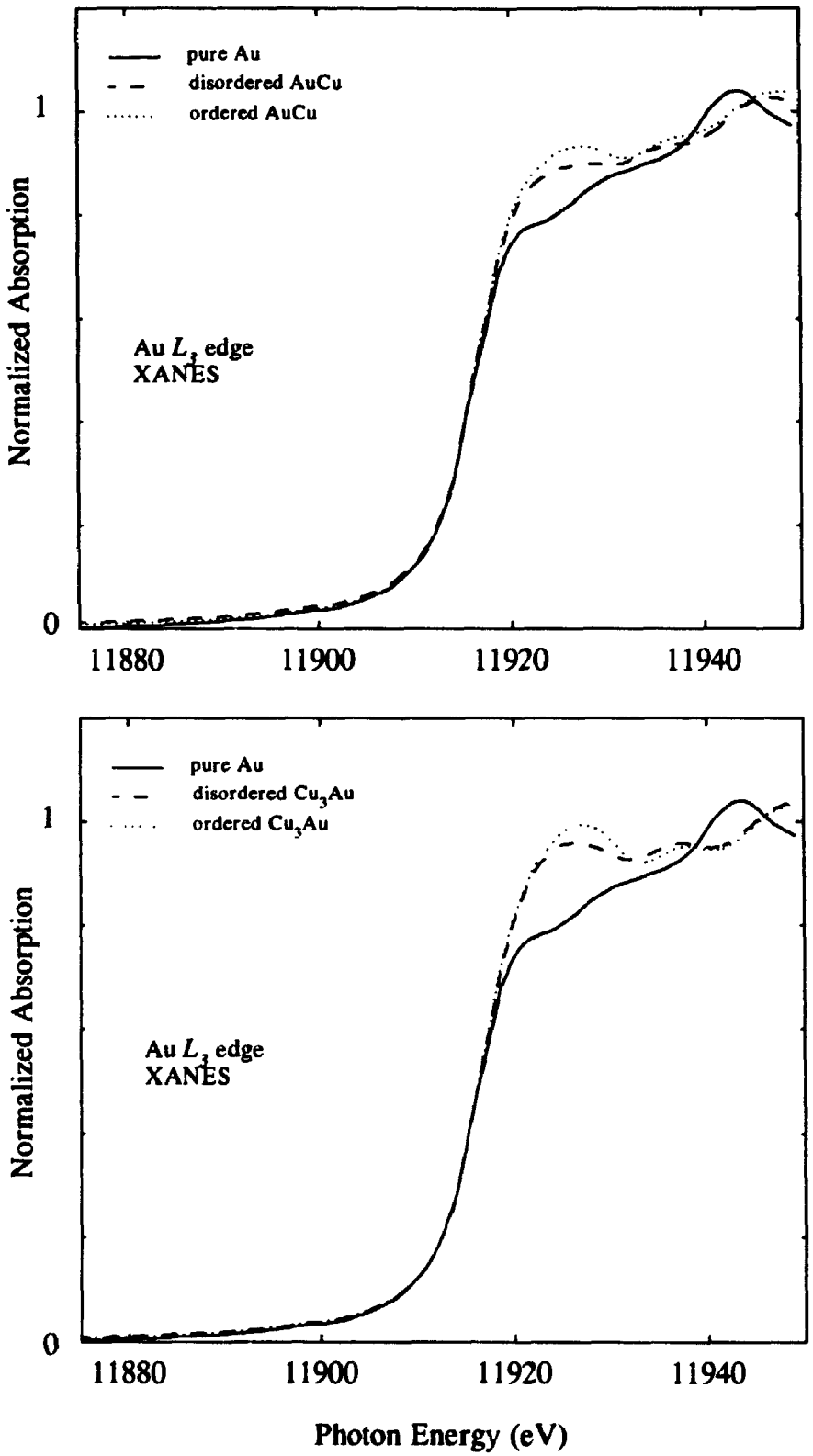

Figure 4.30: XANES of the Au L_3 edges of ordered and disordered AuCu (top panel) and ordered and disordered Cu_3Au (bottom panel). Note the larger whiteline areas for the ordered samples.

to this study. Absolute numbers can be determined by including the original configuration of pure Au. Also, by direct comparison with pure Au data, which includes the contribution of unoccupied *s* states, we do not have to deal with the ambiguity of assuming and assigning parameters to simulate the edge jump. Changes in the unoccupied *s* density of states, upon alloying, are accounted for by the normalization procedure, assuming there are no intense features. An example of the determination of the whiteline area, relative to pure Au, is given in Figure 4.31. The pure Au L_3 edge XANES is subtracted from that of disordered Cu_3Au. The resultant difference spectrum is integrated from the halfway point of the edge jump (as outlined above) to ~ 15 eV above the edge. The analysis was limited to 15 eV above the edge to include unoccupied *d* state distribution, lifetime effects (~ 8 eV for the Au L_3 edge), photon resolution (2-3 eV), but to avoid including features due to multiple scattering effects. The resultant whiteline areas are given in Table 4.2.

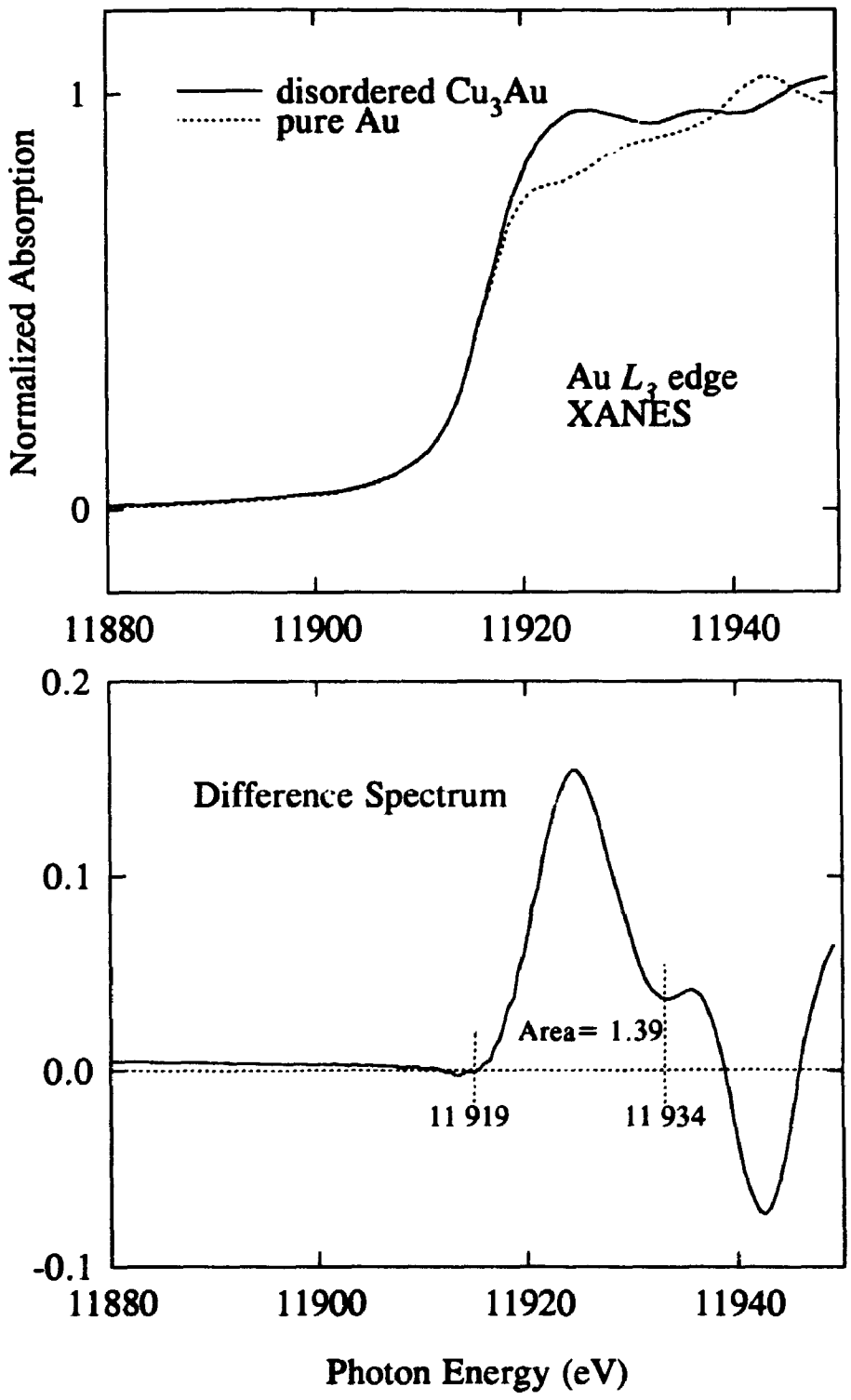

Figure 4.31: Representative spectra of the Au L_3 edge XANES region of disordered Cu_3Au and pure Au. The bottom panel shows the difference spectrum and indicates the truncation used for integration to determine the change in area relative to pure Au.

Compound	L_3 edge area (relative to pure Au) (±5% atom eV)	L_2 edge area (relative to pure Au) (±5% atom eV)
disordered Au_3Cu	0.25	0.08
ordered Au_3Cu	0.25	0.17
disordered AuCu	0.80	0.45
ordered AuCu	1.30	0.46
disordered Cu_3Au	1.39	0.79
ordered Cu_3Au	1.67	0.98
$Cu_{0.875}Au_{0.125}$	1.71	1.22
$Cu_{0.95}Au_{0.05}$	1.91	0.91

Table 4.2: Au L_2 and Au L_3 edge areas for the Au-Cu alloy series, relative to pure Au, after normalization and calibration procedures as described in the text.

The Cu *K* edge XANES have also been normalized and calibrated for qualitative examination. Representative spectra are given in Figure 4.32. The small but clearly noticeable pre-edge feature at the absorption edge is attributed to a $1s \rightarrow d$ transition, usually forbidden by dipole selection rules, but from hybridization due to solid formation, the Cu *d* band contains $l=1$ character and therefore the matrix element is not zero.[4] We note the largest area under this feature for pure Cu which decreases with increasing Au composition. Recently completed Cu $L_{2,3}$ studies ($2p \rightarrow d$ transition) have also shown, qualitatively, a decrease in the whiteline area as the Au composition is increased.[5] For both cases there are differences associated with the disordered and ordered samples. the ordered samples exhibit larger decreases in area relative to pure Cu.

In this last section, we will focus on the extended X-ray absorption region (50 to 1000 eV above the edge). Using the single scattering EXAFS formula from Section 3.4 we will analyze the Au L_3 edge spectra of our alloy samples to derive the local configuration and distances. The purpose of this is to confirm the composition of our alloys and especially the change in structure associated with the order-disorder phase transition. A comprehensive X-ray crystallography study[6] has been performed on a large number of Au-Cu alloys and we will attempt to compare the trends of our values with those of the previous study.

There is a large number of ways to analyze the EXAFS spectra. The following will summarize the procedure used in our study to extract the nearest-neighbour distances and configurations for each alloy sample. The EXAFS formula, $\chi(k)$, is given by Equation 3.23 and can be separated into two components, amplitude and phase. The

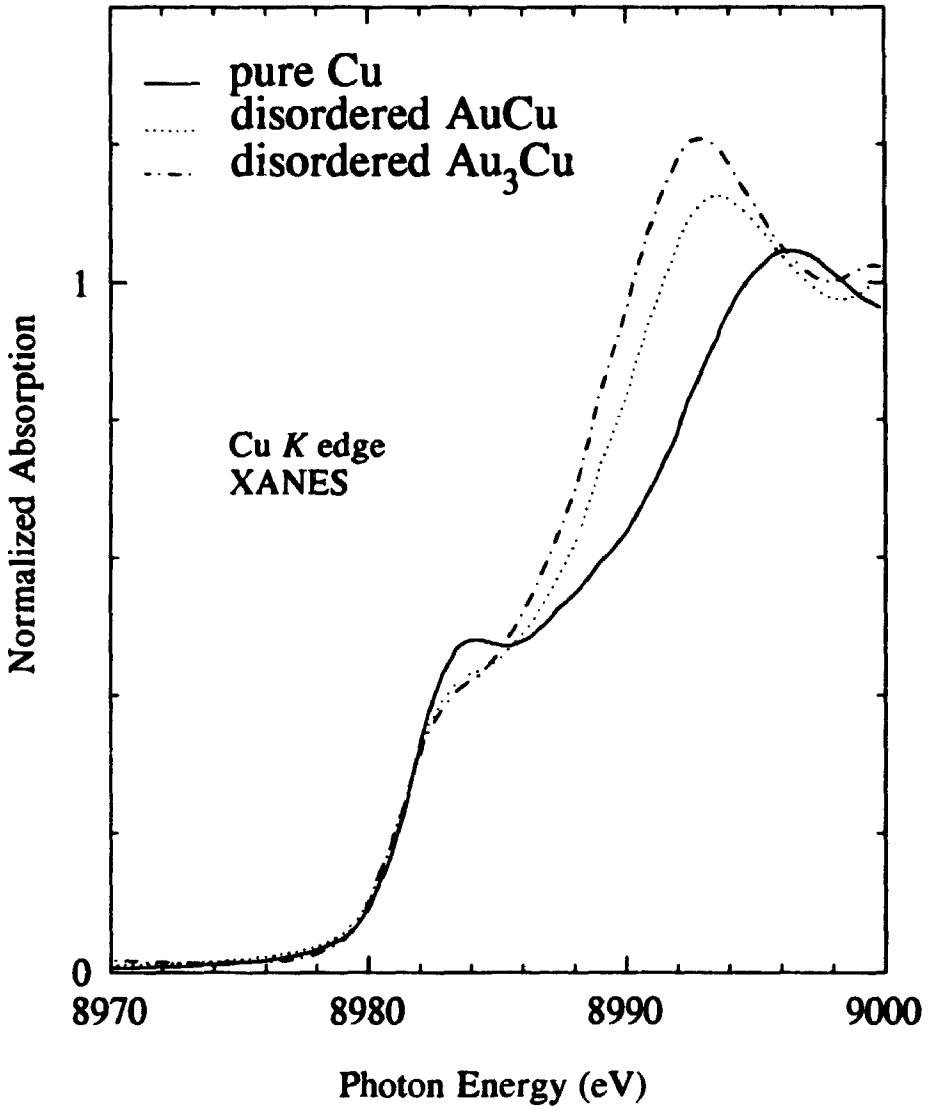

Figure 4.32: Qualitative comparison of the XANES region at the Cu *K* edge. There is a reduction of the feature at the edge as the Au composition is increased.

actual experimental data comprise measured absorption coefficients as a function of the photon energy, i.e. $\mu(E)$. The EXAFS formula can be defined as:

$$\chi(k)=\frac{\mu(E)-\mu_0(E)}{\mu_0(E)} \tag{4.3}$$

where $\mu_0(E)$ is the atomic absorption coefficient. In our case we have performed a pre-edge linear background subtraction followed by a cubic spline subtraction with a third-degree k weighting of the experimental spectra to accentuate high k data. Therefore a McMaster correction for the energy dependence of the background was not applied. This leads to a lower amplitude of $\chi(k)$ at higher k values where the deviation from a linear energy dependence is the largest.

To solve for the various structural parameters we have applied a non-linear least-squares curve fitting routine called EXAFIT.[7,f] In this program empirical or theoretical scattering amplitude and phase functions are fitted to the experimental spectra. In our study we are concerned with the immediate Au environment (Au L_3 edge). For this reason we have calculated theoretical FEFF phase and amplitude functions for two cases. In the first Au is surrounded by 12 Au atoms and in the second Au is surrounded by 12 Cu atoms. Therefore, we are fitting two shells in which the final weighting of these two theoretical functions will determine the number of Au and Cu nearest neighbours in our alloy samples. As will be described shortly, the extracted nearest-neighbour distances,

---

[f] This program was used courtesy of E.D. Crozier of the Physics Department, Simon Fraser University, B.C and D.T. Jiang (formerly located there). Access to the program was from the University of Western Ontario via telnet. The program does not allow extraction of the fitted plots but only the fitted parameters.

r_i, are much more accurate than the nearest-neighbour distribution values.

Insertion of both the normalized experimental spectra and the theoretical amplitude and phase functions into the EXAFIT program allows for a number of options in treatment of the data. EXAFS data are normally fitted in *k*-space but in this case we have opted for a fit in *r*-space. By fitting in *k*-space artifacts can be introduced when a back Fourier transform is performed. In the treatment of the EXAFS data a Fourier transform is performed to separate out the various coordination shells. A window is then selected encompassing the shell of interest and a back transform is performed after which the fitting is then begun. Problems occur if after the Fourier transform there is overlap between the shells and therefore a single shell cannot be isolated. This is not a serious problem in our data. However, the EXAFIT program in fitting in *r*-space has the advantage that it treats the experimental and model data identically whereas in *k*-space fitting the experimental data is Fourier filtered while the model is not. Therefore, in *r*-space fitting any artifacts introduced by the Fourier transform will be cancelled out. The typical treatment of the data (and model data) is a Fourier transform with a window with a reasonably large *k* value spread (typically 3.5 to 15 $Å^{-1}$). This range is selected by the zero-crossing values at low and high *k*. A Fourier transform is performed and a fitting interval is selected to encompass the first coordination shell. Fitting of the model function to the experimental data is then performed. As was stated earlier, the EXAFS formula can be viewed as having an amplitude and phase component. The phase component has only one variable, namely the interatomic distance. The amplitude depends on a number of variables: the interatomic distance, the nearest-neighbour

configuration, the vibrational component, and an amplitude reduction term, S_0^2, due to many-body effects. This term, S_0^2, was set at 0.85 when the model calculations were performed. Without the McMaster energy correction we have underestimated the experimental amplitude and this will manifest itself with lower than expected values for the variables which determine the amplitude for the fit. Although the interatomic distance is also incorporated in the amplitude function, the strong dependence of this variable on the phase function will mean that it will be relatively unaffected in the amplitude fitting as compared to the other variables. It is for these reasons that more confidence can be given to the values for interatomic distances than for the other parameters. The last variable that is introduced into the fitting is ΔE. This variable is introduced to account for the different reference levels (Fermi levels) between the muffin-tin zero of the theoretical calculations and the experimental Fermi level and thus allows for a relative shift of the k values. It is incorporated into the fit by a k' variable defined as:

$$k' = [k^2 - \frac{\Delta E}{3.81}]^2 \qquad (4.4)$$

For the fit of our experimental spectra we have allowed eight variables, namely ΔE, r, σ^2, and N for both shells. Only in the case of the dilute Au alloys were we forced to fix certain parameters.

The values for the interatomic distances, r, and the nearest-neighbour ratio and absolute numbers, N, for the series of Au-Cu alloys are given in Table 4.3. The first shell is Au-Au while the second shell is Au-Cu.

Compound	r_1 (Å)	N_1	r_2 (Å)	N_2	N_1/N_2
disordered Au_3Cu	2.793 (±0.02)	7.4 (±3)	2.739 (±0.08)	2.9 (±3)	2.6
ordered Au_3Cu	2.798 (±0.02)	6.4 (±3)	2.777 (±0.07)	3.2 (±3)	2.0
disordered AuCu	2.754 (±0.03)	4.0 (±3)	2.662 (±0.03)	5.3 (±3)	0.8
ordered AuCu	2.780 (±0.01)	4.0 (±3)	2.673 (±0.01)	7.4 (±2)	0.5
disordered Cu_3Au	2.638 (±0.06)	2.6 (±5)	2.626 (±0.01)	7.7 (±1)	0.3
ordered Cu_3Au	-----	-----	2.630 (±0.01)	12.1 (±1)	-----
$Cu_{0.875}Au_{0.125}$	2.737 (±0.1)	0.6 (±3)	2.609 (±0.01)	10.6 (±3)	0.1
$Cu_{0.95}Au_{0.05}$	-----	-----	2.600 (±0.01)	12.1 (±3)	-----

Table 4.3: Nearest-neighbour distance and configuration parameters determined from EXAFS spectra for the various Au-Cu alloys.

The EXAFS analysis has yielded interatomic distance and local configuration values. The interatomic distance values for the two shells yield significant results. The absolute values can be compared to those determined by the X-ray crystallography study.[6] However, it is interesting to note that in each alloy there is clearly a local distortion of the fcc lattice in which, generally, the Au-Cu distances are shorter than the Au-Au distances, a fact that cannot be revealed by X-ray crystallography studies and has been noted before for EXAFS analysis of $Cu_{1-x}Au_x$ solid solutions.[8] Direct comparison, therefore, to lattice parameters (an average of the Au-Au, Au-Cu and Cu-Cu distances) will be complicated. We can, however, compare the trend of interatomic distance as derived from the lattice parameters with the weighted average of the Au-Au and Au-Cu distances as a function of composition and ordering. Also, we can compare the ratios of the nearest-neighbour shells with those predicted by the ordered and disordered fcc lattice structure. As was mentioned previously, there are larger errors associated with the fit of the amplitude (and thereby its variables) because of the uncertainty in the normalization of the experimental spectra and the value of S_0^2. However, by comparing the ratios of the nearest-neighbour distribution we eliminate the problem of the errors involved in the determination of the absolute values. The results are tabulated in Table 4.4.

Compound	r_{avg}(exp.)	r_{avg}	N_1/N_2 (exp.)	N_1/N_2 (pred.)
disordered Au_3Cu	2.766	2.816	2.6	3.0
ordered Au_3Cu	2.790	2.814	2.0	2.0
disordered AuCu	2.702	2.739	0.8	1.0
ordered AuCu	2.710	2.733	0.5	0.5
disordered Cu_3Au	2.629	2.654	0.3	0.3
ordered Cu_3Au	2.630	2.650	-----	-----
$Cu_{0.875}Au_{0.125}$	2.616	-----	0.1	0.1
$Cu_{0.95}Au_{0.05}$	2.600	-----	-----	0.05

Table 4.4: Comparison of nearest-neighbour distances and configurations with experimental results and predicted results, respectively. The r_{avg} values in column two are taken from Reference 6.

Table 4.4 points out some interesting results. Although comparison of the interatomic distances as derived from Reference 6, assuming a pure fcc structure, shows a consistently smaller value from our studies, the trends through the range of compositions are the same. As the Cu composition is increased there is a reduction in the lattice constant and a corresponding reduction in the averaged Au-Au and Au-Cu distances. The X-ray crystallography study shows a small, almost negligible, reduction in the interatomic distance between the ordered and disordered samples. This is not seen in our EXAFS data, but we have a much larger experimental error and have not included the contribution of Cu-Cu bond lengths. The comparison of the predicted nearest-neighbour distribution with that extracted from the EXAFS spectra is very promising. The values in all cases are similar, if not exact, and the differences are clear between the ordered and disordered sample despite the larger error associated with these values. In the case of ordered Cu_3Au the Au-Au shell went to zero in the fitting procedure. Similarly, there was no evident contribution from the Au-Au shell in the $Cu_{0.95}Au_{0.05}$ sample.

With these results, specifically the trend of bond lengths with composition and the accuracy of the nearest-neighbour distribution change between the disordered and ordered samples, we are confident of the local structure and configuration of our samples.

4.5 References

1. J.J. Yeh and I. Lindau, Atomic Data and Nuclear Data Tables, **32**, 1 (1985).

2. L.G. Parratt, Rev. Mod. Physics, **16**, 393 (1967).

3. L.M. Mattheiss and R.E. Dietz, Phys. Rev. B **22**, 1663 (1980).

4. J.E. Müller, O. Jepsen, and J.W. Wilkins, Sol. St. Com. **42**, 365 (1987).

5. T.K. Sham, A. Hiraya, and M. Watanabe, 1992 UVSOR Annual Report, 67 (1993).

6. S.S. Lu and C.-K. Liang, Chin. Journ. Physics, **22**, 505 (1966).

7. K.R. Bauchspiess, Jpn. J. Appl. Phys. **32**, 131 (1993).

8. K. Lu, Z. Wu, J. Dong, X. Chen, and Z. Feng, Jpn. J. Appl. Phys. **32**, 631 (1993).

CHAPTER FIVE

Analysis and Discussion

5.1 Introduction

In this chapter we will focus on analyzing the results of the XPS, synchrotron and X-ray absorption data. Using the framework of the charge compensation model the core level shifts and existing Mössbauer data will be used to derive the amount and character of charge transfer to and from the Au site. Using the XANES spectra the amount of Au *d* charge transfer will be independently calculated and compared with the results of the conventional model. Both the XPS and synchrotron valence band spectra will be examined for determination of the nature and extent of the Au and Cu *d*-band interactions. Resonant photoemission results will be evaluated in terms of determining the change in Cu *d* character, upon alloying, and will be compared to the results of the Cu *K* edge XANES. The overall resultant interactions, dependent upon composition of the components and ordering of the system, will be examined in terms of the local structure of the alloys.

5.2 Estimation of Au 5*d* Hole Counts in Au-Cu Alloys from XPS and Mössbauer Results: The Charge Compensation Model

The XPS core level shifts will be examined for qualitative confirmation of the charge compensation model. When combined with existing Mössbauer data a semi-quantitative measurement of the amount and type of charge transferred to and from the Au site will be made.

The apparent opposite trends of XPS Au 4*f* binding energy and Mössbauer isomer shifts (Tables 4.1 and 5.1) with respect to electronegativity difference and dilution between Au and Cu is in accord with the observations of bimetallic Au systems generally.[1,2,3,4,5,6,7,8]

We first analyze the XPS core level binding energy shifts within the single-particle framework. According to the charge compensation model (which demands that Au loses *d* charge and gains non-*d* charge and the overall charge gain is small and in the direction predicted by electronegativity) we would expect the Au 4*f* core levels to shift to higher binding energies with increasing Cu composition, indicating a loss of *d* charge at the Au site. The loss of *d* charge is the dominant term. It leads to a higher effective Coulombic potential for the remaining electrons giving a shift to higher binding energies, even though there is an overcompensation of (less effective) conduction charge as required by electronegativity considerations. The results given in Table 4.1 do indeed show a shift to higher binding energies throughout the Au-Cu series. These results indicate that the smaller the number of like nearest neighbours the higher the binding

energy shift. The corollary of the shifting of the Au 4*f* peaks is the expected shifting of the Cu core levels. The Cu $2p_{3/2}$ levels investigated, shift to lower binding energies with increasing Au composition. This indicates that Cu is gaining *d* and/or non-*d* charge. We will briefly examine the results of the absorption at the Cu *K* edge. The Cu *K* edge XANES clearly reveal a decrease in the density of unoccupied *d* states, upon alloying, with a decreased area in the feature at the absorption edge (see Figure 4.32). This is also shown by recent Cu $L_{2,3}$ XANES results which also show a decrease in the density of unoccupied *d* states, upon alloying.[9] This indicates an increase of *d* charge at the Cu site. The loss of *d* electrons (as exhibited by the increase in whiteline intensity at the Au $L_{2,3}$ edges), and gain of conduction electrons (as exhibited by positive Mössbauer shifts), and the requirement that Au must gain overall charge (as required by electronegativity arguments) at the Au site, eliminates the possibility of the shifts being due to a gain of *s-p* like conduction charge at the Cu site. The differences found in the ordered and disordered samples will be discussed later.

By using Au $4f_{7/2}$ binding energy shifts (ΔE_{Au}) and the corresponding conduction (primarily 6*s*) charge flow (Δn_c) derived from Mössbauer isomer shifts, the 5*d* count depletion at the Au site (Δn_d) and the net charge flow (δ) can be obtained. The procedure used for determining Δn_d has been described in Chapter 3 and will only be outlined here. Simply stated, the shift in the Au 4*f* core levels is related to changes in the one-electron energy and the position of the Fermi level. The former is related to the Coulombic interaction of the core levels with both the valence 5*d* electron and the 6*s* conduction electron at the Au site in an alloy, and the net charge transfer in the

normalized atom scheme[2] (within the Wigner-Seitz volume of the Au atom), while the latter is related to work function changes. If we neglect any difference in final state screening effects (a reasonable assumption for a metallic system), and volume effects, the binding energy shifts can be expressed as:[2]

$$\Delta E_{\text{alloy-Au}} = -(\Phi_{\text{alloy}} - \Phi_{\text{Au}}) - \Delta n_c[F^0(4f,c) - F^0(4f,5d)] - \delta[F^0(4f,5d) - F(\text{latt})] \quad (5.1)$$

which is a rearrangement of Equation 3.5. The Φ's are the work functions, which, to the first approximation, represent the Fermi level shift relative to the vacuum upon alloying (values used for the various alloys were estimated by assuming a linear variation of Fermi shift with mole fraction; see Table 5.1). The F^0 terms are the Coulomb integrals associated with the removal of a conduction or *5d* electron and are estimated to account for the relaxation of the system in question. F(latt) is a Madelung-like potential energy associated with charge transfer in and out of the Wigner-Seitz volume and is evaluated by placing a charge at the Wigner-Seitz radius. The overall charge transfer is given by $\delta = \Delta n_c + \Delta n_d$. The conduction charge transfer, Δn_c, is given by Equation 3.9 using Mössbauer data given by the results of Huray *et al.*[10]

The analysis based on Equation 5.1 and the various parameters used are given in Table 5.1 and are shown schematically in Figure 5.1. As we increase the Cu composition there is an increase in the loss of *d* charge and also an associated higher loss of *d* charge for the ordered species. The loss of *d* charge varies from 0.05 for Au_3Cu to 0.22 for $Cu_{0.95}Au_{0.05}$ and the corresponding gain in *s* charge is 0.09 to 0.34. There is also a corresponding increase in the overall transfer of charge to the Au site in accord with electronegativity arguments. The ratio of ($\Delta nd/\Delta nc$), however, remains essentially

a constant in accord with previous observations.[4]

Compound	ΔE (Au $4f_{7/2}$) (±0.05 eV)	ΔΦ (eV)	Δn_c (charge count) ±0.005	Δn_d (charge count) ±0.005	δ (charge count) ±0.005	$\Delta n_d/\Delta n_c$
disordered Au_3Cu	0.06	-0.10	0.086	-0.047	0.039	-0.55
ordered Au_3Cu	0.06	-0.10	0.086	-0.047	0.039	-0.55
disordered AuCu	0.25	-0.21	0.189	-0.121	0.068	-0.64
ordered AuCu	0.31	-0.21	0.194	-0.131	0.063	-0.68
disordered Cu_3Au	0.24	-0.31	0.286	-0.166	0.121	-0.58
ordered Cu_3Au	0.37	-0.31	0.301	-0.192	0.110	-0.64
$Cu_{0.875}Au_{0.125}$	0.43	-0.36	0.327	-0.209	0.118	-0.64
$Cu_{0.95}Au_{0.05}$	0.47	-0.39	0.335	-0.215	0.120	-0.64

Table 5.1: Summary of the parameters derived from the XPS core level shifts and Mössbauer isomer shifts using Equation 5.1. Δn_c is given by Equation 3.9 and Slater integral values of -3.0 eV for $F^0(4f,c)$-$F^0(4f,5d)$ and 7.7±1 eV for $F^0(4f,c)$-F(latt) were used.

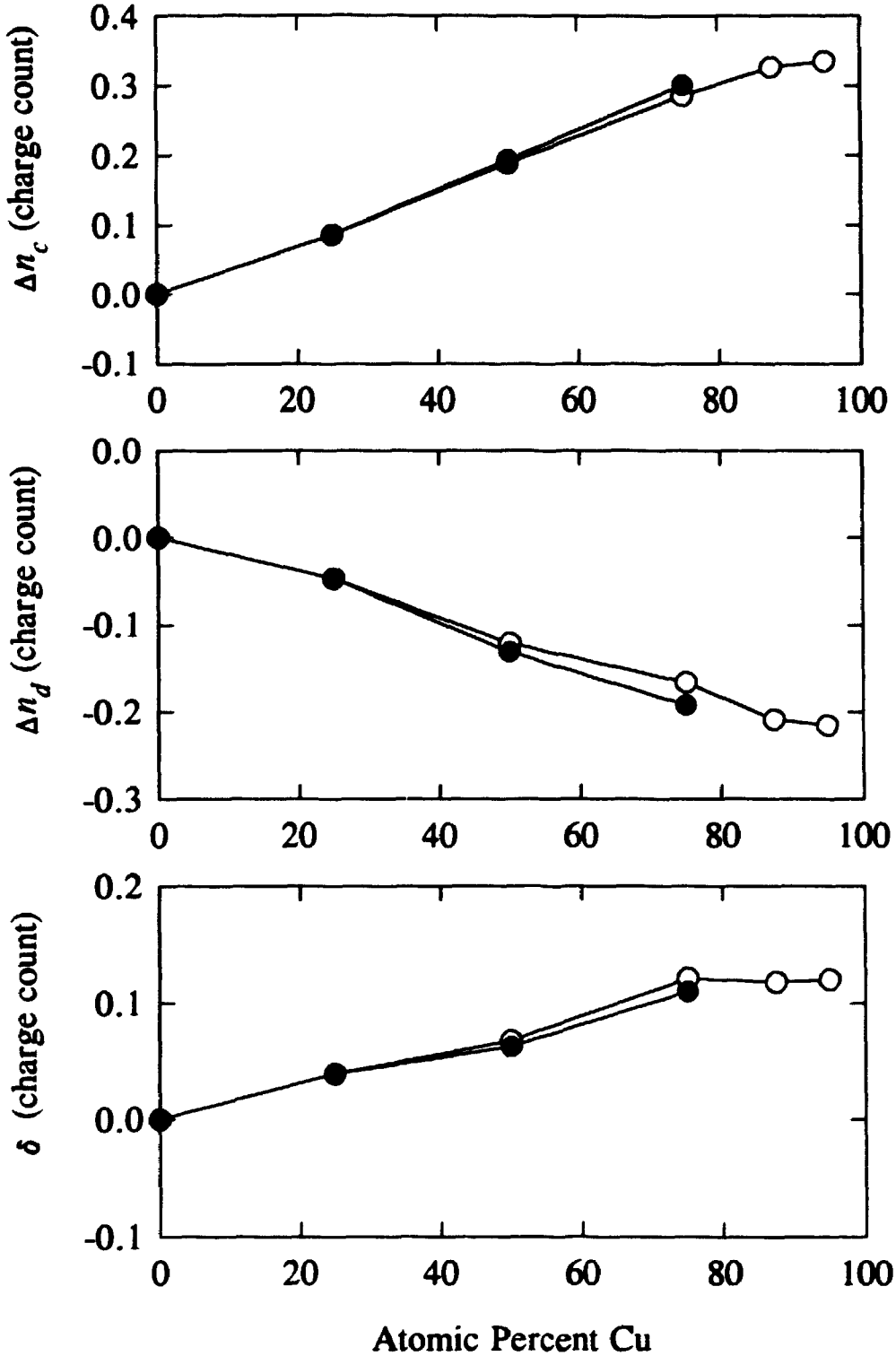

Figure 5.1: Comparison of the parameters used and derived from XPS and Mössbauer isomer shifts data (conduction charge transfer, *d* charge transfer, and overall charge transfer, all at the Au site) incorporated into a conventional charge transfer model. Hollow circles are used for the disordered species while filled circles are used for the ordered species.

5.3 Charge Redistribution, Valence band spectra, and Dilution

Examination of the centroid shifts of the *d*-band components in both the XPS and synchrotron valence band data lends support to the *d-d* repulsion model as outlined in Chapter One. We observe a large shift of the "Au" centroid away from the Cu and the Fermi level (Figures 4.12 and 4.16) The largest movement is that of the "Au $5d_{5/2}$" band. Accompanied with this is a smaller shift of the "Cu" centroid towards the Fermi level. This repulsive behaviour is typical for the Au-Cu system and has clearly been seen for two-dimensional Au-Cu alloys on Ru(001) as will be revealed later on. The photon dependent valence band emissions, as shown in Figure 4.16, clearly show that there is very little overlap between the "Au" and "Cu" contributions to the alloy valence band. By attenuating the Au *d*-band emission at 160 eV we can see the "Cu" contribution to the alloy valence band. The "Cu" region remains located at 2.5 to 4.5 eV below the Fermi level and no features are discernible for contribution to the alloy valence band in the region of 5 to 7 eV below. Unfortunately, the same type of photon dependent studies, to attenuate the Cu 3*d* emission could not be performed as this band does not have a Cooper minimum. However, the relative cross-sectional differences of Au 5*d* and Cu 3*d* were used to relatively enhance the Au *d*-band emission. In the top panel of Figure 4.16 we see that the Au *d*-band emission is located at 5 and 7 eV below the Fermi level. By overlapping the valence band spectra of the pure components we see a large overlap in energy for the pure Au $5d_{5/2}$ and Cu 3*d* bands at 3 eV below the Fermi level. Upon alloying, this strong interaction pushes the "Au $5d_{5/2}$" band away from the

"Cu 3*d*" band while the "Au $5d_{3/2}$" band, which has little or no initial overlap, remains relatively fixed. Along with dilution, this effectively reduces the apparent Au *d*-band splitting. Dilution of the Au-Au and Cu-Cu interactions, which occur upon alloying, also reduce the alloy *d*-band components widths. Although dilution can account for the narrowing of the *d*-band components, it does not account for the movement of the "Au $5d_{5/2}$" component away from the "Cu 3*d*" component, of which the centroid moves towards the Fermi level.

We next investigate the effect of charge redistribution on the XPS valence band behaviour. Assuming that the valence band features primarily separated *d* bands, as outlined above, a comparison of the change in the splitting of the "Au" portion of the alloy *d* band, $\Delta_{apparent}$(alloy), versus an empirically derived relationship:[11]

$$\Delta_{apparent}(\text{alloy}) = [(\Delta_{atomic})^2 + (\Delta_{electronic})^2]^{1/2} \qquad (5.2)$$

can be made (Figure 5.2). The apparent alloy *d*-band splitting, below 3 eV relative to the Fermi level, is assumed to be dominated by the Au *d* bands and is related to the convolution of two terms: an atomic Au 5*d* spin-orbit splitting term of 1.5 eV and an intrinsic band term. Using experimental values for pure Au (1.5 eV for the atomic splitting and the experimental value of 2.75 eV for the apparent splitting), the electronic band term is estimated to be 2.3 eV. For the series of alloys, Δ_{elec} is determined by using the pure Au value and the reduction of like nearest neighbours in the disordered alloy with the following relationship:[12,13]

$$\frac{\Delta_{elec}(\text{pure})}{\Delta_{elec}(\text{alloy})} = \frac{(N(\text{pure}))^{1/2}}{(N(\text{alloy}))^{1/2}} \qquad (5.3)$$

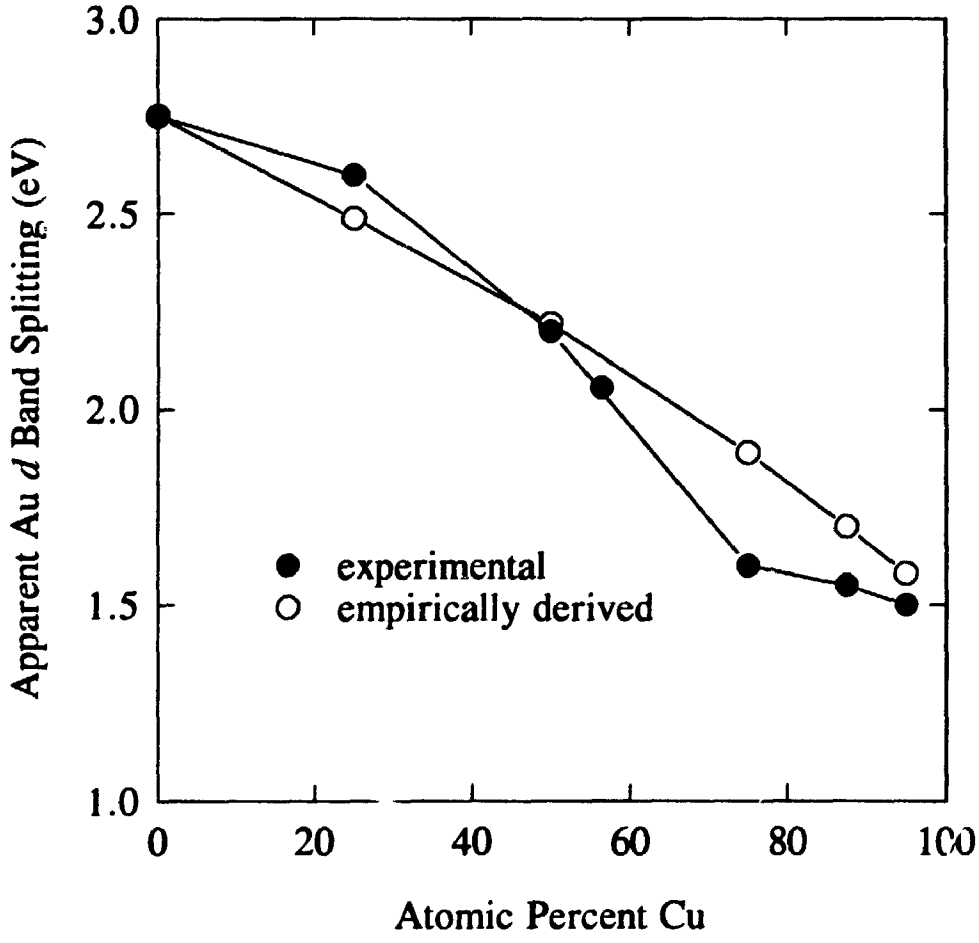

Figure 5.2: The experimental apparent "Au 5*d*" band splitting as compared with an empirically derived relationship based on a Au-Au dilution model.

This model assumes that little or no Au-Cu *d*-band mixing occurs and that the changes in the alloy *d*-band widths are a function of dilution only (i.e. dominated by Au - Au interaction). The relative movements, however, are dictated by the *d-d* repulsion model. For systems in which ordered and disordered states exist the nearest-neighbour values for the disordered state (statistical probability) only were used. To properly evaluate the ordered states we would have to include second-order effects i.e. the distribution in the second shell. For example, the ordered Cu_3Au system has 12 Cu nearest neighbours surrounding each Au site. This would lead to an atomic splitting parameter of 1.5 eV which is not the case as seen in Figures 4.12 and 4.16. Ordered Cu_3Au, however, has a larger than statistical number of Au next-nearest neighbours which may help in increasing the apparent splitting from the atomic value. In examining Figure 5.2, we see that the Au portion of the experimental *d*-band splitting correlates with the dilution model at low Cu compositions but deviates as the Cu composition is increased. A maximum deviation is observed for Cu_3Au. The experimental values of the splitting have a large error due to the low resolution of the spectra and the fact that at low Au compositions the emissions are very weak (see Figure 4.12).

The experimental alloy *d*-band width decreases linearly in the low Cu composition regime but falls off drastically once higher Cu compositions are reached ($\sim$90%, Figures 4.12 and 4.13). Again, there is a larger error in determining the width at high Cu compositions since Au is so dilute that the emission is quite weak and the onset of the band is harder to determine. Assuming that the "Au" and "Cu" components of the alloy *d* band are still valid we find, from Figure 4.12, that there is a reduction in the width of

the respective "Au" and "Cu" components as we reach higher compositions of unlike nearest neighbours (The "Au" width decreases going down Figure 4.12 while the "Cu" width reduces going up Figure 4.12).

No discernible differences are detectable in the valence band features between the ordered and disordered Au-Cu alloys from the XPS valence band spectra. The error in measurement is relatively large (± 0.1 eV) compared to possible changes that are present upon ordering. It can be argued that from the dilution model we would expect the apparent splitting and *d*-band width to be smaller in the ordered alloys since the ordered alloys have fewer Au nearest neighbours (features which are dominated by Au-Au interactions). However, the ordered alloys do have a larger number of Au next nearest neighbours and thereby second-order effects may contribute to maintaining both the *d*-band width and apparent splitting. High resolution is needed to resolve these small differences. The higher resolution synchrotron valence band data did possibly indicate a small narrowing of the Cu_3Au order sample at a photon energy of 60 eV. However, because of the high surface sensitivity at kinetic energies of 50 to 60 eV (as shown by the electron escape depth curve in Figure 2.4) care must be taken due to possible surface segregation of one or the other constituent giving a surface valence band contribution which is not characteristic of the bulk. Scanning Auger microscopy studies on Cu_3Au order and disorder do show a substantial difference in the surface ratios of Au and Cu (Figure 5.3).

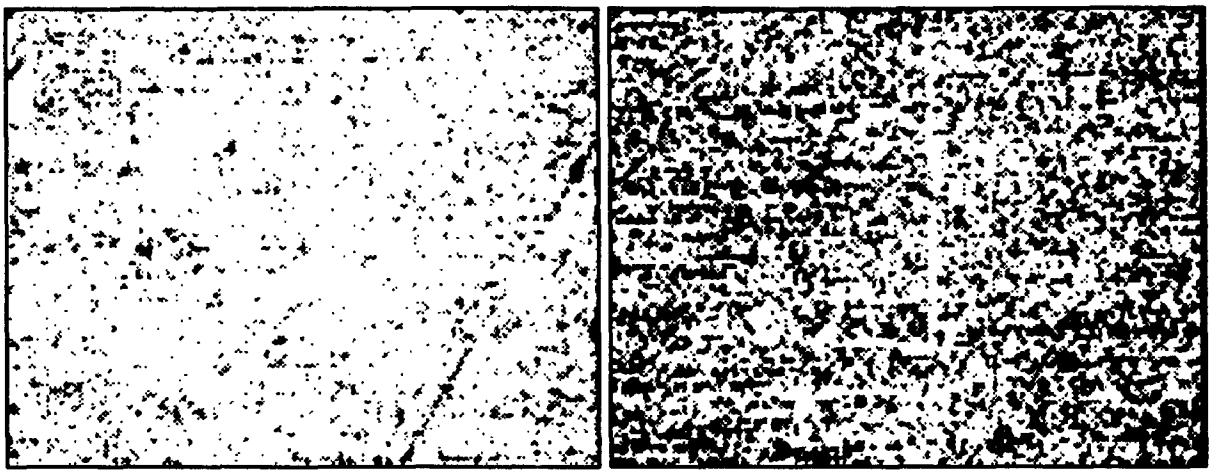

disordered Cu_3Au: Au Cu

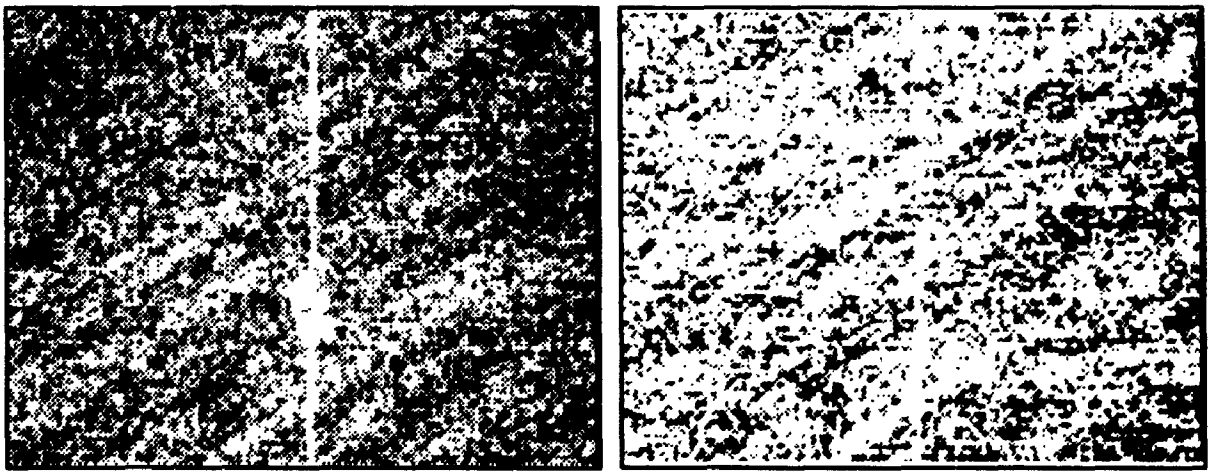

ordered Cu_3Au: Au Cu

Figure 5.3: Scanning Auger Microscopy images showing the surface layers of ordered and disordered Cu_3Au. The Au and Cu images for disordered Cu_3Au are shown in the top left and right, respectively, while Au and Cu images for ordered Cu_3Au are shown in the bottom left and right, respectively.

5.4 XANES (X-ray Absorption Near Edge Structure) and Au 5*d* Hole Count

In Chapter 3 a method was developed to use the whiteline areas of the X-ray absorption near edge spectrum to quantify the *d* hole count in the system of interest which was originally Pt. This method will be extended through a series of approximations to be used for the Au $L_{2,3}$ edges in a series of Au-Cu alloys. In Chapter 4 it was noted that an absolute determination of the whiteline area would be hard to accomplish due to the fact that the contribution of the *s* unoccupied states are hard to simulate. Since we are concerned with the electronic changes that occur upon alloying, it is more appropriate to relate the whiteline areas to that of pure Au and thereby, not only do we account for the *s* contribution, but we also have all the parameters relative to pure Au (i.e. the effect of alloying).

Therefore, using Equations 3.17a and 3.17b we relate the area of the whiteline to the difference between the absorption coefficient of the alloy and pure Au. The areas thus derived from our experimental data can be expressed as:

$$A_2 = \int [\mu_{L_2}(\text{alloy}) - \mu_{L_2}(\text{Au})]dE \tag{5.4a}$$

$$A_3 = \int [\mu_{L_3}(\text{alloy}) - \mu_{L_3}(\text{Au})]dE \tag{5.4b}$$

The area is related to the change in *d* hole counts (Δ) by:

$$A_2 = C_0 N_0 E_2 (R_d^{2p_{1/2}})^2 (\frac{\Delta h_{3/2}}{3}) \tag{5.5a}$$

$$A_3 = C_0 N_0 E_3 (R_d^{2p_{3/2}})^2 \left(\frac{6\Delta h_{5/2} + \Delta h_{3/2}}{15}\right) \tag{5.5b}$$

where $C_0 = 4\pi^2\alpha/3$ (α is the fine structure constant), N_0 is the density of Au atoms, $E_{2,3}$ are the absorption edge energies and the R term is the radial dipole integral. If, in the first approximation, we let the radial dipole-moment integral for the two excitation processes be the same we can, after some manipulation, derive the relationship between the change in hole counts, relative to pure Au, to the whiteline areas:

$$\Delta h_{5/2} = \frac{1}{2C}\left(5\frac{E_2}{E_3}A_3 - A_2\right) \tag{5.6a}$$

$$\Delta h_{3/2} = \left(\frac{3A_2}{C}\right) \tag{5.6b}$$

where

$$C = C_0 N_0 E_2 (R_d^{2p})^2$$

To quantify the change in d hole counts a measurement must be made of the dipole matrix element. Unfortunately the matrix element for the $2p \rightarrow d$ dipole transition for Au has not been calculated and in the first approximation the calculated value for Pt (3.103×10^{-11} cm) will be used. This can be justified by comparing both predicted and experimental whiteline areas for Pt and Au pure metals.[14]

$$A_{expt} = A_{3(expt)} - aA_{2(expt)} \tag{5.7a}$$

$$A_{theor} = A_{3(theor)} - aA_{2(theor)} \tag{5.7b}$$

Here a is an experimental normalization parameter required to line up the intensity of the

Au L_2 edge beyond the whiteline area with the Au L_3 edge. For Pt the value of a is 2.25 while it is 2.20 for Au. Figure 5.4 shows the resultant difference spectra after normalization. The experimental area, A_{expt}, was found to be 0.28×10^4 cm^{-1} eV. This area was determined[15] by taking the experimental derived area from the normalized spectrum (1.38 atom eV) and multiplying it by the edge jump absorption coefficient of a Au atom at the Au L_3 edge (105.3 cm^2 g^{-1})[16] and the density of Au (19.3 g cm^{-3}). Using the calculated d hole counts for Au from Mattheiss and Dietz ($h_{5/2}$=0.283, $h_{3/2}$=0.118) and the dipole matrix element of Pt (3.103×10^{-11} cm) the theoretical area, A_{theor}, was found to be 0.20×10^4 cm^{-1} eV. Similarly, Mattheiss and Dietz found values of A_{expt} and A_{theor} to be 1.86×10^4 cm^{-1} eV and 1.57×10^4 cm^{-1} eV for Pt, respectively. Given that the experimental/theoretical ratio is similar for both Au and Pt, the use of the Pt dipole matrix element for calculations involving Au is reasonable in the first approximation. The differences between the calculated and theoretical areas can be attributed to errors in the calculated matrix element and d hole counts, and the assumption that the matrix element for the two excitation processes are the same. Errors are also involved, again, in determining the onset of the Fermi level. For lining up the Au $L_{2,3}$ edges, we have opted to calibrate the inflection points, since the unoccupied density of d states is not localized at the Fermi level due to hybridization.

Returning to Equations 5.6a and 5.6b, having determined a reasonable value for the matrix element, we use the Au atomic number density of 5.894×10^{22} atoms cm^{-3}, and the L_2 edge energy of 1.373×10^4 eV, to get C = 7.484×10^4 cm^{-1} eV.

To normalize our data and incorporate the appropriate units (cm^{-1} eV), the

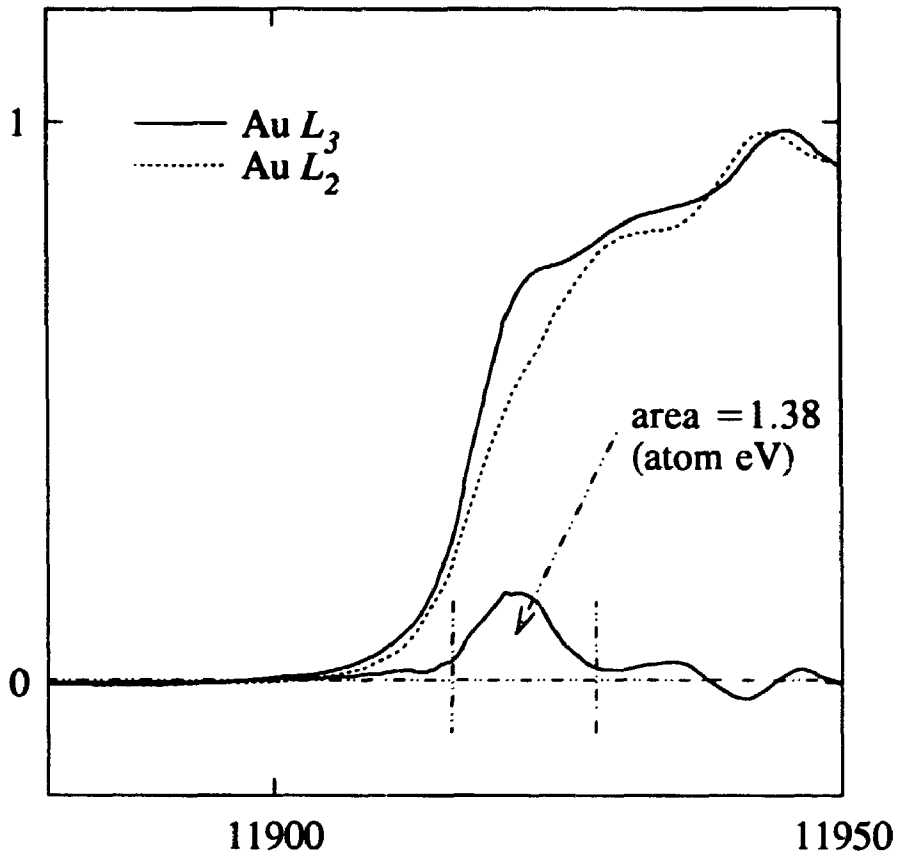

Figure 5.4: Difference spectrum of the pure Au $L_{2,3}$ edges. The intensities were normalized by multiplying the L_2 spectrum by 2.2 and the spectra calibrated by lining up the inflection points. The area of the difference spectrum was calculated by integration between the points specified on the spectrum.

integrated areas determined from the experiment (Table 4.2 in units of atom eV) must now be multiplied by the edge jump absorption coefficient of a Au atom for each respective edge ($cm^2 g^{-1}$)[16] and the density of Au (g cm^{-3}). From the multiplicity of the initial states we expect a ratio of 2 to 1 in edge heights, yet experimentally the ratio is found to be 2.2 to 1, and reported in the tables McMaster *et al.*.[16] as 2.1 to 1. The difference can be explained by the fact that we have assumed both transition dipole moments to have the same value. Therefore, to directly compare the derived areas from the L_2 and L_3 spectra, we have scaled the $\Delta\sigma$ values (edge jump coefficients) to reflect the experimental ratio, arbitrarily selecting the smaller Au L_2 value to adjust.

The calculated areas and hole populations are given in Table 5.2. Figure 5.5 summarizes the trends shown by the previous calculations. As we increase the Cu composition, that is, Au becomes more dilute, there is a large increase in the total hole count which slows as higher compositions of Cu are reached. The ordered samples consistently have higher hole counts than their disordered counterparts. The total change in hole count relative to pure Au varies from 0.02 for Au_3Cu to 0.18 for $Cu_{0.95}Au_{0.05}$. It can also be seen that there is a larger contribution to the total hole count from the $h_{5/2}$ states than from the $h_{3/2}$ states and that the higher total hole counts for the ordered samples arise directly from increased number of $h_{5/2}$ states.

Compound	A_3 (cm^{-1} eV)	A_2 (cm^{-1} eV)	$\Delta h_{5/2}$	$\Delta h_{3/2}$	Δh_t	h_t	$\Delta h_{5/2}/\Delta h_{3/2}$	$h_{5/2}/h_{3/2}$
disordered Au_3Cu	0.050	0.008	0.019	0.004	0.022	0.423	3.50	2.48
ordered Au_3Cu	0.050	0.015	0.018	0.006	0.024	0.425	2.33	2.43
disordered AuCu	0.162	0.041	0.060	0.017	0.076	0.477	2.55	2.54
ordered AuCu	0.264	0.043	0.099	0.017	0.116	0.517	4.22	2.83
disordered Cu_3Au	0.282	0.073	0.104	0.029	0.133	0.534	2.60	2.63
ordered Cu_3Au	0.339	0.091	0.125	0.036	0.161	0.562	2.53	2.65
$Cu_{0.875}Au_{0.125}$	0.348	0.113	0.126	0.045	0.171	0.572	2.00	2.51
$Cu_{0.95}Au_{0.05}$	0.388	0.084	0.144	0.034	0.178	0.579	2.82	2.81

Table 5.2: The table lists the results of the Au $L_{2,3}$ edge XANES analysis. Parameters used in the calculation are listed in the text. The h_j values are determined by $h_j = h_f(\text{Au}) + \Delta h_j$ where the h_j values are calculated by Mattheiss and Dietz. Uncertainty in change of hole counts is $\pm 5\%$.

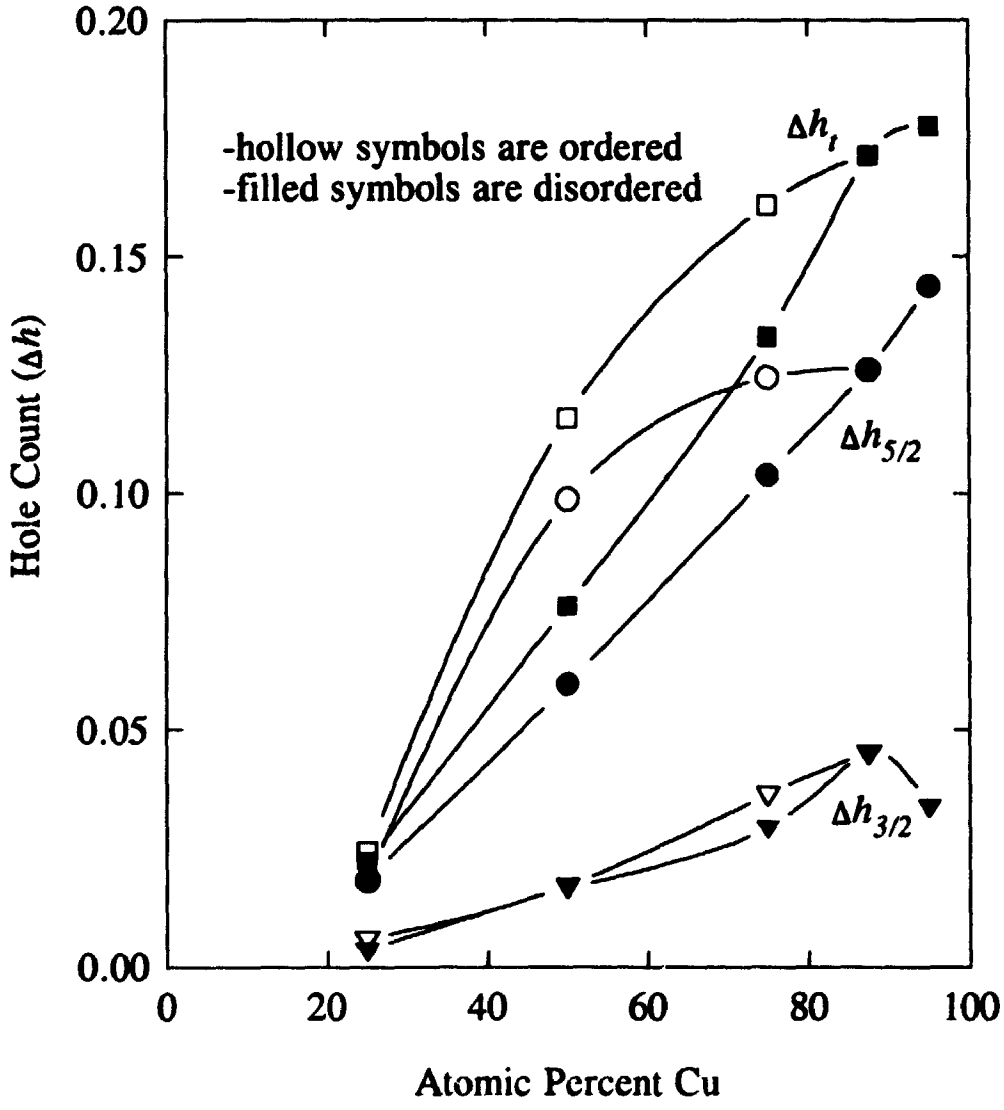

Figure 5.5: The *5d* hole count at the Au site as determined by the XANES analysis for the various Au-Cu alloys. We note the larger contribution of the $h_{5/2}$ states and the larger overall hole counts for the ordered species.

5.5 Determination of Change in *d* Character at the Cu Site by Resonant Photoemission and Cu *K* Edge XANES

For most of this study the focus has been on the electronic changes, upon alloying, that occur from the Au perspective. This is largely due to the greater amount of data that are available from the Au site. In this section we will concentrate on determining the change in *d* character via two different methods, resonant photoemission and Cu *K* edge XANES.

Resonant photoemission was carried out by varying the photon energy across the Cu 3*p* threshold to see what occurs to a previously reported valence band satellite structure which was thought to be of atomic origin.[17,18,19,20] Figures 4.14 and 4.15 give the results for pure Cu and Cu_3Au, respectively. For the pure Cu we observe two satellite peaks at 75.5 eV corresponding to the ^1G and ^3F of a d^8 configuration, consistent with the results of M. Iwan *et al.*.[17] They describe the resonant satellite by a quasiatomic shakeup involving two correlated 3*d* holes plus a low-lying excited *nl* electron in the final state. Off-resonance the two-hole excitation (shake-up) occurs in the following way:

$$3p^6(3d^{10})4s^1 + h\nu \rightarrow 3p^6(3d^8nl)4s^1 + e^- \qquad (5.8)$$

At the Cu 3*p* threshold we have an additional excitation channel and Auger decay which yields the same final state:

$$3p^6(3d^{10})4s^1 + h\nu \rightarrow 3p^5(3d^{10}nl)4s^1 \rightarrow 3p^6(3d^8nl)4s^1 + e^- \qquad (5.9)$$

A resonance occurs leading to an enhancement at the Cu 3*p* threshold which manifests

as a resonance in the constant initial state (CIS) plot of the photoemission spectra. Experiments performed by Chandesris *et al.*[19] on Cu vapour show a resonance effect with about 15% intensity of the main 3*d* line similar to the results produced for solid Cu by Iwan *et al.*[17]

The resonant satellite has been used to probe chemical changes. For example, results obtained by Iwan *et al.*[18] on Cu phthalocyanine show a resonance intensity of 40%. This, they argued, shows the importance of more empty 4*s* levels while Chandesris *et al.* argued that the ground state configuration of Cu in this case must have some $3d^9$ component and that the enhancement is partially due to more unoccupied *d* states. In spite of this minor disagreement, it is accepted that the resonance effect is atomic-like in nature.

Since the resonance effect at threshold is dependent upon a $p \rightarrow nl$ transition, the availability of appropriate *nl* states will lead to an increase or reduction in the intensity of the resonance. Using the dipole selection rule, $\Delta l = \pm 1$, the amount of unoccupied *s* and *d* character will determine the resonance intensity with the unoccupied *d* states having a greater effect since the matrix element for that transition will be higher than for the transition to unoccupied *s* states.

Using the charge compensation model we can apply this technique to Au-Cu alloys with the prediction that, relative to pure Cu, Au-Cu alloys should experience a decrease in the resonance due to a decrease in unoccupied *d* character from charge transfer, although this may be compensated somewhat by an increase in the unoccupied *s* character, again due to charge transfer. For both the pure Cu and ordered Cu_3Au we

obtain a resonance intensity relative to the main Cu 3*d* line of 15 ± 5%. These observations indicate that the resonant satellite intensities, with their large experimental uncertainties (as shown by Figures 4.14 and 4.15), are not very sensitive to small changes in *d* character (and also, less importantly, *s* character) at the Cu site, upon alloy formation.

These small changes, though, are readily detectable by the Cu *K* edge XANES (Figure 4.32) which indicate an increase of *d* character at the Cu site, upon alloy formation, and also an increase in *d* character of the ordered samples as compared to their disordered counterparts. These results show how powerful the XANES technique can be in determining small electronic changes which are not readily detectable by photoemission techniques. One reason for this is the low signal to noise ratio of the XANES technique when performed in the transmission mode. If the samples could not be prepared to a thickness close to an absorption length then the experiment must be performed in either fluorescence or electron yield mode. The fluorescence mode also gives a good signal to noise ratio while the electron yield mode has a much larger background noise. Photoemission also has a larger signal-to-noise ratio.

5.6 Correlation of XANES Au *d* holes (Δh_t) and Mössbauer Isomer Shifts

Using the change in total hole count, Δh_t, derived from XANES analysis and Mössbauer isomer shifts we can establish the relationship between 6*s* gain and 5*d* depletion at the Au site. One of the important uses of Mössbauer results is to correlate the isomer shift (relative to pure Au) with changes in electronic structure.

The following analysis will use the Au 5*d* hole count derived by XANES analysis as an independent verification of the contribution of the Au 5*d* charge transfer to Mössbauer isomer shifts and provide further verification of the charge compensation model.

Taking into account all possible contributions, the ^{197}Au isomer shift or change in contact density at the nucleus, upon alloy formation, can be empirically expressed as:

$$IS \propto a\Delta n_s + b\Delta n_d + d\Delta n_p \tag{5.10}$$

where Δn_s is the change in the number of 6*s* electrons, Δn_d is the change in the number of *d* electrons and is included since the effective potential experienced by s electrons varies with the change in the number of *d* electrons which have a high screening ability and this effect cannot be ignored as shown in Chapter 3, and Δn_p is the change in the number of *p* electrons. The term, Δn_p, can be ignored because of its modest contribution in hybridization and its ambivalent contribution in $p_{1/2}$ contact density and screening and the fact that overall its screening ability is much smaller than for *d* electrons ($\Delta n_p << \Delta n_s$). The isomer shift and Δn_c ($\sim \Delta n_s$) are related by the empirical equation Δn_c

= 0.086 x IS for intermetallic systems. In Figure 5.6 we have plotted the isomer shift versus the *d* hole count and observe a linear relationship. The line does not go through zero but, as will be explained shortly, the XANES derived *d* hole counts are most likely slightly underestimated and have a larger error at low Cu concentrations (low hole counts). If the *d* hole values are underestimated by a constant 10-15% then the correlation line will go through zero and with a larger error for the low values the underestimation may be only 10%. By comparison of the values obtained for Δn_d and the independently-derived values for *d* hole counts, Δh_t, (Table 5.2) we are able to substitute the *d* hole values for Δn_d ($\Delta n_d \sim -\Delta h_t$). Since both Δn_d and Δn_c vary linearly with the isomer shift we can set the ratio of the two to be a constant. To maintain electroneutrality, that is required for metallic systems, we note that Δ and especially δ must be small as is seen in our case with values no higher than 0.3 and 0.1, respectively. Therefore, if we let $\Delta n_d/\Delta n_c$ = c and substitute for IS we can express IS in terms of Δn_c:

$$IS = a\Delta n_c \quad (cb)\Delta n_c = \Delta n_c(a+cb) \tag{5.11}$$

but Δn_c = 0.086 x IS, therefore:

$$a+cb = 11.63 \tag{5.12}$$

We can also substitute for Δn_c, into the original equation, where we can express IS in terms of Δn_d:

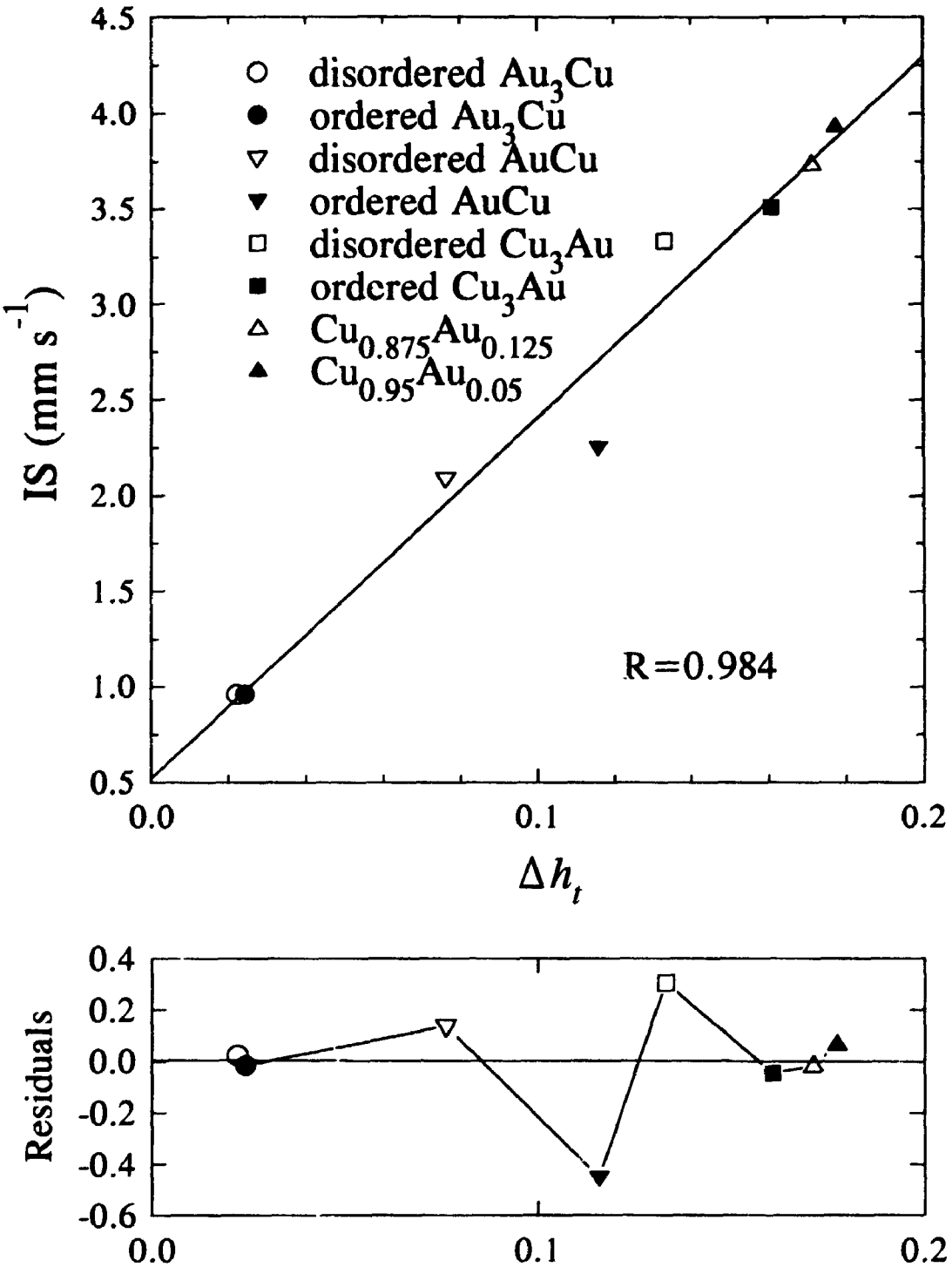

Figure 5.6: Comparison of the Mössbauer isomer shift with the hole count derived by the XANES analysis. The residuals are given in the bottom panel. The R value is the correlation coefficient as determined by a linear regression.

$$IS = \Delta n_d \left(\frac{a}{c} + b\right) \tag{5.13}$$

From the plot of IS versus Δh_t (Figure 5.6) the slope was determined to be 18.9 therefore:

$$\frac{(a + c \times b)}{c} = -18.9 \tag{5.14}$$

Substituting Equation 5.12 into Equation 5.14 we get:

$$c = \frac{\Delta n_d}{\Delta n_c} = -0.62 \tag{5.15}$$

Thus, for the Au-Cu system, we have determined the ratio of *d* charge versus *s* conduction charge transfer to be -0.62. This value is in good accord with the $\Delta n_d / \Delta n_c$ ratios given in Table 5.1 and is also consistent with values previously seen for a variety of Au intermetallics.[4] Since this result has been independently arrived at through analysis using Mössbauer and XANES results it further confirms the charge compensation model.

5.7 Comparison of Au 5*d* Hole Counts Derived from XPS-Mössbauer and XANES and Comparison with Valence Band Features

It is interesting to compare the change in *d* counts derived from these two methods. Both methods give the same trend for the hole values with the numbers derived from the XANES analysis consistently giving slightly lower values (Tables 5.1 and 5.2 and Figure 5.7). For the estimation of the *d* charge transfer, as determined by core level shifts and Mössbauer isomer shifts, there is uncertainty in the Coulomb integral values (see Table 5.1) and the work functions; and it must also be taken into account that the XPS core level shifts may also introduce uncertainty since XPS is sensitive to contributions from the surface layer in terms of surface segregation. Scanning Auger studies of the polycrystalline Cu_3Au samples have clearly shown different surface ratios of Au and Cu for the ordered and disordered species (less clear for the AuCu and Au_3Cu alloys). Also, XANES spectra, which are not surface sensitive, clearly show a large difference between the two AuCu samples in their whiteline areas but this is not reflected as clearly by the experimental Au 4*f* core level shifts. Yet, when examining Figure 5.7, it is clear that there is a strong correlation between the XPS-Mössbauer derived hole counts with the bulk values derived from the XANES analysis. It can be understood, however, that even though the XPS core level shifts may be slightly skewed by surface segregation, these shifts are small as compared to errors associated with work function and Coulomb integral values as the latter are dominant terms (see values in Table 5.1). The values determined by the XANES analysis are likely to be

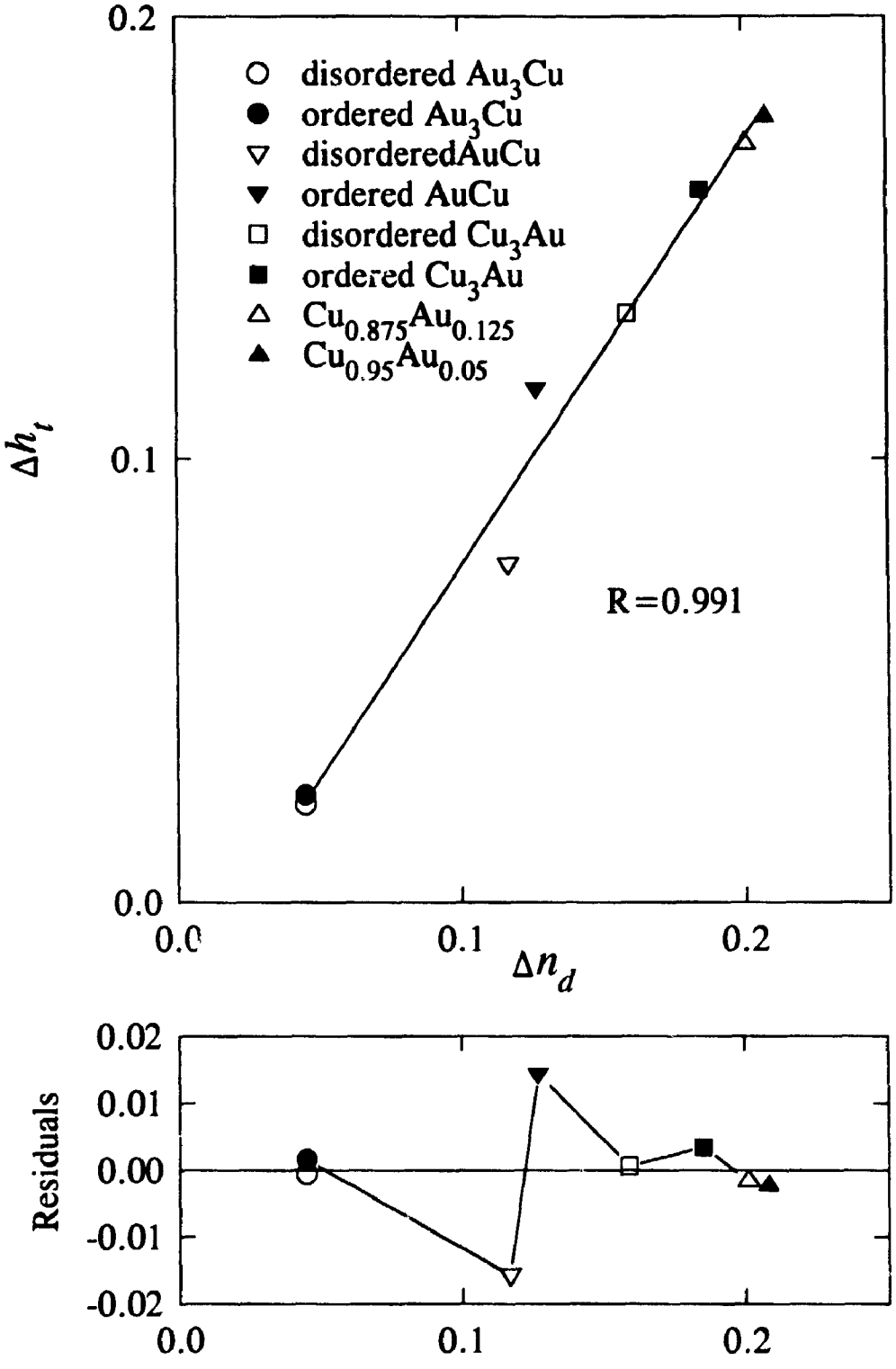

Figure 5.7: Comparison of the *d* hole count derived from the XANES analysis to that derived from XPS and Mössbauer core level shifts. The residuals are given in the bottom panel. The R value is the correlation coefficient as determined by a linear regression. The intercept is -0.021.

slightly underestimated because of uncertainty in the transition matrix element and because of omission of some of the dispersed unoccupied *d* states above the Fermi level by limiting the analysis to 15 eV above the edge. The difference spectrum of the pure Au L_3 and L_2 edges (Figure 5.4) shows the distribution of unoccupied states of *d* character which appears concentrated within about 20 eV above the edge. We have limited the analysis to 15 eV to include lifetime contributions ($\sim$8 eV for the L_3 edge of Au),[21] unoccupied *d* hole distribution and photon resolution, but to avoid including features attributed to multiple scattering effects and therefore have not included a portion of the tail of the distribution. This, of course, assumes that the alloy *d* states have a similar distribution and that upon alloying the centroid of the distribution does not shift higher by more than a few eV (Our data does indicates a more localized distribution of empty *d* states from the relative intense whiteline as compared to the pure Au sample.). This underestimation and the larger errors in the small hole counts could easily compensate for the correlation of the two methods to go through zero. It must also be stated, that the absolute values for *d* hole counts are not as necessary as examining the trend, relative to the pure components, for determining the electronic behaviour upon alloying.

Overall, the XANES results independently confirm the charge compensation model. However it is expected that the XANES analysis will give closer to true values since this analysis is derived from first principles and contains fewer assumptions and closer estimations of those values which cannot be directly determined, while the formula, Equation 5.1, based on Mössbauer and Au 4*f* binding energy shifts for elucidating *d* charge transfer has large uncertainties in all its parameters (see Table 5.2).

In addition, XANES results show that not only is the total hole count important but also the ratio of the $d_{5/2}/d_{3/2}$ unoccupied densities of states and the ratio of these states to the total hole count change upon alloying. The unoccupied d states have a non-statistical ratio considerably higher than the statistical ratio. For example, the $\Delta h_{5/2}/\Delta h_{3/2}$ ratios (Table 5.2) varies between 2 and 4 and are much higher than the statistical value of 1.5. Also, if we include the calculated distribution of d holes in pure Au,[22] we get a $h_{5/2}/h_{3/2}$ ratio that varies between 2.4 and 2.8. The answer lies in taking a look at the alloy valence band from a chemical perspective. The valence band for all the alloys show that the $5d_{5/2}$ band lies about 2.3 to 3.0 eV closer to the Fermi level than the $5d_{3/2}$ band due to the apparent d-band splitting. The Au $5d_{5/2}$ band also overlaps strongly with the Cu $3d$ band. The strongest interaction and mixing of states involve those overlapping in energy and closest to the Fermi level. In this case this involves the Au $5d_{5/2}$ and the Cu $3d$ electrons and for this reason we may expect a proportionally larger loss of Au $5d_{5/2}$ electrons to the Cu site and thereby a non-statistical ratio of d hole states. This change in d hole count is less evident in the occupied density of Au $5d$ states since we are talking about, in the most extreme case, the loss of approximately 0.2 electrons from a band originating from about 10 electrons per atom. This indicates the higher chemical activity of the Au $5d_{5/2}$ over the Au $5d_{3/2}$ band. The Au-Cu interaction can also be viewed as the disruption of the Au-Au interaction.

It is also interesting to compare the XANES derived d hole counts with other parameters derived from the XPS analysis, namely alloy d-band width and apparent d-band splitting (Figure 5.8). In previous analysis the d-band width and splitting did not

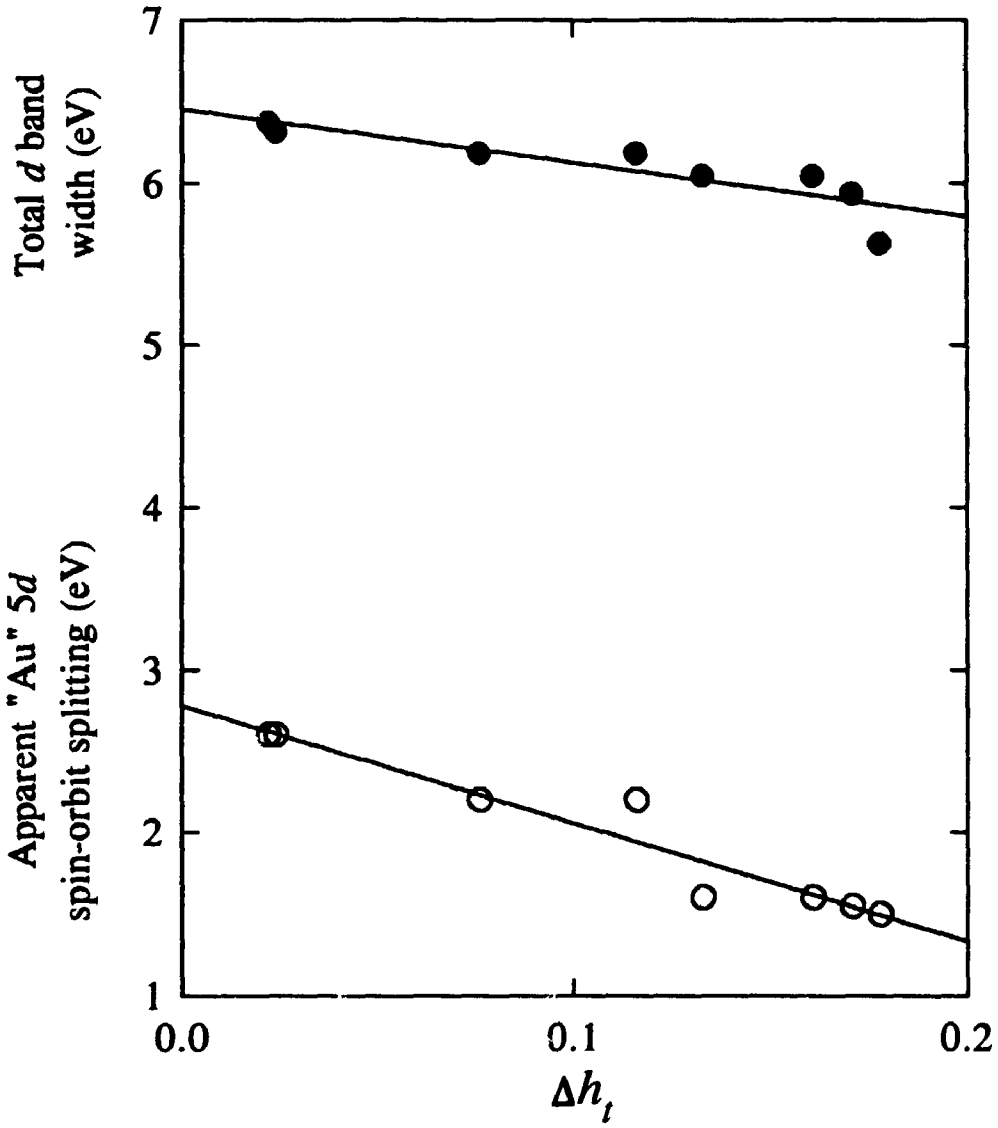

Figure 5.8: Comparison of the XANES derived hole count with the experimental alloy *d*-band width (top) and apparent "Au 5*d*" band splitting (bottom) for the Au-Cu alloy series. Both comparisons have been fitted with a linear regression; the top has a correlation coefficient of 0.874 with an intercept of 6.46, the bo.. m has a correlation coefficient of 0.952 with an intercept of 2.78.

correlate that well with compositional changes (see Figure 4.13). Yet, when these parameters are plotted against the *d* hole count there is a strong linear dependence, especially for the disordered species. A line of best fit was calculated and extrapolated to Δh_t equal to zero (corresponds to pure Au). The calculated values of *d*-band width and splitting for pure Au compare favourably with the experimental values, 6.46 versus 6.44 eV, and 2.78 versus 2.75 eV, respectively. This relationship shows the interplay between *d* charge transfer and the dilution model with which the "Au" 5*d* splitting and alloy *d*-band width changes are rationalized.

5.8 Charge Redistribution and the Local Structure at the Au Site

To examine these results more quantitatively the structures of these alloys and the interatomic distances must be taken into account. We could use the interatomic distances and nearest-neighbour distributions as determined by the EXAFS analysis of Chapter 4, however, as was shown there are distortions in the local site in the nearest shell distances and errors involved in the absolute numbers for the nearest shell configuration. We have shown, however, that our results correspond closely to a comprehensive X-ray crystallography study[23] and that the Au/Cu ratios in the nearest shell are accurate throughout the compositional range, and especially between the respective ordered and disordered samples. Leaving aside the ordered species, the disordered alloys exhibit changes in average nearest-neighbour distribution and distances with changing composition. In the disordered fcc structure of Cu_3Au, Au has an average of nine Cu neighbours with a lattice parameter of 3.754 Å.[23] In the disordered fcc structure of AuCu, Au has an average of six Cu neighbours with a lattice parameter of 3.874 Å.[23] In the disordered fcc structure of Au_3Cu, Au has an average of three Cu neighbours with a lattice parameter of 3.983 Å.[23] In examining Figure 5.5 it is clear that a linear relationship exists between the XANES derived hole counts and the number of nearest Cu neighbours (reflected by the percentage of Cu), for the disordered species and the dilute Au species. This relationship has been suggested previously.[24] This is evident in the total hole counts and especially the contribution from the $d_{5/2}$ hole counts. The $d_{3/2}$ counts show a deviation from linearity which is probably due to a larger error associated

with the much smaller values. From these observations it is not yet clear what role the change in number of Cu neighbours and the changing distances play in charge redistribution. It can be stated that the decrease in interatomic distance seems to play a less important role than the coordination number of Au and Cu nearest neighbours: the latter is in line with electronegativity arguments. In addition, the increase in hole counts is linear upon increasing Cu composition (thereby the number of Cu nearest neighbours) and the hole count is not increased further by a smaller Au-Cu distance. This can easily be clarified by comparing these results to the respective ordered species.

The lattice parameters for the ordered counterparts of Cu_3Au, AuCu, and Au_3Cu are 3.747 Å, 3.865 Å, and 3.980 Å,[23] respectively, which is, comparatively, a small reduction from the disordered species. Yet, when examining the experimental data, there are large differences exhibited between these species in terms of XANES measurements, Mössbauer isomer shifts, and XANES and XPS derived *d* hole counts. Smaller changes are noted for core level shifts and no changes can be observed in *d*-band width and splitting because of our experimental resolution. Figure 5.5 shows a large deviation from linearity, for the ordered species, which is not associated with a reduction in Au-Cu distance, but must be associated with a large change in the immediate environment of Au. For ordered Cu_3Au, Au has twelve Cu neighbours in the first shell as compared to nine for disordered Cu_3Au. For ordered AuCu, Au has eight Cu neighbours in the first shell as compared to six for disordered AuCu. Finally, for ordered Au_3Cu, Au has four Cu neighbours in the first shell as compared to three for disordered Au_3Cu. In examining Figure 5.5 an estimation of the number of nearest Cu neighbours for the

ordered species can be determined by their hole counts (Figure 5.9). By extending the total hole count across to intercept a straight line that best fits the disordered and dilute Au species the number of Cu nearest neighbours for the ordered species can be read off (i.e. 25% Cu corresponds to 3 Cu neighbours and 75% Cu corresponds to 9 Cu nearest neighbours). For Au_3Cu and AuCu the estimate corresponds very well to the actual local Au environment. The exception is Cu_3Au which has 12 Cu neighbours but has a lower hole count than the dilute Au species. Second-order effects come into play as the dilute Au samples have a higher number of Cu next nearest neighbours (reducing the Au-Au interaction) than Cu_3Au which has 6 and also interatomic distances may play a more important role since the fcc structure for these alloys is that of pure Cu.

The ordered and disordered Au_3Cu samples exhibit the same XAFS spectrum and have almost the same hole count, within experimental error, via both analysis methods. They also exhibit no difference in core level shifts. We cannot, however, conclude upon annealing the disordered sample at 463 K for two weeks, that it did not undergo a phase transition to the ordered state. With the highly concentrated Au samples, small changes to the number of Cu nearest neighbours (4 Cu neighbours for the ordered state versus 3 Cu neighbours for the disordered state) and Au nearest neighbours (8 versus 9), will not have a great effect on either the near edge absorption nor the core level shifts.

The order and disorder AuCu samples show large differences in *d* hole counts. Cu *K* edge XANES spectra clearly show that the annealed sample has a higher occupied Cu 3*d* count (i.e. a gain of *d* charge at the Cu site because of increased Au-Cu interaction) and preliminary EXAFS analysis (Figure 3.6) indicates a longer range order

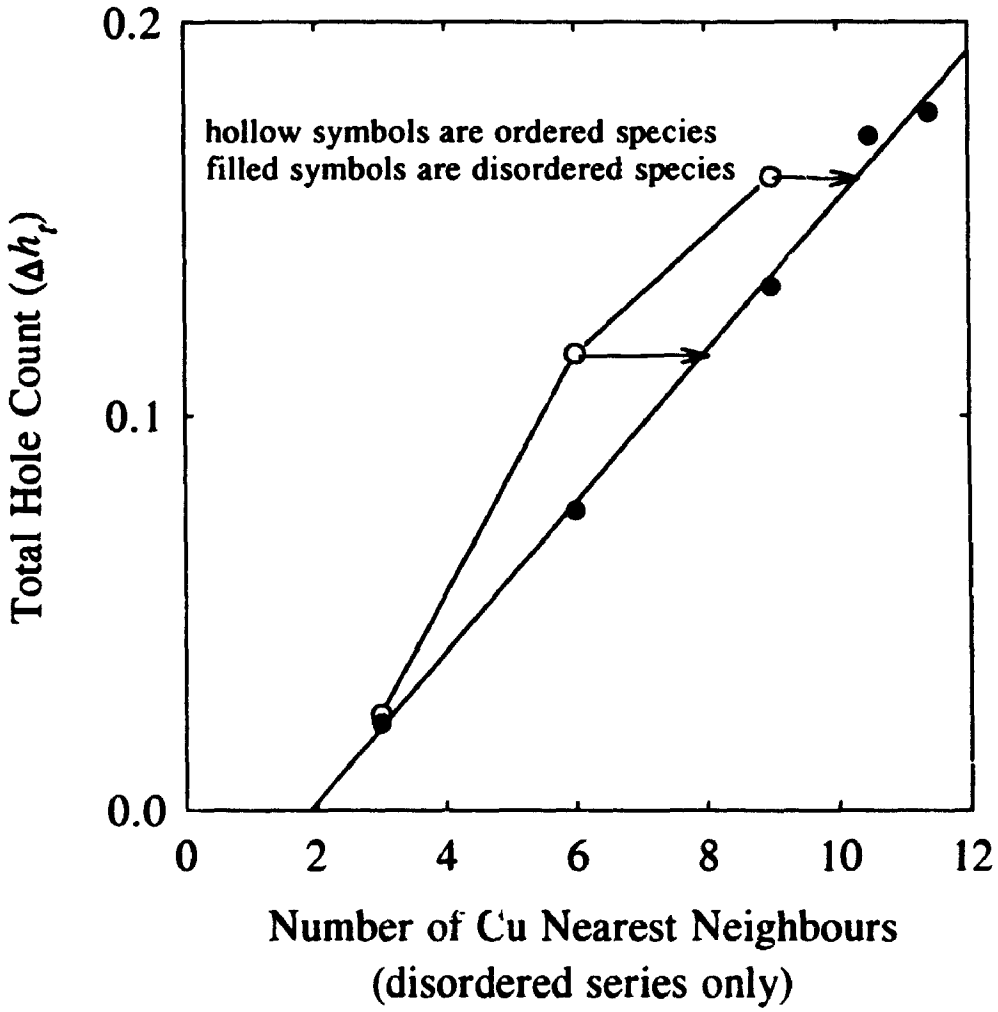

Figure 5.9: Comparison of the total hole count from the XANES analysis with the Cu nearest-neighbour distribution. A linear regression, for the disordered series only, was calculated with a correlation coefficient of 0.998 with an intercept of -0.036. The arrows indicate where the values for the ordered species would intercept the line of best fit.

exhibited by the annealed sample. The core level shifts are also consistent, qualitatively, but the difference between the two samples is not as large as expected. This does show the advantage of XANES spectra in that they show more dramatic differences with small changes in the *d* states than do core level shifts. Previous experimental work indicates considerable differences in electronic structure with a larger bandwidth and more well defined valence band features for the ordered species.[25] Our present XPS and synchrotron work does not show such an apparent difference in the valence band features but the large differences in derived hole counts do support their conclusions. Calculations have been performed to evaluate the nature and the amount of charge transferred in an ordered AuCu alloy.[26] These calculations indicate a loss of 0.066 *d* electrons from the Au site and an overall gain of 0.176 *s-p* electrons (conduction) at the Au site upon alloying. These compare favourably with values determined in this study of 0.116 electrons and 0.187 electrons, respectively.

A large body of work has been done experimentally on the Cu_3Au system. Recently, more theoretical work has appeared and will be the focus of comparison as the experimental data agree well with previous studies. A *d*-band splitting parameter of 1.55 eV was calculated using the atomic spin-orbit splitting parameter $5/2\xi_d$ in which ξ was estimated to be 0.62.[27] The value derived from the XPS and synchrotron valence spectrum was also 1.55 eV. The same study gave a core level shift of 0.3 eV which compares well to a shift of 0.37 eV exhibited here. Calculated valence band spectra also have shown more defined features for the ordered states[28,29,30] which were assigned to be due to a well defined nearest-neighbour shell of 12 identical Cu atoms, which would

allow resonant scattering leading to more enhanced and defined features in the valence band spectra.[29] Again the resolution and cross-section of the valence band prevented this study from seeing all but the most subtle of differences in the two alloys. There was also a study indicating that the Au site gains 0.17 *d* electrons upon alloying.[28] However, the XANES results clearly indicate that Au loses *d* charge in direct contradiction with this study. A first-principles calculation has shown Au 5*d* loss of 0.21 and 0.17 electrons for the ordered and disordered species, respectively,[31] while a fast LMTO-CPA (linear-muffin-tin-orbital method using the coherent potential approximation) study indicated a loss of 0.43 and 0.22 electrons.[29] The values derived here were 0.16 and 0.13 electrons in reasonable accord with the first-principles study. The second study[29] also indicated that Au loses not only *d* charge but also combined *s-p* charge giving an overall loss of charge for both alloys in direct contradiction with the charge compensation model, electronegativity arguments, and the results of this study.

The last two samples analyzed were the random alloys $Au_{0.125}Cu_{0.875}$ and $Au_{0.05}Cu_{0.95}$. These can be viewed as having a pure Cu structure with Au atoms as impurities in the lattice. In both cases the first shell, statistically would be dominated by Cu and therefore the Au-Cu interaction from the Au viewpoint would be at its strongest and the Au-Au interaction at its weakest. These alloys exhibit the largest core level and isomer shifts, have the highest hole count and from the point of view of the charge compensation model they also have the largest overall gain of charge at the Au site, in good accord with electronegativity arguments, albeit the amount is small to preserve electroneutrality. Second-order effects become important in these dilute alloys

in terms of the local configuration in the second shell and beyond.

5.9 Conclusions

We have reported a wide range of experimental data for a series of Au-Cu alloys in order to elucidate trends in the electronic behaviour upon alloying and ordering. Strong correlations have been found in the experimental parameters examined here (XPS, Mössbauer, XANES). The sensitivity of the XANES technique has clearly been demonstrated and the validity of the charge compensation model shown by the independent determination of the nature and amount of charge transfer. Au gains overall charge in line with electronegativity arguments. The degree of Au-Cu interaction is determined mainly by first order local effects (number of Cu nearest neighbours) and not so much by the Au-Cu separation within the first coordination sphere. The results of this study compare favourably with most experimental and theoretical work and although the valence band spectra do not show the large differences associated with the transition between ordered and disordered samples, the XANES and XPS (core level shifts) derived parameters clearly indicate significant differences in electron distribution.

With this study the indication is that there is not much overlap between the constituent *d* bands as indicated by the movement of the Au portion of the alloy band away from the Fermi level and the movement of the Cu portion towards the Fermi level (*d-d* repulsion model). Also, even as the significance of the Au-Cu interaction was stressed to point out differences that are associated with compositional and local environment changes, it must be noted that the overall synergy (redistribution) of charge is still relatively small.

This study has examined the electronic structure of a series of Au-Cu alloys and has confirmed the validity of the charge compensation and *d-d* repulsion models. The parameters and correlations derived from this bulk study will be used to determine the structure and electronic properties of bimetallic Au-Cu surface alloys.

5.10 References

1. T.K. Sham, R.F. Watson, and M.L. Perlman, Ad. Chem. Series **194**, ACS.39 (1981).

2. T.K. Sham, Y.M. Yiu, M. Kuhn, and K.H Tan, Phys. Rev. B **41**, 11881 (1990).

3. R.E. Watson, J. Hudis, and M.L. Perlman, Phys. Rev. B **4**, 4139 (1971).

4. T.K. Sham, M.L. Perlman, and R.E. Watson, Phys. Rev. B **9**, 539 (1979).

5. G.K. Wertheim, R.L. Cohen, G. Crecelius, K.W. West, and J. Wernick, Phys. Rev. B **20**, 860 (1979).

6. P.M. Th. M. van Attekum, G.K. Wertheim, G. Crecelius, and J. Wernick, Phys. Rev. B **22**, 3998 (1980).

7. W. Eberhardt, S.C. Wu, R. Garrett, D. Sondericker, and F. Jona, Phys. Rev. B **31**, 8285 (1985).

8. V.L. Morruzzi, A.R. Williams, and J.F. Janak, Phys. Rev. B **10**, 4856 (1974).

9. T.K. Sham, A. Hiraya, and M. Watanabe, 1992 UVSOR Annual Report, 67 (1993).

10. P.G. Huray, L.D. Roberts, and J.O. Thomson, Phys. Rev. B **4**, 2147 (1971).

11. R.E. Watson and M.L. Perlman, Physica Scripta **21**, 529 (1980).

12. R.M. Friedman, J. Hudis, M.L. Perlman, and R.E. Watson, Phys. Rev. B **8**, 2433 (1973).

13. F. Cyrot-Lackmann, Adv. Phys. **16**, 393 (1967).

14. C.C. Tyson, A. Bzowski, P. Kristof, M. Kuhn, R. Sammynaiken, and T.K. Sham, Phys. Rev. B **45**, 8924 (1992).

15. A.N. Mansour, J.W. Cook, Jr., and D.E. Sayers, J. Phys. Chem. **88**, 2330 (1984).

16. W.H. McMaster, N.K. Del Grande, J. Mallett, and J.H. Hubbell, "Compilation of X-ray Cross-Sections", NTI Service, Springfield, VA, 1969.

17. M. Iwan, F.J. Himpsel, and D.E. Eastman, Phys. Rev. Let. **43**, 1829 (1979).

18. M. Iwan, E.E. Koch, T.C. Chiang, D.E. Eastman, and F.J. Himpsel, Sol. St. Com. **34**, 57 (1980).

19. D. Chandesris, C. Guillot, G. Chauvin, J. Lecante, and Y. Petroff, Phys. Rev. Lett. **47**, 1273 (1981).

20. L.C. Davis, Phys. Scr. **2T17**, 13 (1987).

21. L.G. Parratt, Rev. Mod. Physics, **16**, 393 (1967).

22. L.M. Mattheiss and R.E. Dietz, Phys. Rev. B **22**, 1663 (1980).

23. S.S. Lu and C.-K. Liang, Chin. Journ. Physics, **22**, 505 (1966).

24. Z.W. Lu, S.-H. Wei, and A. Zunger, Phys. Rev. B **45**, 10314 (1992).

25. R.G. Jordan, A.M. Begley, Y. Jiang, and M.A. Hoyland. J. Phys.: Condens. Matter **3**, 1685 (1991).

26. S.-H. Wei, A.A. Mbaye, L.G. Ferreira, and A. Zunger, Phys. Rev. B **36**, 4163 (1987).

27. J.W. Davenport, R.E. Watson, and M. Weinert, Phys. Rev. B **37**, 9985 (1988).

28. G.K. Wertheim, L.M. Mattheiss, and D.N.E. Buchanan, Phys. Rev. B **38**, 5988 (1988).

29. I.A. Abrikosov, Yu. H. Vekilov, and A.V. Ruban, Phys. Lett. A **154**, 407 (1991).

30. P. Weinberger, A.M. Boring, R.C. Albers, and W.M. Temmerman, Phys. Rev. B **38**, 5357 (1988).

31. Z.W. Lu, S.-H. Wei, and A. Zunger, Phys. Rev. B **45**, 10314 (1992).

SECTION II
SURFACE Au-Cu STUDIES

CHAPTER SIX

Introduction and Experimental Considerations

6.1 Introduction

The following section of this study, consisting of two chapters, will deal with preliminary surface studies on Au-Cu alloys on a Ru(001) crystal. As mentioned in the introductory chapter, bimetallic systems are of great relevance in the design of new materials, especially those which exhibit catalytic properties.

For this study we will focus not only on the electronic properties of the bimetallic system (i.e. Au on Ru(001)) but also on the properties of a trimetallic system, Au-Cu on Ru(001). This is accomplished by first examining the separate behaviour of Au and Cu on Ru(001) as a function of coverage, submonolayer to multilayer. Sequential deposition of the components is then performed and the electronic behaviour of the system again examined not only for the interaction of the components with the substrate but also for the interaction among themselves. The questions that need to be answered are if the two components on the surface form an alloy (mix to some degree) at room temperature, and

if not what conditions are required for the ıormation of an alloy. The role of the substrate must also be examined. The results of the work on the bulk alloys, in terms of the effect of alloying on valence band behaviour and core level positions, will be used to determine if alloying occurs and to what degree. The charge compensation and *d-d* repulsion models will be examined here for compliance and any deviations from those results of the bulk studies.

Industrial catalysts are complicated systems in which the catalytic effects are enhanced or diminished by a variety of variables: particle size, temperature, bimetallic composition, and many more. At the heart of the catalytic properties is the electronic behaviour of the system. To examine these effects a well-ordered and defined system is studied first. An example of this is the Cu on Ru(001) system which is a well studied catalytic system. Ru(001) is used because the (001) plane of the hexagonal-close-packed structure (hcp) is a close-packed surface with the same fcc structure that bulk Cu and Au exhibit.[1,2,3,4,5,6,7,8,9] The fact that both Cu and Au do not penetrate the Ru lattice makes it easier to characterize the physical properties of the system and allows determination of the coverage through thermal desorption spectroscopy (TDS), also referred to as temperature-programmed desorption.

The focus of the studies carried out here will be, first the characterization of the Au on Ru(001) system which has not been studied in any great detail, followed by examining the much more complicated co-deposited systems. The studies are of a preliminary nature. Techniques not available in this study are required to determine the exact physical structure of each system, unlike the bulk Au-Cu studies in which the

structure of each alloy was well characterized. Therefore, the focus will be on electronic behaviour and these results will be used to shed some light on the exact physical structure. The order of the deposition and temperature, both at deposition and at later annealings, may also play an important role in the thermodynamics of the system. Wherever possible, coverages and measurement temperatures were kept constant.

As was mentioned previously this surface study will be divided into two chapters. This chapter will focus on experimental considerations such as sample preparation and experimental measurements. The type of experiments performed were photoemission (XPS and synchrotron), low energy electron diffraction (LEED) and thermal desorption spectroscopy (TDS).

6.2 Sample Preparation

To begin these studies a well-characterized and clean substrate is required. A Ru crystal in the shape of a disc approximately 15 mm in diameter and 2 mm thick was used. The crystal was cut to expose the (001) plane within 0.5 degrees and polished on both sides. The high degree of precision of the cut is required to minimize stepped surfaces which would allow preferential adsorption at these high energy sites and complicate characterization.

Cleaning the crystal requires that we be able to heat the crystal resistively to 1500 K. This is accomplished by using an appropriate sample manipulator and mounting technique. Figure 6.1 shows the manipulator and mounting method used. The manipulator used was the same as described in Chapter 3. In consists of a shaft, which effectively acts as a Dewar for cooling using liquid nitrogen, and two isolated Cu rods which allow for resistive heating and quick cooling as the rods pass through the Dewar. Inside the chamber the two Cu rods are connected via an in-line connector to two Ta wires. These wires are spot-welded to short wires of W which have been prepared with "dumbbells" at the ends. These "dumbbells" are required for spot-welding to the Ru crystal. Both Ru and W are difficult to spot-weld but the high temperature properties of W are required to allow the temperatures required to clean the crystal. To provide a large enough surface area for good contact "dumbbells" are employed as upon spot-welding they will melt and provide a larger contact area. The W wires are spot-welded to one face of the crystal close to the midline but as close to each edge to allow the

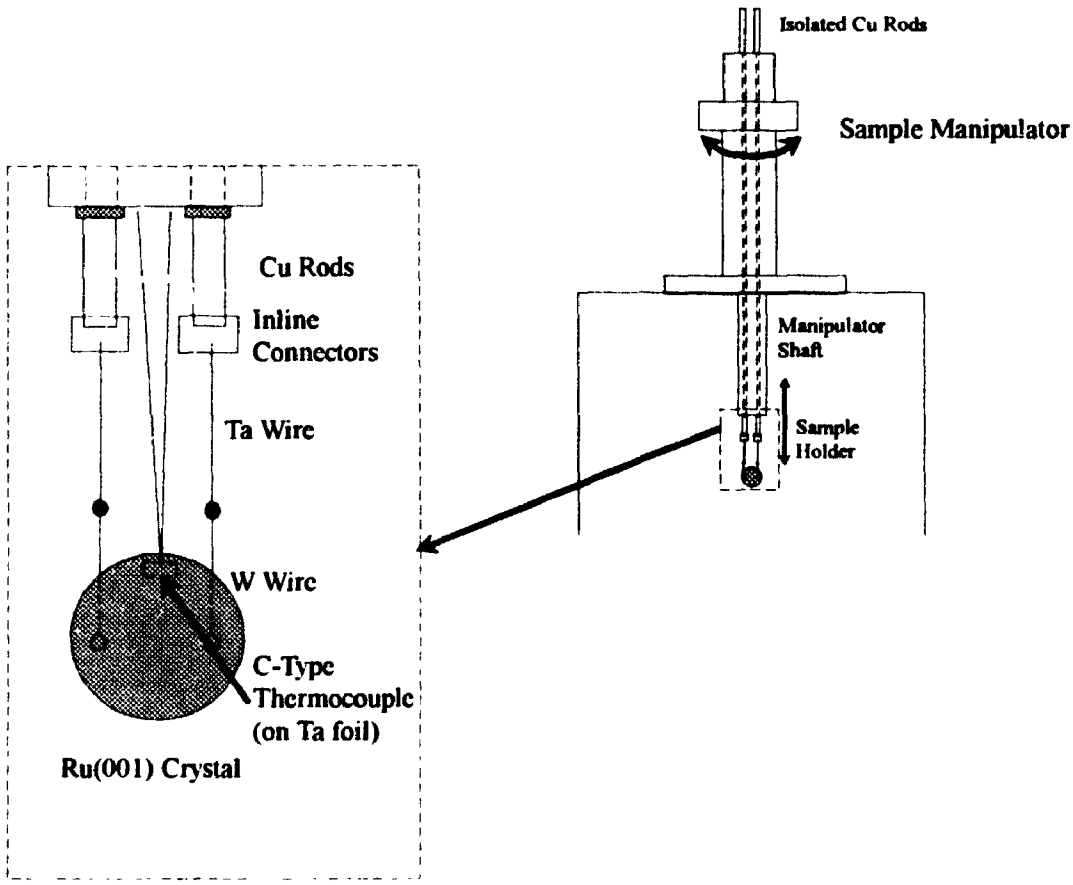

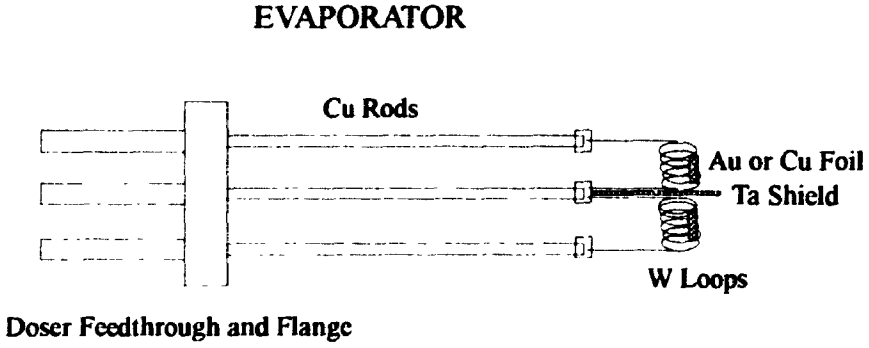

Figure 6.1: Representative diagram of mounting system for Ru(001) crystal (top) and noble metal evaporators (bottom).

longest current path possible and evenly heat the crystal. To monitor the crystal temperature 5% W-Re 26% W-Re (C-type) thermocouple was employed. The thermocouple was mounted on the manipulator shaft via a feedthrough at the top of the manipulator and because of the difficulty of spot-welding directly on the crystal, it was first spot-welded to a small piece of Ta foil which could easily be spot-welded to the top of the back of the crystal. Using this mounting system with the manipulator the sample has x,y, and z motion and can be rotated by an angle, θ. The disadvantage of this mounting system is that the spot welds are very sensitive to movement and frequently break requiring remounting. Unfortunately, the W spot-welds are required since radiative heat is created at the W-Ta and W-Ru junction which heats the crystal.

The Ru(001) crystal was cleaned using two methods. In the original method,[10,11] before mounting, the crystal and mounting assembly was cleaned in an ultrasonic bath to remove organic contaminants. After mounting, the crystal was first cycled from room temperature to 1500 K a number of times under ultra-high vacuum. This requires a power supply capable of of an output of 5-10 V and 25-35 A. For any surface studies the best possible vacuum is required to maintain surface cleanliness during the studies. For most measurements in this study the vacuum was in the 10^{-10} Torr regime. O_2 is introduced at a constant pressure of $1x10^{-6}$ Torr and the crystal was cycled from room temperature to 1500 K a number of times. This formed a surface oxide layer with the contaminants (mainly C). Argon sputtering was then performed at an Ar pressure of $5x10^{-5}$ Torr for at least 30 minutes on both sides of the crystal to remove the oxide layer. Sample current was monitored to maximize the sputtering rate and the sputtering was

rastered to cover the entire sample. After sputtering the crystal was again ramped to 1500 K to anneal the damaged surface. Possible remaining contaminants were removed by introducing 6 Langmuirs of O_2 at room temperature (one Langmuir=$1x10^{-6}$ Torr sec; in our case 6 Langmuirs were introduced by a pressure of $2x10^{-8}$ Torr of O_2 for 300 seconds) and then heated to 1500 K. This was continued until a c(2x2) LEED pattern was observed upon cold O_2 deposition. The top of Figure 6.2 shows the 1x1 LEED pattern of a Ru(001) crystal. If the crystal was clean, upon deposition of O_2, a c(2x2) superlattice was formed as atomic oxygen occupies every second site of the Ru(001) surface. In the bottom of Figure 6.2 this manifests itself as a compressed LEED pattern (reciprocal space).

The most recently developed method involves replacing the Ar sputtering with repeated cold deposition of O_2 followed by heating to 1500 K. This requires that the crystal be relatively clean originally. Usually the crystal has been protected by either layers of Au or atomic oxygen before the experimental chamber was exposed to atmosphere. This avoids the damage of sputtering to the crystal. Cleanliness of the surface can be monitored by co-deposition of Au and O_2 in which the temperature at which O_2 comes off is monitored by TDS. Desorption of Au occurs at approximately 1300 K. With a clean surface, desorption of O_2 occurs sharply at ~ 1100 K, while for a contaminated surface, O_2 desorption is broad in the range of 1400 K and above. This method has the advantage of not requiring a LEED system for monitoring surface cleanliness. Between experimental runs the surface was protected by a thick inert layer of Au or a surface layer of atomic oxygen. In our studies, repeated desorption of Au and

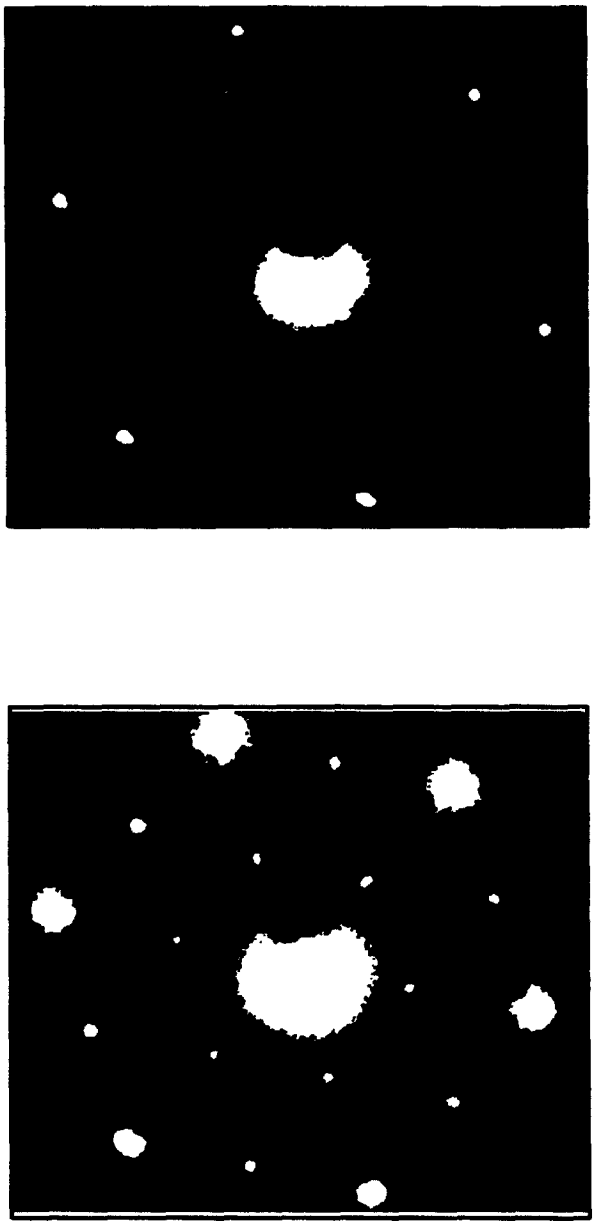

Figure 6.2: LEED images of the clean Ru(001) surface and the subsequently O_2 treated surface. The clean surface (top) exhibits the close-packed structure of the (001) plane. Upon treatment with 6 Langmuirs O_2 a c(2x2) overlayer is seen (bottom).

Cu overlayers also helped to maintain surface integrity.

Both Au and Cu were dosed onto the clean surface using simple evaporators employing resistive heating and are shown at the bottom of Figure 6.1 These evaporators consisted of W loops which were mounted via inline connectors to Cu feedthroughs. Small amounts of Au and Cu metal foils were melted unto the loops. Dosing was accomplished by controlled heating by the use of a steady current. The flux was easily monitored using a mass spectrometer. Both dosers were mounted on one feedthrough and cross dosing was prevented by a Ta shield.

6.3 Experimental Photoemission Setup

Photoemission experiments will be the focus of the surface studies to determine the electronic behaviour of the deposited Au and Cu overlayers on Ru(001). Both lab and synchrotron sources were used.

XPS measurements were carried out on a XPS system located in the Chemistry Department at Brookhaven National Laboratory, Upton, New York. The experimental setup is similar to that described for the bulk synchrotron studies outlined in Section 3.6b with the exception that other analytical tools were also used. Figure 6.3 outlines the orientation and typical setup of the experimental system employed for both XPS and synchrotron studies. There are a couple of exceptions. LEED optics were not available for the XPS studies and for the experiments performed on the Grasshopper beamline. Programmed thermal desorption studies could not be performed at the Stainless Steel Seya beamline located at the Synchrotron Radiation Centre in Madison, Wisconsin. The photon source for the XPS experiments was an unmonochromatized Mg $K\alpha$ anode, which works on the same principle as the previously described Al $K\alpha$ source (Section 3.6a) but has a photon energy of 1248.8 eV. The photon resolution of the unmonochromatized source is poorer than that used for the bulk studies ($\sim$0.9 eV versus $\sim$0.6 eV). The analyzer used was a VSW-150 hemispherical analyzer with multichannel detection. Base pressure of the system was 1×10^{-10} Torr. Measurements were performed with a take-off angle of $\sim 30°$ to enhance surface sensitivity. Multiple scans of each region were performed and the data converted to ASCII code for later analysis.

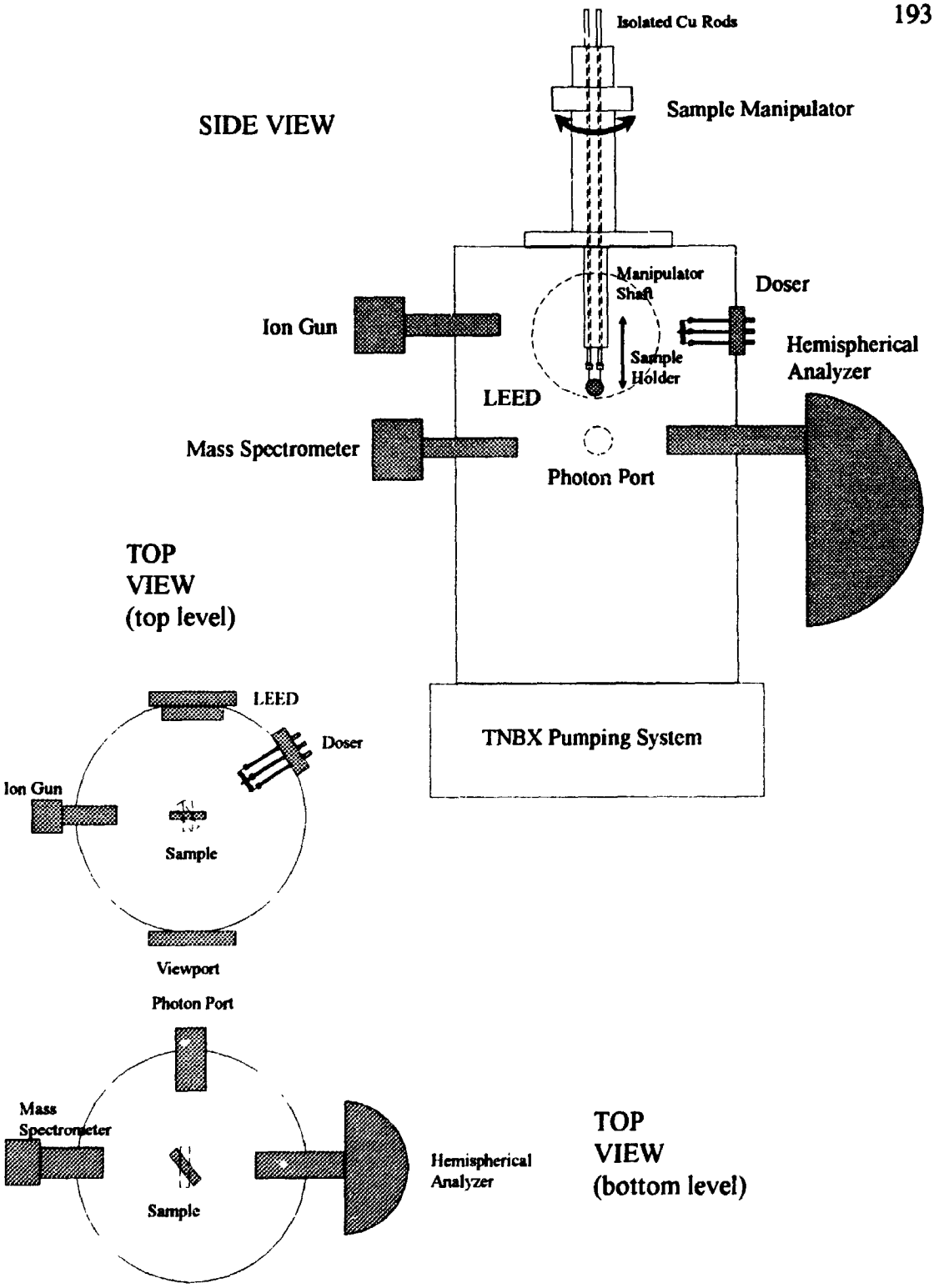

Figure 6.3: Typical experimental setup for surface studies employing a variety of surface science instruments.

Two series of synchrotron experiments were performed. The Grasshopper beamline was employed for photon energies in the range of 60 to 200 eV. These energies were used to probe both the valence bands (lower energies to enhance the cross-section) and Au 4*f* core levels (higher energies). The measurements were taken with the sample at normal emission. Slits were set at 30 μm using an 1800 lines/mm grating. This gives an ultimate photon resolution of 0.19 eV at a photon energy of 170 eV. The pass energy for the valence band data was set at 25 eV while it was set at 12.5 eV for the Au 4*f* core level data. The base pressure of the system was $3x10^{-10}$ Torr. Multiple scans were performed on each region and the raw data converted for later analysis.

For high resolution valence band studies the Stainless Steel Seya monochromator beamline was used. The cross-section of the valence band is at maximum at low photon energies, 10 to 40 eV. The Grasshopper monochromator with the 600 lines/mm grating is capable of photon energies as low as 50 eV but because of the nature of the beamline the flux is quite low. The SS Seya beamline, on the other hand, has its maximum flux at 22 eV with a 1200 lines/mm grating, which is ideal for valence band studies. The SS Seya beamline employs similar types of optical elements as does the Grasshopper beamline, except that the monochromator and optical elements are designed for normal incidence radiation whereas the Grasshopper monochromator and optics are based on grazing incidence radiation. The relationship can be seen by examining the grating equation (Equation 3.24). The smaller the angle of incidence the smaller the wavelength and subsequently the higher the energy of the monochromatized light. Employing large angles of incidence lowers the energy of the monochromatized light. The typical spectral

range for the SS Seya beamline is 5 to 40 eV. Base pressure of the system was $3x10^{-10}$ Torr. The sample was mounted at normal emission. Multiple scans were taken of each region and converted for later analysis.

Returning to Figure 6.3 we examine the location and orientation of various analytical instruments used during the course of these studies. Both chambers used in these studies are two level chambers. The top level is reserved for sample preparation while the bottom level is where the photon source and analyzer are located. Along with the LEED (if available), the ion gun and doser are located in the top level. The doser is orientated such that it is pointed away from the LEED optics to prevent contamination. Since the LEED optics sticks into the chamber a few inches the doser is built short enough so that it does not stick in front of the optics. The chamber located at Madison for the experiments on the Grasshopper beamline has a port located between the two levels and therefore this was used for the doser. The ion gun was also located such that it did not sputter the sample surface towards the LEED optics. The second level contained the photon port and analyzer. The mass spectrometer was located 180° from the analyzer to prevent contamination of the electron lenses during thermal desorption studies.

6.4 Low Energy Electron Diffraction (LEED)[12,13] and Thermal Desorption Spectroscopy (TDS)[14,15]

Both LEED and TDS are surface sensitive analytical techniques which can reveal a large amount of information on the structure, coverage and kinetics of the system under investigation. For our studies LEED was mainly used to determine the cleanliness of our substrate surface and where possible it was used to observe any changes upon Cu and Au adsorption. TDS was used to determine the surface coverage of both Au and Cu and also to extract some kinetic information upon desorption of the separately and co-adsorbed species.

The basis of the LEED technique is the diffraction of monoenergetic electrons which are focussed on a sample surface. These electrons are then scattered from the surface, and if certain conditions are met, a diffraction pattern can be detected from which information on the nature of the surface can be deduced. The surface sensitivity of the technique comes from the fact that the electrons have a kinetic energy of a few eV to a few hundred eV and therefore can only penetrate a few layers into the surface. Diffraction of the electrons can only occur if their energy is of the same order as the crystal lattice spacing. The wavelength of an electron is given by the de Broglie equation:

$$\lambda = \frac{h}{(2mE)^{1/2}} \qquad (6.1)$$

where h is Planck's constant, m is the electron mass, and E is the energy of the electron.

Therefore for energies specified above the range is on the order of the lattice spacing. For diffraction to occur the Bragg equation must be satisfied:

$$n\lambda = 2d\sin\theta \qquad (6.2)$$

where n is the order of the diffraction, d is the interlattice spacing, and θ is the scattering angle. For a two-dimensional surface the Bragg equation must be satisfied in both directions. When this occurs diffraction spots can be detected when the electrons hit a fluorescent screen. The order of the surface, adsorbate-covered or clean, can be deduced by the brightness and localization of the diffraction spots. As the surface becomes less ordered the spots become dimmer and more diffuse. Also, the orientation of the surface can be deduced by the type of LEED pattern displayed (i.e. hexagonal, square, etc.). A close packed surface such as hcp(001) or fcc(111) has different lattice spacings in the two directions and this manifests itself as a hexagonal LEED pattern (Figure 6.2). A square pattern would be observed if the lattice spacings were equal. For the purpose of this study LEED was used foremost to determine the surface cleanliness both by the detection of a bright hexagonal pattern and a c(2x2) pattern observed for O_2 adsorption. Wherever possible the LEED pattern was observed for Au and Cu adsorption.

Thermal Desorption Spectroscopy (TDS) is used in this study to gain information on the coverage of the adsorbates and can also be used to deduce kinetic information on the adsorbate-substrate and adsorbate-adsorbate interactions. Experimentally, the technique involves applying a controlled temperature ramp (usually linear) to an adsorbate-substrate system and monitoring the partial pressure of the evolved species, using a mass spectrometer. In our system, a UTI-100C quadrupole mass spectrometer

(capable of detecting up to 300 atomic mass units) was controlled by a Teknivet interface linked to a PC based computer. The linear heating ramp was supplied by a feedback controlled Sorenson power supply (10 V and 50 A) using a RHK temperature controller. Under computer control up to 16 different masses could be monitored during the desorption process.

The rate of desorption of a single species, i, on a surface is given by the Polanyi-Wigner relation:

$$\frac{-dN_i}{dt} = \nu_i N_i^{n_i} e^{\left(\frac{-E_i}{RT}\right)} \tag{6.3}$$

where N_i is the population of the adsorbate in molecule area^{-1}, υ_i is the frequency factor, n_i is the reaction order and E_i is the desorption activation energy.

The partial pressure is related to the desorption rate by:

$$\frac{dN_i}{dt} = \left(\frac{V}{AkT_g}\right)\left[\frac{dP}{dt} + \left(\frac{S}{V}\right)P\right] \tag{6.4}$$

where V is the volume of the system, A is the absorbent area, T_g is the gas phase temperature, P is the pressure above background, and S is the system pumping speed. If the pumping speed to volume ratio is large (as it should be for a good UHV system) and the heating rate is low (dT/dt or β) then $dP/dt << (S/V)P$ and the desorption rate is proportional to the rise in pressure. The heating rate cannot be too low since re-adsorption will become prevalent.

If we assume, in the first approximation, that the frequency factor and desorption

activation energy are independent of the coverage the shape and position of the desorption trace can lead to information on the order of the process. If we define T_p to be the peak temperature and that for a given system the heating rate β, the frequency factor and the desorption activation energy are constant, we find the following relationship:

$$N_i^{n-1} \propto \frac{e^{(E_d / RT_p)}}{RT_p^2} \tag{6.5}$$

Given that the contribution from the exponential term is smaller for a varying peak temperature the following relationships can be derived. For a zero-order process T_p will rise as a function of the coverage. For a first-order process there is no dependence of T_p on the coverage. For a second-order process the peak temperature will decrease as the coverage is increased. The peak shape can also be used to determine the order of the process. For a zero-order process there is a rising edge which falls drastically after the peak temperature is reached, in effect a large asymmetry towards the low temperature side. For a first-order process there is a smaller asymmetry also to the low temperature side. For a second-order process the peak is symmetric about T_p. Using these parameters we can approximate the reaction order simply by comparing the desorption spectra of various coverages. Care must be taken in interpretation since fractional orders are very prevalent for many of these systems. Also we assumed the independence of the desorption energy and the frequency factor from the temperature which is also usually not the case.

Further, more detailed analysis is required to determine values for the desorption

energy and the frequency factor. The desorption energy can be related to the heat of adsorption by assuming that the activation energy of adsorption is close to zero. These analyses have previously been performed on deposits of Cu and Au on Ru(001). For the purpose of this study only a rough comparison will be made to verify the condition of the adsorbate surface (i.e. cleanliness). The co-deposited spectra will be more closely examined and compared to the spectra of the deposited pure metals.

TDS was used primarily for a more practical purpose in this study. As we heat the sample and desorb all of the species on the surface we are in effect measuring the partial pressure as a function of time, which is correlated to a temperature by a constant heating rate. Integrating the resultant spectra would give us an indication of the initial coverage on the surface. Absolute coverages cannot be determined without complete knowledge of the system (distance, angle, efficiency of mass spectrometer, etc.) but given a frame of reference relative coverages can be determined. If the experimental conditions are kept constant, such as distance and angle to the mass spectrometer, heating rate, and mass spectrometer settings, then the relative change in coverage can be measured. Even more desirable would be the area of a known coverage so that an absolute coverage (usually in terms of monolayers) can be estimated. For the case of Au and Cu adsorption on Ru(001) this can be accomplished by using the different reaction orders of monolayer and multilayer coverages. Figure 6.4 shows the desorption spectra of a series of Au coverages on Ru(001) and Cu on Ru(001). For Au, the initial coverages result in a peak centred at approximately 1300 K which increases as a function of the coverage. A new peak emerges at approximately 1200 K while the area under the

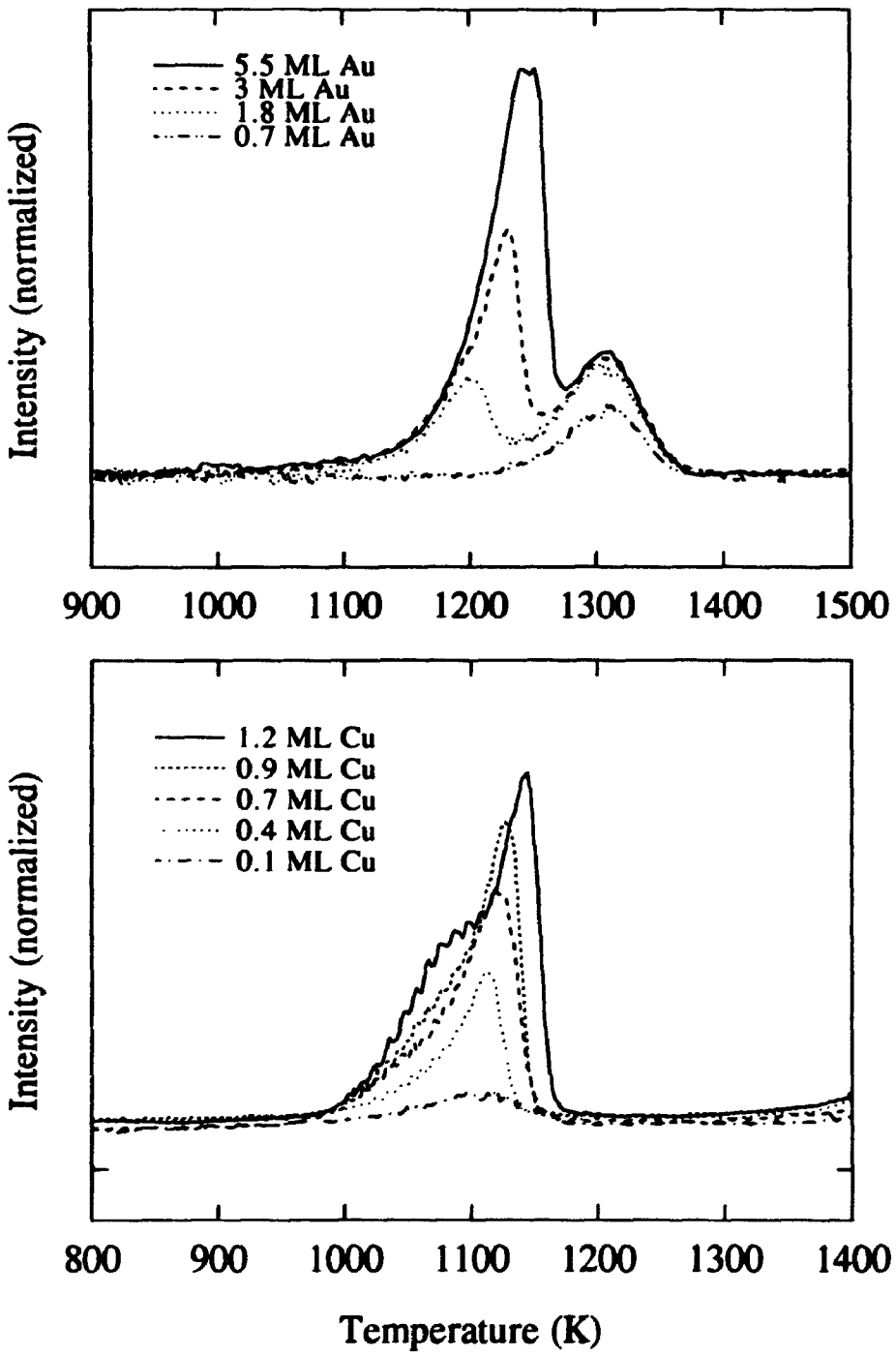

Figure 6.4: A series of thermal desorption spectra of various coverages of Au on Ru(001) (top) and submonolayer to monolayer coverages of Cu on Ru(001) (bottom). The absolute coverage was calibrated by the saturated area of the first peak (monolayer) evident at higher temperatures for both systems.

initial peak remains the same. The peak at 1300 K is attributed to monolayer coverage and remains the same once saturation of the first layer occurs. Therefore, the area under this peak can become the frame of reference for one monolayer and absolute coverages can now be determined. We also note that with increasing coverage the first peak maximum remains the same and that the lineshape is slightly skewed to the low temperature side. This indicates that the monolayer desorption is a first-order process. With increasing coverages beyond one monolayer the peak maximum shifts to higher temperatures and a large asymmetry towards the lower temperature side is seen. This indicates zero-order desorption for coverages higher than one monolayer. Similar behaviour is observed for Cu desorption from Ru(001) for multilayer coverages but close examination of the submonolayer desorption spectra reveals a small shift to higher temperatures accompanied by a more asymmetric lineshape than is observed for first-order monolayer Au desorption (Figure 6.4). The leading edges of the desorption spectra did not line up as seen for typical zero-order desorption. This indicates a fractional desorption order close to first-order. For simplicity, we will refer to the monolayer Cu desorption order as pseudo-first-order.

6.5 References

1. J.H. Sinfelt, Bimetallic Catalysts (Wiley, New York, 1983).

2. J.H. Sinfelt, Rev. Mod. Phys. **51**, 569 (1979).

3. J.C. Vickerman, K. Christmann, G. Ertl, P. Heimann, F.J. Himpsel, and D. Eastman, Surf. Sci. **134**, 367 (1983).

4. J.E. Houston, C.H.F. Peden, D.S. Blair, and D.W. Goodman, Surf. Sci. **167**, 427 (1986).

5. (a) J.E. Houston, C.H.F. Peden, P.J. Feibelman, and D.R. Hamann, Phys. Rev. Lett. **56**, 375 (1986).
   (b) J.E. Houston, C.H.F. Peden, P.J. Feibelman, and D.R. Hamann, Surf. Sci. **195**, 457 (1987).

6. C. Harendt, K. Christmann, W. Hirschwald, and J.C. Vickerman, Surf. Sci. **165**, 413 (1986).

7. C. Park, E. Bauer, and H. Poppa, Surf. Sci. **183**, 86 (1987).

8. T.K. Sham, T. Ohta, T. Yokoyama, Y. Kitajima, M. Funabashi, N. Kosugi, and H. Kuroda, J. Chem. Phys. **88**, 475 (1988).

9. T.K. Sham, J. Hrbek, and K.H. Tan, Surf. Sci. **236**, 259 (1990).

10. J. Hrbek (private communication).

11. I.J. Malik and J. Hrbek, J. Phys. Chem. **95**, 2466 (1991).

12. G.A. Somorjai, Chemistry in Two Dimensions (Cornell University Press, Ithaca, 1981).

13. L.C. Feldman and J.W. Mayer, Fundamentals of Surface and Thin Film Analysis (North Holland Elsevier Press, New York, 1986).

14. P.A. Redhead, Vacuum **12**, 203 (1962).

15. D.A. King, Surf. Sci. **47**, 384 (1975).

CHAPTER SEVEN

Results and Analysis

7.1 Introduction

The results of a series of photoemission and thermal desorption studies (some LEED results also) for a series of deposited Au, Cu and Au-Cu films on a Ru(001) surface will be examined. The outline of this section will follow a chronological order for the experiments. The reason for this is that experimental conditions were found to be hard to duplicate from experiment to experiment. Wherever appropriate and possible, cross-references will be made between the numerous coverages studied.

The first section will deal with high resolution valence band data collected at the SS Seya beamline (20 to 40 eV photon energy for high cross-section of valence band) at SRC and TDS data taken at the University of Western Ontario. The following section will deal with Au 4*f* core level and valence band data taken at the Canadian Grasshopper beamline (70 to 200 eV photon energy for high cross-section for Au 4*f* core levels) at SRC. The last section will deal with variable temperature XPS core level and valence band data taken at the Department of Chemistry, Brookhaven National Laboratory.

7.2 SS Seya Valence Band Data

A series of valence band spectra were taken of Cu on Ru(001), Au on Ru(001) and Au and Cu on Ru(001) (Figures 7.1, 7.2 and 7.5). Deposition and measurements were carried out at room temperature. The spectra were taken at photon energies of 23 and 30 eV. The 23 eV photon energy was chosen as it corresponds to the maximum flux of the SS Seya monochromator. It was found, however, that energy emissions from the Ru 4*d* band which has features from the Fermi level to ~7 eV below are very localized and intense. Two features especially, proved troublesome since they overlapped with the Cu 3*d* and Au 5*d* bands (Figure 7.3). These features could not be greatly attenuated by changing the angle with respect to the photon beam and analyzer. It was found that at a photon energy of 30 eV these emissions were greatly attenuated (see Figure 7.3). The escape depth of the photoelectrons are lowered (more surface sensitive) and the corresponding relative Au and Cu *d*-band cross-sections have been increased slightly.

We will first focus on the Au on Ru(001) series since we are attempting to correlate bulk *d*-band behaviour, Au 5*d*-band splitting and relative movements of the Au 5*d* components along with the Cu 3*d* band. The coverage dependence on these parameters must first be determined for Au on Ru(001) and Cu on Ru(001) before comparison to the co-deposited species. Figure 7.1 shows the valence band features for a series of Au depositions from 15 seconds to 10 minutes. The Ru valence band contribution was roughly subtracted by taking the clean Ru spectra and normalizing the intensity to the first Ru *d*-band feature at the Fermi level which does not have any

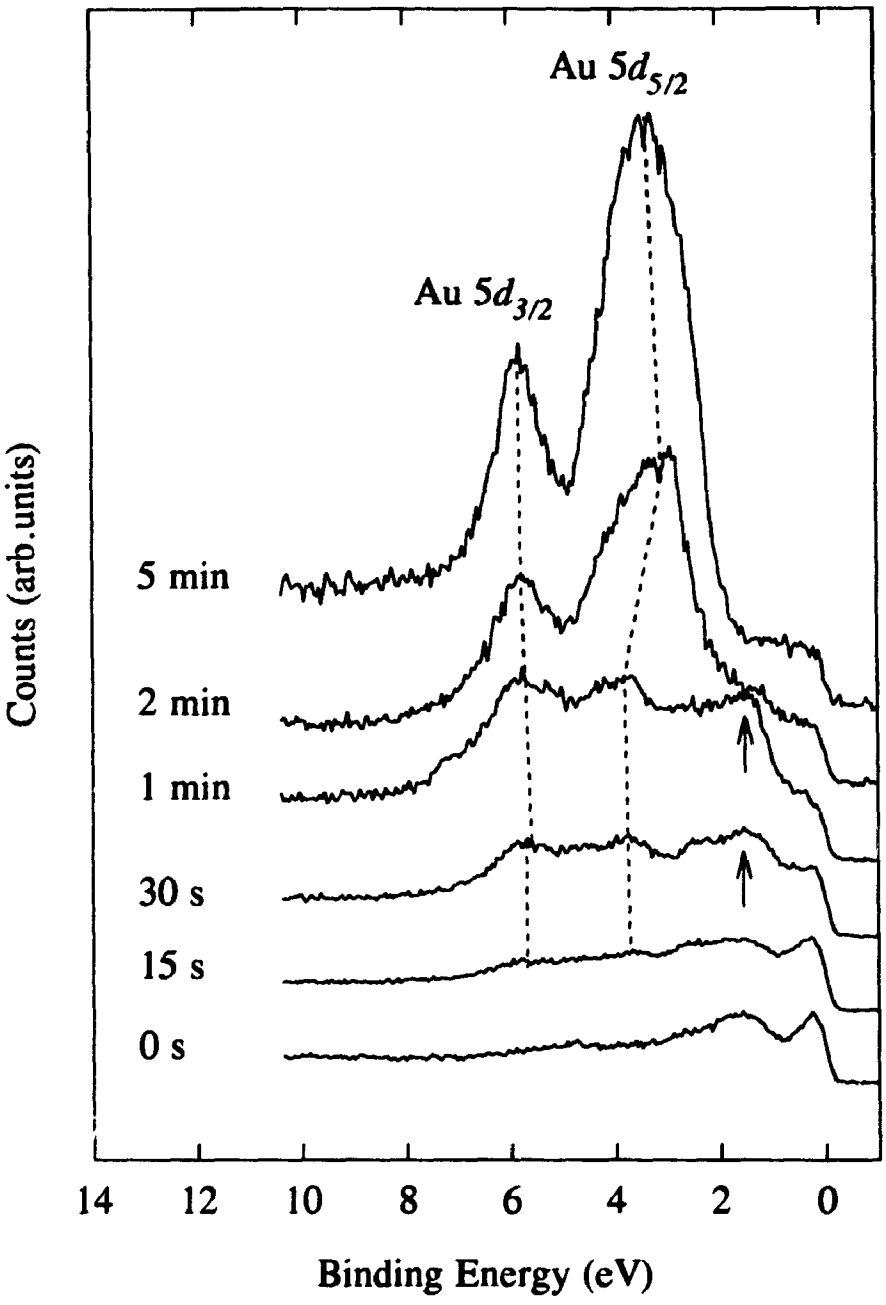

Figure 7.1: A series of valence band spectra of various coverages of Au taken at a photon energy of 30 eV. The dashed line follows the centroid position of the Au *d*-band components while the arrows indicate the position of the adsorbate-induced states.

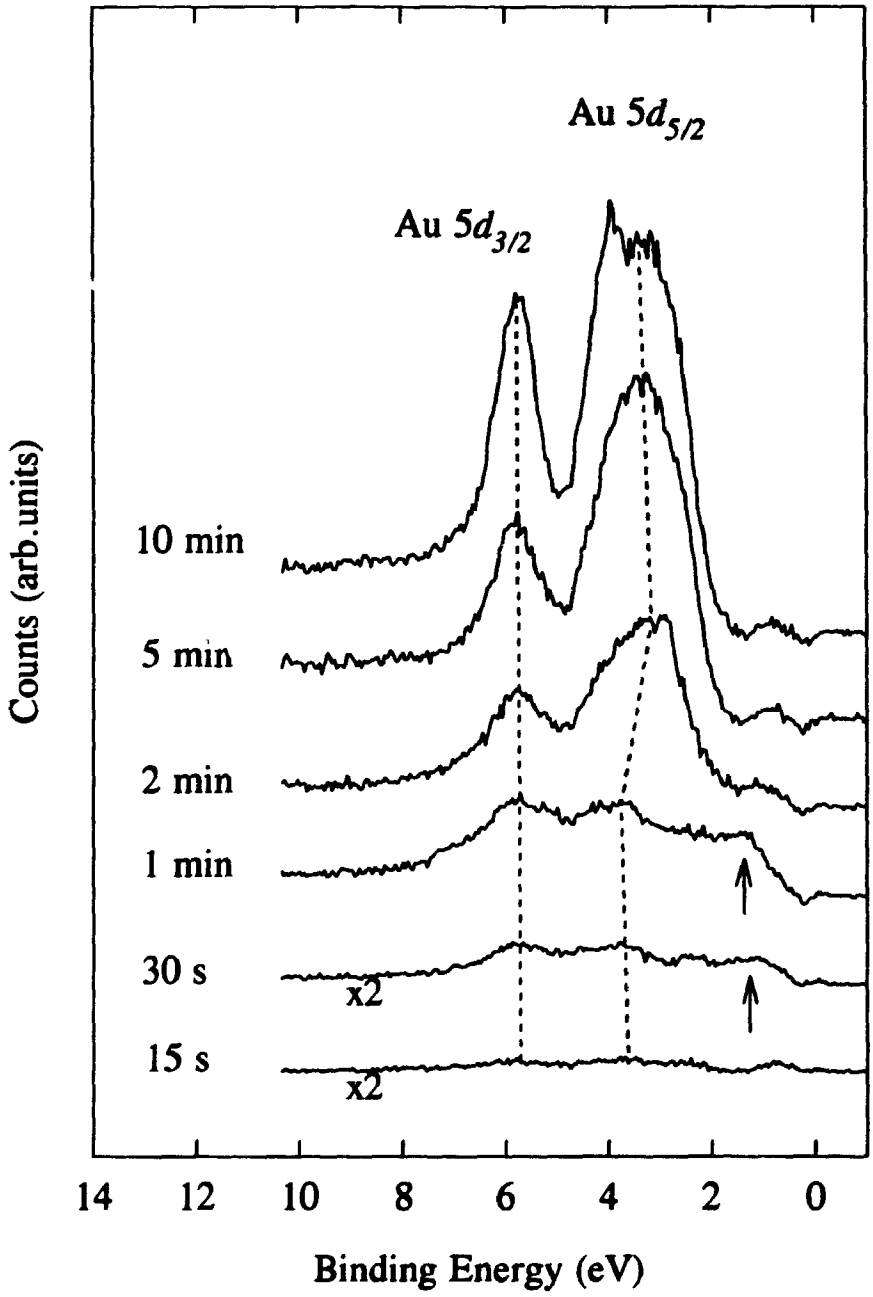

Figure 7.2: Similar spectra as in Figure 7.1 except that the Ru contribution to the signal has been artificially removed. Note the presence of Au *d*-band features at extremely low coverages.

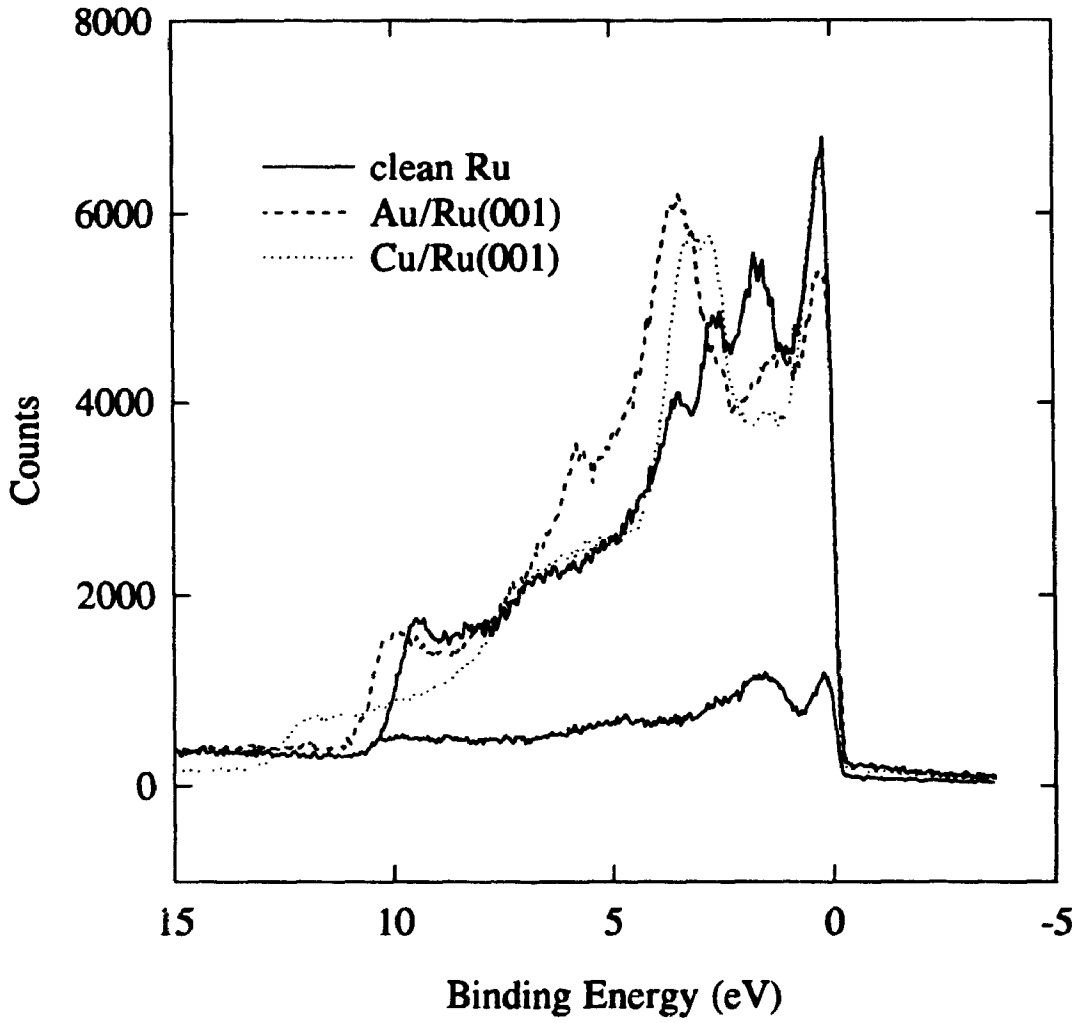

Figure 7.3: Valence band spectra taken at 23 eV photon energy. Note the energy overlap of two Ru *d*-band features at 3 and 4 eV with the Cu and Au *d* bands. The electron emission cutoff is due to the presence of a strong magnetic field due to the proximity and alignment of the experimental chamber to the storage ring bending magnet.

contributions from the Au 5*d* band. Errors manifest themselves at higher Au coverages since there will be an increasing contribution from the broad Au *s-p* band in that energy region. The result is shown in Figure 7.2. From Figure 7.3 it is clear that Ru *d*-band contributions interfere strongly with the Au emissions and for this reason the focus will be on the parameters derived from the 30 eV spectra. Table 7.1 and Figure 7.4 summarize the positions of the Au *d*-band components and the apparent splitting. The positions were determined by taking the peak maximum of a Gaussian fit.

Deposition Time	$\Delta E_{apparent}$ splitting (±0.1 eV)	Au $5d_{5/2}$ position (±0.05 eV)	Au $5d_{3/2}$ position (±0.05 eV)
15 s	2.1 (2.1)	3.6 (3.5)	5.7 (5.6)
30 s	2.1 (2.2)	3.8 (3.7)	5.9 (5.9)
1 min	2.1 (2.1)	3.7 (3.6)	5.8 (5.7)
2 min	2.5 (2.6)	3.2 (3.3)	5.7 (5.9)
5 min	2.5 (2.5)	3.3 (3.4)	5.8 (5.9)
10 min	2.6 (2.6)	3.3 (3.4)	5.9 (6.0)

Table 7.1: Au 5*d* peak positions and the associated apparent splitting. All values are for an incident beam of 30 eV except for those in parentheses which are for a photon energy of 23 eV.

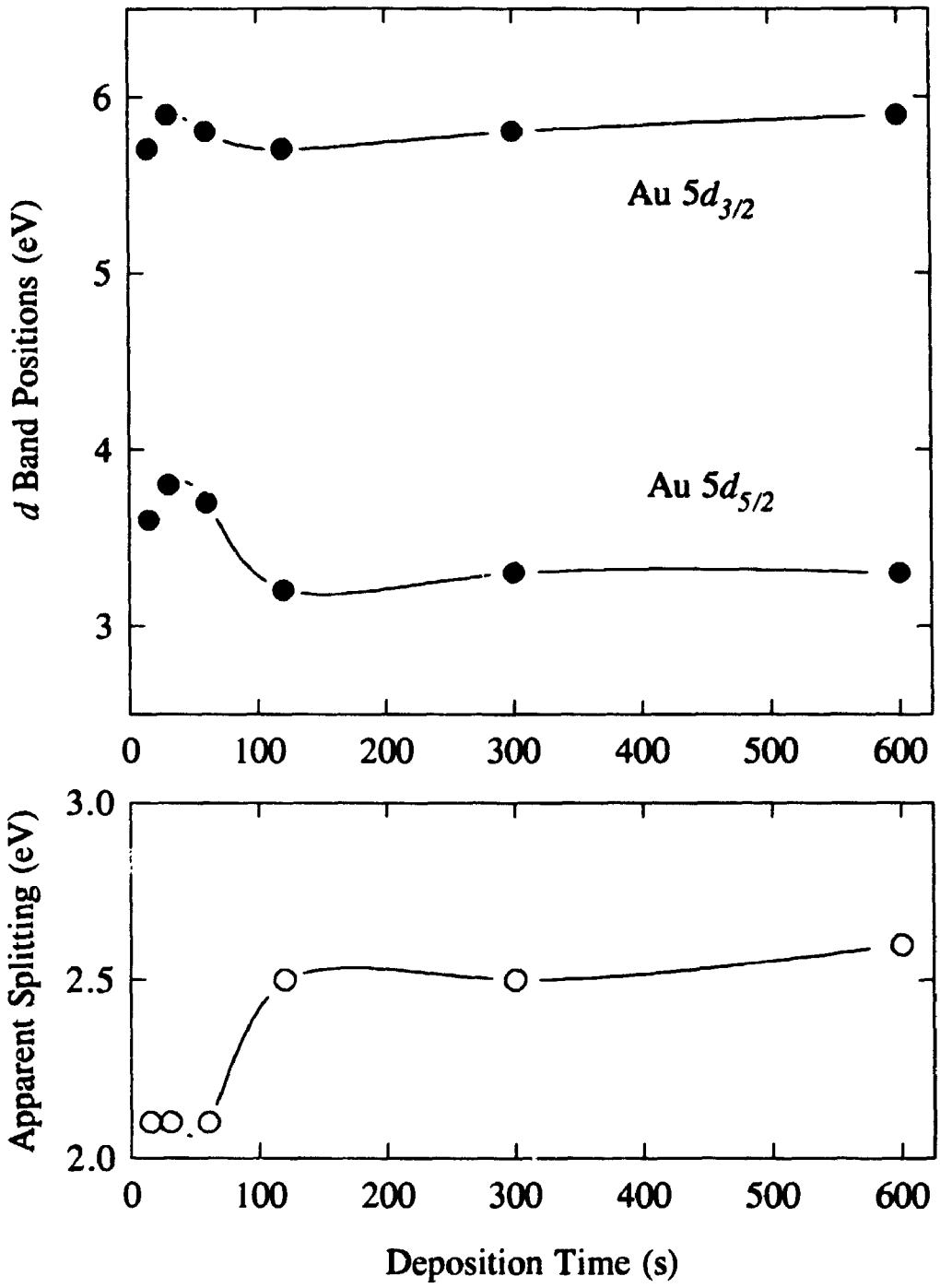

Figure 7.4: Plot of the position of the two Au *d*-band components as a function of Au deposition times (top). The bottom plot shows the apparent splitting as a function of Au deposition time.

Several features are noted in Figures 7.1 and 7.2. At lower depositions, a doublet appears with about equal intensity at 3.6 and 5.7 eV which becomes more intense as the coverage increases while the energy positions remain unchanged. These peaks are assigned to the Au $5d_{5/2}$ and Au $5d_{3/2}$ components of Au atoms dispersed on the Ru surface. The corresponding apparent splitting is 2.1 eV. This value is between the atomic value (1.5 eV) and the value for pure bulk Au (2.7 eV) indicating that the effective Au-Au interaction is relatively weak, and that there exists some Au-Ru interactions. This is based on bulk properties of which we have shown that the Au apparent splitting is dominated by the amount of Au-Au interaction. Once we reach a deposition time of 2 minutes and above the Au $5d_{5/2}$ component shifts towards the Fermi level and the apparent splitting approaches the Au bulk value and the Au $5d$ band appears "bulk-like" (the $d_{5/2}$ component becomes more intense than the $d_{3/2}$ component). This is clearly a turn-on of significant Au-Au interaction and is attributed to a monolayer to multilayer transition.[1] From surface free energy considerations it is expected that Au will wet the Ru surface at least up to a one monolayer coverage. From these results it is clear that further Au growth is not layer by layer but that significant 3-D growth occurs. This is consistent with a Stranski-Krastanov growth mode (S-K). Furthermore, the non-atomic apparent splitting value at low coverages indicates a 2-D island growth mode at sub-monolayer coverages. Both observations have recently been confirmed by STM images of Au on Ru(001).[2] Also, the aforementioned submonolayer Au d-band features are accompanied by an additional feature located ~ 1.5 eV below the Fermi level (noted by the arrows in Figures 7.1 and 7.2). This is clearly observed in the difference

spectrum and its intensity increases with coverage initially then decreases again as the coverage increases to above a monolayer. This indicates that the turn-on of the Au-Au interaction quenches this state. This state is also attenuated by the decreased signal from the Au-Ru interface due to the build-up of Au layers on top of the interface. The appearance of this state at these coverages strongly points to its adsorbate-induced nature. Similar adsorbate-induced states[3] have been noted for Cu adsorption on Ru(001) and for Cu-Ru bimetallics prepared on a Cu surface,[4,5] along with evidence of an S-K growth mode.[6,7]

It is clear from these results that there is a coverage dependence on the valence band features that we are attempting to use to determine alloying behaviour. To avoid confusing coverage effects with alloying effects care must be taken to separate out their contributions to the valence band behaviour. This is easily accomplished by keeping the coverage constant for comparison purposes (i.e. 1 ML Au on Ru(001) compared to 1 ML Au and 1 ML Cu on Ru(001)). The presence of the adsorbate induced states clearly indicates a strong Au-Ru interaction. The relative movement of the Au $5d_{5/2}$ away from the Fermi level and the non-statistical ratio of the two *d*-band components (smaller than expected intensity of the Au $5d_{5/2}$ band) at low coverages again points to the chemically active Au $5d_{5/2}$ band being strongly involved in the Au-Ru interaction. It would be expected then that these states would be quenched once Au-Au interactions dominate.

The most interesting observation in this study is the 2-D behaviour of sequentially deposited Au and Cu overlayers on Ru(001). From the Au on Ru(001) studies we have noted a significant turn-on of Au-Au interactions between 1 and 2 minutes of deposition.

We have interpreted this as arising from saturation by the first monolayer. Therefore a deposition of 2 minutes is used to approximate one monolayer of Au. Since similar coverage dependent features are not exhibited by Cu overlayers the Cu coverage was estimated by comparing the intensities of valence band features (Cu has a cross-section about 70% of the Au value in the photon energy regions studied). More estimates of the coverage were performed later on by TDS where we attempted to maintain similar conditions such as using the same evaporators, sample distance and angles. The depositions were performed at room temperature and each series was annealed to ~ 600 K for 2 minutes.

Figure 7.5 shows a series of valence band spectra of the as-deposited and annealed samples of Au/Cu/Ru(001) and Cu/Au/Ru(001) (henceforth denoted Cu-first and Au-first, respectively) with relevant parameters summarized in Table 7.2.

Deposition Time	$\Delta E_{apparent}$ (±0.1 eV)	Au $5d_{5/2}$ (±0.1 eV)	Au $5d_{3/2}$ (±0.1 eV)
2 min Au	2.5	3.2	5.7
2 min Au + 3 min Cu	2.0	4.0	6.0
2 min Au + 3 min Cu (ann.)	2.0	4.1	6.1
3 min Cu + 2 min Au	2.1	3.9	6.0
3 min Cu + 2 min Au (ann.)	1.9	4.1	6.0

Table 7.2: Au *5d* peak positions and the associated apparent splitting for the series of Au/Cu/Ru(001) and Cu/Au/Ru(001) coverages.

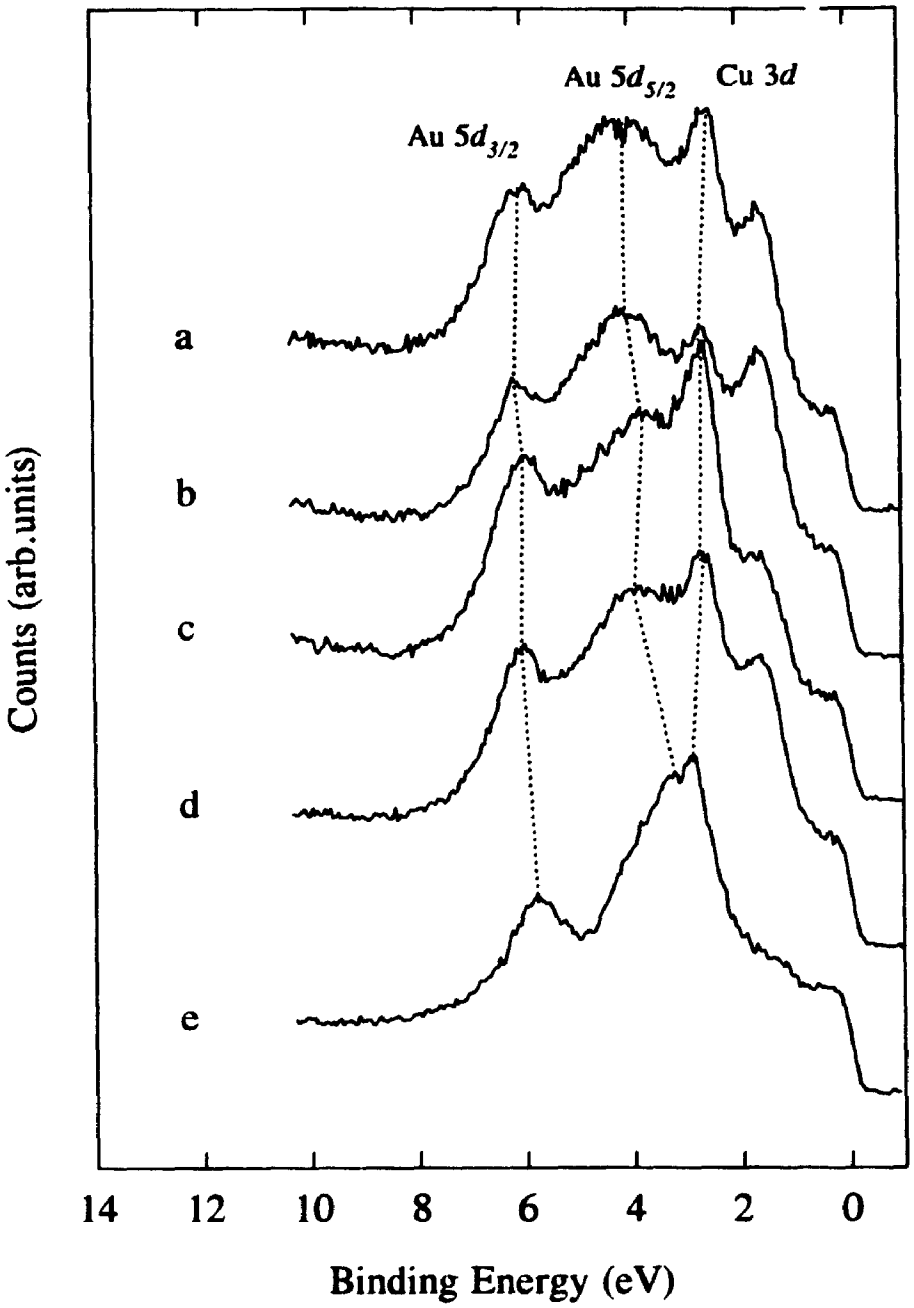

Figure 7.5: Valence band spectra taken at 30 eV for a series of co-deposited Au-Cu systems. (a) 1 ML Au followed by 1 ML Cu; (b) same but annealed for 2 min at 600 K; (c) 1 ML Cu followed by 1 ML Au; (d) same but annealed for 2 min at 600 K; (e) sum of separate 1 ML Au and 1 ML Cu depositions.

Several important observations can be made from Figure 7.5 and Table 7.2. First, all bimetallic spectra (Figure 7.5(a)-7.5(d)) exhibit five distinct bands which are denoted, in decreasing binding energy, the partial densities of state deriving from the Au 5*d* bands ($5d_{3/2}$, $5d_{5/2}$), the Cu 3*d* band, the interfacial alloy *d* bands, and the attenuated upper *d* bands of the Ru substrate. These features are totally uncharacteristic of the individual adsorbate on Ru(001) (Figure 7.5(e)). Secondly, close examination of the spectra of the as-deposited samples reveals that the Au *d* bands of the Au-first sample are at a slightly lower binding energy and have a smaller apparent splitting (Δ) than those of the Cu-first sample. Thirdly, upon annealing, the spectrum of the Au-first sample remains unchanged while the Au *d* bands of the Cu-first sample move towards the Fermi level and this is accompanied by a small decrease in the apparent splitting. In fact it looks exactly the same as those of the Au-first sample.

These photoemission results, along with the observation of a compressed 1x1 LEED pattern, are strong indicators of 2-D alloying at room temperature and can be explained satisfactorily on the basis of the known behaviour of the Au 5*d* and Cu 3*d* bands upon alloying in the bulk.

To accomplish this we compare the "added" spectra of Figure 7.5(e) with those of the as-deposited species. Figure 7.5(a) shows the spectra of ~ 1 ML of Au followed by ~ 1 ML Cu. There is a reduction in the apparent splitting of the Au *d* band of 0.5 eV with the Au $5d_{5/2}$ moving away from the Fermi level. There is an accompanying shift of the Cu 3*d* band towards the Fermi level. This is the exact behaviour observed in the bulk Au-Cu alloys where the reduction in *d*-band splitting is attributed to a dilution of Au-Au

interactions and the relative movements of the *d*-band components is attributed to *d-d* repulsion. The Au *d*-band splitting, especially, points to alloying (versus layer-layer interactions) since the reduction in Au-Au interaction with equal coverages must be due to intermixing of Cu and Au layers. No changes are observed upon annealing indicating that a stable phase is formed. Similar arguments can also be made about the Au/Cu/Ru(001) system with the exception that annealing is required to complete the alloying process. The similarity of the valence band features and the apparent splitting values indicate that similar stable phases are created regardless of the order of deposition. Figure 7.6 is a comparison of a valence band spectrum of bulk AuCu (ordered) with that of the annealed Au-first sample. Two important points are evident from Figure 7.6. First, relative to Au multilayers (Figure 7.1), there is substantial Au *d*-band movement and the apparent splitting has decreased from the Au metal value ($\sim$2.6 eV) to 2.0 eV. Second, the surface alloy spectrum grossly resembles the bulk alloy in the relative positions and apparent splitting of the *d*-band components as compared to the sum of the individual adsorbates (Figure 7.5(e)). There is a small shift of both Au *d*-band components to lower binding energy for the surface alloy. The intensities of the *d*-band components are not comparable due to the different photon energies used and the cross-sectional dependence of these features to the photon energy.

We propose a mechanism for the 2-D alloying behaviour on the basis of adsorption and alloying energetics. To do this we must first examine the adsorption behaviour of both Au and Cu on Ru(001). In Chapter 6 the behaviour of both Au and Cu was outlined as a function of coverage. Monolayer coverages of Au follow a first-

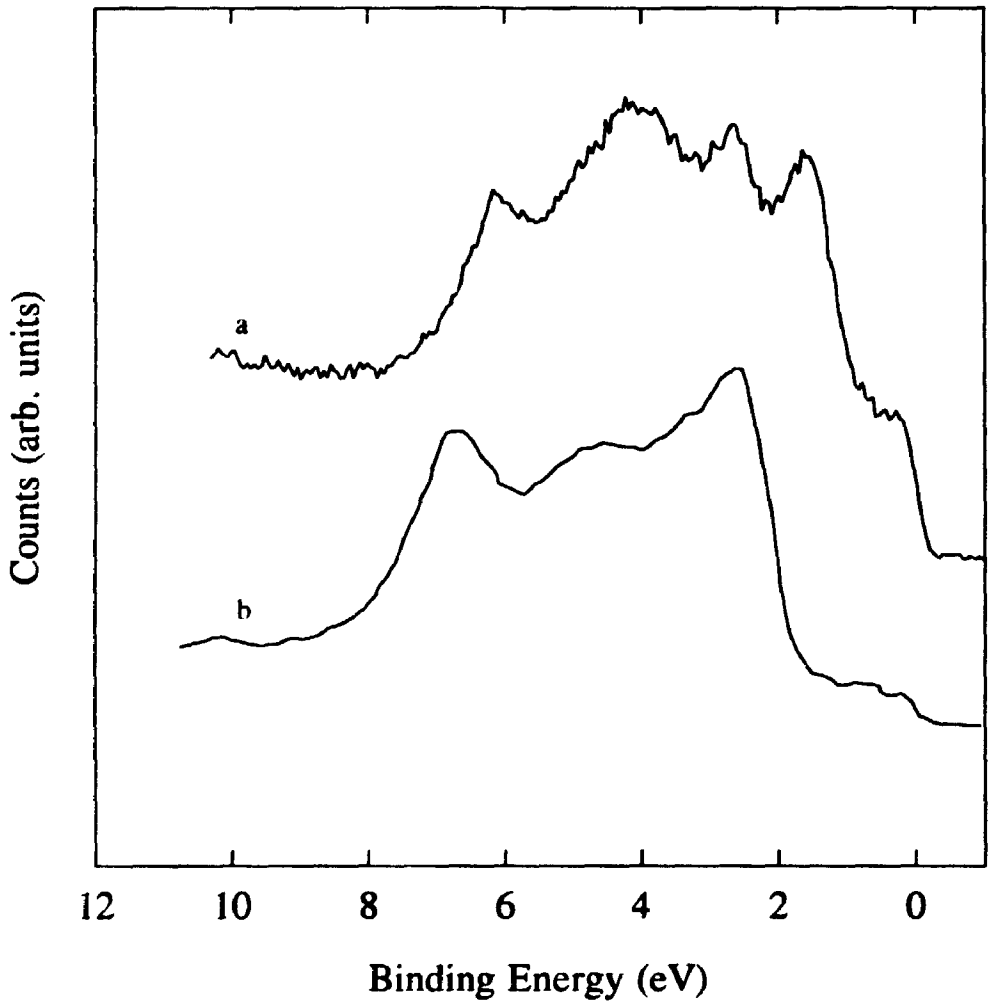

Figure 7.6: Comparison of the valence band spectra of (a) annealed 1 ML Cu on 1 ML Au and (b) AuCu bulk alloy done by XPS.

order behaviour while Cu monolayers follow a pseudo-first-order process. In both systems multilayers follow zero-order kinetics. Given that the adsorption activation energy barrier is close to zero then the desorption energy shown by TDS is the same as the heat of adsorption. Focusing on the monolayer systems, Au has a higher heat of adsorption than Cu. There is a small overlap in temperature at which both species desorb. Figure 7.7 shows the desorption spectra of separate one monolayer coverages and the co-adsorbed coverages. There are some subtle changes that occur for the co-adsorbed system. For Cu, the desorption temperature increases slightly and the profile of the spectra becomes quite symmetric indicating a second-order process. For Au, the temperature of desorption decreases but there is no change to the order of the process. Also of importance is the heat of formation of the various Au-Cu alloys. The heat of formation is favourable for the whole range of Au-Cu compositions and even more so for the ordered Cu_3Au and AuCu systems.[8] Lastly, the role of the substrate must be taken into account.

When the first monolayer is Cu and the second layer is Au, the energies involved are the heats of adsorption of Au and Cu on Ru(001) and heats of formation of Au-Cu alloys. Since the heat of adsorption of Au is higher it is not surprising that Au will diffuse through Cu to reach the Ru-adsorbate interface pushing Cu atoms to the surface and thereby allowing alloy formation. This behaviour is not seen in the bulk at room temperature. This results in the dilution of Au as reflected in the behaviour of the alloy *d*-band components. Similar behaviour has been observed in the 2-D alloying of Au and Ag on Ru(001).[9,10] What is surprising, however, is the 2-D alloying of Au and Cu at

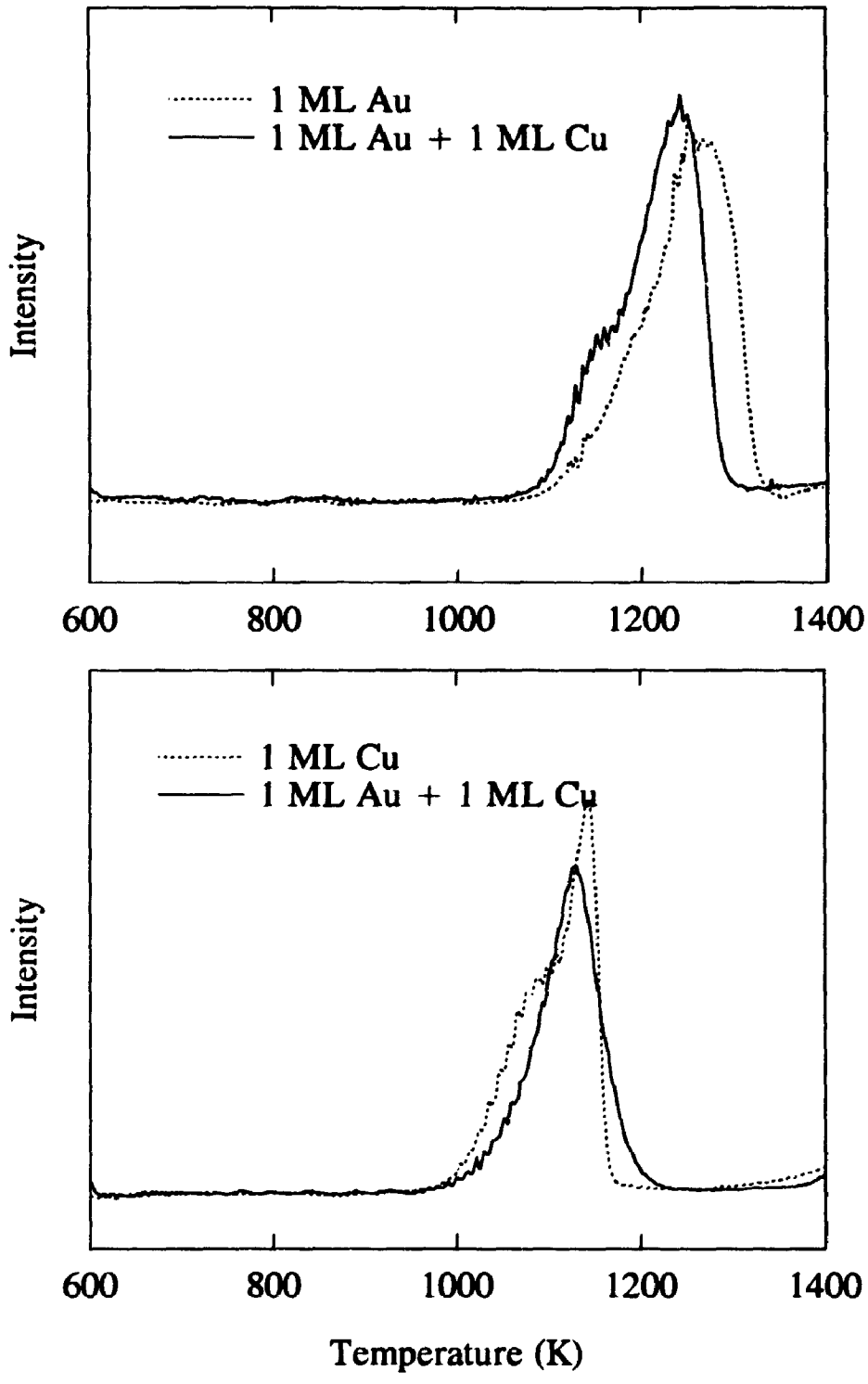

Figure 7.7: Comparison of the TDS spectra of separate 1 ML Au with that of 1 ML Au from alloy (top) and separate 1 ML Cu with that of 1 ML Cu from same alloy (bottom).

room temperature when the first monolayer of adsorbate is Au. In this case the adsorption energetics are not favourable for Cu diffusion through Au to the Ru-adsorbate interface. It must then be the heat of formation of the 2-D Au-Cu alloy that compensates for the difference in the heats of adsorption between Au and Cu. This process is most likely activated by the adsorbate-substrate interaction. It should be noted that in contrast to the Au-Cu results, when the first layer is Au, 2-D alloying of Au and Ag on Ru(001) was only observed at elevated temperatures (>350 K).[9,10] This difference may be accounted for by the trend of heat of adsorption for the first monolayer on Ru(001) of metals of interest, that is Au > Cu > Ag, and the less favourable heat of formation for Au-Ag alloys.[8] With these factors, even with the possible influence of the substrate, the large differences between the heat of adsorption for Au and Ag with a smaller difference from the heats of formation cannot be overcome. It is also interesting to note that Cs adsorbed on a monolayer Au-covered Ru(001) does not form an alloy at any temperature with Au despite the fact that Cs and Au form a stable AuCs compound in the bulk.[11,12,3] The difference in the heats of adsorption for the two species is quite large.

The changed behaviour of the Cu desorption in the alloy can be attributed to the breaking of the Au-Cu bonds and migration to the surface before desorption. For Au, the lower temperature desorption can be attributed to the small overlap with the Cu adsorption and the possibility of large 3-D cluster formation caused by segregation which would allow for more bulk-like desorption behaviour (i.e. at lower temperatures).

We have reported observations of 2-D alloying of Au and Cu on Ru(001) using photoemission with emphasis on the sensitivity of the *d*-band components upon alloying.

It emerges from these initial studies that two factors are important: first, the difference in the energetics of the adsorption of the first monolayer; second, the activation energy and heat of formation of the alloys and its possible modification by the substrate.

Since the bulk valence band behaviour has been shown for the surface alloys, a remaining question is whether the same applies for the core level behaviour (i.e. charge compensation model). Also, the alloying behaviour of Au-Cu alloys of different stoichiometries needs to be studied to find out if such alloys also can be formed and from this the influence of the substrate can be determined by the changing the deposition order and amount of coverage.

7.3 Grasshopper Core Level Data

A series of valence band and Au 4*f* core level data were taken for various combined Au-Cu coverages on Ru(001). Depositions were performed at a crystal temperature of 340 K while measurements were carried out at room temperature. Unlike the previous SS Seya study various Au-Cu stoichiometries were studied, especially those ratios which have an order-disorder transition in the bulk, namely Cu_3Au, AuCu, and Au_3Cu. Although the coverages that were measured by TDS vary slightly from the exact stoichiometric values desired (up to $\pm 10\%$), for simplicity the values quoted will be rounded to the nearest integer. We attempted to create each alloy by monolayer depositions, i.e. 3 ML Cu + 1 ML Au for Cu_3Au. For each series reverse deposition was carried out and the system annealed to ~ 600 K for 5 minutes.

The main purpose of this study was not only to focus on the valence band behaviour but also to evaluate any Au 4*f* core level shifts in the framework of the charge compensation model. The valence band data were taken at 70 eV, both to maximize the cross-section but also to maintain reasonably high flux from the 1800 lines/mm grating and also to retain high resolution. Au 4*f* core level data was taken at 170 eV for similar reasons. At these photon energies the kinetic energy of the photoelectrons is ~ 60 and 80 eV for the valence band and Au 4*f* core levels, respectively. This means that with an electron escape depth on the order of 5-7 Å, the majority of the signal comes from the first three layers, making it extremely surface sensitive. The Au 4*f* core level data have been normalized to the initial photon flux using a Ni mesh (an exception is the 3 ML Au

data which were taken when such equipment was not available).

This section will be organized as follows: first, we examine the separate depositions for 1 and 3 ML of Au and also 1 and 3 ML of Cu; second, we examine each stoichiometric ratio separately; lastly, we summarize the overall relationship between the stoichiometry, deposition order, and the effect of annealing.

Separate Depositions of Au and Cu on Ru(001)

Before we attempt to correlate any core level shifts and valence band changes to possible alloying behaviour, the coverage dependence of both valence band behaviour and core level behaviour must be examined. In the SS Seya study the effect of the coverage of Au and Cu on valence band features has already been discussed.

We now focus on the effect of coverages of Au on core level shifts. Different chemical environments will manifest themselves as core level shifts. For bulk Au, including Au supported on Ru(001) on the order of a few monolayers and greater, there are two distinct Au environments, that of the bulk and that of the surface. With a surface sensitive technique and good resolution there will be contribution to the photoelectron signal from both Au sites. The surface Au atoms have been shown to have a lower binding energy on the order of 0.3 to 0.4 eV. There is *d*-band narrowing at the transition metal surface due to a lower number of neighbours to contribute to the *d*-band width (for close-packed surfaces the surface atoms have only 9 nearest neighbours as compared to 12 in the bulk). This will effect the relative core level positions since both the bulk and the surface must maintain a common Fermi level in a metal. There are two

possible shifts which are dependent on the occupancy of the *d* band. With a *d* band less than half-filled the equalization of the Fermi levels manifests itself as a relative shift to higher binding energies. For the case of a transition metal with more than a half-filled *d* band, and in our case, a noble metal with a "full" *d* band, the shift is to lower binding energies. The shift has been shown to be roughly equivalent to the deviation from the half-filled *d* shell, therefore it will be largest for both Au and Cu.[14] For bulk Au a $4f_{7/2}$ value of 84.0 eV is accepted and a corresponding value of 83.65 is accepted for the surface $4f_{7/2}$ core level.

For a single monolayer of Au on Ru(001) there is also a "surface-like" core level shift relative to the binding energy for bulk Au. The direction and amount of this shift is modified due to charge transfer from Au-Ru interactions. From electronegativity arguments it would be expected that, since Au is the most electronegative metal, charge should flow from Ru to Au leading to, at first glance, a decrease in the Au 4*f* binding energy. But Au and Ru do not form stable alloys in the bulk. Nevertheless, there must be some interaction since there is a strong chemisorption bond as evidenced by TDS. This interaction could be through polarization or charge transfer following the charge compensation model which has been seen for a variety of Au-intermetallics. In the case of charge compensation there would be a positive contribution to the Au 4f binding energy. There may also be a breakdown in the electronegativity argument since this argument is based on bulk electronic behaviour. It has been stated that for a variety of monolayer covered transition metal surfaces the changed electronic distribution of both the overlayer and metal surface (changes in the pure and hybrid orbitals used in

bonding), as compared to the bulk, can lead to a change in relative electronegativities and that the charge flow is in the opposite than expected direction.[15,16,17] For Cu on Ta(110) there is a positive Cu $2p_{3/2}$ binding energy shift relative to the surface atoms on Cu(100), while a negative binding energy shift has been found for Cu on Ru(001).[18] These core level shifts have been rationalized as charge transfer from Cu to early transition metals (less than half-filled *d* shells) and charge transfer to Cu from late transition metals due to the fact that Cu has a half empty 4*s* valence band which can transfer and receive charge dependent on the occupancy of the host metal surface.[19] Care must be taken, however, since it has been shown that not only is the amount of charge transfer important but also the nature of the charge. By invoking the charge compensation model the positive core level shifts for Cu on Ta(110) can be rationalized by a loss of *d* charge from Cu but with an overcompensation of *s-p* charge which agrees with the bulk electronegativity values (Cu > Ta). Similarly, the negative core level shifts of Cu on Ru(001) can be explained since Ru has a higher electronegativity than Cu. This has been accomplished without attempting to determine adsorbate and substrate surface electronegativity changes. Surface extended X-ray absorption fine structure (SEXAFS) studies either at the Cu K or $L_{2,3}$ edges would resolve the role of the Cu *d* valence electrons. Similar studies have not been performed for monolayer Au coverages on Ru(001) but since Au has a higher electronegativity than Ru we could expect a positive binding energy shift of the Au on Ru(001) Au 4f core levels as compared to the Au on Au (bulk).

For coverages beyond 1 ML, specifically 3 ML, the growth mode of Au will

determine the type of Au atoms that will contribute to the photoelectron spectrum. Given that the first monolayer of Au wets the Ru surface and subsequent depositions do not completely wet the previous layer leading to 3-D islands, we would then expect a variety of chemically different Au species. There would be those Au atoms which are at the surface of a bulk-like cluster of Au atoms, Au atoms which at the Au-Ru interface and exposed, atoms at the Au-Ru interface and covered by Au atoms, and bulk-like Au atoms within the clusters (Figure 7.8). With these many possible contributions deconvolution of each species from a Au 4*f* photoelectron spectrum becomes quite difficult.

Figures 7.9 and 7.10 show the Au 4*f* and valence band spectra of 1 ML and 3 ML of Au on Ru(001), respectively. Each spectra was fitted using a many-body lineshape (Doniach-Šunjić)[20] convoluted with a Gaussian to account for photon and instrumental resolution (and also inherent phonon broadening). Asymmetry on the high binding energy side of the photoelectron peak is observed for core levels of all metals. The asymmetry is due to a variety of sources. There are extrinsic energy losses to the photoelectron as it travels through the solid. If there is a high density of density states at the Fermi level, promotion of low-lying electrons near the Fermi level into the conduction band can occur upon interaction with the outgoing photoelectron (shake-up). The D-S lineshape is based on an intrinsic energy loss mechanism involving coupling of the core hole and the screening conduction electrons.[21,22,23] Simply stated, a high density of *d* states at the Fermi level leads to a higher asymmetry given by the singularity index, α. Therefore, Au and Cu will have a lower asymmetry than the transition metals due to a lower density of states at the Fermi level.

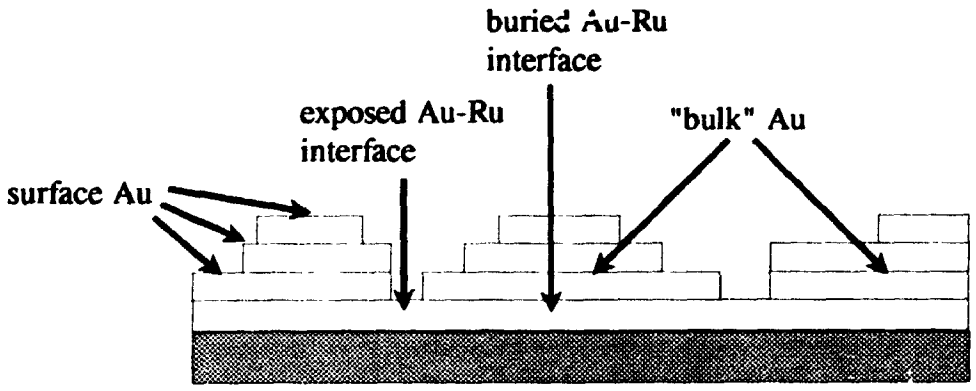

Figure 7.8: Schematic of the growth of 3 ML of Au on Ru(001). Chemically different Au species are indicated.

For 1 ML of Au the position of the Au $4f_{7/2}$ level is given to be 83.88 eV. This value is lower than for bulk Au at 84.0 eV but higher than that of Au on Au(bulk) at 83.65 eV. This indicates that there is some contribution to the core level energy from Au-Ru interactions (the Au-Ru interaction has been shown by the presence of interfacial states as outlined in the SS Seya study). The asymmetry parameter, given by α, is small as predicted. The valence band spectrum shows similar features as discussed in the SS Seya study. The splitting is similar at $\sim$2.5 eV, somewhere between the atomic value of 1.5 eV and the bulk value of 2.7 eV. The dashed line in the valence band spectrum represents the spectrum after normalization to the first Ru *d*-band feature and subtraction of the Ru spectrum. There is a small error involved since we have ignored the contribution to the signal from the Au *s-p* band and the attenuation of the Au-covered Ru signal. The TDS spectrum shows that we have a 1 ML coverage as indicated by the first-order desorption and the very small onset of the lower temperature multilayer peak. The coverages have also been calibrated by a series of Au (and also Cu) depositions as described in Chapter 6.

For the 3 ML Au coverage we see a distinct shoulder on the higher binding energy side of each peak and therefore each level was fitted with two peaks. Higher resolution would be required to justify more than two peaks. The two components are positioned at 83.64 and 83.99 eV with the higher binding energy component having a slightly larger full width at half-maximum (FWHM). The areas of the two are similar. Using electron escape depth considerations, the 1 ML Au results, the surface core level results, and Figure 7.8, we can tentatively assign the origin of the peaks. The peak

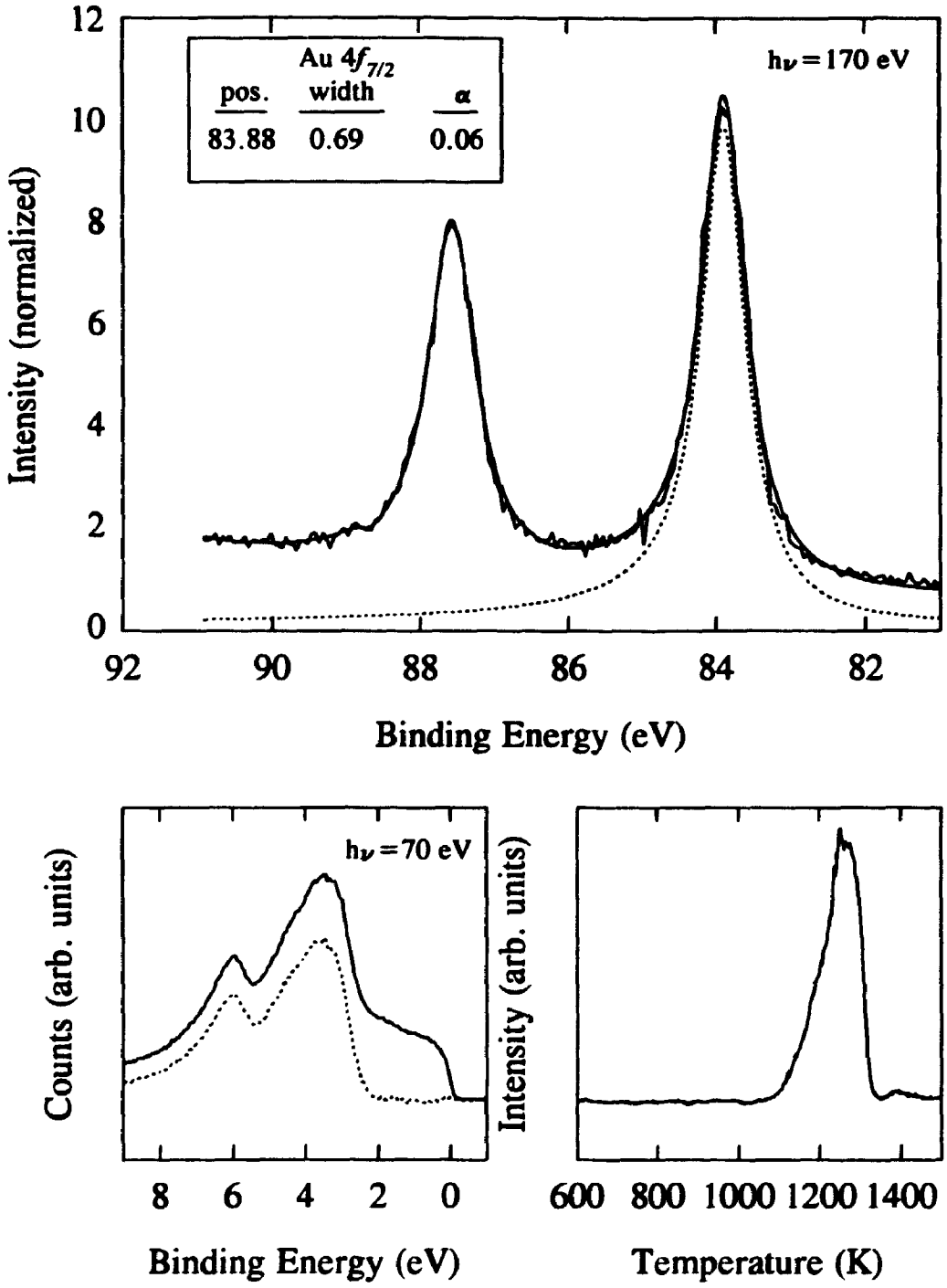

Figure 7.9: Photoemission and TDS results for 1 ML Au on Ru(001). Au 4*f* core level (top) and valence band (bottom left) spectra along with the resultant TDS spectra (bottom right).

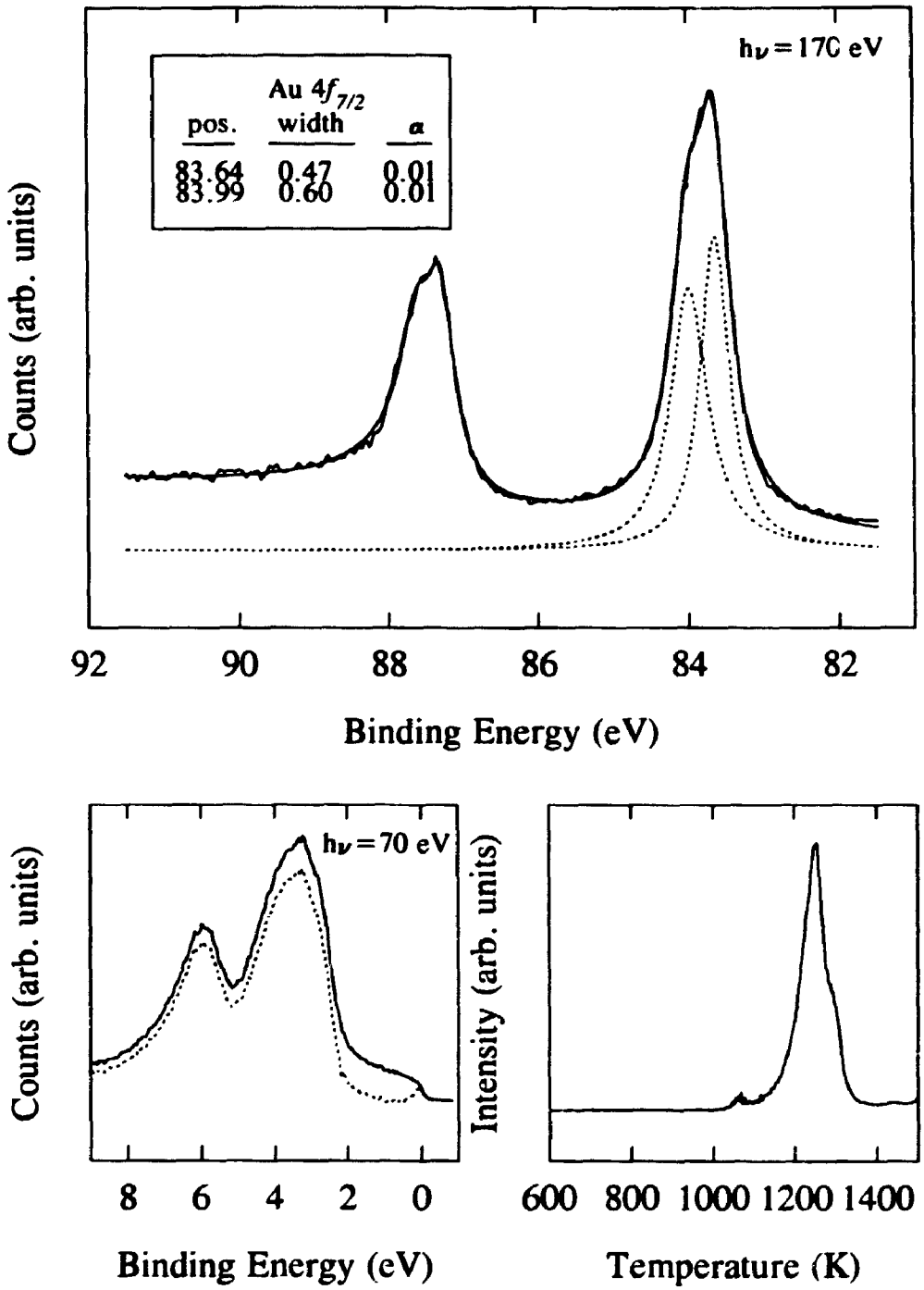

Figure 7.10: Photoemission and TDS results for 3 ML Au on Ru(001). Au 4*f* core level (top) and valence band (bottom left) spectra along with the resultant TDS spectra (bottom right).

positioned at 83.64 eV has a value which is the same as a Au on Au(bulk) surface peak, much lower than a bulk Au peak but lower to that of 1 ML Au on Ru(001) and therefore is assigned to be due to the Au surface atoms. The higher energy component with a value close to bulk Au is assigned to be due to the large number of Au atoms in the 3-D clusters. The similar areas is not surprising since although there are a larger number of atoms in the second and third layers their signal will be largely attenuated by the short electron escape depth. Not much of a signal is expected from those atoms buried deep in the clusters and the buried Au-Ru interface since the electron escape depth is ~ 7 Å.

The valence band spectra, again, is similar to that seen for the SS Seya study with a bulk-like apparent Au 5*d* splitting of 2.6 eV. The dashed line shows the spectra after normalization to the first Ru *d*-band feature and subsequent subtraction of the Ru component. As compared to the 1 ML Au coverage there is now a larger error since the ignored Au *s-p* band will now have a larger contribution to the signal at and near the Fermi level and the attenuation of the signal from the Ru substrate has been increased.

Figure 7.11 shows the valence band spectrum for both 1 ML and 3 ML Cu on Ru(001) with their respective TDS results. Both spectrum have been normalized and the Ru signal subtracted as described above. The TDS spectra show the pseudo-first-order desorption for monolayer Cu and other results[24] have shown the zero-order desorption of the multilayers. The desorption temperature for both components is lower than for Au.

All the subtracted spectra will be added to simulate the expected valence band behaviour of the co-deposited layers if no intermixing were to occur. They retain their

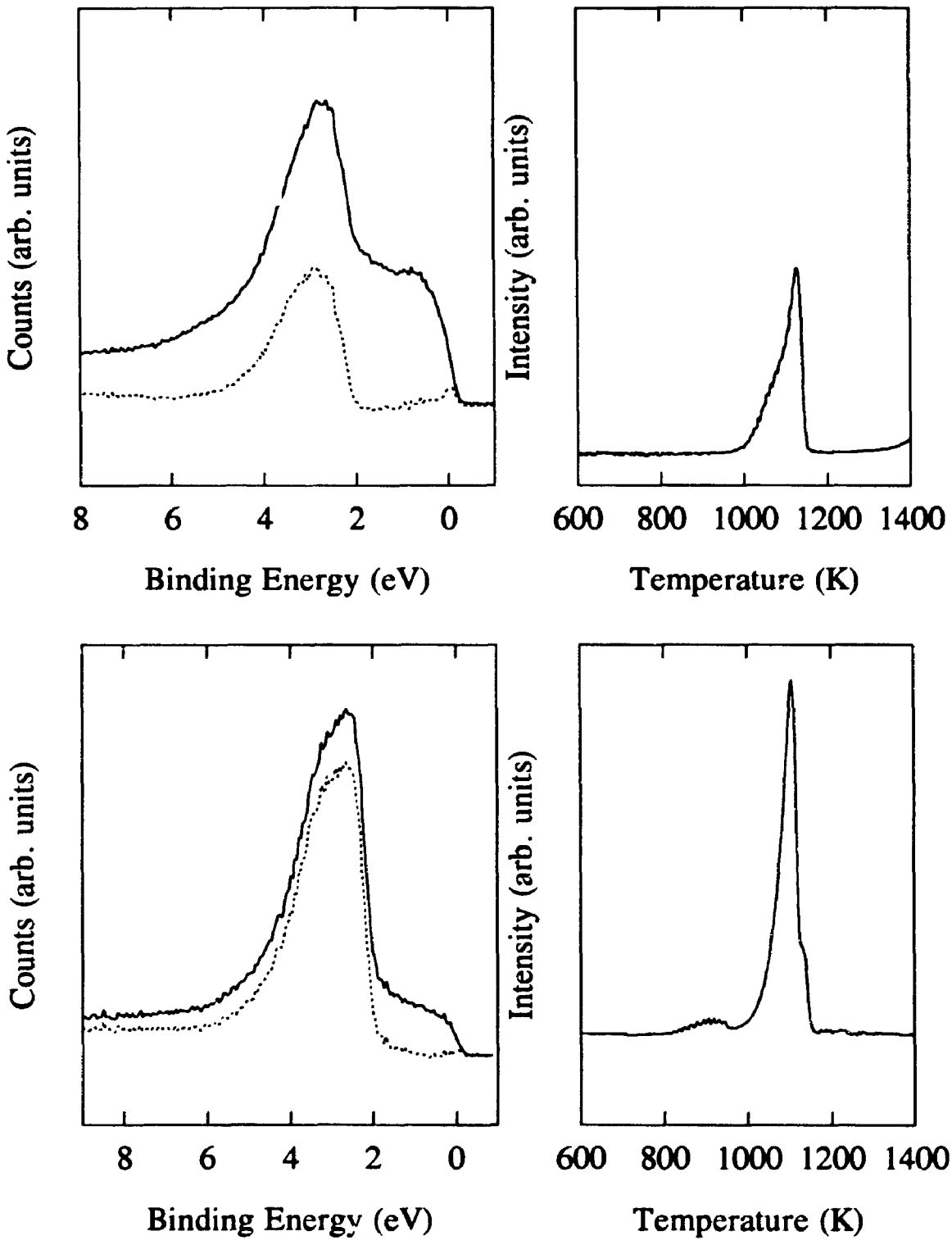

Figure 7.11: Photoemission and TDS results for 1 and 3 ML on Ru(001). 1 ML Cu valence band spectrum (top left) and TDS spectra (top right). 3 ML Cu valence band spectrum (bottom left) and TDS spectrum (bottom right).

layered structure). For coverages higher than 1 ML of each species there will be some error since attenuation of the experimental signal must be accounted for.

3 ML Cu and 1 ML Au

We first examine the 3 ML Cu/1 ML Au on Ru(001) and 1 ML Au/3 ML Cu coverages. Figures 7.12 to 7.15 summarize the Au 4*f* core level positions, valence band behaviour, and the associated desorption behaviour.

Figure 7.12 shows the Au 4*f* spectra, with the fit of the Au $4f_{7/2}$ core level, of the 1 ML Au/3 ML Cu/Ru(001) system (in this notation 3 ML of Cu was deposited first followed by 1 ML Au) as deposited (top) and annealed (bottom). The spectra show no discernible multiple components so a single component was fitted. The as-deposited peak position is located at 83.99 eV with a shift to 84.16 eV for the annealed sample. The widths are on the order of 0.6 to 0.7 eV and the asymmetry parameter is small. The intensity of the peaks (area) is much smaller and the core level position higher than for the 1 ML on Ru(001) sample (Figure 7.9). The peak positions are also much higher than for Au surface atoms on Au(bulk).

Because of the reduction in the intensity, it is clear that the Au atoms no longer reside completely on the surface and upon deposition migrate into the bulk-like Cu. This is unlike results seen for Au monolayer deposition on 10 ML (and greater) Cu on Ru(001) in which no migration of the Au surface layer was noted until higher temperatures.[25] Upon annealing the intensity is maintained but a substantial shift occurs.

Figure 7.13 shows the valence band behaviour of both the as-deposited and

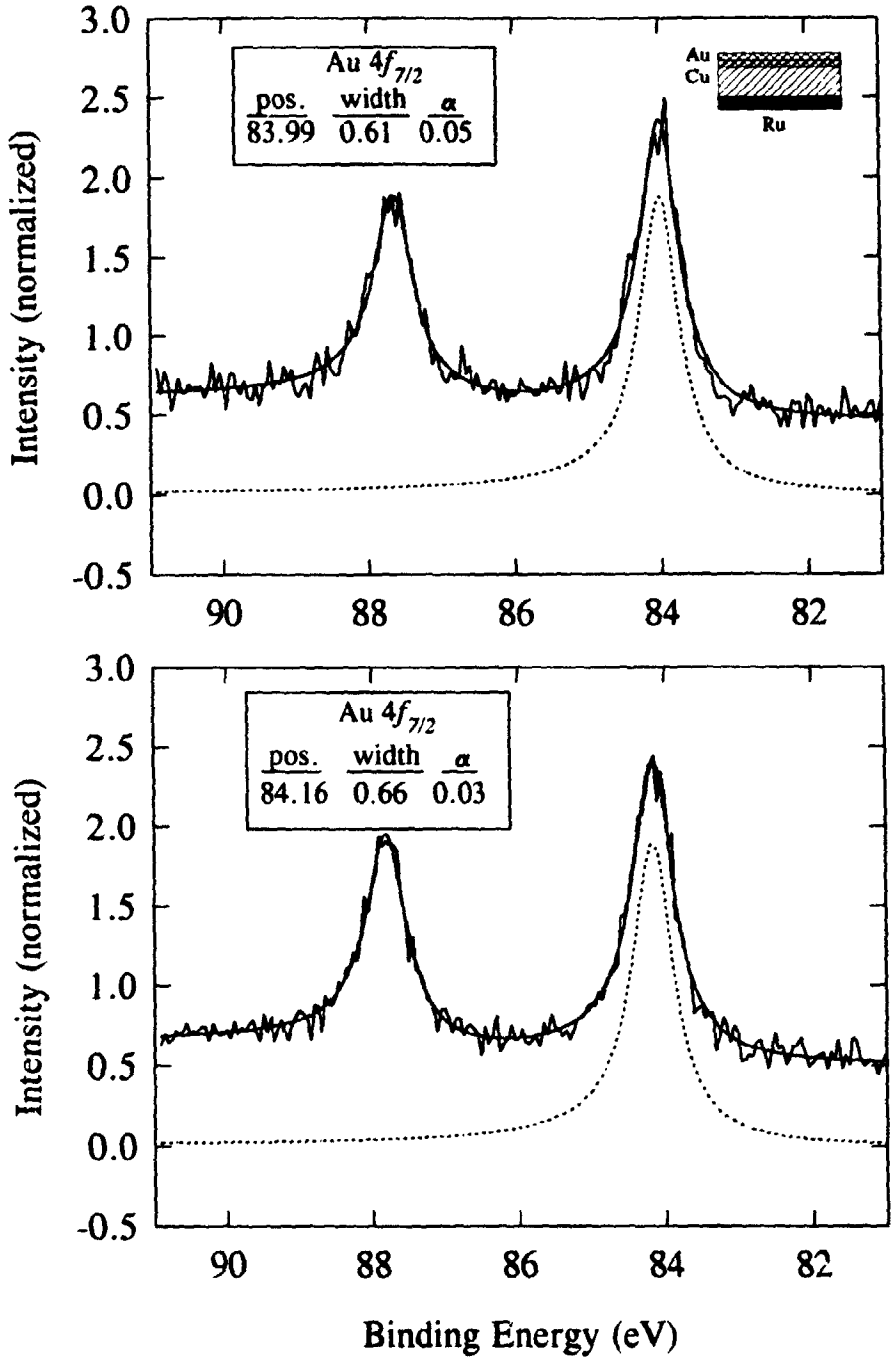

Figure 7.12: Au 4*f* spectra for 1 ML Au/3 ML Cu on Ru(001). Spectra of as-deposited system (top) and after annealing for 5 min at 600 K (bottom).

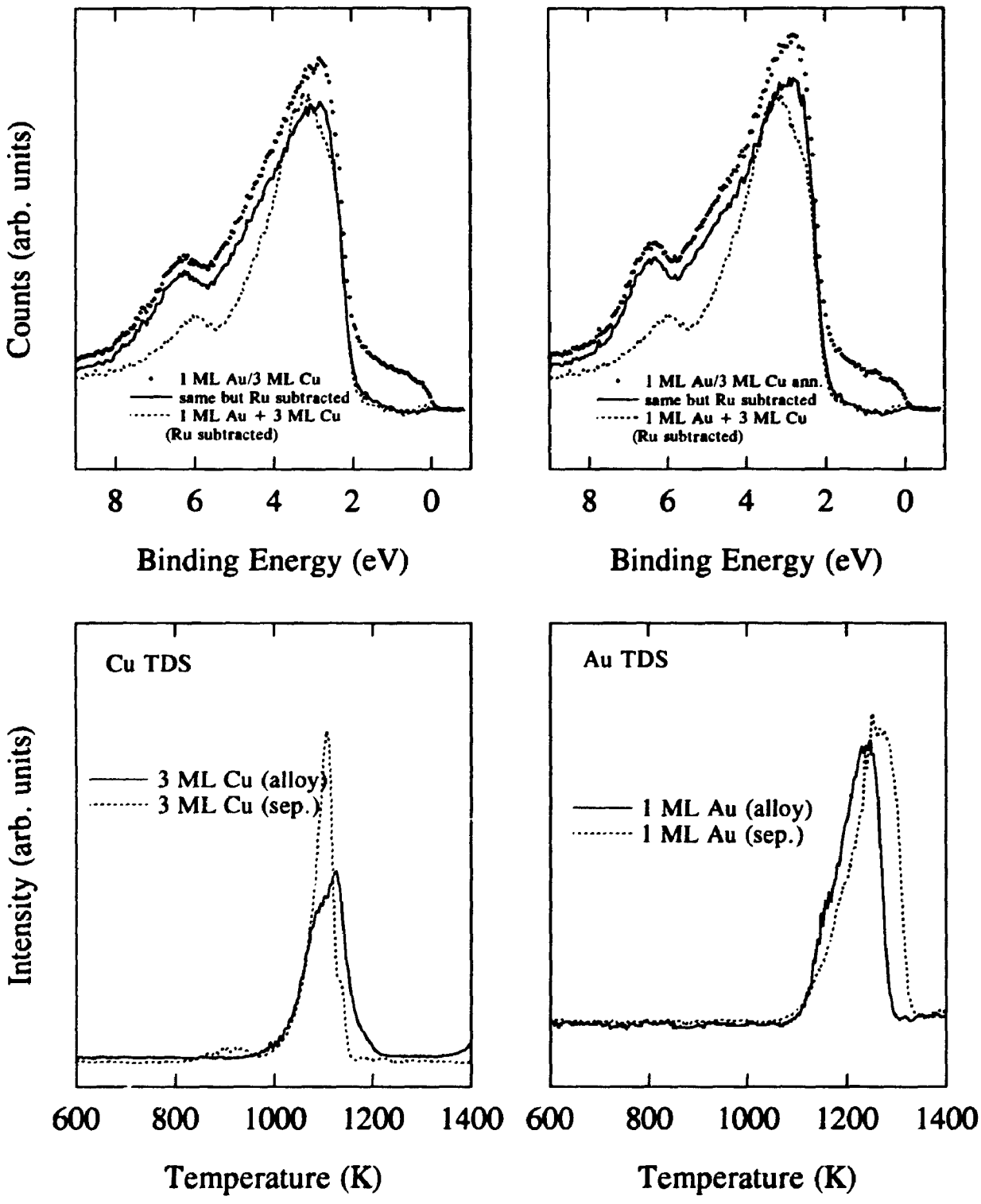

Figure 7.13: Valence band and TDS spectra for 1 ML Au/3 ML Cu on Ru(001). Spectra of as-deposited system (top right) and after annealing for 5 min at 600 K (top left). TDS results at bottom.

annealed samples (top) and the results of the subsequent desorption (bottom). Focussing on the as-deposited sample, we note some subtle differences between the subtracted experimental spectrum and the subtracted added spectra. We clearly see in all the valence band spectra the presence of the Au $5d_{3/2}$ band at ~ 6 eV. The Au $5d_{5/2}$ band is not resolved but knowing the position and extent of the Cu *d* band we can attribute contribution to the valence band spectra from this band in the region of 4 to 5 eV. Also we must account for possible attenuation effects that are not accounted for in the added spectra. Nevertheless, we can clearly see a shift of the Au $5d_{3/2}$ component away from the Fermi level and the added Au $5d_{3/2}$ component. This behaviour has been noted for the monolayer valence band study although its movement is not as dramatic as that of the Au $5d_{5/2}$ band. Accompanying this is an increase in the density of states between 4 and 5 eV which cannot be compensated for by increasing the Au contribution in the added spectra. This is typical valence band behaviour upon alloying and therefore we conclude, along with the core level attenuation and shift that alloying (intermixing) does occur upon deposition. The expected movement of the Cu *d* band towards the Fermi level is not as evident, since determining the position of the Cu centroid from these valence band spectra is very difficult, although there appears to be a higher density of states near the Fermi level for our sample.

Now we examine the annealed sample. Again there is a shift of the Au $5d_{3/2}$ band which is now even more pronounced than for the as-deposited sample. Similarly, there is a further increase in the density of states between 4 and 5 eV which we attribute to the presence of the Au $5d_{5/2}$ band. Lastly, there is an increased density of states near the

Fermi level although this may be attributable to an increase in the Cu signal to the valence band spectra.

From the valence band and core level results we can conclude that alloying does indeed occur upon deposition and that further alloying occurs upon annealing. The adsorbed monolayer of Au diffuses into Cu forming an alloy with a high Au concentration. Upon annealing further migration occurs and the alloy formed has increased Cu concentration (decreased Au concentration). This argument is based on the results of the bulk studies. For alloys with small Cu concentrations, the core level shifts are smaller and the changes in the valence band features are less obvious. With increased Cu concentration there is a shift of the Au core levels to higher binding energies, a reduction in the apparent Au 5*d* splitting (because of dilution of Au-Au interactions), and the increased effect of *d-d* repulsion. All of these bulk observations are evident here.

The TDS results show again, as pointed out in the SS Seya study, changes to the desorption behaviour of both Au and Cu. The Cu desorption shows a non-zero-order process and is shifted to higher temperatures. There is a small multilayer desorption peak as indicated by the lining up of the rising edge of the separate 3 ML Cu spectrum with that of the alloy. The alloy Au desorption follows the same process as exhibited by that of 1 ML Au but is shifted to lower temperatures.

We next examine the 3 ML Cu/1 ML Au on Ru (001) system. The Au 4*f* core level is found at 84.01 eV with no shift upon annealing. The Au signal is attenuated and increases upon annealing. The widths are comparable and the asymmetry is small. The

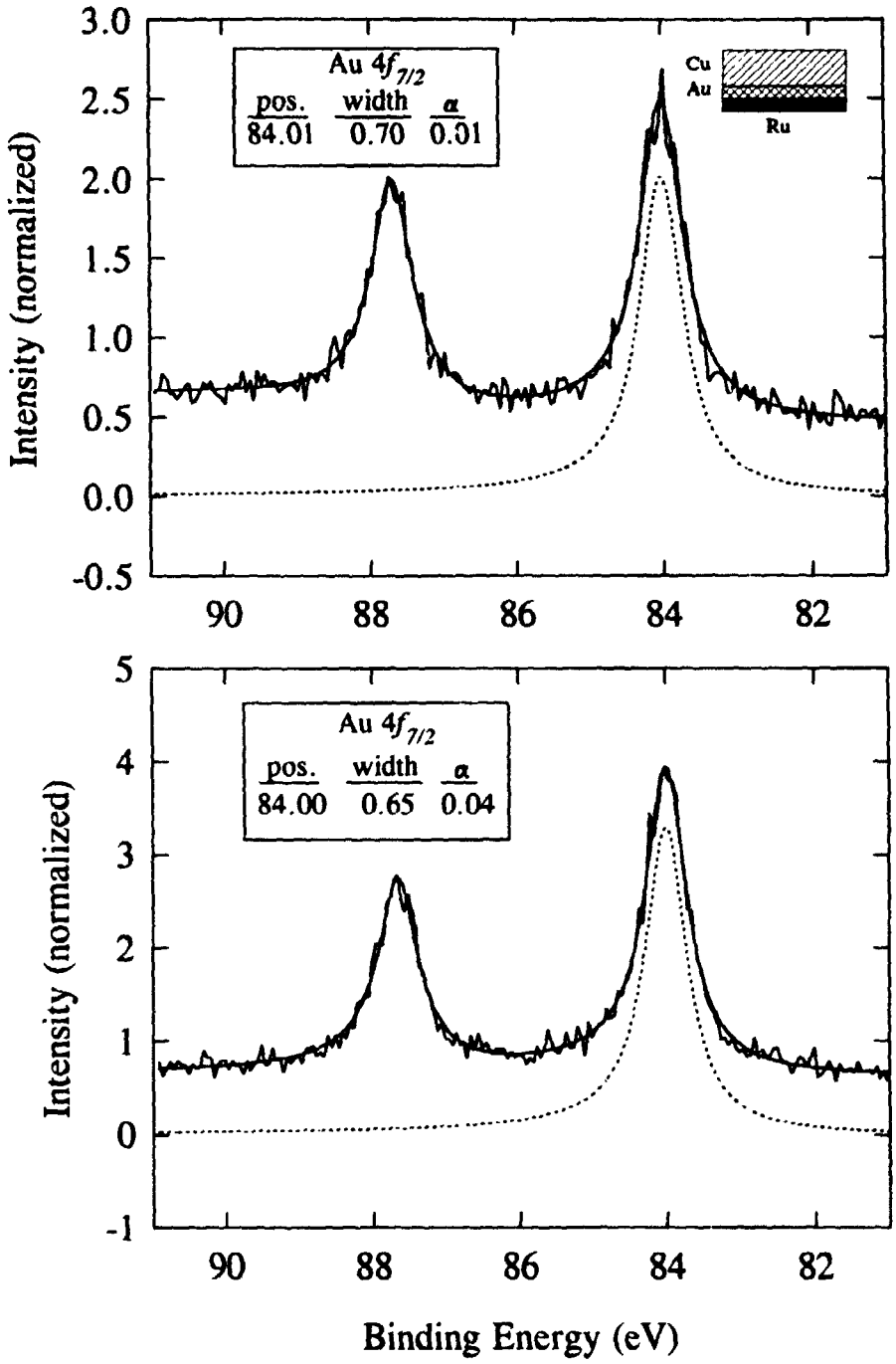

Figure 7.14: Au 4*f* spectra for 3 ML Cu/1 ML Au on Ru(001). Spectra of as-deposited system (top) and after annealing for 5 min at 600 K (bottom).

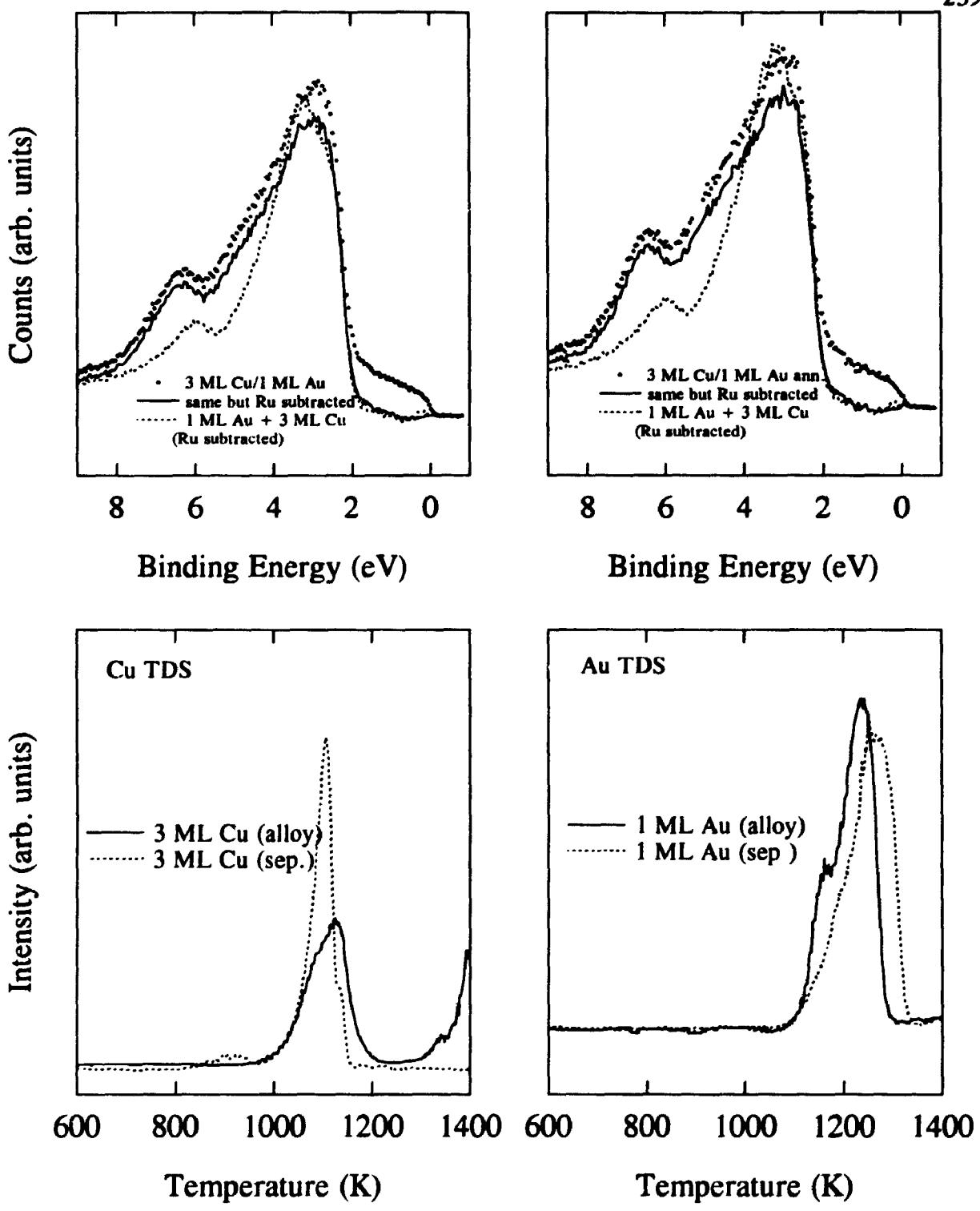

Figure 7.15: Valence band and TDS spectra for 3 ML Cu/1 ML Au on Ru(001). Spectra of as-deposited system (top left) and after annealing for 5 min at 600 K (top right). TDS results at bottom.

valence band features show the same shift of the Au $5d_{3/2}$ level away from the Fermi level and also indicate an increased density of states from the movement of the Au $5d_{5/2}$ away from the Fermi level due to *d-d* repulsion and a reduction in the apparent Au 5*d* splitting due to dilution. No discernible changes at the Fermi level from the Cu *d*-band movement is detected. Upon annealing, the Au $5d_{3/2}$ band intensifies as does the signal in the 4 to 5 eV region indicating further movement of the Au $5d_{5/2}$ band.

The valence band behaviour indicates that alloying does occur. It is most likely that for the as-deposited system there is little intermixing (low Cu concentrations) but that an alloy with a higher Cu:Au ratio is formed by annealing. The core level spectra do show an increase, upon annealing, in the Au signal indicating that Au is migrating from the Au-Ru interface. The fact that a Au signal is evident from a system in which the Au monolayer is covered by three monolayers of Cu with an escape depth only 5-7 Å, indicates that Cu does not grow layer by layer on Au/Ru(001) and therefore the buried Au signal can still be detected. The core level positions do not shift detectably upon annealing, indicating that the final alloy must still have a relatively high Au concentration.

The TDS results are the same as described for the 1 ML Au/3 ML Cu on Ru(001) system.

Overall these results indicate that the order of deposition is important in determining the final alloy that is formed. For the case in which Au is deposited on Cu, the Au atoms migrate through Cu to try to reach the Ru interface, as has been shown for monolayer coverages. Since Cu has the same growth mode as Au, the initial deposition

of Au will result in some Au atoms within one layer of the substrate and therefore under its influence (Au has a higher heat of adsorption than Cu). For the case in which we have Cu on Au, a high Au concentration alloy is formed near the Ru interface. The same alloy is not formed in both cases.

3 ML Au and 1 ML Cu

The core level shifts and valence band behaviour of the 1 ML Cu/3 ML Au on Ru(001) system are shown in Figures 7.16 and 7.17. The widths and shape of the Au 4*f* peaks indicate more than one contribution to their signal. We have fitted them with two components locating them at 83.79 and 84.14 eV. Upon annealing both components shift to lower binding energy to 83.75 and 84.06 eV, respectively. For the as-deposited species we attribute the low energy component to Au surface atoms and the higher energy component to Au atoms in the bulk. Both values are shifted to higher energies due to Au-Cu interactions. The high values indicate a high Cu:Au ratio. Upon annealing the Cu migrates further and a lower Cu:Au ratio alloy is formed lowering the component binding energy values. This is also shown by the increased intensity of the Au signal showing a larger amount of Au atoms near the surface.

The valence band spectra are not as clear. Although there appears to be a contribution of the Au $5d_{5/2}$ band in the region of 4 to 5 eV and movement of the Au $5d_{3/2}$ band away from the Fermi level for the as-deposited system, these effects seem to disappear upon annealing. The answer to this is the surface sensitivity due to the energy of the photons leading to an electron escape depth very close to the minimum of 5 Å.

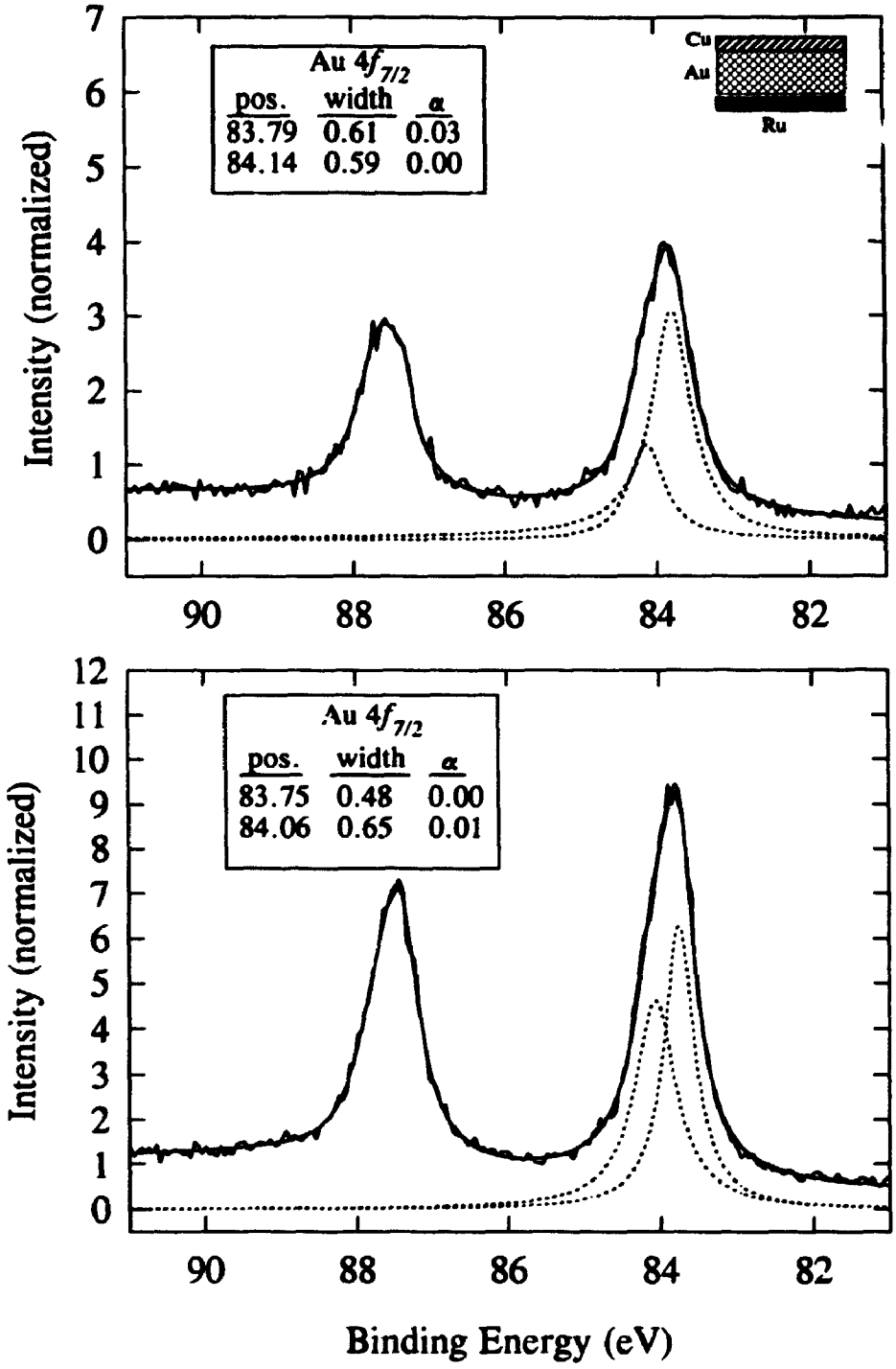

Figure 7.16: Au 4*f* spectra for 1 ML Cu/3 ML Au on Ru(001). Spectra of as-deposited system (top) and after annealing for 5 min at 600 K (bottom).

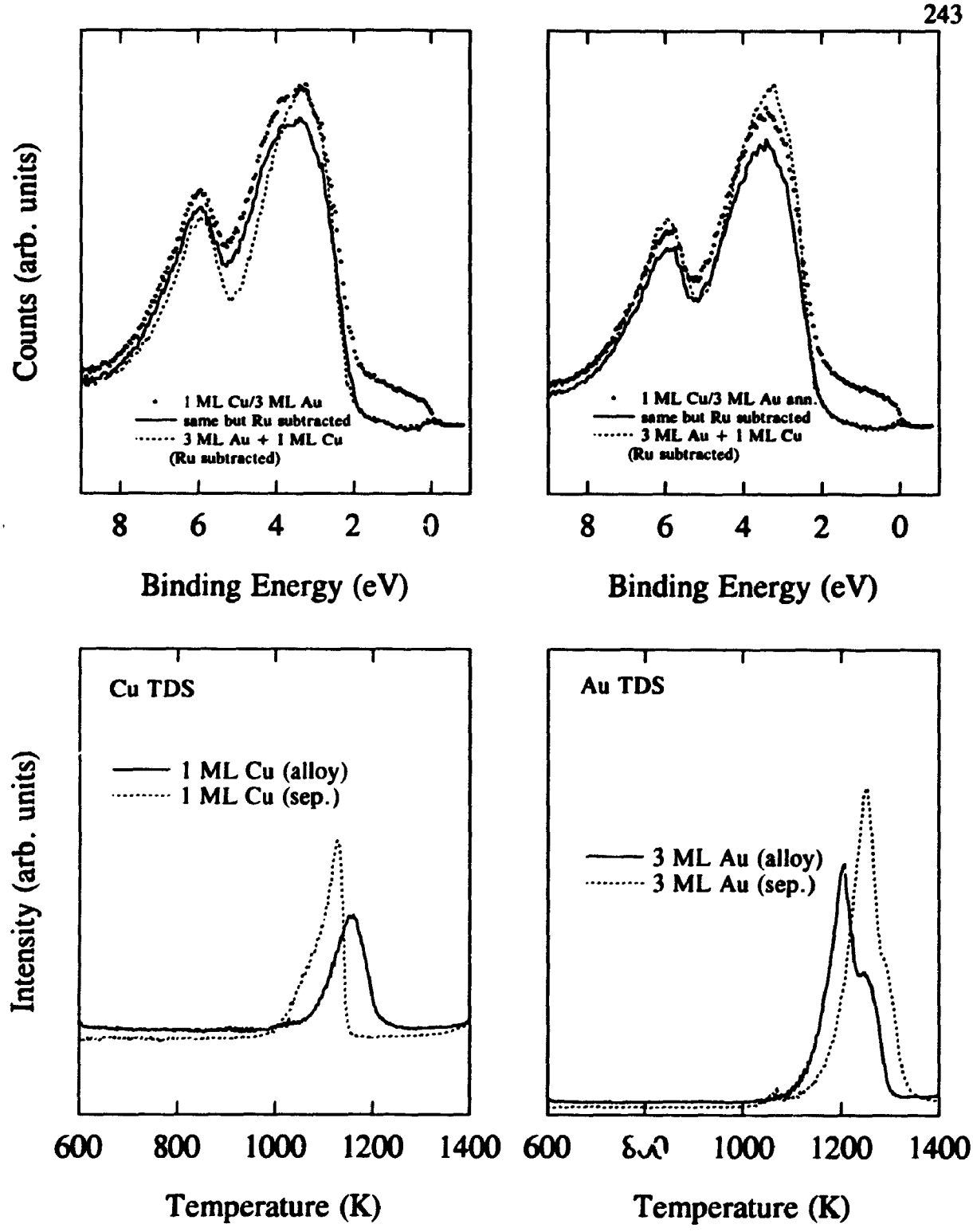

Figure 7.17: Valence band and TDS spectra for 1 ML Cu/3 ML Au on Ru(001). Spectra of as-deposited system (top left) and after annealing for 5 min at 600 K (top right). TDS results at bottom.

It is clear that with annealing and further migration of the Cu into Au that the remaining top layer is dominated by Au and the spectra show a decreased sensitivity to the Au-Cu interactions.

The TDS spectra are consistent with those described previously in that the monolayer Cu desorption shifts to higher temperatures and no longer follows a pseudo-first-order desorption process while the 3 ML Au alloy retains its multilayer zero-order and monolayer first-order kinetics but is shifted to lower temperatures.

The results for the 3 ML Au/1 ML Cu on Ru(001) system are shown in Figures 7.18 and 7.19. Again, for both core level spectra, we see a large linewidth and asymmetry indicating more than a single contribution to the photoelectron signal. We have fitted the spectra with two components which occur at 83.65 and 84.00 eV for the as-deposited sample and do not shift upon annealing. The intensities also remain the same. The valence band features are very similar to the added spectra and no discernible changes are noted for the annealed sample. These results indicate that no alloying is detected. The core level positions agree exactly with those determined for the separate 3 ML Au on Ru(001) system, with a surface and bulk Au component. The valence band features show no shift of the Au *d*-band components or *d-d* repulsion which again indicates that no alloying has occurred. However, we cannot rule out that the buried Cu layer has intermixed with the first Au layer since the buried alloy would have little contribution to either the Au 4*f* or valence band emission because of escape depth considerations. Based on heats of adsorption and the behaviour seen for the monolayer coverages in the SS Seya study it would be expected that the Cu layer will intermix with

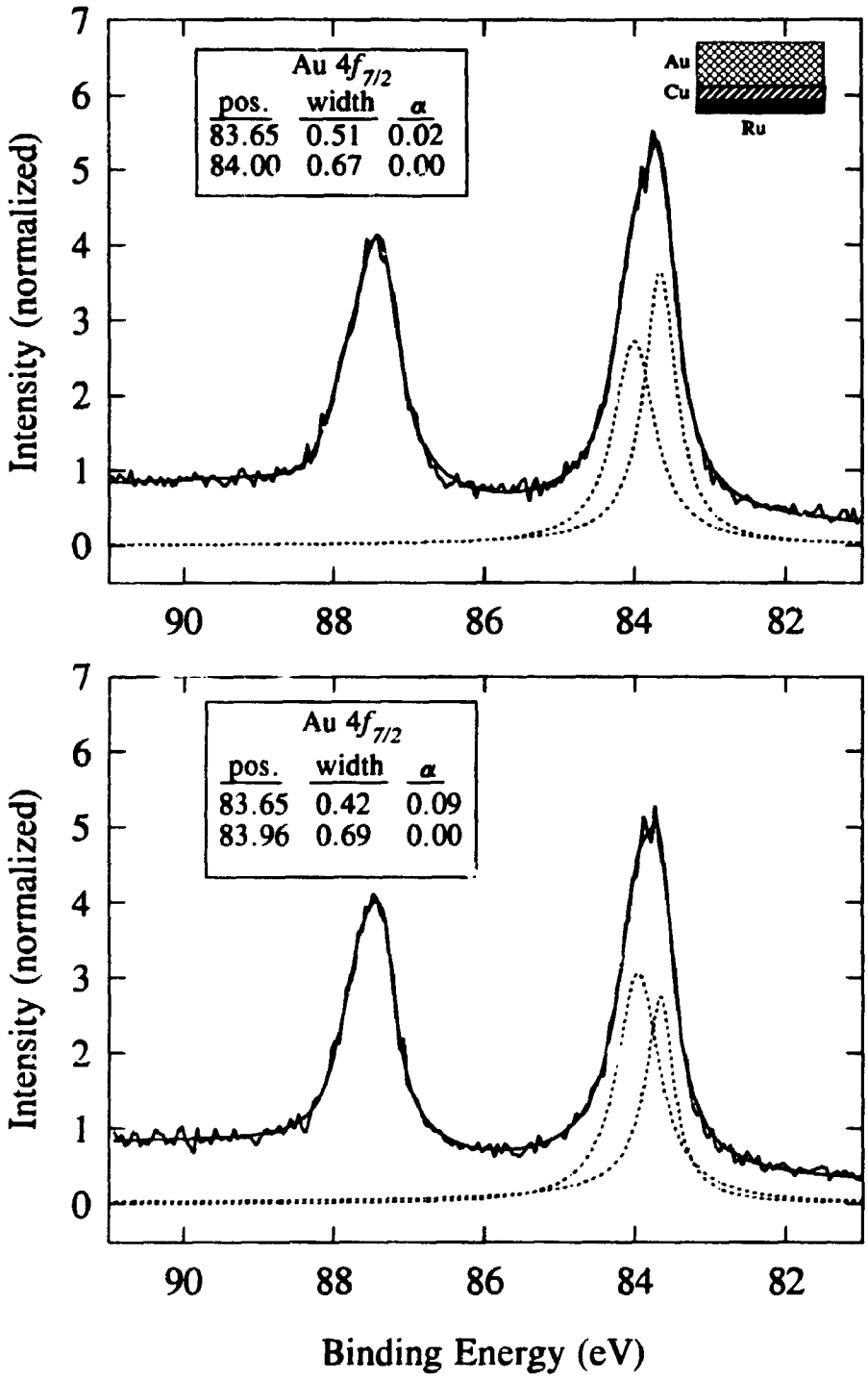

Figure 7.18: Au 4*f* spectra for 3 ML Au/1 ML Cu on Ru(001). Spectra of as-deposited system (top) and after annealing for 5 min at 600 K (bottom).

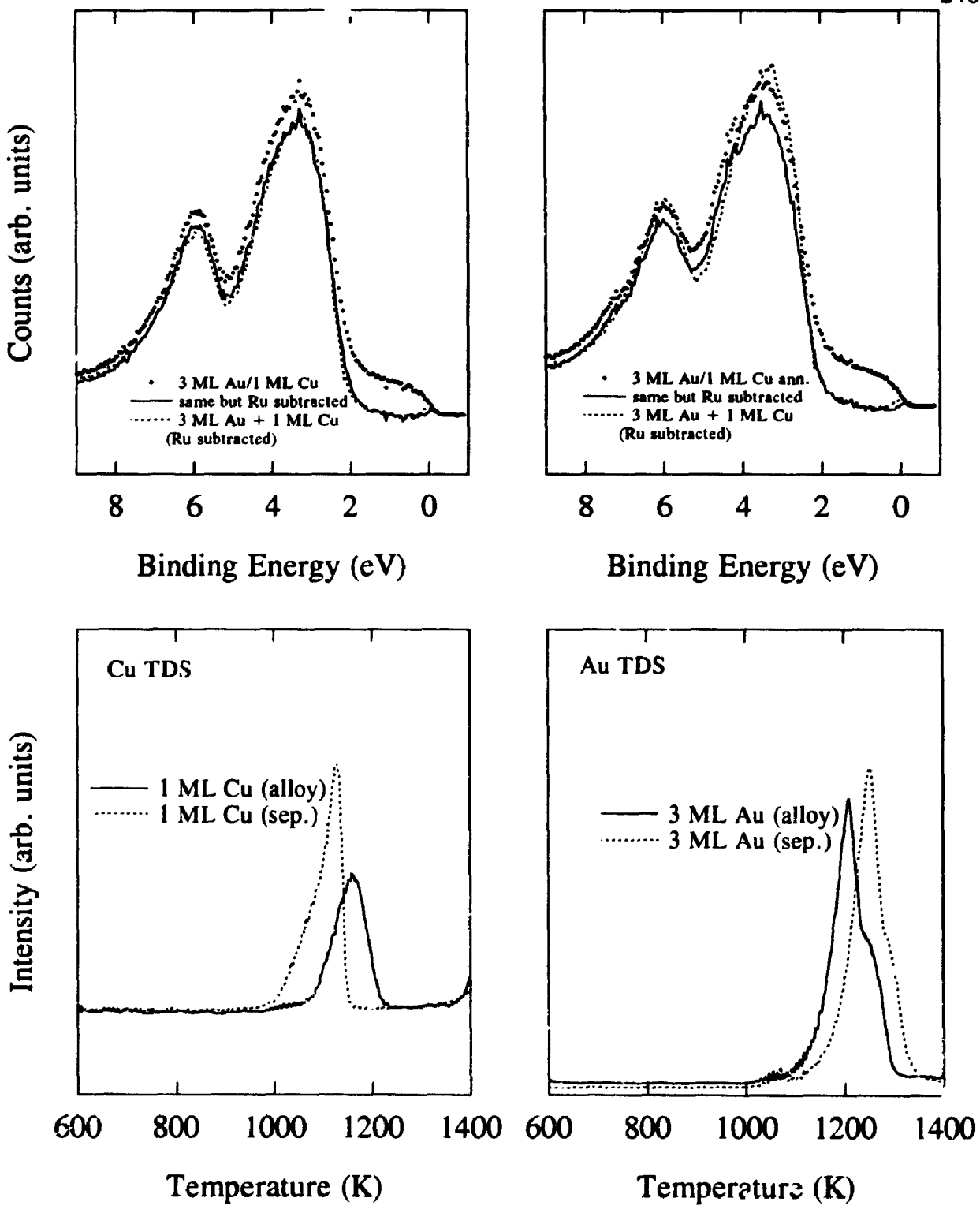

Figure 7.19: Valence band and TDS spectra for 3 ML Au/1 ML Cu on Ru(001). Spectra of as-deposited system (top left) and after annealing for 5 min at 600 K (top right). TDS results at bottom.

the first Au layer. The TDS results are the same as discussed for the 1 ML Cu/3 ML Au on Ru(001) system.

1 ML Au and 1 ML Cu

Figures 7.20 and 7.21 outline the results for the Au 4*f* core level and valence band behaviour for the 1 ML Au/1 ML Cu on Ru(001) system. The fitted Au $4f_{7/2}$ peak positions are 83.92 eV for the as-deposited sample and 83.89 eV after annealing which is not much different than the value of 83.88 eV given for the separate 1 ML Au on Ru(001) system. The valence band spectra, however, do show a small shift of the Au $5d_{3/2}$ component away from the Fermi level and an increased signal in the 4 to 5 eV region indicating the movement of the Au $5d_{5/2}$ component reducing the apparent Au *d*-band splitting. Further movement is seen upon annealing, especially of the Au $5d_{5/2}$ component. This indicates that alloying has occurred and that upon annealing there is a further reduction in the Au-Au interaction indicating increased alloying behaviour. This is exactly what was seen for the SS Seya study and gives us further confidence that we have correctly calibrated the coverages in the SS Seya study. The TDS spectra follow the exact behaviour as described in the TDS study completed after the SS Seya run. Although the Au 4*f* core levels are slightly higher than the separate coverage of 1 ML on Ru(001) they are the same within experimental error. This indicates that the alloy formed has a high Au concentration and therefore only a small core level shift would be expected. From the previous coverages it has been shown that a high Cu concentration (large degree of Au-Au dilution) is required before a core level shift would

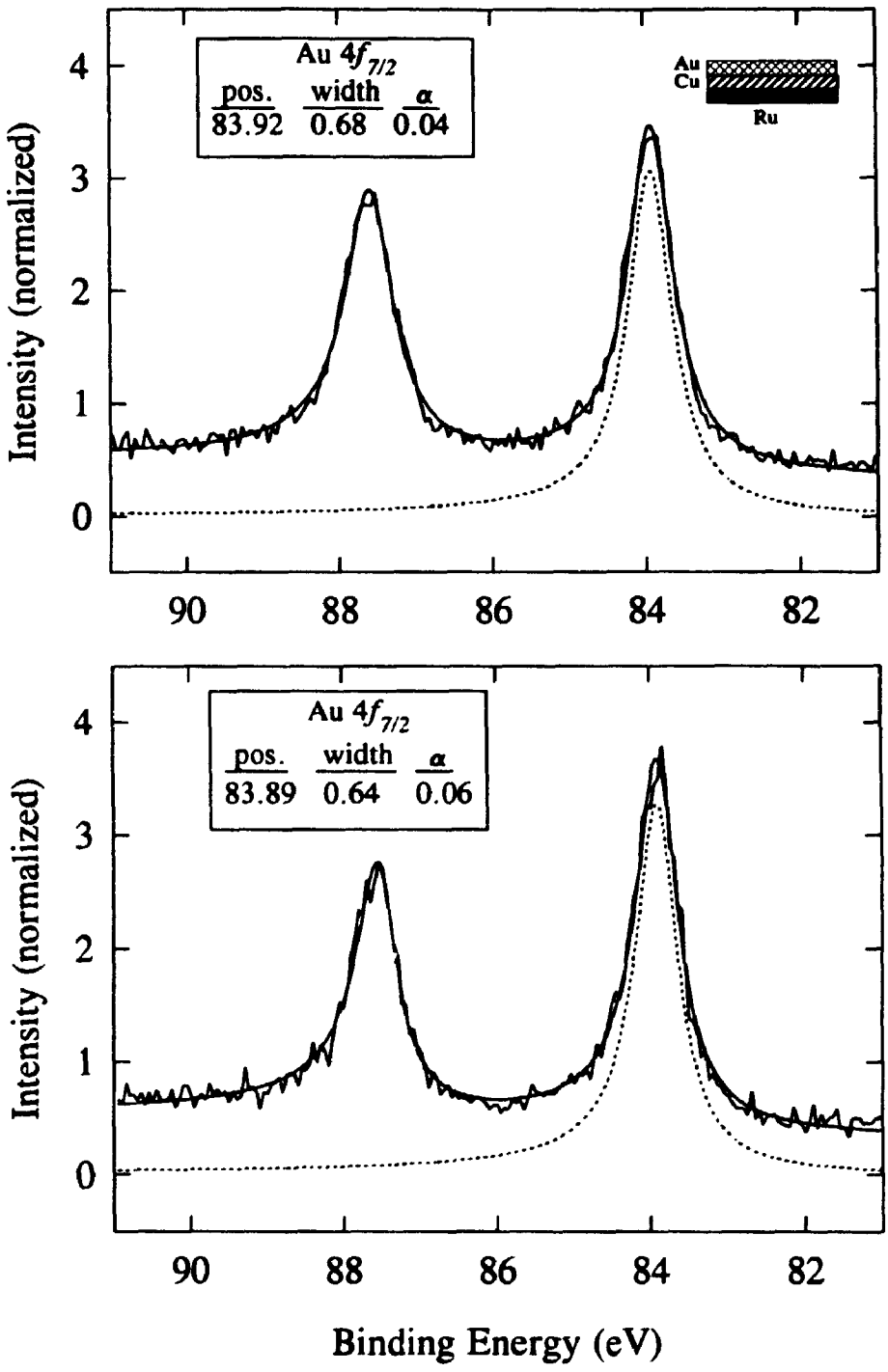

Figure 7.20: Au 4*f* spectra for 1 ML Au/1 ML Cu on Ru(001). Spectra of as-deposited system (top) and after annealing for 5 min at 600 K (bottom).

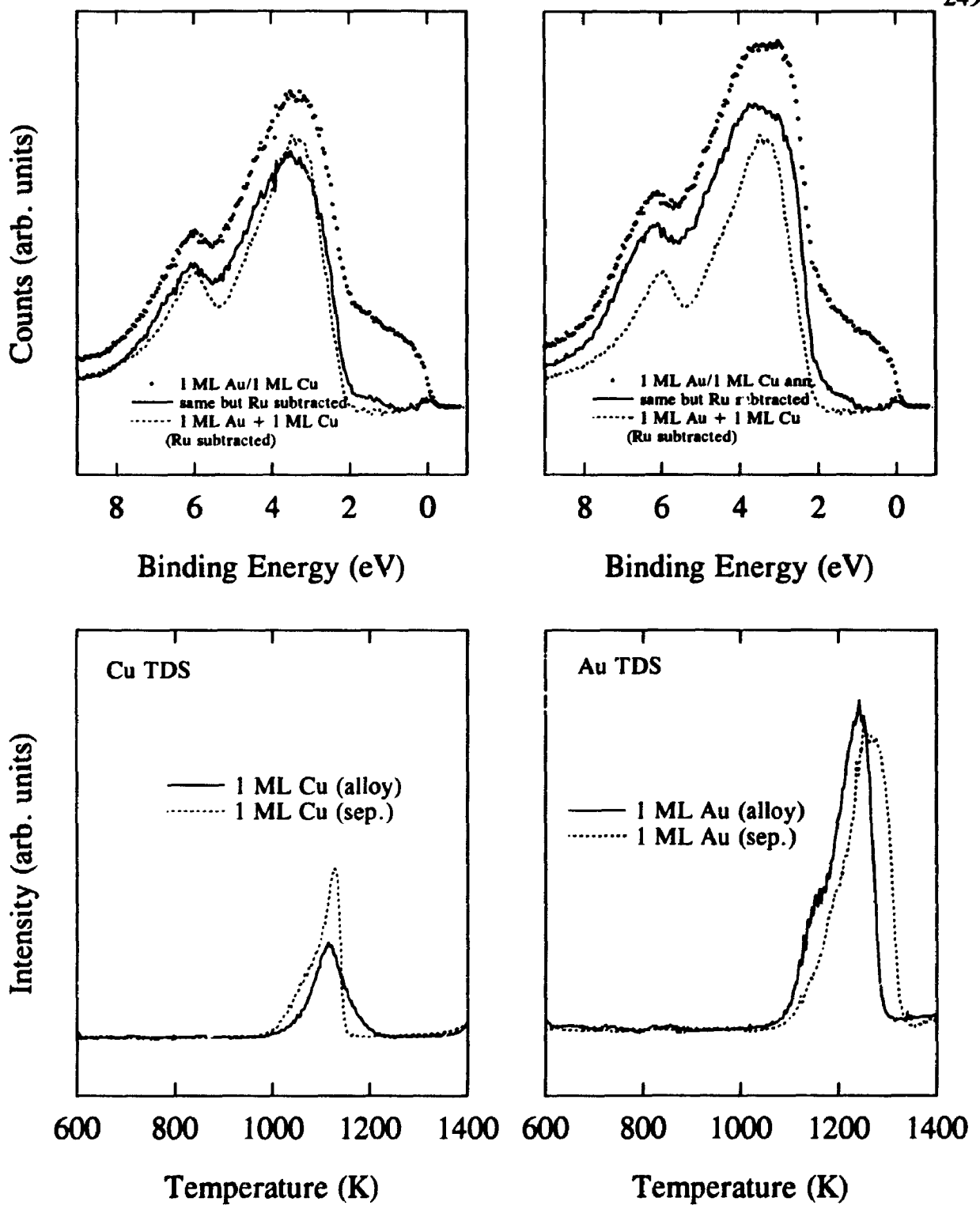

Figure 7.21: Valence band and TDS spectra for 1 ML Au/1 ML Cu on Ru(001). Spectra of as-deposited system (top left) and after annealing for 5 min at 600 K (top right). TDS results at bottom.

be detectable. The reduction in the intensity from the separate 1 ML Au coverage does indicate that there is Au migration from the surface towards the Ru interface.

Figures 7.22 and 7.23 outline the results for the reverse deposition of 1 ML Cu/1 ML Au on Ru(001). The Au $4f_{7/2}$ core level is found at 83.92 eV with no shift upon annealing. The valence spectra show the same movements of the Au *d*-band components with no obvious changes visible after annealing. If we compare these valence band spectra with that of the annealed 1 ML Au/1 ML Cu on Ru(001) annealed spectra we find them to be identical, which is a feature that was noted in the SS Seya study. It is clear then, when the first species is Au, Cu deposition forms a stable alloy as indicated by the lack of changes in the electronic behaviour upon annealing. To reach the same alloy when the first species is Cu, annealing is required. The reason for this behaviour is unclear since, based on heats of adsorption, the movement of the Au atoms through Cu to the Ru interface should be the most active process. The TDS results again are similar to the reverse deposition TDS results with the exception that in this case we seem to have slightly higher than single monolayer coverages of both species.

Conclusions

We have shown that in all the cases studied here that alloying (intermixing) does occur (with the possible exception of the 3 ML Au/ 1 ML Cu on Ru(001) coverage). For the higher coverages this behaviour is different than exhibited by the bulk. The role of the substrate is clearly important in activating the alloying process. For the higher coverages, because of the growth mode of both Au and Cu, the adsorbed monolayer can

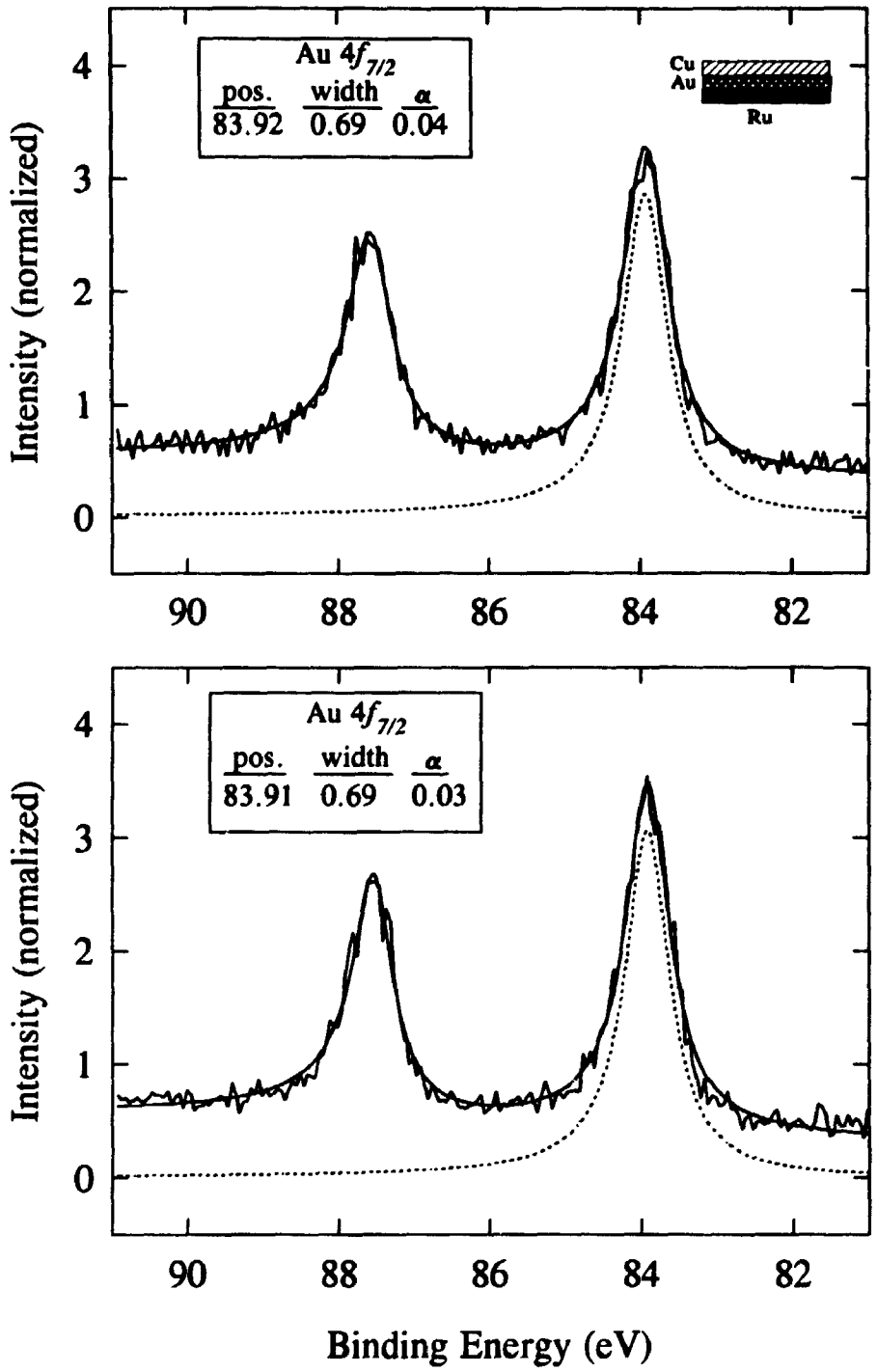

Figure 7.22: Au 4*f* spectra for 1 ML Cu/1 ML Au on Ru(001). Spectra of as-deposited system (top) and after annealing for 5 min at 600 K (bottom).

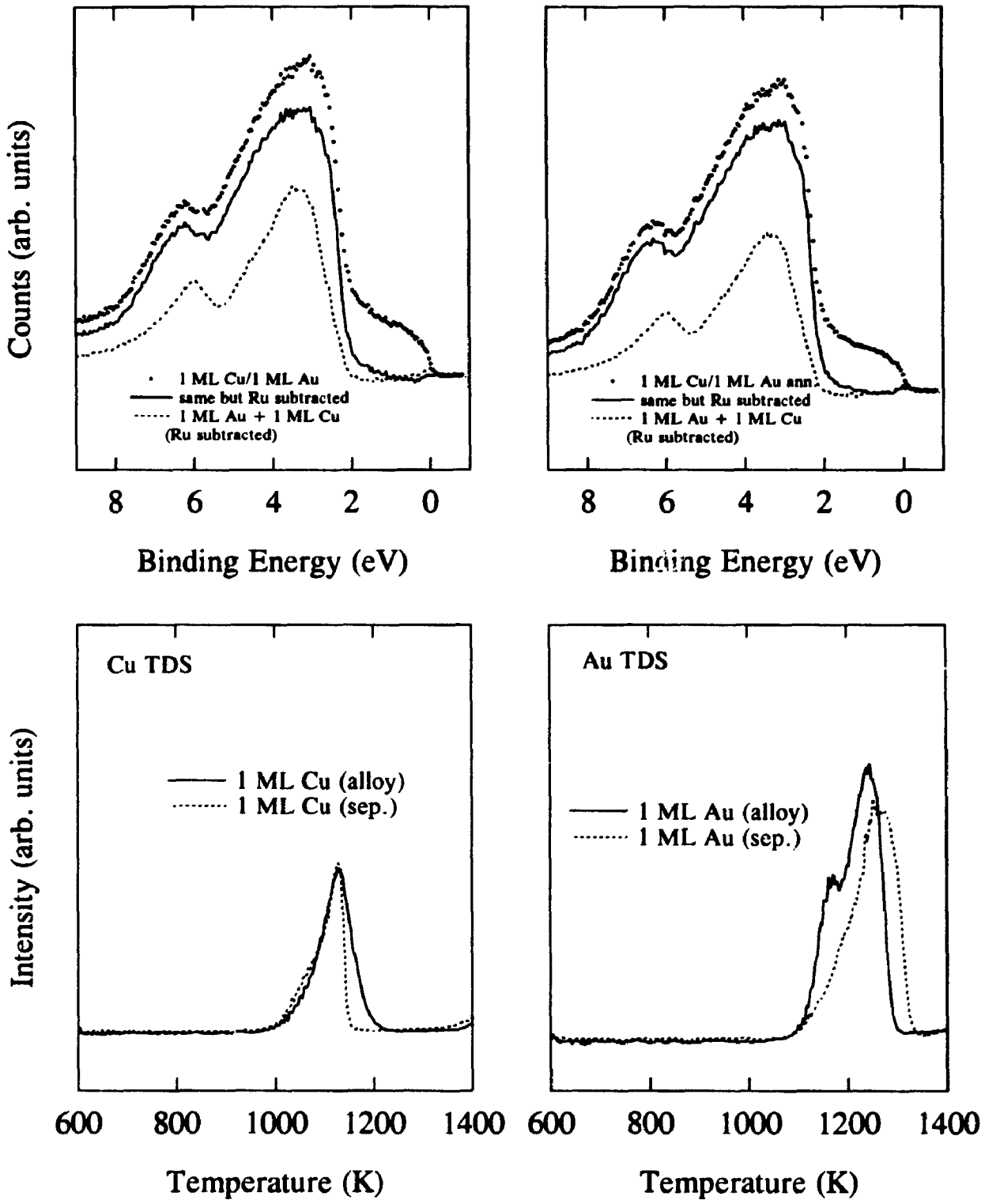

Figure 7.23: Valence band and TDS spectra for 1 ML Cu/1 ML Au on Ru(001). Spectra of as-deposited system (top left) and after annealing for 5 min at 600 K (top right). TDS results at bottom.

still be deposited within one or two layers of the substrate and therefore be under its influence.

The core level shifts did not reveal the expected information in view of the charge compensation model. Although some positive Au 4*f* binding energy shifts were observed it is clear that a high Cu:Au ratio is required for a core level shift to become detectable. With monolayer coverages the Au-Cu signal to background ratio is inherently higher and small shifts will be hard to determine since our confidence in the fitting will be lower. Therefore using the bulk core level shifts for the various stoichiometries of Au-Cu alloys to try and determine the surface composition is not feasible at this time. There is the added complication of the contribution to the photoelectron signal from chemically different Au species making the deconvolution of the signal complicated. This is a problem not experienced in the bulk since all the Au and Cu species are equivalent. The exception, of course, is the surface contribution and possible surface segregation. To ever determine quantitative values for the amount and nature of charge transfer using the conventional model a few parameters must first be determined. The work function of each coverage must be measured since they will vary from the bulk values. A measure of the conduction charge transfer must be made. Lastly, volume effects must be determined since the physical structure of the alloy is partially determined by the substrate and therefore will not necessarily have bulk lattice parameters. A possible experiment, that was mentioned previously, that could be performed would be a SEXAFS study which could directly probe the changes in the unoccupied density of states at both the Au and Cu sites and also give structural information from the EXAFS oscillations.

The valence band behaviour, however, was clearly the strongest measure of the alloying process. The use of bulk valence band parameters was invaluable in assigning the spectra. Since the photon energy of the Grasshopper beamline is limited to 50 eV or so it would advantageous to perform high resolution valence band studies on these alloys using a beamline such as the SS Seya.

It is clear that these surface alloys are unique and exhibit behaviour which is different from that of the bulk. Physical characterization of these systems is required (LEED, ion beam, STM, etc.).

7.4 Brookhaven XPS Data

Au-Cu coverage studies similar to those performed on the Grasshopper beamline were done using a Mg X-ray source. The XPS studies were performed mainly to complement the high resolution Au 4*f* data and also to probe the Cu 2*p* core levels which were not attainable using the Grasshopper monochromator. Also of interest is a temperature dependent (liquid nitrogen temperatures and higher) study of the behaviour of a monolayer coverage of Au and Cu. The high electron escape, low coverages, and low cross-section did not allow for extracting any useful information from the valence band spectra. The low resolution of the source coupled with the bulk sensitivity of the technique does not allow for extraction of useful data from the Au 4*f* core level positions. An example of this is the fact that we could not resolve more than a single component from the multilayer Au coverages in the Au 4*f* spectra. TDS measurements were also performed for calibration of the coverages and the study of the alloys desorption behaviour. The results are consistent with those seen previously and therefore will not be examined here. For these reasons we will focus mainly on the Cu 2*p* core level results (keeping in mind that we will also be unable to resolve chemically different Cu species at multilayer coverages) and the temperature dependent study.

Cu $2p_{3/2}$ Core Level Alloy Study

As was stated in the introduction a series of coverages of Au and Cu on Ru(001), similar to those studied in the Grasshopper study, were examined for changes to the Cu

$2p_{3/2}$ core level position. Depositions were carried out at 400 K and measurements performed at room temperature. Each alloy sample was subsequently annealed to 800 K for two minutes. Figure 7.24 shows the Cu $2p$ spectrum of a monolayer coverage (top) and a 3 ML coverage (bottom) with the associated fit of the $2p_{3/2}$ core level. Calibration of all these spectra were performed by determining the Ru $3d$ core level position which has been referenced to the Fermi level. It is assumed that the majority of this signal has a contribution from bulk Ru and therefore is invariant in this study.

The representative Cu $2p$ core level results of the alloy studies are given by Figures 7.25 to 7.27. Table 7.3 summarizes the Cu $2p_{3/2}$ and Au $4f_{7/2}$ core level positions and intensities of the of these emission levels of the separately deposited and co-deposited species.

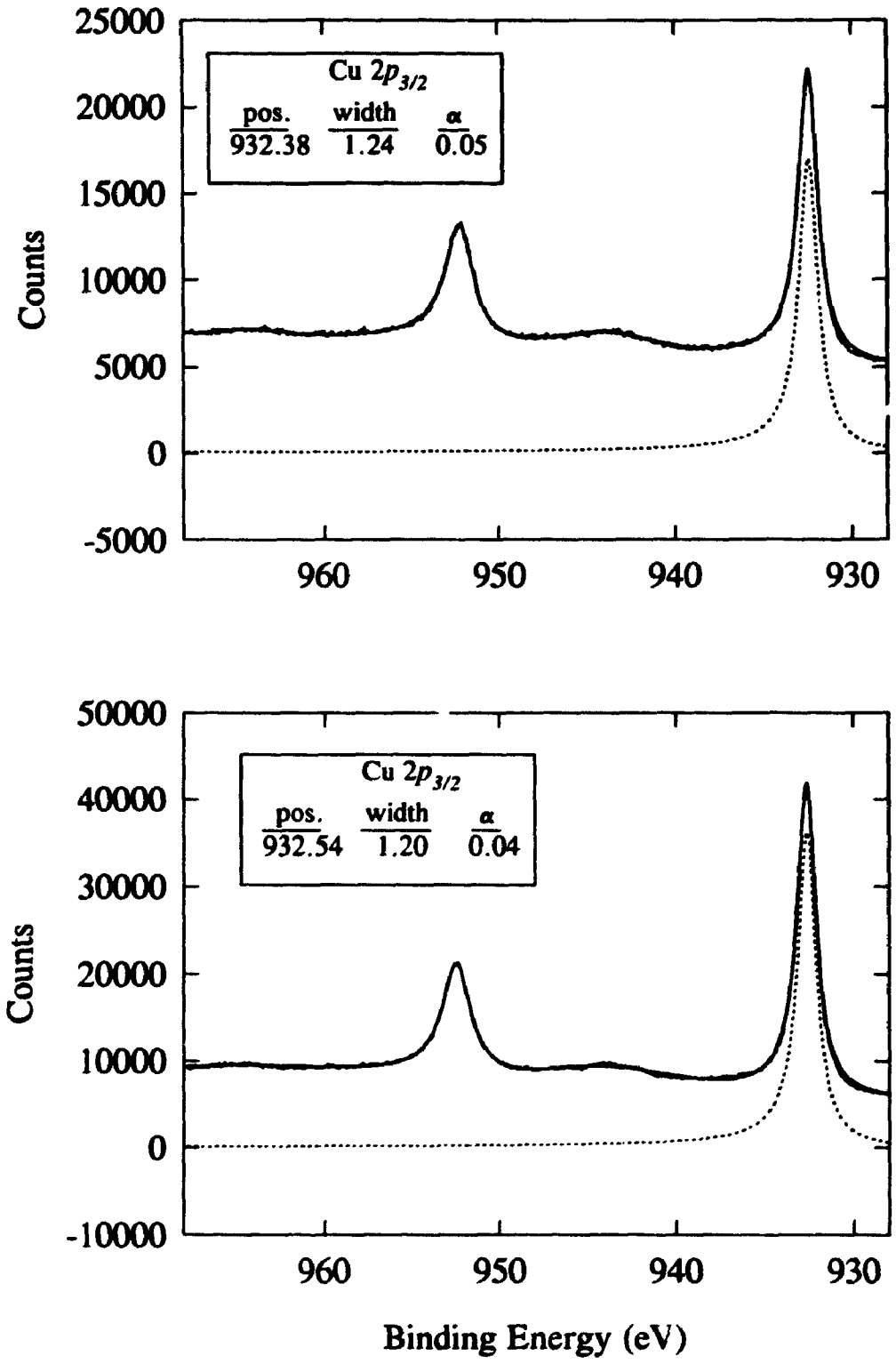

Figure 7.24: Cu $2p$ spectra for 1 ML Cu (top) and 3 ML Cu (bottom) on Ru(001).

Coverage	Au $4f_{7/2}$ (±0.05 eV)	Cu $2p_{3/2}$ (±0.1 eV)
1 ML Au	83.87 (956)	-----
3 ML Au	83.95 (2 380)	-----
1 ML Cu	-----	932.38 (17 000)
3 ML Cu	-----	932.54 (36 000)
1 ML Cu/1 ML Au	84.07 (915)	932.37 (11 590)
annealed 800 K	84.07 (955)	932.33 (12 320)
1 ML Au/1 ML Cu	84.05 (944)	932.40 (14050)
annealed 800 K	84.10 (915)	932.34 (14 470)
1 ML Au/3 ML Cu	84.09 (826)	932.52 (28 035)
annealed 800 K	84.24 (630)	932.43 (23 300)
3 ML Cu/1 ML Au	84.30 (560)	932.49 (32 700)
annealed 800 K	84.17 (440)	932.46 (20 900)
1 ML Cu/3 ML Au	84.05 (2570)	932.35 (12 500)
annealed 800 K	84.06 (2300)	932.31 (8170)
3 ML Au/1 ML Cu	84.01 (2330)	932.37 (5160)
annealed 800 K	84.06 (1850)	932.30 (6670)

Table 7.3: Au $4f_{7/2}$ and Cu $2p_{3/2}$ core level positions for a number of Au-Cu coverages. Intensities are given in the parenthesis.

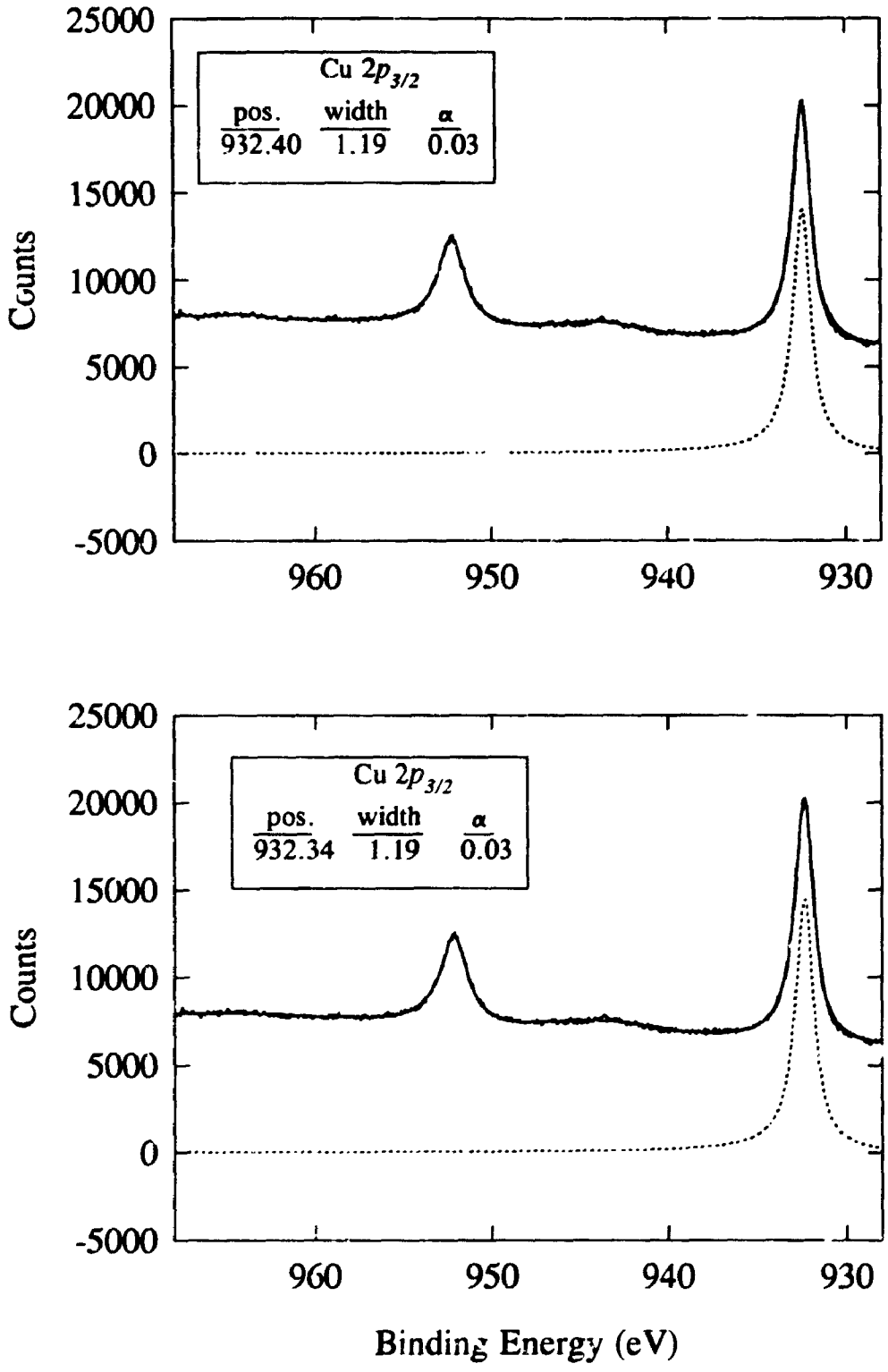

Figure 7.25: Cu 2*p* spectra for 1 ML Au/1 ML Cu on Ru(001). Spectra of as-deposited system (top) and after annealing for 5 min at 600 K (bottom).

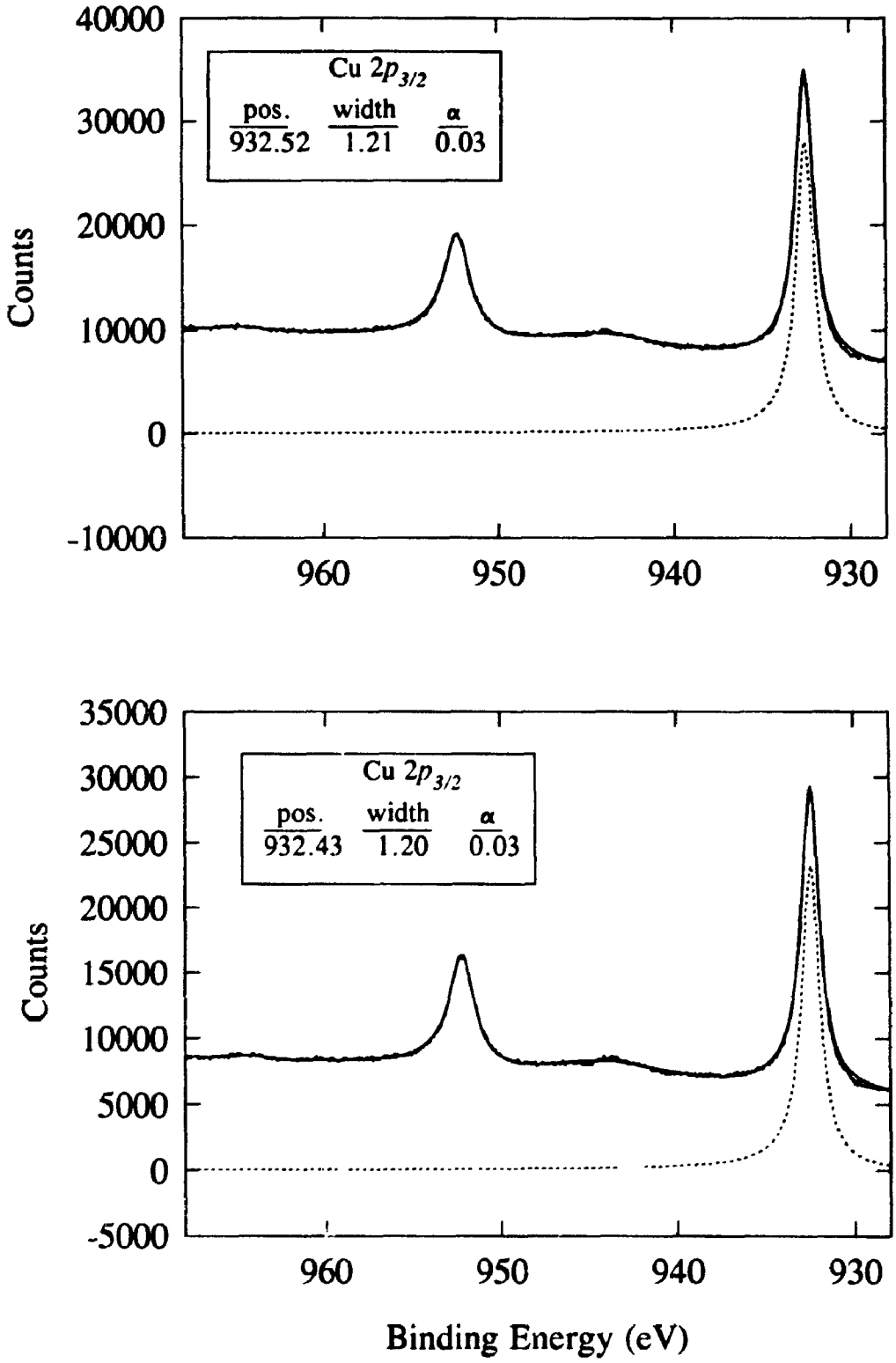

Figure 7.26: Cu 2*p* spectra for 1 ML Au/3 ML Cu on Ru(001). Spectra of as-deposited system (top) and after annealing for 5 min at 600 K (bottom).

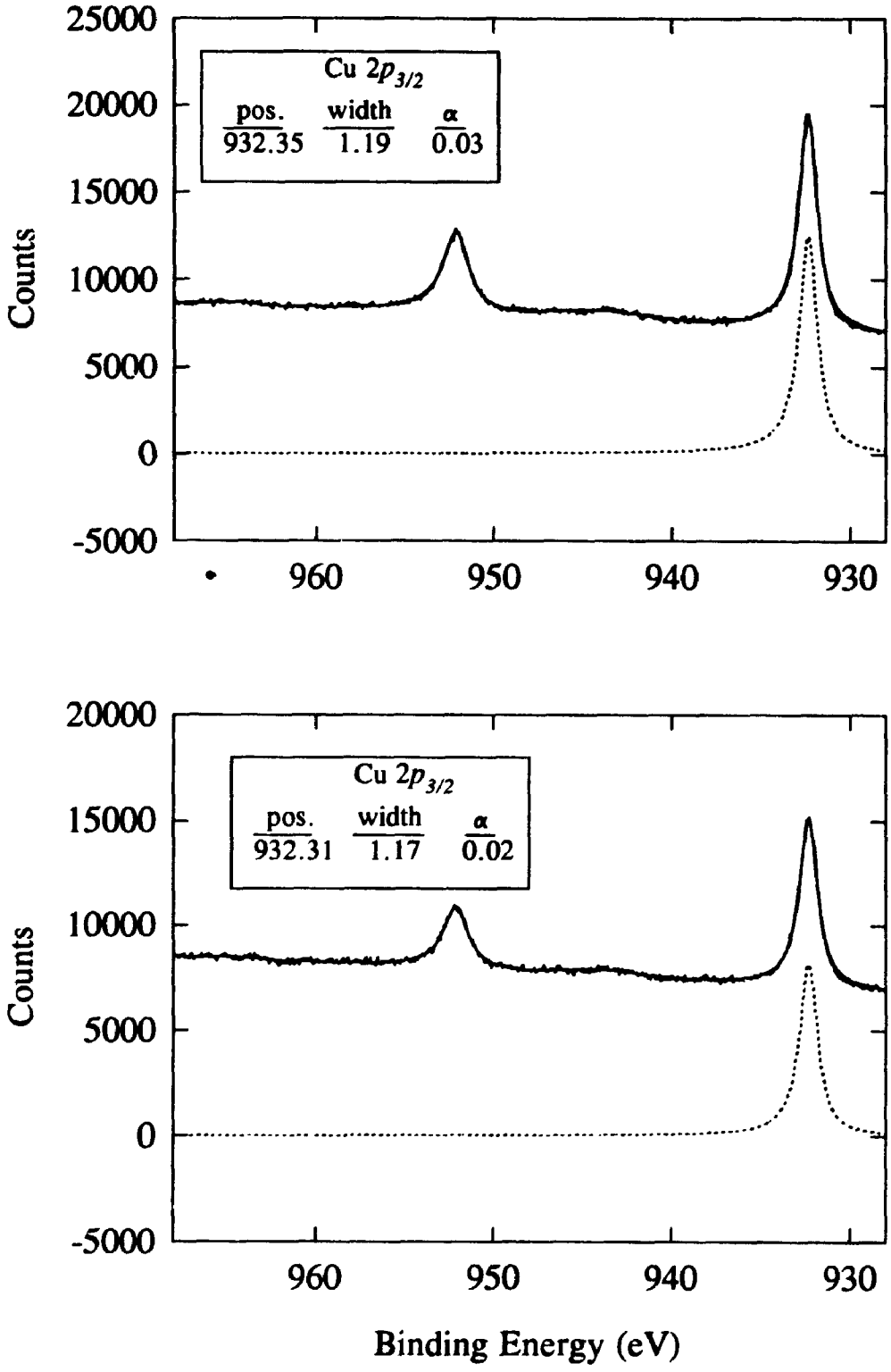

Figure 7.27: Cu $2p$ spectra for 1 ML Cu/1 ML Au on Ru(001). Spectra of as-deposited system (top) and after annealing for 5 min at 600 K (bottom).

We will first examine the numbers for the separate adsorption of the components on Ru(001). Focussing briefly on the Au $4f_{7/2}$ core level results we see that the values are similar as those seen from the higher resolution Grasshopper study. The value for the 3 ML Au deposition is somewhat smaller than for bulk Au which is due to the fact that there is a lower energy surface contribution, as seen in the Grasshopper study, which is not resolvable. The amount of this surface contribution to the overall photoelectron signal will be smaller since the photoelectrons have a much higher electron escape depth upon excitation with an X-ray source. The position of the 1 ML Cu peak is found to be at 932.38 eV which is smaller than the value found for bulk Cu in the XPS study of 932.53 eV. The 3 ML coverage of Cu correlates very well with the bulk Cu value although the small shift to lower binding energies from a surface component is not clearly evident. This may be due to the fact that our uncertainty for the Cu core level positions will be slightly higher since the linewidth is quite large ($\sim$ 1.2 eV) and that the surface core level shift for Cu on Cu(bulk) is smaller (0.24 eV)[26] than that of Au on Au(bulk) (0.35 eV).

The trends for the Au 4*f* core level positions of the as-deposited and annealed samples are similar to that seen in the Grasshopper study. The monolayer values are somewhat higher and the 3 ML Cu on 1 ML Au system shows a reduction, upon annealing, which is not seen in the previous study. The intensities can be compared directly with reasonable confidence ($\pm$10%) since the flux from the XPS source is stable. These relative changes in intensities give further support to the movement of the Au atoms as described previously. For example, in the 1 ML Au/3 ML Cu system not only

is there an increased binding energy shift upon annealing, indicating the creation of a higher ratio Cu-Au alloy, but there is a corresponding reduction in the Au 4*f* signal indicating further migration of Au atoms (Another factor which can contribute to the reduction of the intensity of the photoelectron signal is large 3-D cluster formation, upon annealing, evidence for which will be shown below.).

The pattern for the Cu $2p_{3/2}$ positions and intensities is similar. In the monolayer Au-Cu system there is a reduction in the Cu intensity, as compared to the separate 1 ML Cu deposition, with a small shift to lower binding energy, indicating further alloying following the charge compensation model, which is more evident for the 1 ML Au/1 ML Cu system. The intensities upon annealing remain similar within experimental uncertainties. For the 1 ML Au/3 ML Cu system again we see attenuation of the Cu signal as expected with a bulk core level value. In the Grasshopper study we had noted that a high Au concentration alloy had been formed upon deposition and that upon annealing Au further penetrates the Cu lattice forming a lower concentration Au alloy. In light of this we would, therefore, expect a large shift to lower binding energies for the Cu core level. This is not seen due to the fact that the XPS signal is dominated by the Cu atoms in the bulk and Ru interface which have not been perturbed, as of yet, by interdiffusion of Au atoms. This occurs upon annealing at which point the expected shift is experienced. For the 3 ML Cu/1 ML Au system the Cu core level shift is small and little shift is experienced upon annealing. This is attributed to the formation of a stable Au-Cu alloy at the Ru interface. In both these systems there is a reduction in the intensity not only of Cu but also Au upon annealing. This implies that there is

attenuation of the Au and/or Cu signal due to large 3-D cluster formation. Evidence for this is the increase of the Ru 3*d* signal in all the >1 ML coverages, upon annealing. STM results have shown this behaviour for Au on Ru(001.)[2] In the Grasshopper study this was probably not as evident due to the lower annealing temperature (600 K versus 800 K). The last two systems, 1 ML Cu/3 ML Au and 3 ML Au/1 ML Cu, both show a negative binding energy shift which increases upon annealing. Although there is the similar problem of cluster formation upon annealing, the 3 ML Au/1 ML Cu system shows an increased Cu intensity indicating migration of Cu from the Ru interface.

Temperature Dependent Core Level Behaviour of 1 ML Au/1 ML Cu

A temperature dependent study was performed on the 1 ML Au/1 ML Cu system. A monolayer of Cu was deposited at liquid nitrogen temperatures followed by a monolayer of Au. The system was annealed in 50 K steps for two minutes to 350 K with measurements taken at liquid nitrogen temperatures. Figure 7.28 summarizes the Cu $2p_{3/2}$ and Au $4f_{7/2}$ core level positions as a function of the anneal temperatures. At low temperatures both the Cu and Au core levels remain relatively fixed until an anneal temperature of 200 K is reached. At this point there is a small negative binding energy shift for the Cu core level accompanied by a larger positive binding energy shift for the Au core level. With higher temperatures the Cu core level does not decrease further but there is a continued increase in the Au core level position.

The Au core level shifts indicate the beginning of the alloying process at ~200 K which is governed by the increased mobility of Au and Cu atoms as the temperature is

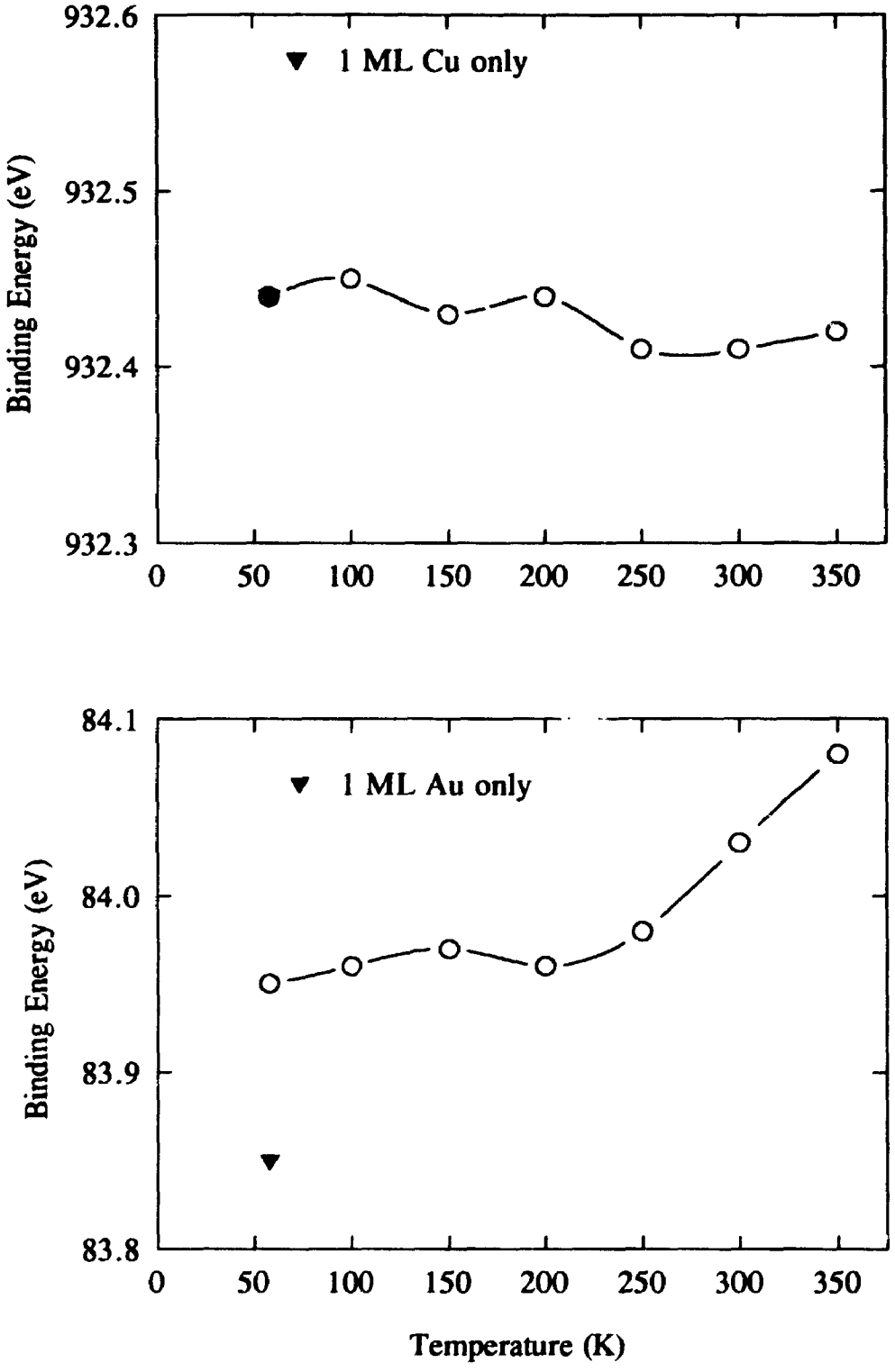

Figure 7.28: Core level positions of 1 ML Au/1 ML Cu on Ru(001) as a function of anneal temperature. Cu *2p3/2* position at top and Au $4f_{7/2}$ position at bottom.

increased. The Ru 3*d* signal remains constant indicating no significant 3-D island formation. The core level positions at 350 K are similar to those exhibited by the 1 ML Au/1 ML Cu system deposited at 400 K. The Cu core level shifts, although they appear to shift in the appropriate direction, are too small, within experimental uncertainty, to base any conclusions upon.

Direct comparison to the mechanism of alloy formation at elevated temperatures cannot be made. The deposition temperature can effect the growth mode of the adsorbate. At low temperatures the mobility of the adsorbate is such that wetting of the surface can be incomplete and there could possibly be significant second layer growth for monolayer coverages. It is for that reason that the Au atoms impinging on the surface cannot all be assumed to interact directly with a Cu overlayer. Nevertheless, it is evident that alloy formation has occurred at low temperatures, significantly lower than is observed for the bulk species. This points to the role of the substrate surface in lowering the barriers (activation and heats of adsorption) to alloy formation.

7.5 Conclusions

From these initial valence band and core level studies on co-deposited Au-Cu overlayers it is clear that much further work is required. Paramount to this is the determination of the exact structure of these samples since each deposition forms a unique system which is dependent on the temperature, amount and order of deposition, and the anneal temperature. Possible experiments to determine the structure have been outlined in the Grasshopper study. The bulk studies have been invaluable in making some rudimentary conclusions on the electronic behaviour of the co-deposited systems, not so much based on the core level shifts but on the valence band behaviour.

The interesting desorption behaviour of the co-deposited species also warrants further study. Thermodynamic and kinetic parameters can be determined by a detailed TDS study.

Lastly, mention must be made on the reactivity of these surface species. One of the initial objects of these studies was to eventually be able to characterize the reactivity of these systems, in terms of their catalytic behaviour, to various adsorbates such as CO and O_2. Several studies were performed not only on these surface species but also on the bulk alloy foils. Both CO and O_2 adsorption were attempted at various temperatures and pressures. For the surface species, although O_2 adsorption occurs on Ru(001) at dosages less than 6 Langmuirs, no such adsorption (or reaction) was detected for any of the co-deposited species at room temperature or on the annealed 1 ML Au/1 ML Cu system at liquid nitrogen temperatures even with higher pressures (although low doses

of O_2 will diffuse through a monolayer Cu to the transition metal interface for a Re(001)[27] and W(110)[28] substrate). Similarly, no reaction of the bulk alloy foils was observed with CO and O_2 at elevated temperatures.

7.6 References

1. S.B. DiCenzo, S.D. Berry, and E.H. Hartford, Jr., Phys. Rev. B **38**, 8465 (1988).

2. R.Q. Hwang, J. Schröder, C. Günther, and R.J. Behm, Phys. Rev. Lett. **67**, 3279 (1991).

3. J.E. Houston, C.H.F. Peden, and P.J. Feibelman, Surf. Sci. **192**, 457 (1987).

4. T.K. Sham, T. Ohta, T. Yokoyama, Y. Kitajima, M. Funabashi, N. Kosugi, and H. Kuroda, J. Chem. Phys. **88**, 475 (1988).

5. T.K. Sham, J. Hrbek, and K.H. Tan, Surf. Sci. **236**, 259 (1990).

6. J.E. Houston, C.H.F. Peden, D.S. Blair, and D.W. Goodman, Surf. Sci. **192**, 457 (1986).

7. F.M. Hoffman and J. Paul, J. Chem. Phys. **86**, 2990 (1987).

8. C.J. Smithells, Metals: Reference Book Volume I (London, Butterworths, 1967) pg. 232.

9. K. Markert, P. Dolle, J.W. Niemantsverdriet, and K. Wandelt, J. Vac. Sci. Technol. A **5**, 2849 (1987).

10. K. Wandelt, J.W. Niemantsverdriet, P. Dolle, and K. Markert, Surf. Sci. **213**, 612 (1989).

11. M. Skottke-Klein, A. Böttcher, R. Imbeck, S. Kennou, A. Morgante, and G. Ertl, Thin Solid Films **203**, 131 (1991).

12. J.A. Rodriguez, J. Hrbek, M. Kuhn, and T.K. Sham, J. Phys. Chem. **97**, 4737 (1993).

13. J.A. Rodriguez, J. Hrbek, M. Kuhn, and T.K. Sham, J. Vac. Sci. Technol. A **11(4)**, 2029 (1993).

14. P.H. Citrin and G.K. Wertheim, Phys. Rev. **27**, 3176 (1983).

15. L.H. Reed and L.C. Allen, J. Phys. Chem. **96**, 157 (1992).

16. J. Hinze and H.H. Jaffe, J. Am. Chem. Soc. **84**, 540 (1962).

17. J. Hinze, M.A. Whitehead, and H.H. Jaffe, J. Am. Chem. Soc. **85**, 148 (1963).

18. J.A. Rodriguez, R.A. Campbell, and D.W. Goodman, J. Phys. Chem. **95**, 5716 (1991).

19. J.A. Rodriguez and D.W. Goodman, Science **257**, 897 (1992).

20. S. Doniach and M. Šunjić, J. Phys. C, **3**, 285 (1970).

21. P.H. Citrin, G.K. Wertheim, and Y. Baer, Phys. Rev. Lett. **35**, 885 (1975).

22. S. Hüfner, G.K. Wertheim, and J.H. Wernick, Sol. St. Com. **17**, 417 (1975).

23. P.H. Citrin, G.K. Wertheim, and Y. Baer, Phys. Rev. B **16**, 4256 (1977).

24. M. Kuhn, A. Bzowski, and T.K. Sham, unpublished results.

25. T.K. Sham and J. Hrbek, unpublished results.

26. P.H. Citrin, G.K. Wertheim, and Y. Baer, Phys. Rev. B. **27**, 3160 (1983).

27. J.A. Rodriguez, R.A. Campbell, and D.W. Goodman, Surf. Sci. **244**, 211 (1991).

28. I. Hamadeh and R. Gomer, Surf. Sci. **154**, 168 (1985).